



# **Microwave Antennas for Biomedical Applications**

A thesis submitted in fulfilment of the requirements for the degree of Doctor of Philosophy

Md Rokunuzzaman Robel

Bachelor of Engineering (Honours) Electronics majoring in Microwave and Communications, Multimedia  
University, Malaysia

Master of Science (Space Science), National University of Malaysia, Malaysia

School of Engineering

College of Science, Engineering and Health

RMIT University

September, 2019

(Blank Page)

# Declaration

I certify that except where due acknowledgement has been made, the work is that of the author alone; the work has not been submitted previously, in whole or in part, to qualify for any other academic award; the content of the thesis is the result of work which has been carried out since the official commencement date of the approved research program; any editorial work, paid or unpaid, carried out by a third party is acknowledged; and, ethics procedures and guidelines have been followed.

I acknowledge the support I have received for my research through the provision of RMIT PhD International Scholarship (RPIS).

Md Rokunuzzaman Robel

06-September-2019

# Acknowledgements

In the name of Allah, the most Benevolent, the most Merciful. By the Grace of Almighty Allah, I have been equipped with the means and determination to complete this research study.

I would like to express my sincerest gratitude and indebtedness to my supervisor, Associate Professor Dr. Wayne S. T. Rowe for his tireless support, without which this thesis would not even be conceived. He has been an ideal role model and guided my research work with a firm, yet nurturing hand. His technical insight into antenna technology has been critical at every step of this thesis.

I would like to extend my deepest gratitude, my good friend Asif Ahmed for all the support he provided me to reach my research goals. Sincerest thanks to all my friends and colleagues at RMIT University. I also would like to extend my sincerest thanks to all the students and staff of the School of Engineering at RMIT University.

Finally, I would like to thank my father, Md. Delowar Hossain, and mother, Rabeya Begum for all their love and encouragement they provided throughout my life. My wife Jamila Fairouz Tuli and my daughter Ruwaida Zaman have always been a constant source of guidance and affection. They have driven me towards greater achievements and higher goals. It is a pleasure to dedicate this thesis to my loving family.

# Abstract

Medical diagnosis is one of the key steps to determine the problem of the human body. The current diagnostic tools are expensive, bulky and long exposure to some of these diagnostic tools can be injurious to the human body. Hence, researchers are now exploring through different possibilities to replace current diagnostic tools. Microwave regime is one of the potential candidate to replace current diagnostic system providing with a chip, portable system suitable for the human body. One of the fundamental tool for a microwave diagnostic system is microwave antenna. The current findings on designing microwave antennas for biomedical diagnosis lacks due to low microwave power penetration inside the human body, high specific absorption rate (SAR), low directivity and compactness. This thesis aims on improving the microwave penetration inside the human body and develop antennas that can perform efficiently for biomedical diagnosis application.

A multi-layer reflection model is investigated for evaluation of the combined material characteristics of different lossy human tissues, along with the enhanced antenna designs, suitable for biomedical application, operating on-body and as an implant, have been presented within this thesis. The rationale behind this work relates to the early detection of cancerous tissues, internal injuries and other characteristic changes inside the human body with the primary goals being to improve microwave power penetration inside the human body and to provide low SAR and compact microwave antenna system for biomedical diagnosis.

The penetration of microwave power inside a human head model is improved by employing calculated permittivity inside a rectangular waveguide used as the microwave transmission source. Firstly, a multi-layer reflection model is created from various human tissue material. The wave impedance of the multi-layer is then extracted from the overall reflection coefficient found at the edge of the multi-layer tissue model. Furthermore, a rectangular waveguide is constructed and an L-probe rectangular waveguide feeding technique is presented. The measured results validate the approach with an increment in power

penetration inside the human head 1.33 dB at 2.45 GHz. Antennas are characterized in-front of homogeneous and a frequency-dependent inhomogeneous human head and shown that inhomogeneous phantom provides with real-life scenario for the measuring antenna whereas the homogeneous phantom only resembles the scenario. The effect of superstrate at the boresight of an on-head matched antenna for biomedical applications is analysed and shown that superstrate layer at the boresight direction of the antenna provides with ~8 dB increased directivity towards the human head with 0.0731 W/kg reduction of SAR compared to the antenna without the superstrate.

The design of a 3-D on-body antenna and a coplanar waveguide (CPW) fed antenna matched with an inhomogeneous human head provides the second investigation area. Specific focus has been given to make the designs compact, increase the front to back ratio (FBR) of the radiation pattern and decrease the SAR of the antenna. The 3-D antenna is realized combining a folded inverted F-like structure and a slot-loaded ground plane and backed by a rectangular cavity to minimize side and back lobe radiation. An FBR of 17 dB with SAR less than 0.0147 W/kg is achieved throughout the operating frequency ranging from 1 - 1.7 GHz by the designed antenna while acquiring a compact dimension of  $0.23 \times 0.23 \times 0.04 \lambda$  in size with respect to the lowest operating frequency. An inhomogeneous human head phantom is constructed and used to analyze the antennas performance in real-life scenario. Moreover, the choice of operating frequency for on-head antennas and effect of a superstrate on on-head matched antennas is investigated. An FBR of 20 dB with SAR less than 0.037 W/kg is achieved throughout the operating frequency ranging from 0.788 - 2.5 GHz by the designed antenna while acquiring a compact dimension of  $0.1 \times 0.1 \times 0.008 \lambda$  in size with respect to the lowest operating frequency.

Finally, the design of an implantable coil antenna is investigated for wireless power transmission inside the human body. The biocompatibility of the building material is analyzed. Polydimethylsiloxane (PDMS) and gold (Au) is utilized as the biocompatible building material to realize the designed implantable antenna. Furthermore, the antenna is characterized in a “complete medium” composed of fetal bovine serum (FBS), penicillin-streptomycin and dulbecco's modified eagle's medium (DMEM) which is used as the cell culture media to resemble designed antennas operation environment. The antenna is impedance matched at 5 MHz frequency with a maximum received voltage of 35 mV is recorded by utilizing the designed implantable antenna.

# Table of Contents

Declaration.....	i
Acknowledgements.....	ii
Abstract.....	iii
Table of Contents.....	v
List of Figures.....	x
List of Tables.....	xvii
Abbreviations.....	xviii
1. Introduction.....	1
1.1. Background and Motivation.....	1
1.2. Microwave and Biomedical Applications – Advantages and Applications.....	4
1.3. Aims of the Thesis.....	4
1.4. Thesis Contribution.....	5
1.5. Publications.....	7
1.5.1. Journal Articles.....	7
1.5.2. Conference Papers.....	7
1.6. Organization of the Thesis.....	8
2. Compact Antenna Design for Biomedical Applications.....	10
2.1. Performance Parameters.....	10
2.2. Challenges of Designing Compact Antennas.....	11
2.2.1. Frequency.....	11
2.2.2. Near Field or Far Field.....	12
2.2.3. Antenna Directivity.....	13
2.3. Biomedical Antennas.....	13

2.3.1.	On-body Antennas.....	14
2.3.2.	Ultra-wideband Antennas.....	15
2.3.3.	Phantom Consideration .....	17
2.3.4.	Simulation and Measurement Challenges .....	18
2.4.	Chapter Summary and Research Gaps .....	20
3.	Biomedical Antenna Design.....	22
3.1.	Rationale of Human Head Phantom.....	22
3.2.	Homogeneous and Inhomogeneous Phantoms.....	25
3.3.	Types of Phantom Materials .....	25
3.3.1.	Liquid Materials .....	26
3.3.2.	Semi-Solid Materials.....	26
3.3.3.	Solid Materials .....	27
3.3.4.	Fabrication of Phantom Materials .....	27
3.3.5.	Characterization of Fabricated Phantom Materials.....	31
3.4.	Improvement of Microwave Power Penetration .....	33
3.4.1.	Multilayer Wave Impedance Formulation .....	34
3.4.2.	Simulation Setup .....	37
3.4.3.	Results and Discussion.....	38
3.4.4.	Dielectric Waveguide Design.....	41
3.4.5.	Conclusion.....	46
3.5.	Antenna Characterization.....	46
3.5.1.	Rationale.....	46
3.5.2.	Antenna Design.....	47
3.5.3.	Results and Discussions .....	50
3.5.4.	Conclusions .....	53



3.6.	Effect of a Superstrate .....	53
3.6.1.	Rationale.....	53
3.6.2.	Design of the Antennas .....	55
3.6.3.	Results and Discussions .....	61
3.6.3.1.	Simulation .....	61
3.6.3.2.	Measurement.....	67
3.6.4.	Conclusion.....	68
3.7.	Chapter Summary.....	69
4.	Compact Antennas for Human Head Medical Diagnosis.....	71
4.1.	Challenges of Compact Antenna Design for Human Head Medical Diagnosis .....	72
4.2.	Compact 3-D Antenna for Medical Diagnosis of the Human Head .....	74
4.2.1.	Design Considerations.....	74
4.2.2.	Configuration of the Proposed Antenna.....	74
4.2.3.	Design Evolution.....	76
4.2.4.	Current Distribution .....	78
4.2.5.	Parametric Studies.....	79
4.2.6.	Human Tissue Effect on Antenna Performance .....	81
4.2.7.	Experiment Setup .....	83
4.2.8.	Field Distribution Inside Human Head .....	84
4.2.9.	Sensitivity Analysis.....	86
4.2.10.	Fabrication of the Antenna.....	89
4.2.11.	Measurement Setup and Results .....	92
4.2.12.	SAR for the Antenna.....	96
4.2.13.	Comparison with the Literature .....	97
4.2.14.	Conclusion.....	98

4.3.	Compact CPW Fed Wideband Directional Antenna for Medical Diagnosis .....	99
4.3.1.	Rationale of the Design .....	99
4.3.2.	Configuration of the Proposed Antenna .....	102
4.3.3.	Design Evolution .....	104
4.3.4.	Simulation Setup .....	107
4.3.5.	Current Distribution .....	108
4.3.6.	Role of the Superstrate .....	109
4.3.7.	Parametric Studies .....	110
4.3.8.	Experiment Setup .....	113
4.3.9.	Field Distribution Inside Human Head .....	113
4.3.10.	Fabrication of the Antenna and Inhomogeneous Human Head Phantom ....	115
4.3.11.	Measurement Setup and Results .....	116
4.3.12.	SAR for the Antenna .....	120
4.3.13.	Comparison with the Literature .....	122
4.3.14.	Conclusions .....	123
4.4.	Chapter Summary .....	123
5.	Implantable Antennas for Biomedical Applications .....	125
5.1.	Challenges for Implantable Antennas .....	125
5.1.1.	Biocompatibility .....	125
5.1.2.	Polarization .....	126
5.1.3.	Dielectric Loss .....	126
5.1.4.	Flexible Materials .....	126
5.2.	Rationale .....	126
5.3.	Implantable Antenna Design .....	128
5.3.1.	Fabrication and Measurement of the Implantable Antenna .....	135

5.4. Conclusions .....	139
6. Summary of the Research.....	141
6.1. Conclusions of the Thesis .....	141
6.2. Future Work .....	144
REFERENCES .....	145

# List of Figures

Fig. 2.1 Reactive/radiation field regions of a radiating antenna [60].	12
Fig. 2.2 Antennas designed for biomedical application (a) TEM horn antenna [45], (b) cavity-backed Vivaldi antenna [74].	14
Fig. 2.3 On-body antennas (a) bowtie antenna [18], (b) reconfigurable antenna [90].	15
Fig. 2.4 UWB antennas (a) planar antenna [97], pentagon antenna [40].	16
Fig. 2.5 Geometry used to show the effect of tissue inhomogeneity [108].	18
Fig. 2.6 (a) CST Voxel family, (b) Cross-section view of male model “Hugo”, (c) Visible female model, (d) Male model “Tom” [110].	19
Fig. 3.1 (a) Real and (b) Imaginary permittivity of different human tissues [115].	24
Fig. 3.2 Fabricated inhomogeneous human head phantom.	30
Fig. 3.3 (a) Evaluation of the inhomogeneous layer material properties, (b) measured permittivity versus reference [115] (c) measured loss tangent versus reference [115].	32
Fig. 3.4 (a) Real and (b) imaginary permittivity of human skin, bone, and brain (derived from [129]). The dashed lines indicate the selected frequency.	35
Fig. 3.5 Experimental setup – rectangular waveguide aperture against an inhomogeneous human head phantom.	38
Fig. 3.6 Normalized Ex-field intensity at 50 mm inside human head versus dielectric-filled waveguide permittivity variation at 2.45 GHz.	39
Fig. 3.7 Normalized Ex-field intensity at 50 mm inside human head versus dielectric-filled waveguide permittivity variation from 1.7 GHz to 3 GHz.	39
Fig. 3.8 Simulated normalized (a) E-plane (xz-plane) and (b) H-plane (yz-plane) near-field pattern at 50 mm distance inside human brain.	40
Fig. 3.9 Power penetration of TEM and TE <sub>10</sub> radiated waves up to 50 mm inside the human head at 2.45 GHz.	41
Fig. 3.10 Fabrication of the waveguide prototype: (a) before assembly, (b) after assembly, (c) side view.	42

Fig. 3.11 Design of the waveguide feeding antenna (a) antenna structure (the gap between the layers is for illustration purpose only, layers 1, 2 and 3 are stacked without any gap in between), (b) parameters (in mm): $a = 28$ , $b = 11.2$ , $c = 4$ , $d = 15$ , $e = 16.8$ , $f = 47$ , $g = 23$ ....	43
Fig. 3.12 Simulated and measured $ S_{11} $ of the open-ended quartz loaded waveguide.....	44
Fig. 3.13 Simulated and measured realized gain patterns of the open-ended quartz loaded waveguide operating at 2.45 GHz in the air (a) E-plane, (b) H-plane. ....	44
Fig. 3.14 Measurement setup of the power penetration pattern.....	45
Fig. 3.15 Measured power penetration pattern at a 50 mm radius inside the inhomogeneous phantom for the quartz loaded waveguide and standard WR 430 waveguide at (a) E-plane, (b) H-plane.....	45
Fig. 3.16 Design of the antenna. Dimensions (in mm): $a = 13$ , $b = 13.5$ , $c = 13.5$ , $l = 30$ , $w = 30$ .....	47
Fig. 3.17 Antenna simulation setup (a) antenna mounted on homogeneous head phantom, (b) antenna mounted on inhomogeneous head phantom. Dimensions (in mm): $x = 3$ , $y = 10$ and $z = 50$ . ....	48
Fig. 3.18 The surface current distribution of the antenna with (a) homogeneous, and (b) inhomogeneous phantom. ....	49
Fig. 3.19 $ S_{11} $ response of the antenna with the homogeneous and inhomogeneous human head phantom. ....	49
Fig. 3.20 E-field distribution inside the (a) homogeneous and (b) inhomogeneous human head phantom.....	51
Fig. 3.21 H-field distribution inside the (a) homogeneous and (b) inhomogeneous human head phantom. ....	51
Fig. 3.22 Near field radiation pattern of the antenna at 50 mm inside the phantoms with the inhomogeneous and homogeneous head phantom (a) E-plane (b) H-plane. ....	52
Fig. 3.23 Normalized power radiation pattern at 50 mm radius centered around the designed antenna. ....	52
Fig. 3.24 Design of the human head phantom matched antennas. Antenna (a) without superstrate, (b) with superstrate. Dimensions (in mm): $a = 13$ , $b = 13.5$ , $c = 13.5$ , $d = 20.8$ , $e = 12.9$ , $f = 28.5$ , $g = 29.4$ , $h = 27$ , $l = 30$ , $w = 30$ .....	56
Fig. 3.25 Simulation setup of (a) Antenna 1 and (b) Antenna 2 with the head phantom. Head phantom tissue (c) permittivity, (d) loss tangent. ....	57

Fig. 3.26 The surface current distribution of (a) Antenna 1, and (b) Antenna 2 at 0.9 GHz while operating on head. ....	58
Fig. 3.27 Reflection coefficient $ S_{11} $ of the Antenna 1 and Antenna 2 for homogeneous and inhomogeneous head phantom.....	59
Fig. 3.28 Parametric study on superstrate (a) permittivity and (b) thickness. ....	60
Fig. 3.29 Free space resonance of Antenna 1 and Antenna 2 (without the phantom at the boresight direction of the antennas). ....	61
Fig. 3.30 Distribution of the E-field inside human head phantom for (a) Antenna 1 and (b) Antenna 2 at 0.9 GHz.....	62
Fig. 3.31 Distribution of the H-field inside human head phantom for (a) Antenna 1 and (b) Antenna 2 at 0.9 GHz.....	63
Fig. 3.32 Normalized power radiation pattern at 50 mm distance from the antenna feed centre for homogeneous head phantom (a) xz-plane, (b) yz-plane at 0.9 GHz. ....	64
Fig. 3.33 Normalized power radiation pattern at 50 mm distance from the antenna feed centre for inhomogeneous head phantom (a) xz-plane, (b) yz-plane at 0.9 GHz. ....	65
Fig. 3.34 Free space normalized power radiation pattern at 50 mm radius (a) xz-plane, (b) yz-plane at 0.9 GHz. ....	66
Fig. 3.35 Free space normalized power radiation pattern at 50 mm radius from Antenna 2 (a) xz-plane, (b) yz-plane at 0.9 GHz. ....	66
Fig. 3.36 Simulated SAR distribution of inhomogeneous head phantom for (a) Antenna 1 and (b) Antenna 2 for an input power of 1 mW. ....	67
Fig. 3.37 Measured $ S_{11} $ response of the antennas attached with inhomogeneous phantom. ...	68
Fig. 3.38 Measured normalized power radiation pattern at 50 mm distance from the antenna feed centre for inhomogeneous head phantom (a) xz-plane, (b) yz-plane at 0.9 GHz. ....	68
Fig. 4.1 Proposed stacked 3D-folded cavity-backed antenna layout where the ground plane is the back of the cavity, and the patch layers are physically separated using FR4 substrate. ....	75
Fig. 4.2 Evolution of the 3D antenna (a) Antenna 1 (b) Antenna 2 (c) Antenna 3 – top view (d) Antenna 4 – bottom view (e) Antenna 5. ....	77
Fig. 4.3 $ S_{11} $ response for the antennas shown in Fig. 4.2. ....	77
Fig. 4.4 Surface current distribution with the inhomogeneous phantom attached at the boresight of the antenna. ....	79

Fig. 4.5 Simulated $ S_{11} $ with different values of the slot length, $j$ .	80
Fig. 4.6 Simulated $ S_{11} $ with different values of patch element 1 length, $g$ .	80
Fig. 4.7 Simulated $ S_{11} $ with different values of skin thickness, $m$ .	81
Fig. 4.8 Simulated $ S_{11} $ with different values of bone thickness, $n$ .	82
Fig. 4.9 Simulated $ S_{11} $ with different values of skin permittivity, $\epsilon_s$ .	82
Fig. 4.10 Simulated $ S_{11} $ with different values of bone permittivity, $\epsilon_b$ .	83
Fig. 4.11 (a) Front view, (b) coronal plane, (c) sagittal plane, and (d) transverse plane of the antenna attached to the Hugo head model.	84
Fig. 4.12 (a) E-field (b) H-field distribution of the antenna with realistic head model at xz-plane.	85
Fig. 4.13 (a) E-field (b) H-field distribution of the antenna with the realistic head model at yz-plane.	86
Fig. 4.14 (a) Top view of the 8-antenna element setup, (b) side view, (c) unhealthy brain with artificial hemorrhage inserted.	87
Fig. 4.15 (a) $ S_{11} $ of the excited antenna and mutual coupling with other antennas, (b) $ S_{11} $ response of the antenna with healthy and unhealthy (hemorrhage) head model, (c) $ S_{11} $ with change in hemorrhage distance from the antenna, and (d) $ S_{11} $ with change in $h$ .	88
Fig. 4.16 Fabricated antenna prototype (a) back (b) side (c) front of the antenna.	89
Fig. 4.17 (a) Evaluation of the inhomogeneous layer material properties (b) measured permittivity versus reference [115] (c) measured loss tangent versus reference [115].	90
Fig. 4.18 (a) Fabricated inhomogeneous human head phantom (b) antenna measurement against a curved phantom.	91
Fig. 4.19 Simulated and measured $ S_{11} $ response of the antenna for the flat surface phantom and the curved phantom.	93
Fig. 4.20 Schematic of the radiation measurement setup in the inhomogeneous phantom.	94
Fig. 4.21 Simulated (a) E-plane (xz-plane) and (b) H-plane (yz-plane) and measured (c) E-plane (xz-plane) and (d) H-plane (yz-plane) near-field pattern at 50 mm distance inside human brain.	95
Fig. 4.22 Simulated power penetration at different distances inside inhomogeneous human head phantom at different frequencies.	95

Fig. 4.23 (a) Simulated maximum SAR distribution with an input power of 1 mW inside in Hugo phantom (b) Simulated maximum SAR in terms of penetration distance. ....	97
Fig. 4.24 (a) Proposed CPW antenna layout using FR4 substrate and superstrate (b) Antenna schematic diagram, (c) Addition of the cavity backing. ....	103
Fig. 4.25 (a) Antenna evolution from CPW monopole to the proposed antenna, (b) simulated $ S_{11} $ response of Antennas 1, 2, and 3, (c) Smith chart response of Antennas 1, 2, and 3.....	107
Fig. 4.26 Antenna simulation setup with the inhomogeneous human head phantom. Dimensions (in mm): $k=3$ , $p=10$ , $q=70$ .....	108
Fig. 4.27 Surface current distribution of the CPW antenna with the inhomogeneous head phantom attached to the superstrate. ....	109
Fig. 4.28 Simulated $ S_{11} $ with different thicknesses of the superstrate, $S_t$ . ....	110
Fig. 4.29 Simulated $ S_{11} $ with different thicknesses of the (a) skin and (b) bone. ....	111
Fig. 4.30 Simulated $ S_{11} $ with different dielectric permittivity of the (a) skin, $\epsilon_s$ , (b) bone, $\epsilon_b$ , (c) brain, $\epsilon_{br}$ . ....	112
Fig. 4.31 (a) Front and (b) side view of the “Hugo” head when the antenna attached to the “Hugo” head model.....	113
Fig. 4.32 (a) Front and side view of the “Hugo” head, distribution of the (b) E-field and (c) H-field of the proposed antenna inside the inhomogeneous head phantom at xz-plane.....	114
Fig. 4.33 Distribution of the (a) E-field and (b) H-field of the proposed antenna inside the inhomogeneous head phantom at yz-plane. ....	115
Fig. 4.34 Proposed antenna made from FR4 material and a copper cavity (a) front view, (b) side view. ....	116
Fig. 4.35 Simulated and measured $ S_{11} $ of the proposed antenna with and without the cavity. ....	117
Fig. 4.36 (a) Radiation measurement schematic (b) cross-section view.....	118
Fig. 4.37 Simulated power pattern in the: (a) E-plane (xz-plane) and (b) H-plane (yz-plane) without the cavity; (c) E-plane and (d) H-plane with the cavity; and the measured pattern in (e) E-plane and (f) H-plane with the cavity. ....	119
Fig. 4.38 Simulated SAR distribution of the inhomogeneous head phantom for the proposed antenna attached to the skin surface with an input power of 1 mW (a) front view, (b) side view (c) Simulated maximum SAR with distance from the skin surface. ....	121



Fig. 5.1 (a) Proposed design of the implantable antenna on PDMS substrate (b) Circuit representation of the antenna. ....	128
Fig. 5.2 Simulation setup of the implanted antenna and the external antenna.....	129
Fig. 5.3 Characteristics of the considered phantom material (a) real, (b) imaginary permittivity.....	130
Fig. 5.4 (a) Reflection coefficients ( $ S_{11} $ and $ S_{22} $ ) of the two antennas, (b) Transmission coefficients ( $ S_{21} $ ) for different distances, “d”. ....	132
Fig. 5.5 Simulated maximum SAR distribution with an input power of 1 mW inside the inhomogeneous phantom for 10g averaging (b) Simulated maximum SAR from the implant antenna surface till the surface of the skin.....	133
Fig. 5.6 S-parameters of the power transfer system without adjusting capacitance to account for the phantom materials, with the external antenna at port 1 and the implanted antenna at port 2. ....	134
Fig. 5.7 S-parameter response of the internal and external antennas when the external antenna is rotated 90° in the xy-plane (d = 30 mm). ....	134
Fig. 5.8 Axial ratio of the antenna .....	135
Fig. 5.9 Fabrication steps of the antenna. ....	136
Fig. 5.10 Fabricated antenna using gold on PDMS substrates .....	136
Fig. 5.11 (a) External coil antenna, (b) implantable antenna inside a “complete media” solution,.....	137
Fig. 5.12 (a) Simulated reflection and transmission coefficient mimicking the setup shown in Fig. 5.11 (b), (b) Measured reflection coefficient of the antenna for setup shown in Fig. 5.11 (b), (c) Voltage received by the implantable antenna at different distances.....	138



# List of Tables

Table 3.1: Advantage and disadvantages of homogeneous and inhomogeneous phantoms....	25
Table 3.2: Composition of different human tissue phantoms .....	28
Table 3.3: Human Tissue Characteristics at 2.45 GHz [129] .....	36
Table 4.1: Dimensions of the proposed antenna .....	76
Table 4.2 Performance comparison between similar antennas .....	98
Table 4.3: Dimensions of the proposed antenna .....	104
Table 4.4: Performance comparison between similar antennas .....	122
Table 5.1: Dimensions of the proposed antenna .....	129

# Abbreviations

3D	Three Dimensions
Al <sub>2</sub> O <sub>3</sub>	Alumina
ASIR	Age-standardized incidence rates
cm	centimetre
CST	Computer Simulation Technology
CT	Computer Tomography
dB	Decibels
DCT	Design comes true
EM	Electromagnetic
FBR	Front to back ratio
FBW	Fractional Bandwidth
GHz	Giga-Hertz (1*10 <sup>9</sup> Hz)
GLOBOCAN	Global Cancer Incidence, Mortality and Prevalence
HFSS	High-Frequency Structural Simulator
Hz	Hertz (cycles per second)
IEEE	Institute of electrical and electronics engineers
IFA	Inverted F antenna
Kg	Kilograms
m	Meters
MBI	Microwave biomedical imaging
mm	Millimetres
MRI	Magnetic Resonance Imaging
MUT	Material under test
PDMS	Polydimethylsiloxane
SAR	Specific Absorption Rate
SNR	Signal to noise ratio
UWB	Ultra-wideband
VNA	Vector network analyser
VSWR	Voltage standing wave ratio
WHO	World Health Organization

# Chapter 1 – Introduction

## 1. Introduction

The motivation and background of this thesis about microwave antenna design for biomedical application are presented in this introductory chapter, highlighting the utilization and impact of the typical microwave antenna systems in biomedical applications. Additionally, the aims of the thesis along with the contributions to the microwave engineering society, are also reported, followed by the final subsection outlining the organization of the thesis.

### 1.1. Background and Motivation

The inside of a human body is made of sophisticated organs that are covered by a biological shield created by the combination of skin, fat, bone, muscle, etc. tissue elements [1]. These elements are prone to injury as well as cancerous tissue, which may start to grow due to malignant tumour tissues [2-4]. Most lingering injuries and cancerous tissue growth can be prevented by early detection and treatments. On the other hand, poorly detectable diagnosis and delayed treatment for such injuries and malignant tissue growth can be deadly [5, 6].

Almost 1.3 million humans worldwide die because of a road accident, and more than 50 million are left with severe aftermath injuries [5]. Moreover, the internal bleeding of the human brain, i.e. a brain haemorrhage caused by the escape of blood from the ruptured vessel

of blood in brain, is one of the major concerns here in Australia. In the year 2012, more than 50,000 Australian people suffered from brain strokes that is 6 strokes in every hour [7].

It was reported that more than 18.1 million new cancer patients were expected to be added to the current tally of cancer-patients in 2018, and the deaths caused by cancer alone will rise above 9.6 million [6]. From the reports provided by Global Cancer Incidence, Mortality and Prevalence (GLOBOCAN) 2012 [8], Australia is among the highest for age-standardized incidence rates (ASIR) cancer, numbering at a rate of 323 persons in every 100,000 persons. Such statistics make these internal human body problems into a crucial public health concern.

As such syndromes of human body are increasing in numbers and require immediate attention to provide vital treatment, a diagnostic solution which can provide a finding fast and efficiently is of paramount importance. At the same time such a solution needs to be inexpensive, user friendly, instantly diagnosable and portable to ideally enable it to be implemented in under-developed countries and remote places in the world [9].

Medical imaging is one of the most crucial steps before any further diagnosis of the human body, wherein an inspection of the human physiology and anatomy is undertaken. For example, the detection of cancerous cells in different phases has been possible through medical imaging [10]. Some of the mentionable imaging tools are Computed Tomography (CT), X-ray, Ultrasound, and Magnetic Resonance Imaging (MRI), and each of these has their advantages and drawbacks. Most of these tools are expensive and inaccessible to the rural parts of the world. Moreover, hospitals in 3rd world countries cannot afford these tools [11-13]. According to the survey published by the World Health Organization (WHO) in 2011 [14], only about one-quarter of the world population has access to a reliable medical imaging system. Hence, many people are still suffering from the lack of affordable medical imaging tools. Furthermore, the imaging tools that exist currently are bulky, and being so it is impossible to use them as portable tools. Such problems demand a more affordable, compact, and efficient medical diagnosis solution, which can operate in real time and render advantages over the existing medical diagnosis tools.

Recently, microwave imaging systems have garnered great interest in the medical imaging industry due to their simplicity and cost-effectiveness, and research is being carried out in many research groups around the world due to its increasing demand and importance to the human population. With the current trend of making portable medical diagnosis systems,

microwave equipment has gained increasing attraction due to reduced complexity and feature-size compared to other techniques. Research on human body diagnostics has gained a great interest among microwave researchers due to its potential in the biomedical industry, e.g., microwave biomedical imaging (MBI) applications [15-18]. Depending on the dielectric properties of tissues, the performance-parameters of the microwave-based biomedical imaging system may vary [19]. Recently, early detection of cancerous tissues, haemorrhages, internal injuries, and other characteristic changes inside the human head utilizing microwave technology have been reported [15, 20-22].

Microwave penetration of radiation inside human tissue is a crucial factor for medical diagnosis, which is highly dependent on the dielectric and dispersive properties of the tissue, and also the efficiency of the microwave radiator near human tissue [23-25]. The material characteristics of the human body must be known to determine the unknown malignant (e.g., tumour, haemorrhage) tissue inside human body [26], and afterward, information about the malignant tissue can be extracted from the received signal obtained by the microwave antenna system. As the human body is a complicated structure comprising a combination of different materials, the complexity of such tissue characteristics is expressed through the dielectric permittivity and conductivity of the respective tissue materials at microwave frequencies. The measurement of human tissue properties has been carried out over a wide range of frequencies [27-29], the characteristics of which are integrated into the latest microwave simulation software packages (e.g. Computer Simulation Technology (CST) Microwave Studio). In the last decade, a wide number of research works have been reported for medical diagnosis and implantable devices for the human body involving the use of microwave technology.

Microwave devices for medical diagnosis have gained popularity due to their nonionizing, low-cost, time-efficient attributes. A crucial element for microwave medical diagnosis of the human body is the microwave antenna, which acts as the radiating and receiving element [16, 30-32]. If a microwave antenna solution can produce similar results to a highly sensitive diagnostic tool for the human body (e.g. MRI, CT scan, X-ray, etc.), the advantages of cost-effectiveness, portability, human body-friendliness of microwave system can provide us with a more optimized solution and affordably to people in both urban and rural areas. Moreover, with the recent progress in the post-processing of microwave biomedical systems [33-37],

these systems can provide real-time monitoring which will be one of the most significant benefits over the other existing medical diagnostic systems.

## **1.2. Microwave and Biomedical Applications – Advantages and Applications**

The number of potential biomedical applications where microwave systems may be employed is increasing day by day. Microwave antennas are being efficiently exploited and utilized for visceral imaging [38], chemotherapy [31], and the detection of breast cancer [39], brain tumours [40], bone fractures [41] and haemorrhages [42]. Due to the advantages of non-ionizing radiation and non-invasive application, microwaves can be exposed to the human body for a longer term without any harm, providing an advantage over other methods such as chemotherapy and imaging. X-ray-exposure can be deadly for the human body, unlike microwave systems which are not detrimental to human health if practical limits are adhered to. Hence, longer-term exposure can yield better imaging while tissues remain unharmed. Microwave devices can be made wideband and directional to enhance image sharpness and localization of detecting bodies [43-45], which is quite complicated for other imaging technologies. Although breast cancer detection research has been ongoing for quite some time, brain tumour detection utilizing electromagnetic technology has received heightened interest in recent times [20, 38, 40, 46-49]. The key obstacle of brain tumour detection compared to breast cancer detection is the presence of bone (i.e. the skull) surrounding the brain. The inhomogeneity of human head makes the diagnosis procedure significantly more complex. Moreover, the positioning of the microwave sensors around the head of a human is an important factor which dictate the performance of the radiating device (i.e. the antenna). In this thesis, the research intends to enhance the performance of microwave antennas when operating near, on or inside the human body, providing a cost-effective, compact, durable, and portable microwave antenna for biomedical diagnosis.

## **1.3. Aims of the Thesis**

This research aims to increase the microwave penetration inside the human body from a microwave source located outside, and to develop compact antennas that provide increased penetration and directionality of microwave radiation for medical diagnosis. The design of



efficient implantable antennas for power transmission into the human body is also among the goals of this research. To achieve these milestones, the following steps are taken:

- a) Improvement of microwave penetration: Microwave penetration inside the human body to be increased by considering the inhomogeneity characteristics of the multiple tissues.
- b) Antenna development: Development of compact antennas with increased front to back ratio for narrowband and wideband biomedical applications for efficient biomedical diagnostic systems.
- c) Antenna array construction: The performance of the proposed antennas in b) need to be evaluated in array formation for specific biomedical applications.
- d) Realistic human body phantom: An inhomogeneous realistic human body phantom need to be developed to evaluate the performance of the conceived antennas in an approximated real-life scenario.
- e) Implantable antenna development: Antenna designs for wireless powering of implantable devices from outside the human body are investigated.

## **1.4. Thesis Contribution**

The contributions are mapped to the Aims in Section 1.3, along with the publications listed in Section 1.5. The original contributions resulting from research in this thesis are provided below:

- a) Improving the microwave penetration inside human body (relates to the Aim 1.3 a) and produced publications [C1, C5]):
  - I. A multi-layer reflection model is investigated to evaluate the combined material characteristics of different lossy human head tissues. A dielectric-loaded waveguide with a calculated permittivity is conceived to maximize the microwave power penetration at the desired frequency.

- II. The penetration of microwave power inside a human head model is shown to be improved by employing a dielectric-loaded rectangular waveguide as the transmission source.
- b) Isolating on-head antennas from the biological tissue which (Aim 1.3 (a), publications [C2, C6]):
- I. Antennas characterised next to homogenous and frequency dependent inhomogeneous human head phantom are shown to have significantly different electromagnetic field and power penetration characteristics.
  - II. The effect of a superstrate on on-head matched antennas is investigated and shown that an antenna with a superstrate can provide increased power penetration compared to antenna design without a superstrate.
- c) Novel on-body antenna optimized with compact size and low-cost for narrow band applications (Aim 1.3 (b), (c) and (d), publication [C3]):
- I. A SAR lower than state of the art with improved directionality radiation pattern towards the human body compared to the literature is achieved by employing a compact 3-D antenna design for microwave medical diagnosis. The antenna is matched to an inhomogeneous human head to allow higher signal penetration.
- d) A wideband on-body biomedical antenna (Aim 1.3 (b) and (d), publication [C4]):
- I. A coplanar waveguide antenna matched with an inhomogeneous human head phantom is designed and investigated over a wide bandwidth. The FBR of the antenna is improved with lower SAR compared to the reported literature for similar applications over a wide bandwidth.
- e) Implantable biomedical antenna for wireless power transfer (Aim 1.3 (e)):
- I. An implantable antenna for increased efficiency in wireless power transmission inside the human body is designed and evaluated.

## **1.5. Publications**

The listings of the peer reviewed publications related to this thesis are listed in this subsection. The first listing details the peer-reviewed journals and letters and the second listing details the peer reviewed conferences in relation this thesis.

### **1.5.1. Journal Articles**

[C1] Md. Rokunuzzaman, Asif Ahmed, Thomas Baum, and W.S.T. Rowe, " Microwave power penetration enhancement inside an inhomogeneous human head," IEEE transactions on Biomedical Engineering (Under review).

[C2] Md. Rokunuzzaman, Asif Ahmed, and W.S.T. Rowe, " Effect of a superstrate on on-head matched antennas for biomedical applications," IET Microwaves, Antennas & Propagation (Under review).

[C3] Md. Rokunuzzaman, Asif Ahmed, Thomas Baum, and W.S.T. Rowe, "Compact 3-D Antenna for Medical Diagnosis of the Human Head," IEEE Transactions on Antennas and Propagation. vol. 67, no. 8, pp. 5093-5103, Aug. 2019.

[C4] Md. Rokunuzzaman, Asif Ahmed, Thomas Baum, and W.S.T. Rowe, "Compact CPW fed wideband directional antenna for medical diagnosis," IEEE Antennas and Wireless Propagation Letters (Under review).

### **1.5.2. Conference Papers**

[C5] Md. Rokunuzzaman, Asif Ahmed, Thomas Baum, and Wayne S. T. Rowe, "UWB Power Penetration Inside a Realistic Human Head Model," IEEE International Conference on Consumer Electronics – Asia, IEEE ICCE-ASIA 2019, Bangkok, Thailand, 12-14 June 2019.

[C6] Md. Rokunuzzaman, Asif Ahmed, Thomas Baum, and Wayne S. T. Rowe, "Biomedical Antenna Characterization in-front of Homogeneous and Frequency Dependent Inhomogeneous Human Head," URSI EM Theory Symposium, EMTS 2019, San Diego, CA, 27– 31 May 2019.

## **1.6. Organization of the Thesis**

The thesis is divided into six chapters, as detailed below.

Chapter 1 presents the background and the motivation behind this research work. In this chapter, the relation between microwaves and biomedical applications is established, and the challenges in this research domain are highlighted. In addition, the aims of this research work and the original research contributions is also presented.

Chapter 2 discusses the important parameters for antenna designs in biomedical applications. Furthermore, the challenges presented in the literature that are generally faced when trying to design an optimum antenna solution are reviewed. Simulation and measurement challenges are also presented in this chapter.

Chapter 3 describes the need for considering a realistic human head phantom. The difference between homogeneous and inhomogeneous phantoms are discussed in terms of their advantages and disadvantages. Moreover, different types of existing phantom materials are included in this discussion. An inhomogeneous human head phantom fabrication method is described in this chapter. Furthermore, an efficient and highly accurate characterization method of the fabricated phantom material is detailed and utilized towards the improvement of microwave power penetration inside the inhomogeneous human head phantom. Antenna characterization in-front of homogeneous and frequency-dependent inhomogeneous human head is also explored along with the effect of an antenna superstrate for isolating the antenna from the lossy human tissues.

Chapter 4 proposes a compact antenna for biomedical applications. Firstly, the challenges and limitations of designing an antenna for on-body biomedical application are discussed. The conception and design of a compact 3-D antenna for medical diagnosis is described and justified with simulation and measurement results. A wideband antenna design with a coplanar waveguide technique is also described, along with experimental validation. Comparison of the designed antennas with the current literature are also drawn.

Chapter 5 presents an initial model of implantable antennas for power transmission into the human body. The wireless power transfer is demonstrated with the aid of an external antenna. The simulation, fabrication, and measurement process along with the proof of concept results are discussed in this chapter.

Chapter 6 concludes the thesis along with suggestions for future work.

## Chapter 2 – Literature Review

### **2. Compact Antenna Design for Biomedical Applications**

The antenna is a vital component to enable communication in any wireless system. The overall efficiency of a microwave-based biomedical system highly depends on the performance of its microwave radiating element which transmits and receives scattered signals from reflecting surfaces, nominally the anomalies to be detected. As the antennas operate near the human body compactness is a vital criterion, along with impedance matching and efficient radiation towards the desired direction to achieve an efficient system. The importance of compactness increases dramatically when the antenna is required to operate on the body. This chapter describes the important parameters that are considered for biomedical antennas, along with reviewing the challenges presented in the literature for microwave antennas to operate efficiently in biomedical applications.

#### **2.1. Performance Parameters**

Several performance parameters are considered while designing a microwave antenna for biomedical applications. Return loss and impedance matching, the field of operation (near-

field, far-field), radiation pattern, directionality, and the SAR are among the important parameters that need characterization before the antenna utilized for a biomedical application [12, 13, 15, 26, 42, 50-58]. One of the key requirements that is specific for a radiating element for medical diagnosis is the SAR, which ensures a safe environment for the human body whilst testing is conducted [59]. SAR can be calculated using:

$$SAR = \frac{|E|^2 \sigma}{M} \quad (2.1)$$

where  $|E|^2$  is the electric field RMS value,  $M$  is the human tissue mass density, and  $\sigma$  is the conductivity of the human tissue.

## **2.2. Challenges of Designing Compact Antennas**

For biomedical applications, a compact diagnostic system is always desired as such application requires the system to operate near the human body in often in a congested environment. For diagnosis applications which require antenna radiation, the dimensions of the antenna define the compactness of the whole system. Hence, a compact antenna design is one of the main strategic considerations for microwave biomedical diagnosis system. The challenges faced during the design of a compact antenna for such application are discussed in this section.

### **2.2.1. Frequency**

A suitable frequency must be chosen within the microwave regime before designing an antenna for a biomedical application. There are few frequency spans reported in the literature as being optimal for biomedical diagnostics. Higher frequencies struggle to penetrate through the human head due to smaller wavelength and interact more with inhomogeneities, and at lower frequencies biological tissues tend to be highly lossy [24, 25]. The overall structure of the antenna for low frequencies also becomes large which can render it impractical for operation near the human body. The frequency band from 1 GHz to 2 GHz has been stated as being suitable for medical diagnosis as it achieves increased penetration with low power radiation to reduce SAR [32].

### 2.2.2. Near Field or Far Field

An antenna's radiated electromagnetic field can be divided into two broad regions, the Near-field and Far-field. The near-field can be further divided into two regions, the Non-radiative (reactive) region and Radiative (Fresnel) region. Fig. 2.1 shows the antenna reactive/radiation field regions.

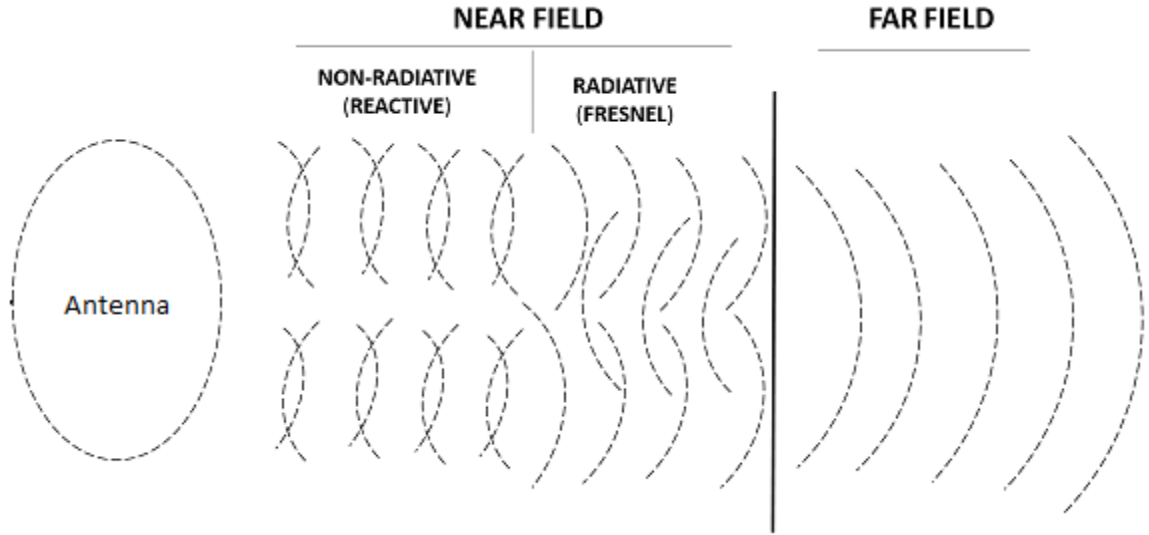


Fig. 2.1 Reactive/radiation field regions of a radiating antenna [60].

The near-field and far-field region of an antenna for a specific frequency of operation can be determined using:

$$Near\_field < \frac{2D^2}{\lambda} < Far\_field \quad (2.2)$$

Here,  $D$  is the largest linear dimension of the antenna and  $\lambda$  is the wavelength of the field. Antennas that are designed to operate in free space or air will exhibit different characteristics when they are placed in the near field of or on the human body. This change in characteristics is because the environment of operation changes from one material to another with different dielectric properties. Hence, it is important to analyse both the far-field and near-field radiation characteristics of an antenna for some applications. In [32], the near-field radiation pattern and the near-field and far-field fidelity factors are explored to determine the performance of the antenna. Also, for biomedical applications the antennas in [16, 20, 22, 26,



32, 42, 49, 51, 61-68] are characterized for both near field and far field to determine the operational principles of the antenna radiation.

### **2.2.3. Antenna Directivity**

The Directivity of an antenna is a measure of where an antenna directs most of its radiated power. If an antenna radiates its power equally at all directions, it is called an isotropic antenna. Practical antennas are sometimes designed to radiate equally over a specific plane (omnidirectionally) or in a particular direction. The directional antennas are used for applications which require unidirectional radiation properties, e.g. satellite television, remote area internet connections etc.

For medical diagnosis purposes, there are various types of antennas proposed where both the omnidirectional and directional type radiation pattern. Printed monopole antennas with their low profile characteristics and ease of design, have gained its popularity among the omnidirectional antennas for medical diagnosis [69, 70]. However, an omnidirectional antenna transmits and receives signals from a wide range of angles, making the whole medical diagnosis system more sensitive to its surroundings. This can make the difference between the scattered signals from a target biomedical entity and the background to diminish or become merged, causing loss of sensitivity and or resolution.

The directional antenna can aim radiation towards more specifically the target biomedical entity, resulting in an enhanced system performance. Some of the directional antenna design examples includes horn antenna [71, 72], log-periodic antenna [73], Vivaldi antenna [39, 74], quasi-Yagi antenna [75], 3D stacked antenna [16], etc. In [76], the difference between an omnidirectional antenna a directional antenna for wideband head imaging is investigated. The directional antenna can perform better compared to the omnidirectional antenna for such applications [76] as a better impulse response with decreased distortion can be achieved. Moreover, directional antennas can detect targets with increased focus and few samples of data compared to an omnidirectional antenna.

## **2.3. Biomedical Antennas**

Antennas are the front end of a microwave based wireless biomedical system. The performance of a biomedical system highly depends on this antenna. Hence, an enhanced

biomedical antenna is one of the main strategic considerations for microwave biomedical diagnosis system. Different biomedical antennas found in the literature that are related to this research are discussed in this section.

### 2.3.1. On-body Antennas

When designing an on-body antenna (i.e. the antenna is in contact with the top of the skin layer of the human body) more complex parameters must be considered compared to designing an antenna in free space or air. Moreover, the near field response of the antenna must be considered as it is in close proximity to the human body and the antenna characteristics will change with the change in its surroundings. The characteristics of the bio-tissue and the placement of the antenna on the human body can influence the performance of the antenna as well. As water is one of the fundamental elements of human body, the percentage water content at a specific location of the human body will mostly determine the electrical properties of that location. Hence, if an on-body antenna is designed for a specific location of the human body, that antenna might not have the same performance in other locations.

The literature shows there are specific antennas designed for operation on specific parts of the human body. Antennas are reported in [31, 45, 70, 74, 77-83] to detect tissue anomalies and for chemotherapy of human breast. Antenna designs dedicated to detecting haemorrhage and brain tissue anomalies can be found in [13, 16, 20, 21, 32, 40, 46-50, 58, 61, 84]. A few different antennas have been reported to detect and monitor fractures in different parts of the human body [41, 85-87].

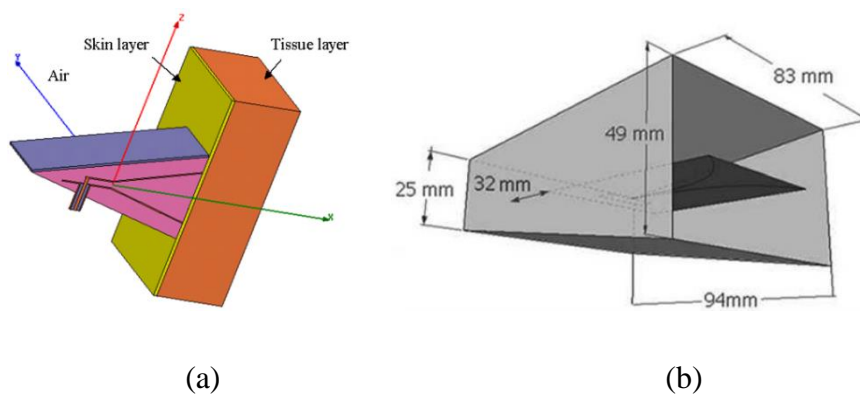


*Fig. 2.2 Antennas designed for biomedical application (a) TEM horn antenna [45], (b) cavity-backed Vivaldi antenna [74].*

Only a few examples of antennas are reported for on-body applications [18, 45, 84, 88-94]. Specifically for the human head diagnosis, an antenna design is reported that operates on-body [18]. The antenna is designed using high permittivity Rogers RT/duroid 6010 substrate material ( $\epsilon_r = 10.2$ ) resulting in a reduction in antenna dimensions. Nonetheless, the antenna suffers from a far-field FBR of less than 15 dB over the operating frequency range, meaning that a reasonable portion of the radiated energy is directed away from the head being diagnosed. Only a far-field characterization of the antenna FBR is performed in simulation, omitting any investigation of the near-field characteristics where the head resides. Furthermore, the antenna design considers a lossless homogeneous phantom, which has been shown to differ substantially from a realistic inhomogeneous and lossy near-field scenario, and also has conductive surfaces in direct contact with the human head which will reduce power transfer efficiency and sensing capability [95]. Lastly, the antenna achieves SAR characteristics of 0.06 W/kg at 0.5 mm inside the skin layer, implying that there will be a higher SAR where the antenna touches the surface of the skin.

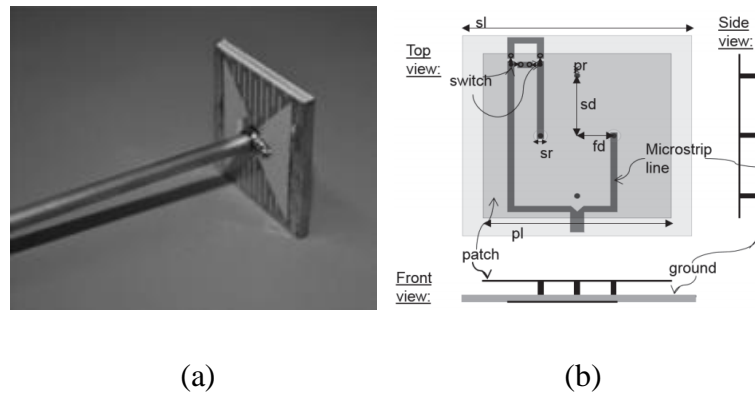


Fig. 2.3 On-body antennas (a) bowtie antenna [18], (b) reconfigurable antenna [90].

### 2.3.2. Ultra-wideband Antennas

Ultra-wideband (UWB) technology has many highly desired attributes for wireless applications, including a large bandwidth and requiring a comparatively low power consumption. The possibility of using UWB antenna technology is being explored to operate near the human body for human body centric application [16, 17, 40, 46-48, 84, 96-101]. In [96], a square patch antenna is designed with a partial ground plane to study the effect of a human head on the performance of the UWB antenna. A simple layered inhomogeneous phantom constructed using skin, cortical bone, grey matter and muscle is considered while

evaluating the performance of the UWB antenna. The reflection coefficient and the radiation performance of the antenna are studied in free space and near the human head phantom. Nonetheless, antennas that operate in air are prone to be less efficient when working at the near field of the human body due to the mismatch loss. Moreover, the antennas operate at a higher microwave frequency (3.1 GHz – 10.6 GHz) which provides with less penetration inside human body compared to lower microwave frequencies. A similar approach was taken in [97] where a more realistic phantom with the shape of the human head is considered, and the antenna performance is evaluated in terms of the reflection coefficient, electromagnetic field, and radiation performance. Nonetheless, the antenna is operating in air which introduces loss due to air-body transition, with most of the power not penetrating through the skin.



(a)



(b)

*Fig. 2.4 UWB antennas (a) planar antenna [97], pentagon antenna [40].*

In [98], an UWB implanted antenna is evaluated where the reflection coefficient of the antenna was of most interest. The simulated radiation pattern is determined using a three-layered human head phantom, i.e. skin, fat and bone. Nonetheless, the antenna exhibits high SAR. An on-body matched UWB antenna design is presented in [84] to detect brain activity inside a human head with the aid of an implanted antenna. However, the connection between the implanted antenna and the external antenna is very low resulting in lower power penetration inside human head. In [48], tumour detection is explored utilizing a UWB antenna by looking at the change in reflected time-domain signal where the multi-layered inhomogeneous spherical human head phantom is considered. The difference in performance with tumour is determined, but only shows very small change as compared to the antennas that operate at lower frequencies. The performance of an UWB antenna is evaluated to detect brain tumour and stroke of a human head in [40]. The method of detecting the tumour or

stroke is mainly based on the reflection coefficient performance of the antenna. However, other characteristics of the antenna system are omitted in this research.

The SAR of an implantable UWB antenna is shown in [99] where radiation characteristics of the antenna are neglected. Another implantable UWB antenna performance is shown in [46] where the considered multilayered human head phantom is spherical, which is not the case for a real human head. Moreover, the SAR and the E and H-field inside the head phantom is not shown.

### **2.3.3. Phantom Consideration**

The human body is a complicated structure made of a combination of different materials. In the microwave regime, the complexity of such tissue characteristics can be expressed through the dielectric permittivity “ $\epsilon$ ” and conductivity “ $\sigma$ ” of the respective tissue material. The measurement of the human tissue properties has been carried out in [27-29] over a wide range of frequencies.

The on-body matched antennas reported in [18, 30, 64, 102] are in contact with the human head to achieve increased impedance matching and increased signal penetration inside the human tissue. The implantable antennas reported in [103-107] are for various application related to human body diagnosis, which requires the antenna itself to be housed inside the human body along with associated electronic circuitry.

Designing antennas to operate near the human body requires the consideration of human tissues when simulating the antenna performance. The complex structure and characteristics of human tissue within the body cause the simulator to solve a wide range of data problems resulting in an exponential increment in the simulation time [18]. However, this complexity can be decreased by considering a homogeneous phantom to represent the human body instead of a more accurate inhomogeneous phantom. For the same reason, a lot of the antennas designed for human body applications do not consider the inhomogeneous and frequency-dependent characteristics of the human body. Recently, the effect of inhomogeneous characteristics of human tissue were investigated for chemotherapy treatment [108]. In this work, the electric field intensity is examined in the human tissue phantom, and it is shown that the electric field distribution is affected by the inhomogeneous structure.

The physical structure of the phantom also needs to be considered, especially for the on-body applications as natural curvatures can govern the parts of the antenna that touch the human tissue. In such cases if a more realistic phantom structure is considered, the resulting antenna design will be more robust and accurate in its intended application compared to other antenna designs.

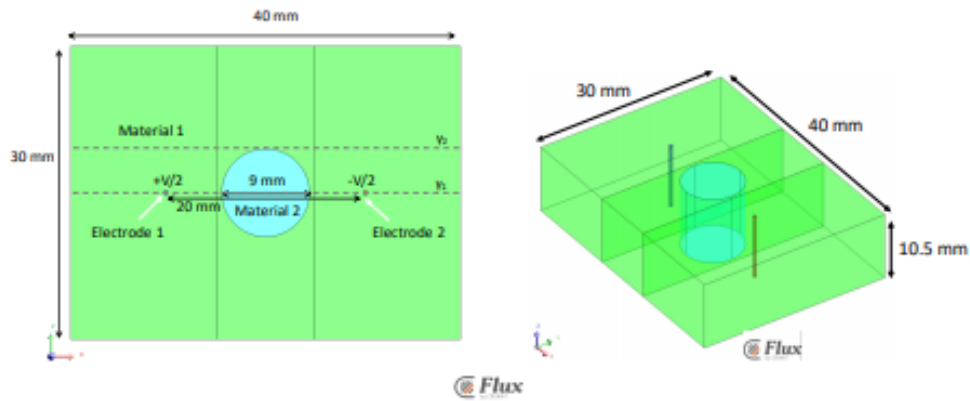
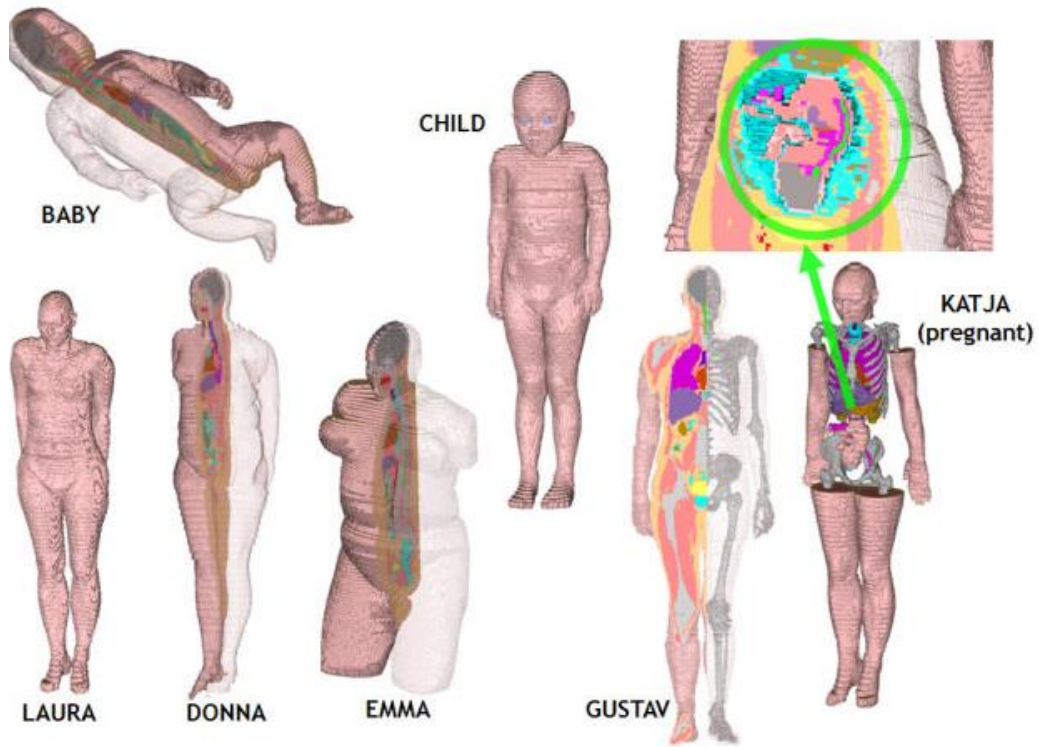


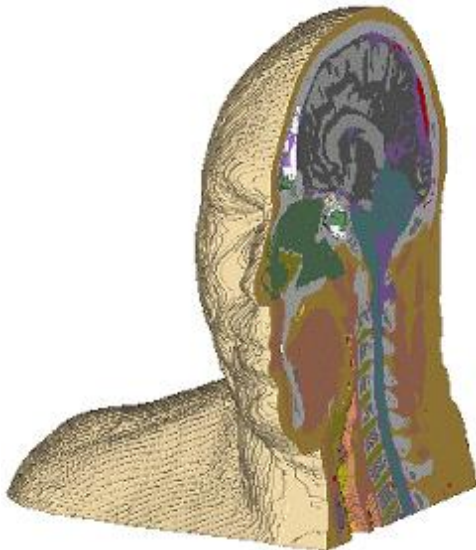
Fig. 2.5 Geometry used to show the effect of tissue inhomogeneity [108].

#### 2.3.4. Simulation and Measurement Challenges

Biological structure of the human body must be considered when designing an antenna for biomedical applications. The human body is a complex structure consisting of different tissues with different characteristics, broadly represented in multiple layers [109]. One of the fundamental materials of human tissue is water, whose ratio varies within different parts of the human body [27-29]. Water is reasonably conductive, making the human tissue material conductive and introducing loss to a microwave signal propagating through the human body [23]. An application dependent on microwave penetration inside the human body may significant performance degradation to this lossy characteristic.



(a)



(b)



(c)



(d)

*Fig. 2.6 (a) CST Voxel family, (b) Cross-section view of male model “Hugo”, (c) Visible female model, (d) Male model “Tom” [110].*

Simulation software such as CST [110], High-Frequency Structural Simulator (HFSS) [111], FEKO [112], and IE3D [113] are equipped with the capability to setup materials with specific

frequency-dependent permittivity and loss tangent. Use of these simulation software packages can assist in analysing microwave systems operating in proximity with the human body. Moreover, CST has a built-in material library of human tissue materials such as skin, bone, brain etc. with their frequency-dependent permittivity and loss tangent characteristics, accelerating the design process. Furthermore, CST has built in human body voxel models as shown in Fig. 2.6, which consider different age and gender scenarios, and can be modified for different poses. Microwave models can be implemented inside and outside of these voxel models making the design of a compact biomedical antennas more realistic in a simulation environment.

The measurement process for a biomedical antenna should ideally be conducted in the practical environment where the antenna will be used. A measurement setup incorporating a real human requires ethical approval, and in particular cases can be invasive. For example, radiation pattern measurement requires probe insertion inside the measuring body, which will be injurious if applied to a real human body. For SAR measurement, the measuring body needs to be exposed to microwave radiation for a long time, which could present a risk. Hence performing the antenna measurements on an approximation of relevant part of the human body in a controlled environment is preferred.

The utilization of human tissue-mimicking phantoms is crucial for characterising antennas for biomedical applications. Different parts of the human body are of a different state, e.g. blood is liquid, whereas the brain is semi-solid and bone is a solid, complicating the creation of a phantom and the resulting measurements. Hence a specific and representative measurement setup to evaluate biomedical antennas is required.

## **2.4. Chapter Summary and Research Gaps**

The design of an antenna for biomedical applications is challenging in terms of simulation and measurement due to numerous factors related to human body. An antenna operating from 1 GHz to 2 GHz has been reported to be most suitable for medical diagnosis as it achieves increased penetration inside human body.

Many biomedical antenna examples in the literature ignore radiation characterization at both near field and far field, which is crucial as the antenna operates in close proximity to the



body. The antennas that do examine fields in the vicinity of the body generally exhibit a lack of directivity and/or power penetration inside human body.

Numerous reported antenna designs ignore the complexity of the human body and its influence on the performance characteristics. Those using homogenous, lossless, or irregular shaped body phantoms cannot be relied upon to behave identically when used in a practical application.

An efficient, effective and robust antenna design for biomedical applications is possible by overcoming all these challenges. The design processes and resulting antenna geometries, substrate and superstrate considerations and power penetration limitations will be presented in the following chapters of this thesis.

# Chapter 3 – Biomedical Antenna Design

## 3. Biomedical Antenna Design

A representative human head phantom plays an important role while designing antennas or other radiating elements near or on the human head. Different types of human head phantom models can be found in the literature, typically defined by the state of the end material (i.e. liquid, semi-solid, solid). This chapter defines the rationale of utilising a representative human head phantom, concentrating on the comparative effects of a homogeneous and inhomogeneous phantom. A discussion on the types of phantom materials that may be utilised is also presented in this chapter. Finally, the crucial design parameters that need to be considered during the design of an antenna (i.e. power penetration, superstrate) near the human head for microwave imaging systems are evaluated.

### 3.1. Rationale of Human Head Phantom

Owing to the advanced simulation softwares available (e.g., CST, HFSS, etc.) it is now possible to consider human body parts or the whole human body in electromagnetic simulations. Such electromagnetic simulation provides valuable information on the performance of a biomedical electromagnetic device when it is performing near, on, or inside the human body. Nonetheless, this simulated result needs to be validated in real life scenario

as it is crucial to characterize the practical performance of the biomedical electromagnetic device. However, characterizing electromagnetic device near a human body can be hazardous and in many cases, as the human body could be exposed to excessive electromagnetic radiation which may cause injury. Moreover, a comparative performance validation of the biomedical electromagnetic device in many different cases may be required, such as between a healthy and unhealthy body, between different types of illness, and the location of the illness or target (e.g. cancerous tissue location, bone fracture location, etc.).

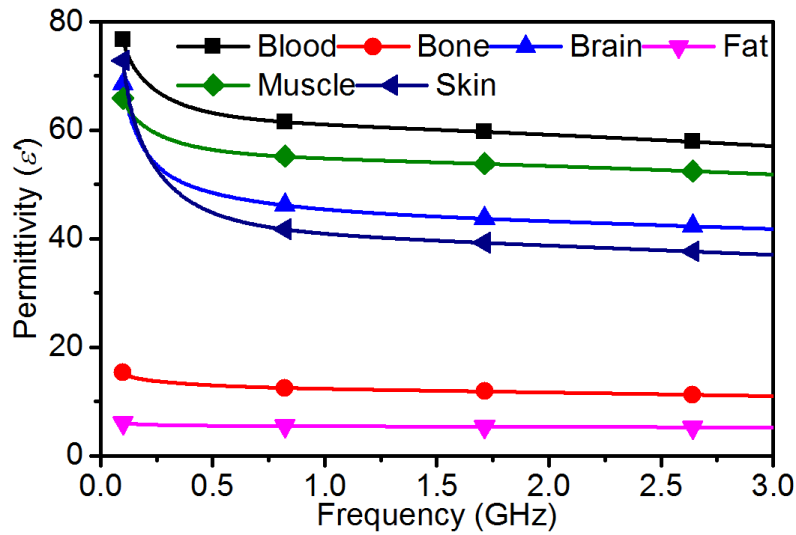
Extracting experimental data is another constraint of utilizing real-life human body. One cannot just insert a probe inside a human body to collect temperature data or SAR measurements. And last but not least, there is a serious ethical issue that arises when involving human-related trials in the characterization of a biomedical device. It is difficult to get ethical approval from the dedicated authority in most cases since it could potentially pose serious risks. Also, such approval requires validation of risk factors in terms of health hazards and environmental effect. Hence, characterizing a new biomedical electromagnetic device directly near the human body is a difficult option. Hence the use of a representative human phantom can alleviate the majority of these concerns.

Making realistic electromagnetic human phantoms is a profound research area of its own. The first challenge in making a representative human phantom for an electromagnetic application is emulating the dielectric properties of different parts of the human body, i.e. permittivity and loss. As the human body contains a high percentage of water [114] and water is a lossy material for electromagnetic wave propagation, when electromagnetic energy tries to penetrate through the human body, it suffers from loss. Fig. 3.1 shows the electromagnetic properties of different parts of the human body [115] within the frequency range from 0.1 GHz to 3 GHz. The imaginary permittivity showed in Fig. 3.1 (b) is the reason for the loss of the penetrated electromagnetic energy inside the human body. Such loss occurs due to the conductivity characteristics of human body tissue.

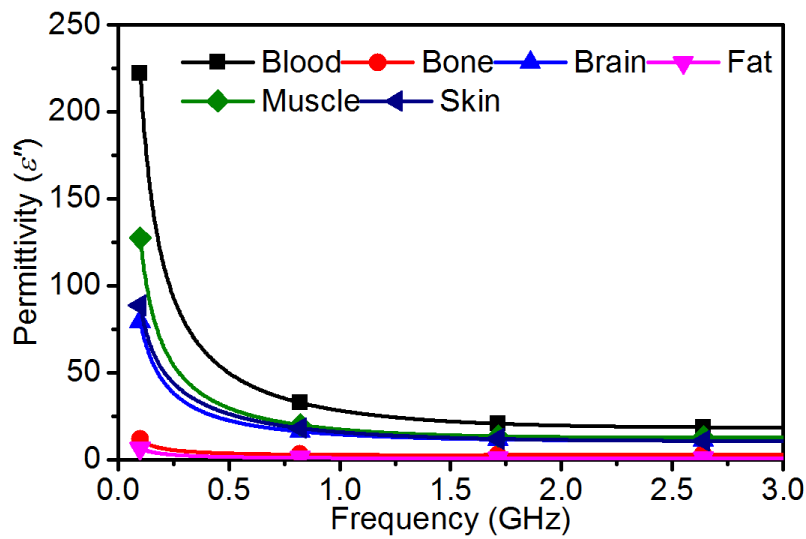
Crucial aspects in the construction of a human body model are achieving an approximate permittivity match over the frequency band of interest, creating realistic and robust dimensions, ease in measurement, and life expectancy.

In Fig. 3.1 the characteristics of the human body tissue vary with the change in frequency. Hence, when making a phantom material for a particular human tissue, the permittivity of the

mimicking material should follow a similar trend, especially if a very wideband of UWB channel is being considered. Measuring and verifying the properties of the human tissue-mimicking material also presents a challenge as the loss of the material needs to be determined.



(a)



(b)

Fig. 3.1 (a) Real and (b) Imaginary permittivity of different human tissues [115].

The majority of the current literature on microwave systems for human body applications mostly utilise a highly simplified version of a human body phantom [18, 38, 116-118]. As the human body is made up of different tissue layers with different characteristics, assuming

such simplicity will affect the veracity of results obtained in the laboratory as compared to a real-life scenario. Hence it is important to employ human phantoms which are closer to a real-life body to provide as close prediction as possible and result in more effective and robust microwave devices.

### 3.2. Homogeneous and Inhomogeneous Phantoms

Both homogeneous and inhomogeneous phantoms have their advantage and disadvantages depending on the situation they are being used. Table 3.1 below highlights the advantages and disadvantages of utilising homogeneous and inhomogeneous phantoms.

Table 3.1: Advantage and disadvantages of homogeneous and inhomogeneous phantoms

	<b>Homogeneous Phantom</b>	<b>Inhomogeneous Phantom</b>
<i>Anatomical Complexity</i>	Easy	Difficult
<i>Fabrication Complexity</i>	Easy	Difficult
<i>Long term utilization</i>	Yes	No
<i>EM Simulation time</i>	Short	More
<i>Can be of liquid form</i>	Yes	No
<i>Measurement setup</i>	Easy	Difficult
<i>Number of materials needed</i>	Less	More
<i>Measurement result</i>	Less accurate	More accurate

### 3.3. Types of Phantom Materials

Depending on the tissues, phantom materials can be of different types. Certain tissue materials require the phantom to be liquid, e.g., blood, saliva, etc., however most of the tissue materials are semi-solid or solid types. Phantoms can be classified into these three different material types, namely: Liquid, Semi-solid, and Solid materials.

### **3.3.1. Liquid Materials**

Most of the human tissue materials have high relative permittivity properties, up to and in excess of 40. Such high relative permittivity is also attributed to the amount of water inside the human tissue. The human tissue that contains less water (e.g. fat, bone, etc.) has lower permittivity compared to the high water-containing tissue materials. To mimic the high water-containing tissue materials, water itself is commonly used combined with other materials to represent the electrical properties of the target tissue material as closely as possible. The most appreciated benefit of the liquid phantom materials is preparation ease. With a proper recipe, it is possible to make a liquid phantom with ease compared to other types of phantom materials. In [119], several liquid phantom material recipes are presented. The ease of preparation, storage and measurement [18] makes the liquid phantom material a common choice. Nonetheless as water tends to evaporate, and by doing so the concentration level in the phantom materials change, the resulting electrical properties can vary with time. Moreover, such liquid phantoms cannot be stacked on each other to mimic a complex system such as the head.

### **3.3.2. Semi-Solid Materials**

One of the most important aspects of semi-solid phantom materials is they can be formed into different shapes. Such an advantage can be used to make phantoms for specific tissue material with specific dimensions. Moreover, such materials can stack on top of each other to make more complexed layered phantoms. The electrical properties of the semi-solid materials (once achieved) are more stable compared to liquid materials [120]. For measurement, it is relatively easy to insert probes inside the semi-solid phantom material to measure field properties.

The fabrication process, however, requires extra attention compared to fabricating liquid materials. For example, separately weighing the materials before mixing, maintain specific timing for mixing the components, adding preservatives to conserve the phantom in its initial form, cooling it down to a specific temperature to form a semi-solid, and storing it at a specific temperature so that the electrical properties of the material does not change. Semi-solid phantom materials may also suffer from bubbles inside due to the mixing process, and these must out-gas it cools down. Moreover, when measuring using a moving object such as an automated probe, this type of material could be deformed. As they are based on water a

semi-solid may dehydrate, changing the electrical properties of the material with time which may invalidate its use [52, 121].

### **3.3.3. Solid Materials**

Solid phantom materials are not dependent on water, hence the drawback of dehydration can be ignored [122]. Ceramic materials commonly constitute the base of the solid phantom materials. By combining different ceramic materials, specific electrical properties are achieved. However, ceramics are a more ideal electromagnetic material with low conductance and hence low loss. It is difficult for such low loss material to mimic the loss that occurs inside the human tissue material. Fabricate details for basic solid phantom materials are provided in [123]. The requirement of high pressure, high-temperature material blending to process the ceramics is a also constraint of fabricating these solid materials. Although the ceramics are relatively cheap, the fabrication procedure makes the overall cost of solid phantom material expensive. Other less common solid phantom materials found in the literature based on carbon fiber and silicon rubber [124]. The main advantages of solid phantom materials are their durability and long-lasting characteristic. However, internal measurement of field properties inside a solid phantom is almost impossible.

### **3.3.4. Fabrication of Phantom Materials**

As semi-solid phantom materials can be formed into different shapes and can be stacked on each other they are a sensible choice for constructing a multi-layer human head model. The advantages of stable electromagnetic properties and a comparatively less complex measurement process also justify choosing semi-solid phantom materials to investigate the performance of the biomedical microwave antennas.

To construct a multi-layer human head phantom, a procedure presented in [125] is followed to control the concentration of oil in the tissue mimicking material to achieve a semi-solid state. The composition of the different materials required to mimic different human tissues are shown in Table 3.2.

Table 3.2: Composition of different human tissue phantoms

Human Tissue	Brain	Bone	Skin
<b>Oil (ml)</b>	47.91	130.585	56.885
<b>Water (ml)</b>	121.84	51.71	114.0425
<b>2-propanol (ml)</b>	5.12	2.17625	4.7925
<b>p-toluic acid (ml)</b>	0.128	0.055625	0.11975
<b>Gelatin (ml)</b>	21.7975	9.26125	20.4025
<b>Formaldehyde Sol. (ml)</b>	0.515	0.217	0.4825
<b>Surfactant (ml)</b>	2.6675	5.98625	3.2775

The mixing steps of the materials are as follows:

For 0-50% of oil

1. In a small beaker mix p-toluic acid (powder) with n-propanol
2. Heat until p-toluic acid is dissolved
3. In a Pyrex beaker, mix solution “2” into 18M cm deionized water (water should be in room temperature).
4. At room temperature, mix Gelatine to solution “3” and stir for a while (the gelatines will be wetted).
5. Cover the beaker with a plastic film held in place with a rubber band and heat (90 °C) the mixture in a double boiler.
6. When the mixture has become transparent (at about 90 °C), and no air bubbles are suspended beneath the surface, remove the beaker from the double boiler.
7. Stir the mixture to produce uniformity and then remove any air bubbles from the surface. Do that in a bath of cool water (20-25 °C) and stir the mixture until it cools to 50 °C. Record the ml amount of the solution for step 12.



8. Remove the beaker from the water bath and pour into another beaker which already contains a quantity rest of the oil at 50 °C.
9. Vigorously stir the mixture with a spoon bent at a right angle at its base until most oil droplets are less than 0.2 mm in diameter. At 50 °C.
10. Continue to do procedure no. “9” while adding surfactant (0.056 ml of surfactant per ml of oil) (the emulsion should become uniform and for larger percentages oil-nearly white). At 50 °C.
11. Cool the emulsion to 40 °C using a cool water bath and keep stirring.
12. Using a needle and syringe add 0.0108 g Formaldehyde solution per ml of the gelatine solution (solution of step 7).
13. Cool the water bath to about 34 °C and pour into a container for cooling and solidifying.
14. Allow 5 days for formaldehyde cross-linking of gelatine to be completed.

#### For 50-80% of oil

1. In a small beaker mix p-toluic acid (powder) with n-propanol
2. Heat until p-toluic acid is dissolved
3. In a Pyrex beaker, mix solution “2” into 18M cm deionized water (water should be in room temperature).
4. At room temperature, mix Gelatine to solution “3” and stir for a while (the gelatines will be wetted).
5. Cover the beaker with a plastic film held in place with a rubber band and heat (90 °C) the mixture in a double boiler.
6. When the mixture has become transparent (at about 90 °C), and no air bubbles are suspended beneath the surface, remove the beaker from the double boiler.
7. Stir the mixture to produce uniformity and then remove any air bubbles from the surface. Do that in a bath of cool water (20-25 °C) and stir the mixture until it cools to 50 °C.
8. Remove the beaker from the water bath and pour into another beaker which already contains a quantity of 100 ml oil at 50 °C.
9. Vigorously stir the mixture with a spoon bent at a right angle at its base until most oil droplets are less than 0.2 mm in diameter. At 50 °C.

10. Continue to do procedure no. “9” while adding surfactant per ml of oil in step “8” (the emulsion should become uniform and for larger percentages oil-nearly white). At 50 °C.

11. Add the extra amount of oil (more than 50%) in 100 ml steps and stir until it becomes uniform. Then add again until the oil percentage is achieved and keep stirring until an emulsion is uniform (the emulsion should become uniform and for larger percentages oil-nearly white).

12. Cool the emulsion to 40 °C using a cool water bath and keep stirring.

13. Using a needle and syringe add 0.0108 g Formaldehyde solution per ml of the gelatine solution (solution of step 7).

14. Cool the water bath to about 34 °C and pour into a container for cooling and solidifying.

15. Allow 5 days for formaldehyde cross-linking of gelatine to be completed.

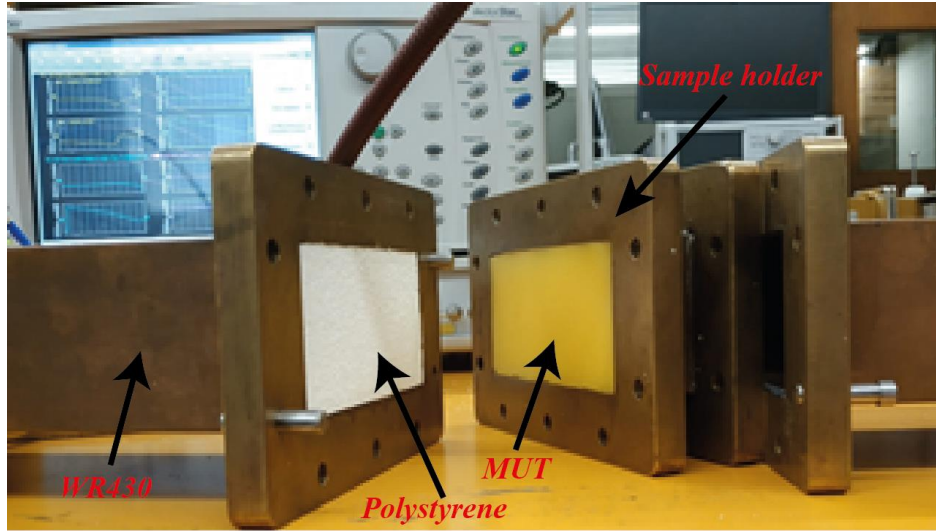
A brain mimicking material was firstly cast in a container to the desired thickness, where it was left to cool and solidify for approximately 5 days. The bone layer was then mixed and poured on top of the solidified brain mimicking material and in a similar fashion to the cooling process for the brain material the bone material was left to solidify for a further 5 days. The skin layer was finally cast and left to solidify following [125]. The dimensions of the final inhomogeneous phantom are approximately  $170 \times 110 \times 70 \text{ mm}^3$ . The constructed three-layer phantom is shown in Fig. 3.2.



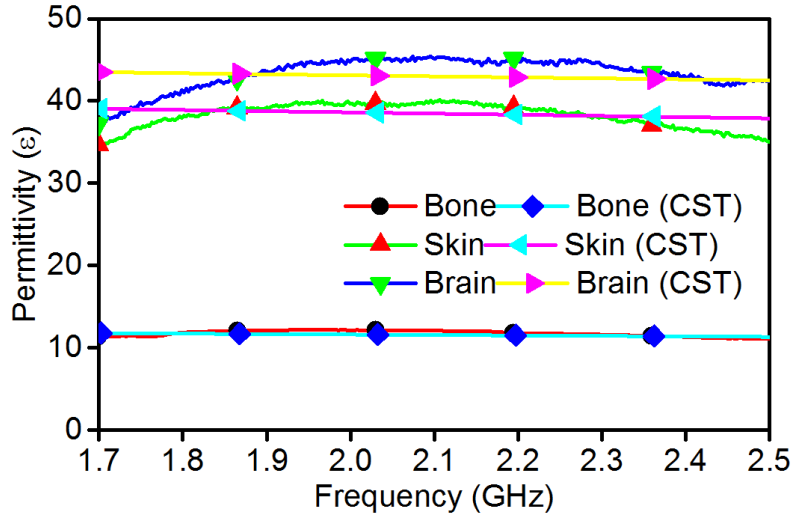
*Fig. 3.2 Fabricated inhomogeneous human head phantom.*

### **3.3.5. Characterization of Fabricated Phantom Materials**

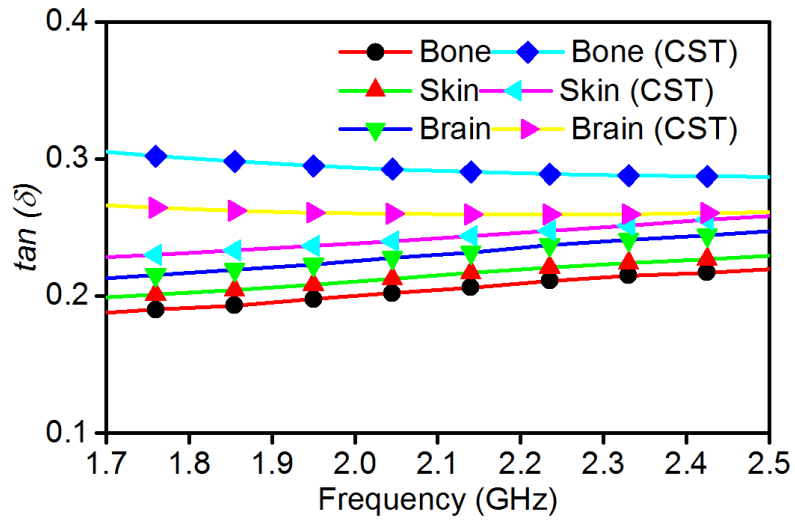
The dielectric characteristics of each fabricated tissue layer were experimentally verified utilizing the procedure described in [126]. The measurement setup is depicted in Fig. 3.3 (a) where polystyrene foam is used before and after the material under test (MUT) to hold the sample straight while measuring inside a WR430 waveguide. A flanged sample holder is used to hold the sample between two WR430 waveguide tubes. It can be observed from the measured results in Fig. 3.3 (b) and (c) that the fabricated phantom layer characteristics show a similar response to the tissue characteristics in the CST tissue library (taken from [115]) within the operating range of WR 430 waveguide.



(a)



(b)



(c)

Fig. 3.3 (a) Evaluation of the inhomogeneous layer material properties, (b) measured permittivity versus reference [115] (c) measured loss tangent versus reference [115].

### **3.4. Improvement of Microwave Power Penetration**

Over the past decade, microwave human body diagnostic system development has gained a great deal of interest among microwave researchers due to its potential in the biomedical sector, specifically in MBI applications [15-18]. Depending on the dielectric properties of human tissues, MBI system sensitivity may vary [19]. The material characteristics of the human body must be known to determine unknown malignant (e.g., tumour, haemorrhage) tissues inside the human body [26]. An investigation into the optimal range of frequencies for power penetration inside different dispersive tissues of the human body has previously been conducted [24]. For a cluster of human head tissues, the ideal operational frequency ranges between 0.5 to 2.5 GHz [15, 26].

A key challenge in MBI is to achieve sufficient power penetration inside dispersive human tissue at these frequencies [25]. Unlike other imaging systems, human head imaging utilizing microwave technology needs to consider the SAR, which limits the power that can be radiated from a transmission source. Moving the transmitter away from the head can relax the limitation imposed by SAR, but consequently, more than half of the total energy radiated can reflect at the air-skin interface [18], diminishing power penetration. Hence, many radiating elements designed for MBI lack power efficiency [15, 16, 26]. The physical distance between the radiating element and the skin introduce further loss to the overall system. The resulting reflections from the malignant tissue (which can be a significant distance inside the human brain) become extremely weak and clouded by other unwanted reflections, making retrieval of information from the signal problematic.

An on-body matched antenna is designed on a high permittivity substrate material, which leads to a smaller antenna dimension to mitigate this problem [18]. Although the antenna reflection performance is better when in contact with skin, it is hard to determine the power penetration inside the dispersive tissue due to lack of evidence. In [127], an antenna designed for free space operation is applied on top of human tissue with a matching layer in between. It is shown that by using a matching layer with the same permittivity of bulk human tissue can provide with higher power penetration. The matching layer is assumed to be lossless and the antenna is operating in the air next to the matching layer. In reality, it is challenging to find material with such characteristics to use as a matching layer. Moreover, the human

tissue has an inhomogeneous structure which is not taken into consideration while introducing the matching layer.

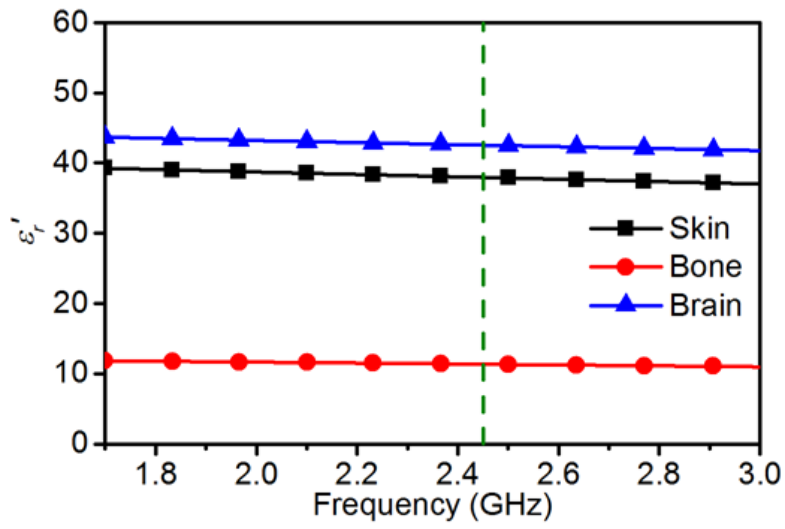
The most disadvantageous feature of microwave diagnostics of the head compared to other parts of the human body is the high water content of brain tissue [128]. Since the brain is more than 75% water, most of the microwave power penetrating through the outer boundary of the human head suffers from high loss. Hence, it is crucial to achieving an efficient transfer of energy through the boundary of the head to achieve a sufficient level of power penetration inside the brain.

Here, microwave power penetration inside a human head phantom is improved by matching the input source to the total impedance faced by a wave propagating through inhomogeneous layered tissue materials. A multi-layer reflection model is considered to estimate the combined material characteristic of the different tissue layers (i.e., skin, bone, brain) at 2.45 GHz. The impedance of a wave in a rectangular waveguide is modified utilizing a low loss material, forming a dielectric-loaded waveguide to match to the inhomogeneous layered material. The power penetration at different depths inside the human brain is evaluated. A Quartz ( $\text{SiO}_2$ ) loaded waveguide is fabricated and fed via a microstrip antenna to validate the results. Human tissue-mimicking inhomogeneous layers are utilized as a human head phantom for the measurements.

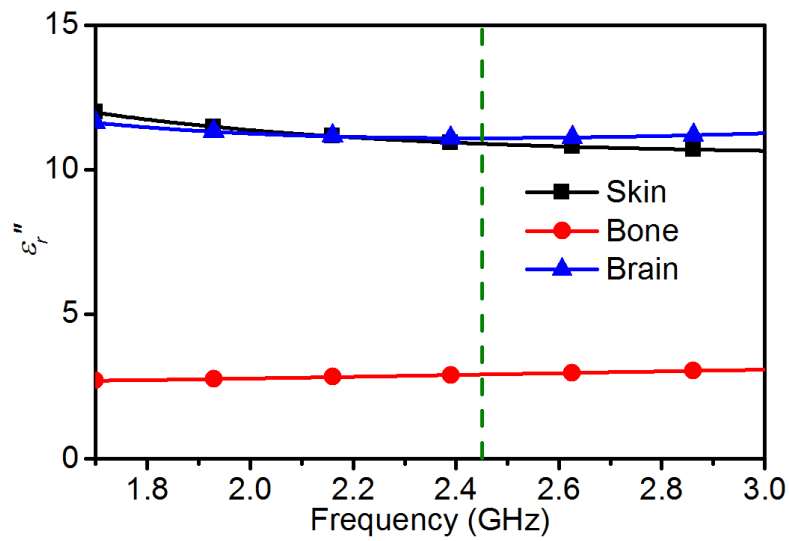
### **3.4.1. Multilayer Wave Impedance Formulation**

The human head consists of several lossy dielectric media but can be approximated with a combination of inhomogeneous layers (i.e., skin, bone, brain) to conceive a model with greater rigor than a bulk approximated phantom as used in [127]. Such a layered structure needs to be formulated to understand the wave propagation throughout the layers before utilizing them for an MBI system. Microwave propagation in a media can be defined by the wave impedance characteristics. For lossy media, the wave impedance can be expressed as a complex impedance where the imaginary part of the impedance represents the loss in the media. The dielectric properties (i.e., permittivity, permeability) at the desired frequency must be known to attain the wave impedance. The complex permittivity parameters for different biological tissues can be found in [129]. The real and imaginary parts of the permittivity for the considered bio-tissues are depicted in Fig. 3.4. For this work, a frequency  $f_l = 2.45 \text{ GHz}$  is chosen as it is close to the upper bound of the optimal range for human head

tissues. A simplified inhomogeneous head model consisting of three layers (i.e., skin, bone, brain) is considered.



(a)



(b)

Fig. 3.4 (a) Real and (b) imaginary permittivity of human skin, bone, and brain (derived from [129]). The dashed lines indicate the selected frequency.

Table 3.3: Human Tissue Characteristics at 2.45 GHz [129]

Material	Complex permittivity, ( $\epsilon' + j\epsilon''$ )	Considered thickness, $d_x$ (mm)	Wave impedance, $\eta_x (\Omega)$
<b>Skin</b>	38.01 + j10.88	1	59.37 - j8.34
<b>Bone</b>	11.36 + j2.916	10	109.18 - j13.78
<b>Brain</b>	42.55 + j11.08	60	56.39 - j7.22

The wavelength  $\lambda_x$  for frequency  $f_l$  in different biological tissue can be calculated using:

$$\lambda_x = \frac{c_0}{f_l \sqrt{\epsilon_x}} \quad (3.1)$$

To characterize the wave propagation inside the layered biological tissues at frequency  $f_l$ , the reflections occurring at each interface can be combined to achieve overall reflection coefficient utilizing:

$$\Gamma_{overall} \cong \Gamma_0 + \sum \Gamma_x e^{-j2x\theta} \quad (3.2)$$

where,  $\theta = \frac{2\pi}{\lambda_x} d_x$  for each layer with tissue thickness  $d_x$ , and  $\Gamma_0$  is the reflection coefficient at the boundary of air and skin. The specific reflection coefficient at the interface between different materials can be found using the normalized Fresnel equation for reflection:

$$\Gamma_x = \frac{\eta_{x+1} - \eta_x}{\eta_{x+1} + \eta_x} \quad (3.3)$$

where,

$$\eta_x = \frac{\eta_0}{\sqrt{\epsilon_x}} \quad (3.4)$$

$\eta_0$  is the wave impedance of free space,  $\eta_x$  and  $\eta_{x+1}$  are the impedances of the incident and transmitted wave materials respectively. For the considered tissue materials, the wave impedances can be found in Table 3.3.



Once the overall reflection coefficient is found using (3.2), the wave impedance of the overall layered biological structure  $\eta_{overall}$  can be found using the general form of the reflection coefficient equation:

$$\eta_{overall} = -\eta_0 \left( \frac{1 + \frac{1}{\Gamma_{overall}}}{1 - \frac{1}{\Gamma_{overall}}} \right) \quad (3.5)$$

As a rectangular waveguide is to be used as the radiation source, the wave impedance of the dominant TE<sub>10</sub> mode can be determined using:

$$\eta_{TE} = \frac{|\eta_{overall}|}{\sqrt{1 - \left(\frac{f_c}{f_1}\right)^2}} \quad (3.6)$$

where  $f_c$  is the cut-off frequency of the waveguide.

Owing to the irremovable conductivity of the biological tissues, the conductive material loss of a propagating wave inside the human head cannot be minimized. However, by matching  $\eta_{TE}$  with  $\eta_{overall}$  at the outer boundary of the layered biological structure, maximum power penetration inside the human head is possible. This matching can be achieved by utilizing a dielectric-loaded rectangular waveguide filled with a material of permittivity  $\epsilon_{wg}$ . Utilizing the wave impedance of the TE wave in (3.6), the  $\epsilon_{wg}$  required can be found from:

$$\epsilon_{wg} = \left( \frac{|\eta_{overall}|}{\eta_{TE}} \right)^2 \quad (3.7)$$

By utilizing the equations, the dielectric-loaded rectangular waveguide permittivity  $\epsilon_{wg}$  is found to be  $3.6 - j5.8$  at  $2.45 \text{ GHz}$ . The imaginary part of the permittivity contributes to the loss of the material, and if included in the waveguide dielectric material will introduce more loss to the overall system. Thus utilizing just the real part of the permittivity  $\epsilon_{wg}$  becomes  $3.6$  at  $2.45 \text{ GHz}$ .

### 3.4.2. Simulation Setup

To evaluate the validity of the calculated result, a CST Microwave Studio simulation setup as depicted in Fig. 3.5 is adopted. The complex permittivities and thicknesses of the human tissue materials are set to those stated in Table 3.3. The broad wall dimension of the dielectric-filled rectangular waveguide,  $a$ , is calculated via:

$$f_{c_{TE_{10}}} = \frac{c}{2a\sqrt{\mu_m\epsilon_m}} \quad (3.8)$$

where  $f_c$  is the selected cut-off frequency,  $\mu_{wg}$  and  $\epsilon_{wg}$  are the permeability and permittivity of the dielectric filling material, and  $c$  is the speed of light in free space. Once the  $a$  is found, the short wall dimension  $b$  is found as:

$$b \leq \frac{a}{2} \quad (3.9)$$

A cut-off frequency of 1.7 GHz was selected to mimic that of an air-filled WR430 waveguide, and the dimensions are found to be  $a = 47 \text{ mm}$  and  $b = 23 \text{ mm}$ .

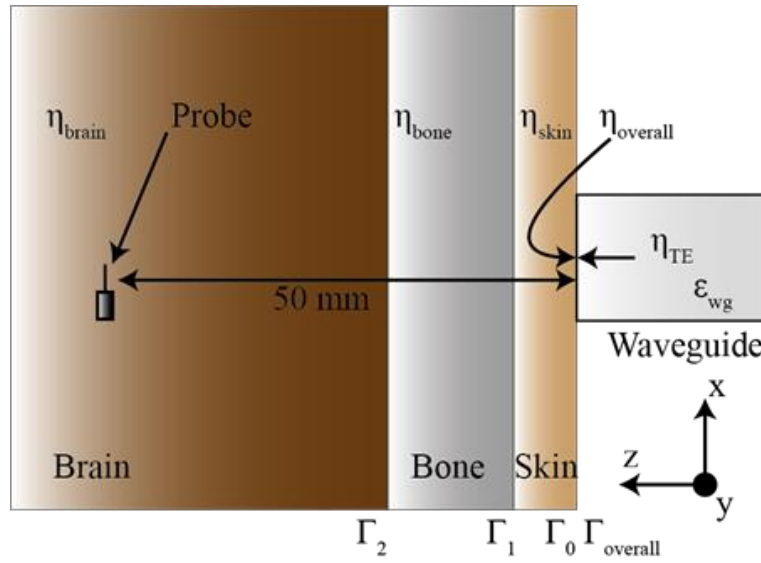


Fig. 3.5 Experimental setup – rectangular waveguide aperture against an inhomogeneous human head phantom.

### 3.4.3. Results and Discussion

The simulated normalized  $x$ -directed  $E$ -field ( $E_x$ ) penetration at 2.45 GHz is shown in Fig. 3.6 at 50 mm inside the head model from the surface of the skin for different permittivity dielectric-loaded rectangular waveguides. For each change of permittivity, the waveguide dimensions were changed accordingly to maintain the same cut-off frequency. The maximum field penetration occurs when the rectangular waveguide dielectric permittivity,  $\epsilon_{wg}$ , is within the range of 3 to 4.

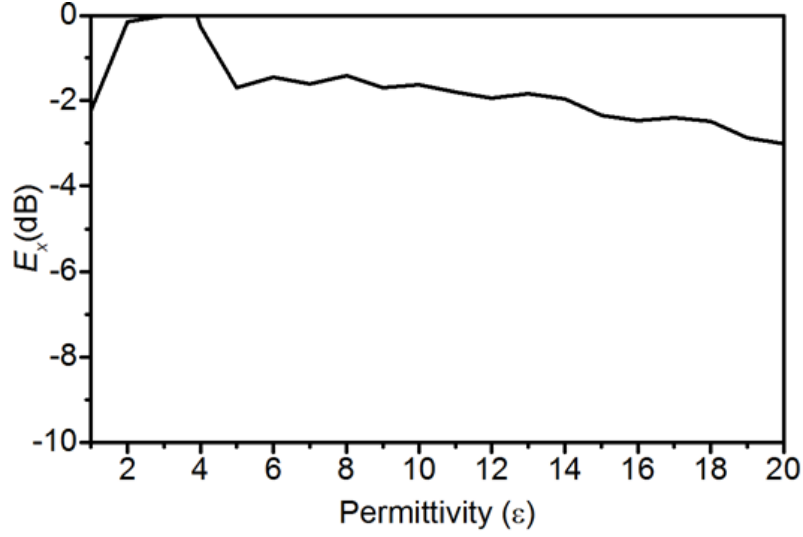


Fig. 3.6 Normalized  $E_x$ -field intensity at 50 mm inside human head versus dielectric-filled waveguide permittivity variation at 2.45 GHz.

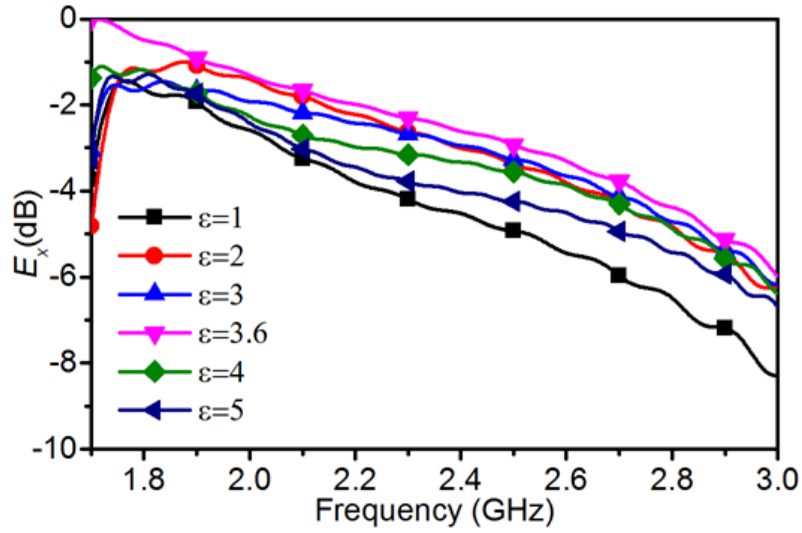


Fig. 3.7 Normalized  $E_x$ -field intensity at 50 mm inside human head versus dielectric-filled waveguide permittivity variation from 1.7 GHz to 3 GHz.

A frequency sweep from 1.7 GHz to 3 GHz in Fig. 3.7 shows the normalized  $E_x$  field penetration performance for different  $\epsilon_{wg}$  from 1 to 5. The maximum E-field penetration occurs at  $\epsilon_{wg} = 3.6$  over the entire range but is particularly pronounced at the lower frequencies. Although the dielectric characteristics of the human head may change slightly with frequency, it can be observed that over the small range of frequencies of interest the E-

field penetration is at maximized the calculated value of 3.6. The penetration is primarily minimum when the permittivity of air ( $\epsilon = 1$ ) is used inside the waveguide.

Fig. 3.8 portrays the simulated normalized E and H-plane near field patterns at 50 mm distance inside the human head for the waveguide dielectric filling of 1 and 3.62 respectively. The resulting radiation beam inside the brain is highly directional when permittivity of 3.62 is used compared to the air-filled waveguide. Hence improved directivity inside the human brain is achieved by using the optimized dielectric-filled waveguide.

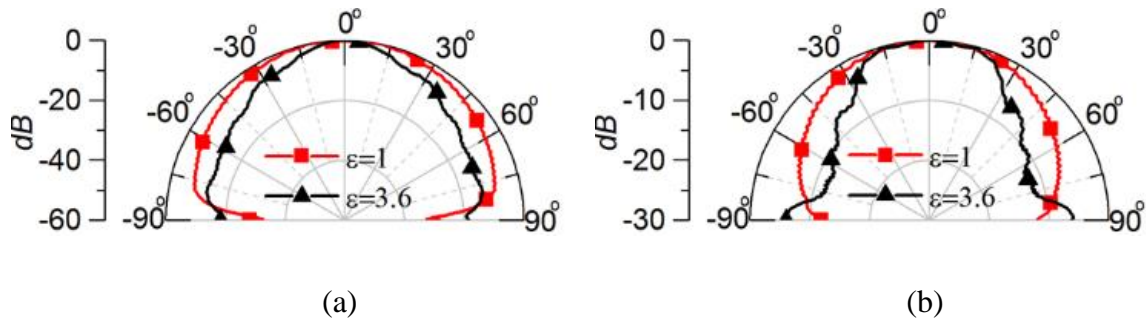


Fig. 3.8 Simulated normalized (a) E-plane (xz-plane) and (b) H-plane (yz-plane) near-field pattern at 50 mm distance inside human brain.

The power penetration  $\vec{P}$  in the propagation direction at a specific location can be calculated using the cross product of the  $\vec{E}$  and  $\vec{H}$ -field at a specific frequency. To observe the different transverse mode propagation characteristics inside the human head, Fig. 3.9 compares the power penetration for a TEM plane wave with  $TE_{10}$  waves radiating from both an air-filled waveguide and an  $\epsilon_{wg} = 3.6$  dielectric-filled waveguide. The highest penetration up to a 50 mm distance inside human head occurs when radiated from the dielectric-loaded waveguide. The  $TE_{10}$  wave emanating from the air-filled waveguide exhibits 3 to 7 dB less penetration and is also lower than TEM propagating wave from air into the human head. The loss due to the high-water content of the brain and other tissues can be observed from the penetration power level difference of around 20 dB between 0 and 50 mm inside the head.

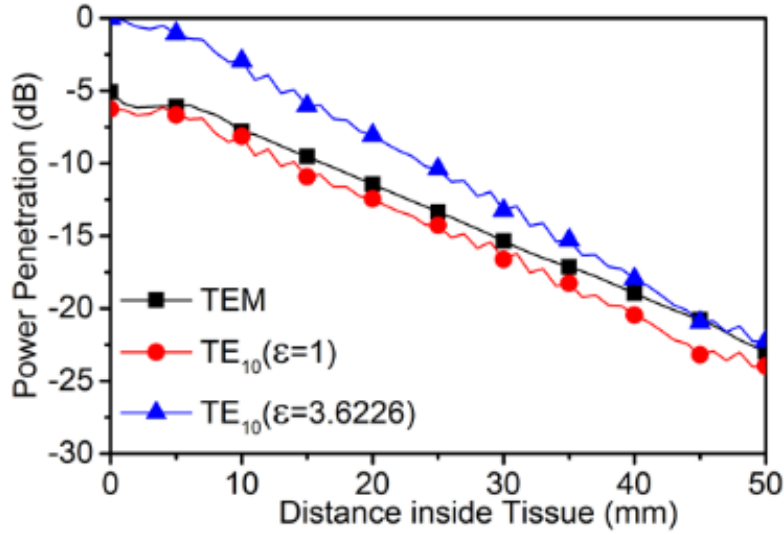


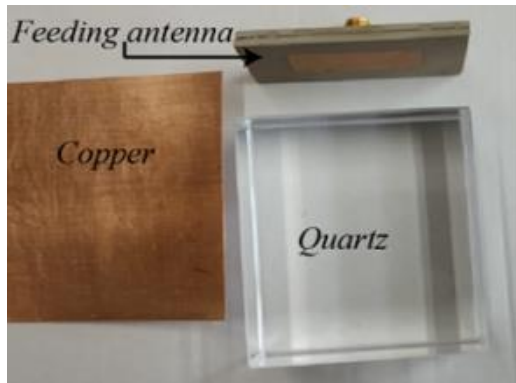
Fig. 3.9 Power penetration of TEM and TE10 radiated waves up to 50 mm inside the human head at 2.45 GHz.

#### 3.4.4. Dielectric Waveguide Design

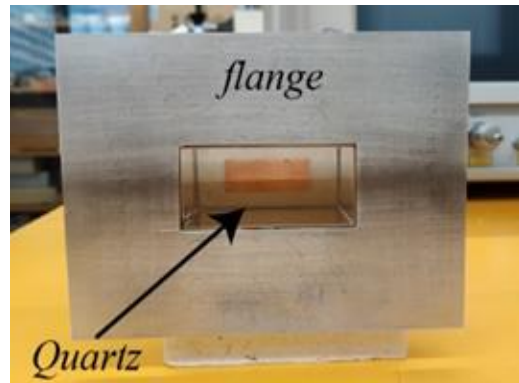
A  $47 \times 23 \times 54.65 \text{ mm}^3$  quartz block with the permittivity of 3.75 and  $\tan\delta$  of 0.0004 is selected as the closest suitable material to realize the approximate permittivity of the dielectric-loaded waveguide calculated earlier. A copper sheet of 0.5 mm thickness is enfolded around the quartz block to realize the waveguide tube. The constituent components are shown in Fig. 3.10 (a) are assembled, and a waveguide flange with the dimension of  $0.25 \lambda_{2.45 \text{ GHz}}$  at all sides is realized using aluminum as depicted in Fig. 3.10 (b). The side view of the fabricated waveguide is shown in Fig. 3.10 (c), showing a waveguide frame made of transparent plastic to hold the constructed waveguide to its rectangular shape.

An antenna feeding technique is utilized to excite the waveguide. Although such a feeding technique lacks broadband performance, the complication of probe feeding a rectangular waveguide via a delicate hole in the fragile quartz block can be avoided. Moreover, the findings of this research are focused on the specific frequency of 2.45 GHz, so a broadband solution is not warranted. The physical structure of the antenna is shown in Fig. 3.11. An L-probe technique is adopted to feed the rectangular patch. Two layers Rogers RT6010 with relative permittivity of 10.2 and thickness of 1.9 mm is used as the substrate material for the antenna. A 50 Ω SMA connector is used to connect the L-probe and the ground plane. The dimensions of the antenna are optimized to operate at 2.45 GHz while acting as a feed for the dielectric waveguide, in contact with the quartz block and covering one aperture end.

The simulated and measured  $|S_{11}|$  response of the dielectric rectangular waveguide with a patch antenna feed is depicted in Fig. 3.12. The  $|S_{11}|$  performance shows good agreement with only  $\sim 1\%$  shift in the resonant frequency, which can be attributed to the fabrication tolerances of the waveguide and feed antenna. The simulated and measured realized gain radiation pattern of the open-ended quartz loaded waveguide in free space is depicted in Fig. 3.13, also exhibiting good agreement in shape.



(a)

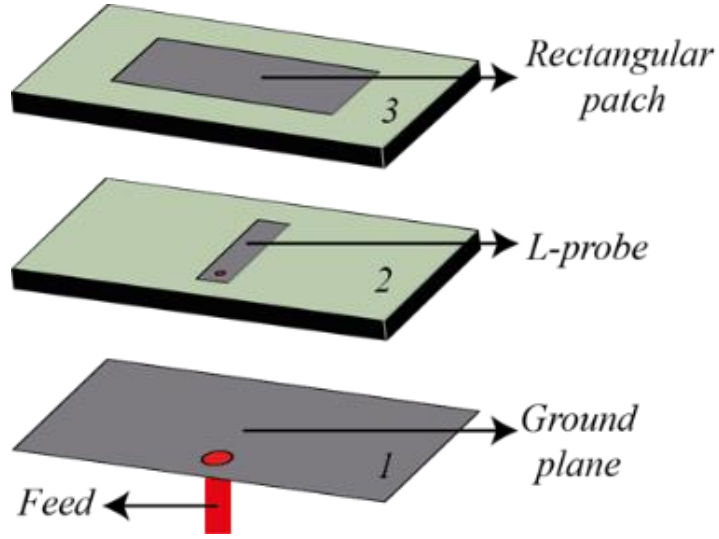


(b)

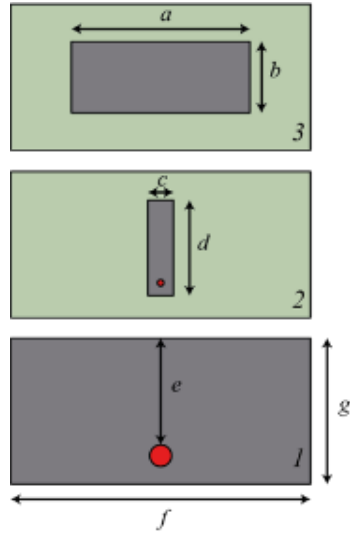


(c)

*Fig. 3.10 Fabrication of the waveguide prototype: (a) before assembly, (b) after assembly, (c) side view.*



(a)



(b)

*Fig. 3.11 Design of the waveguide feeding antenna (a) antenna structure (the gap between the layers is for illustration purpose only, layers 1, 2 and 3 are stacked without any gap in between), (b) parameters (in mm):  $a = 28$ ,  $b = 11.2$ ,  $c = 4$ ,  $d = 15$ ,  $e = 16.8$ ,  $f = 47$ ,  $g = 23$ .*

A measurement setup is implemented which includes the inhomogeneous head phantom, the rectangular waveguide excitation source, an electrically small monopole probe, an Anritsu (MS4644B) vector network analyser (VNA), and a computer as shown in Fig. 3.14. The same setup is utilized for both the quartz loaded waveguide and a standard WR 430 waveguide to obtain a comparison. The input power was adjusted to achieve the same output

power at the aperture for the different waveguides. The power penetration for each waveguide is then measured by placing it against the inhomogeneous human head without any air gap. The electrically small monopole probe is utilized as an E-field probe for radiation pattern measurement in both E and H planes. The monopole probe is fabricated from a semi-rigid coaxial cable, and the angle of measurement for the radiation pattern is changed manually by inserting the probe into the human head phantom. The received power is measured via the probe at 50 mm radius from the centre of the waveguide aperture which is mounted flush to the surface of the skin mimicking layer of the inhomogeneous phantom.

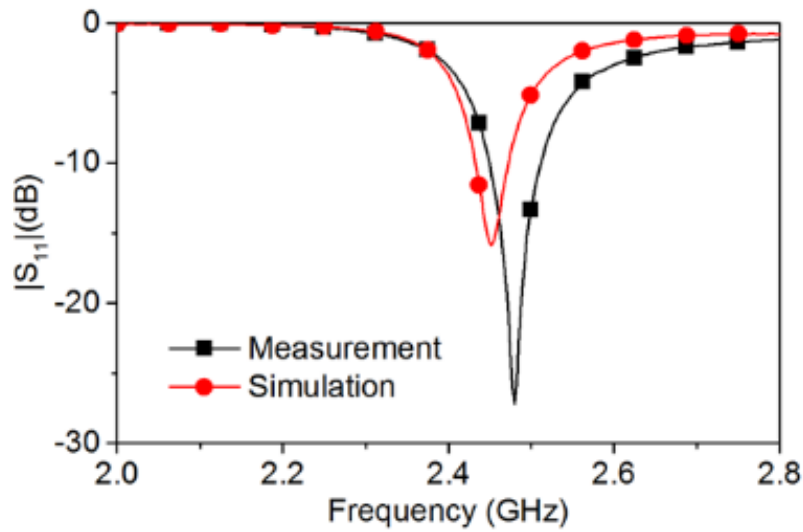


Fig. 3.12 Simulated and measured  $|S_{11}|$  of the open-ended quartz loaded waveguide.

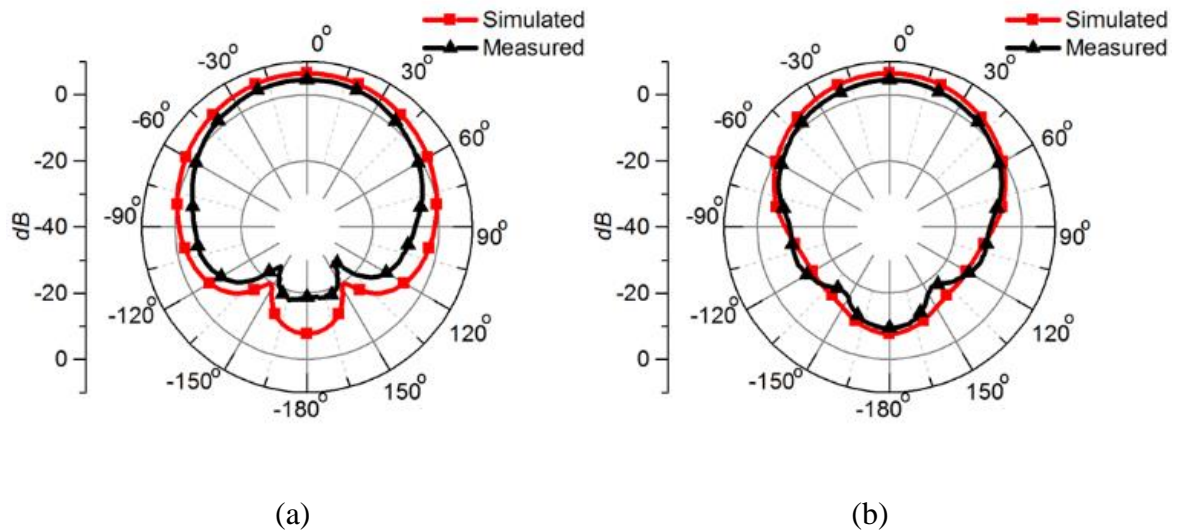
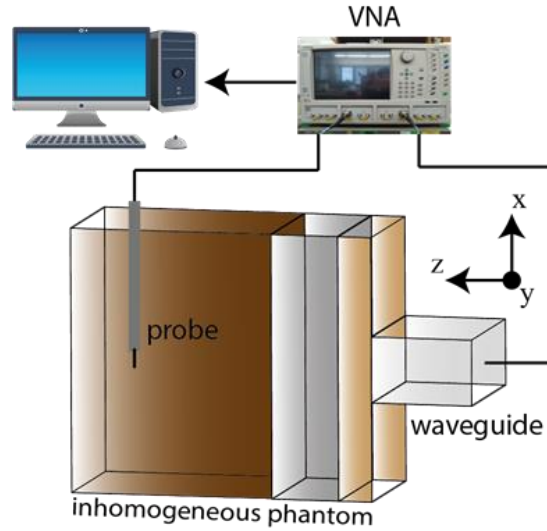


Fig. 3.13 Simulated and measured realized gain patterns of the open-ended quartz loaded waveguide operating at 2.45 GHz in the air (a) E-plane, (b) H-plane.





*Fig. 3.14 Measurement setup of the power penetration pattern.*

The near field power radiation pattern at both E-plane and H-plane for both the dielectric-loaded and standard WR430 waveguide is depicted in Fig. 3.15. The measured results follow a similar form as predicted in the simulations seen in Fig. 3.8, with the dielectric-loaded waveguide showing enhanced directivity. A power penetration increment of  $1.33 \text{ dB}$  is achieved utilizing the quartz loaded waveguide in the boresight direction. Moreover, due to the use of the high dielectric material compared to air, the waveguide source shrank significantly compared to the standard WR430 waveguide, with an  $81.9\%$  decrease in aperture size. The measured power penetration performance validates this wave impedance matching technique for increasing the power penetration into the human head for microwave medical diagnostic systems.

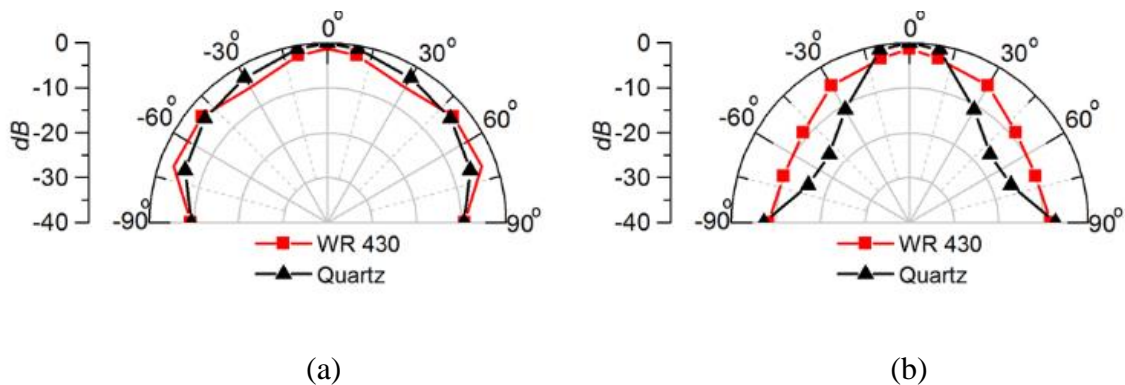


*Fig. 3.15 Measured power penetration pattern at a 50 mm radius inside the inhomogeneous phantom for the quartz loaded waveguide and standard WR 430 waveguide at (a) E-plane, (b) H-plane.*

### 3.4.5. Conclusion

Improvement of the microwave power penetration inside an inhomogeneous human head phantom is achieved by utilizing a dielectric-loaded rectangular waveguide for microwave medical diagnostic applications. The combined complex reflection properties of a layered human head model are calculated between skin, bone, and brain tissue. A wave impedance matching technique is applied by utilizing a dielectric-loaded rectangular waveguide to modify the  $TE_{10}$  mode characteristics at  $2.45\text{ GHz}$ . An antenna fed Quartz ( $SiO_2$ ) loaded rectangular waveguide is fabricated along with a layered inhomogeneous human head phantom to measure the power penetration. A measured  $1.33\text{ dB}$  power penetration increment is achieved at  $50\text{ mm}$  inside the human head phantom by utilizing the designed dielectric-loaded waveguide as compared to the standard WR430 waveguide filled with air, and an  $81.9\%$  reduction in the aperture size is also attained.

## 3.5. Antenna Characterization

### 3.5.1. Rationale

Specially designed antennas for medical diagnosis and achieving efficient and user-friendly communications between an implant and external devices have gained much interest amongst antenna researchers. Such antenna designs can be divided into three general categories: near field, on-body, and in-body antenna systems according to their operational proximity to the human body. The antennas reported in [16, 32, 50, 61, 130] operate with the human body (specifically the human head) in the antennas near field. The on-body matched antennas reported in [18, 30, 64, 102] are in contact with the human head to achieve increased impedance matching and hence increased signal penetration inside the human tissue. The implantable antennas reported in [103-107] are for various application related to human body diagnosis, which requires the antenna itself to be accommodated inside the human body.

Designing antennas to operate near the human body requires the consideration of human tissues when simulating the antenna performance. The complex structure and characteristics of human tissue urge the simulator to solve a wide range of data problems resulting in an exponential increment in the simulation time [18]. Such complexity can be decreased by using a homogeneous phantom to represent the human body instead of the inhomogeneous phantom. For this reason, a lot of the antennas designed for human body applications do not

consider inhomogeneous and frequency-dependent characteristics of the human body. Recently, the effect of inhomogeneous characteristics of human tissue is investigated for chemotherapy treatment in [108]. The electric field intensity is investigated in the human tissue phantom, and it is shown that the electric field distribution is affected by the inhomogeneous structure.

To investigate the differences in antenna, an antenna matched to both a homogeneous and inhomogeneous human head phantom is designed. The effect of choosing a homogeneous head phantom over realistic inhomogeneous human head phantom for antenna characterization is shown by examining the E-field, H-field, radiation pattern at the near field, and the power penetration inside the human tissue. The antenna is compact for low frequency (sub 1 GHz) operation.

### 3.5.2. Antenna Design

The proposed homogeneous and inhomogeneous human head matched antenna is depicted in Fig. 3.16. The antenna as a meandered wire configuration and the conducting plane of the antenna touches the surface of the human phantoms shown in the characterization setups of Fig. 3.17 (a) and (b). The overall dimensions of the antenna is  $30 \times 30 \times 1.6 \text{ mm}^3$ . A cheap and readily available FR4 substrate material of thickness  $1.6 \text{ mm}$  is employed to design the antenna. The meandered line extends from the feed point with the length  $a + b + c$  to achieve antenna resonance at  $0.9 \text{ GHz}$ .

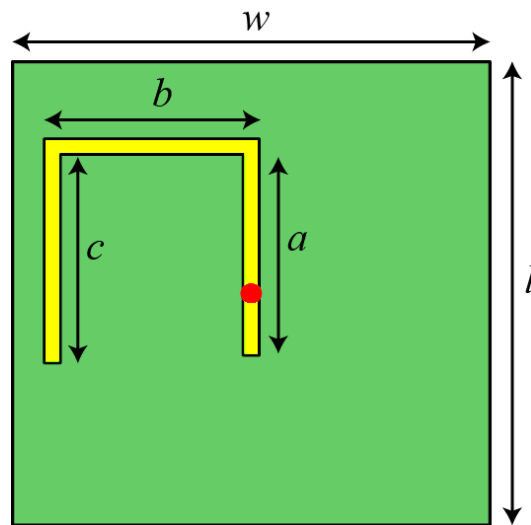


Fig. 3.16 Design of the antenna. Dimensions (in mm):  $a = 13$ ,  $b = 13.5$ ,  $c = 13.5$ ,  $l = 30$ ,  $w = 30$ .

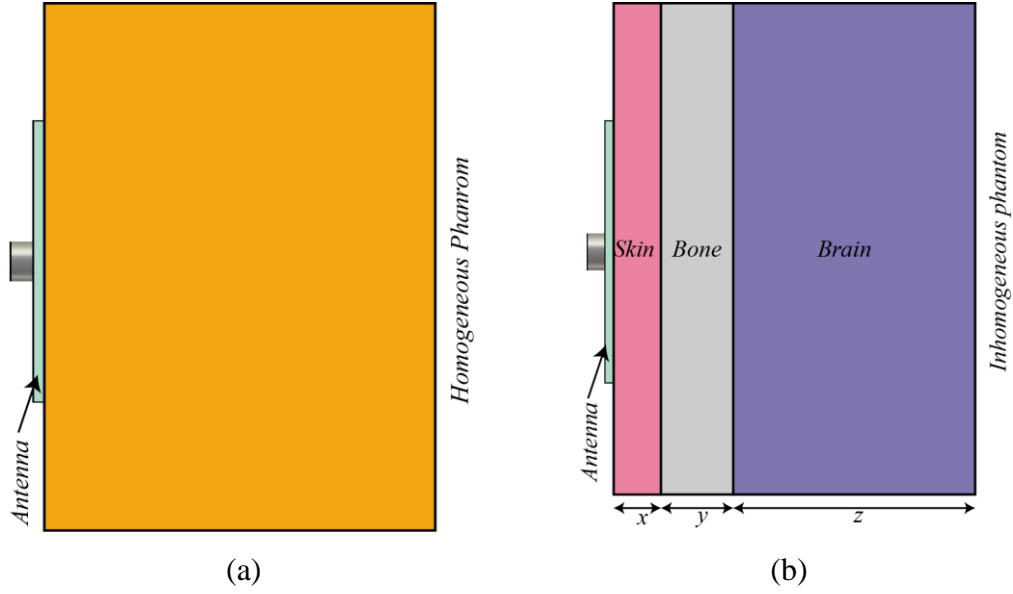


Fig. 3.17 Antenna simulation setup (a) antenna mounted on homogeneous head phantom, (b) antenna mounted on inhomogeneous head phantom. Dimensions (in mm):  $x = 3$ ,  $y = 10$  and  $z = 50$ .

The line extension backward from the feeding point (shown by the red-colored circle in Fig. 3.16) provides a degree of freedom for impedance matching at the desired frequency. For both human phantom cases, the resonance of the antenna is almost identical. Having the same resonance for both setups results in fewer simulation variables to be considered at the antenna end. With the aid of the high permittivity characteristics of the human tissue, the maximum dimension of the antenna is reduced to less than  $\lambda/11$  at the center frequency  $0.9 \text{ GHz}$ .

The phantom considered in [18] is used for the homogeneous head model in this research, having a permittivity  $\epsilon_{\text{homo}} = 35$  and conductivity  $\sigma_{\text{homo}} = 0.5 \text{ S/m}$ , which are independent of changes in operating frequency. For the inhomogeneous head phantom, the three major layers: skin, bone, and brain are considered with thicknesses of  $x = 3 \text{ mm}$ ,  $y = 10 \text{ mm}$  and  $z = 50 \text{ mm}$  respectively. The frequency-dependent permittivity and conductivity characteristics of these tissue materials are taken from the bio-materials library of the CST 2017 [131]. Fig. 3.18 depicts the surface current distributions of the antenna when it is touching each of the two phantoms. The current distribution is similar for both the homogeneous (Fig. 3.18 (a)) and inhomogeneous (Fig. 3.18 (b)) phantoms. The location of the null occurring midway

along the meander line shifts its placement due to the difference in material characteristics at boresight of the antenna.

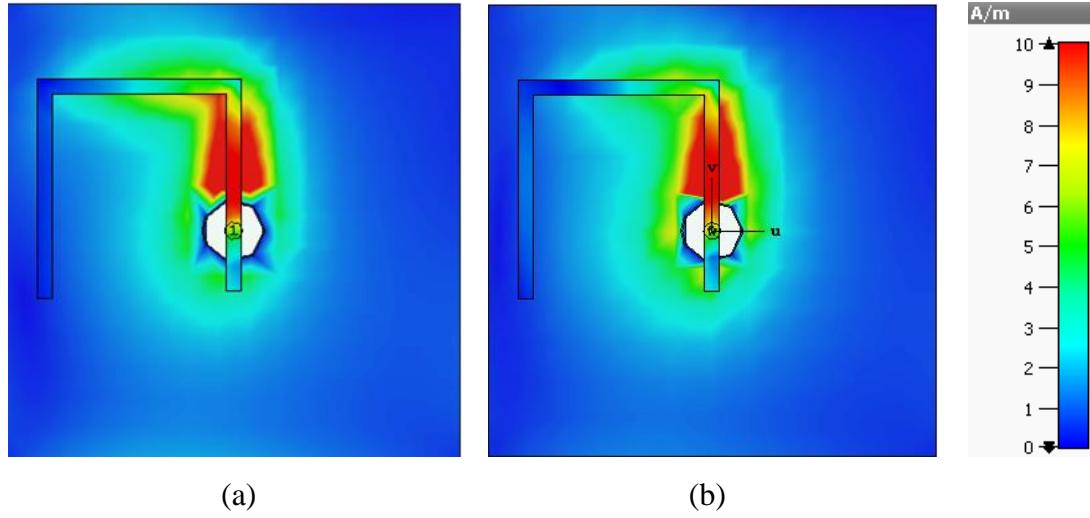


Fig. 3.18 The surface current distribution of the antenna with (a) homogeneous, and (b) inhomogeneous phantom.

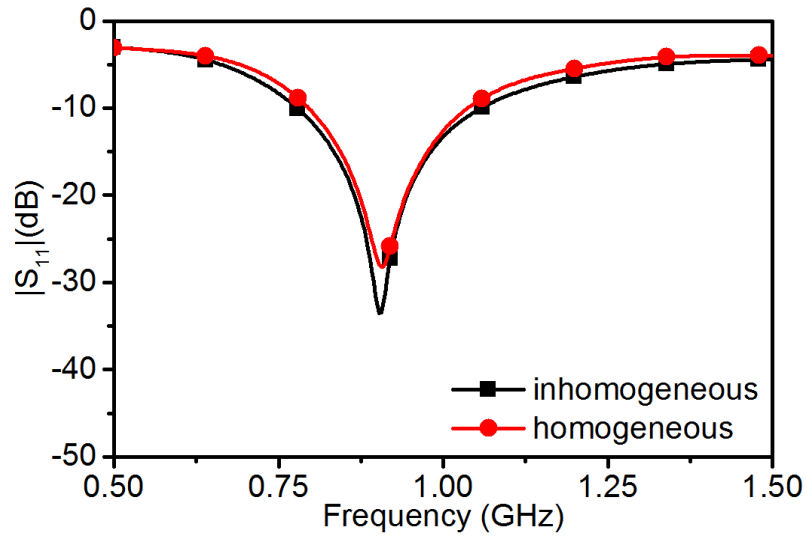


Fig. 3.19  $|S_{11}|$  response of the antenna with the homogeneous and inhomogeneous human head phantom.

The  $|S_{11}|$  of the antenna for both phantom cases are shown in Fig. 3.19. The  $|S_{11}|$  responses are congruent with each other over the simulated frequency region, except for a slight variation at the resonance point. At 0.9 GHz frequency, the antenna shows a  $|S_{11}|$  response that is approximately 5 dB lower for the inhomogeneous phantom compared to the

homogeneous phantom. Nonetheless, both are well matched exhibiting below  $-25\text{ dB}$  at  $0.9\text{ GHz}$ , which is sufficient for most applications.

### 3.5.3. Results and Discussions

CST studio suite 2017 [131] was used to simulate the E-field and H-field distribution of the antenna inside the homogeneous and inhomogeneous head phantoms. Fig. 3.20 depicts the E-field distribution inside both the considered human head phantoms. It can be realized from the E-field distribution in Fig. 3.20 (a) that the penetration of E-field is scattered into three different regions inside the homogeneous phantom. For the inhomogeneous phantom in Fig. 3.20 (b) however, the E-field displays a stepped distribution. This is due to the permittivity inhomogeneity in front of the antenna which changes the wavelength of the propagated wave while penetrating through the phantom, and reflections at the boundaries between the layers. Field variations can also be seen in the H-field distribution. In Fig. 3.21 (a) the H-field distribution transitions highly directed towards the bottom side of the antenna inside the homogeneous phantom. The H-field distribution depicted in Fig. 3.21 (b) for the inhomogeneous phantom shows a similar response with nearly half intensity compared to the response for the homogeneous phantom. Overall, the E-field and H-field intensity are lower in the inhomogeneous head phantom, implying that an erroneously higher field penetration is present in the homogeneous phantom.

The E-field radiation pattern in the near field of the antenna at both E-plane and H-plane is shown in Fig. 3.22, with the boresight measurement at a distance  $50\text{ mm}$  inside the homogeneous and inhomogeneous phantoms when the antenna is mounted at the outer surface of the phantom. The near field radiation patterns for homogeneous and inhomogeneous phantom are normalized in terms of the maximum value found from both cases. In both E-plane and H-plane, penetration inside the phantoms is maximum for the homogeneous phantom. Both the E-plane and H-plane distribution for the homogeneous and inhomogeneous phantom differ from each other. The penetration at the boresight of the antenna shows ripples for the homogeneous phantom in E-plane whereas it is comparatively smooth for the inhomogeneous phantom.

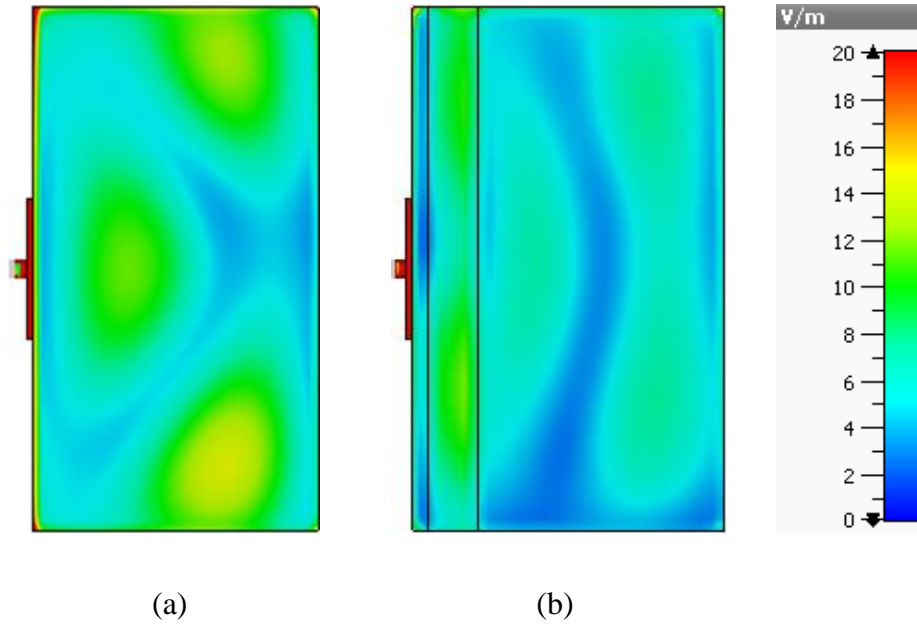


Fig. 3.20 E-field distribution inside the (a) homogeneous and (b) inhomogeneous human head phantom.

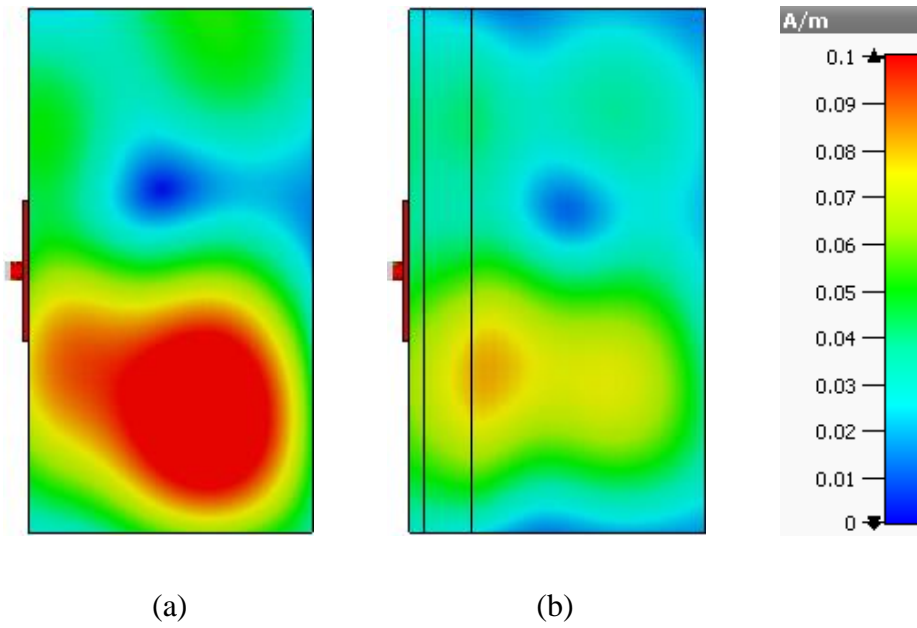
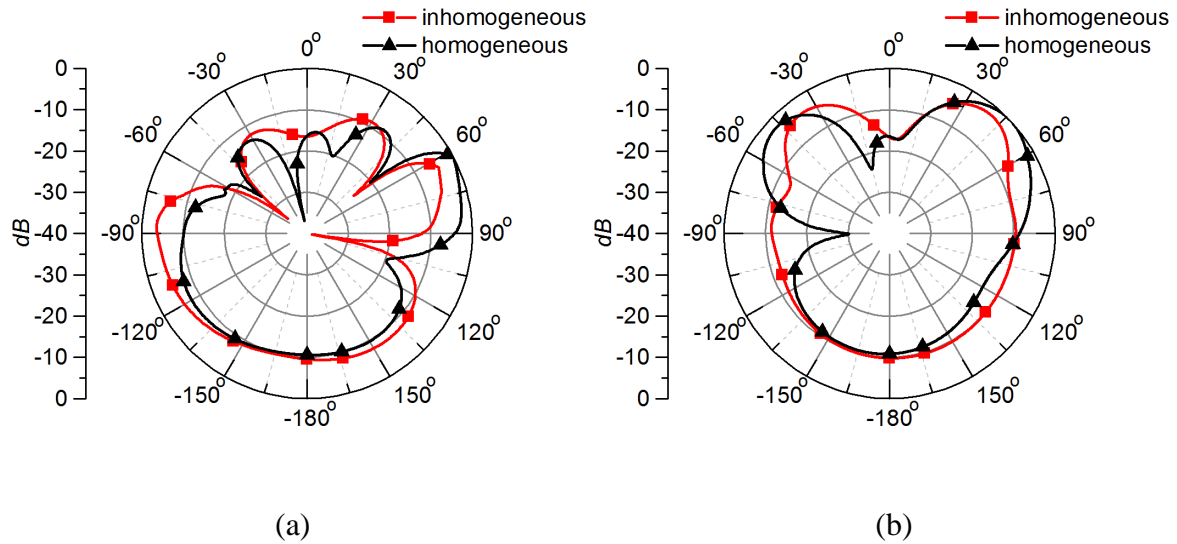


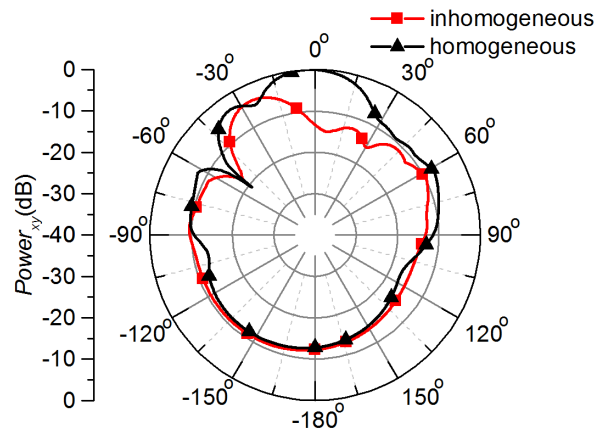
Fig. 3.21 H-field distribution inside the (a) homogeneous and (b) inhomogeneous human head phantom.

Fig. 3.23 shows the power penetration at 50 mm radius centered around the designed antenna where the human head phantom is situated at the boresight ( $0^\circ$ ) of the antenna. The power penetration pattern from  $-90^\circ$  to  $90^\circ$  centered at  $0^\circ$  shows power within the phantom, and the

pattern from  $90^\circ$  to  $-90^\circ$  centered at  $-180^\circ$  shows the power radiating in the air (at the back of the antenna). The power penetration is higher in the homogeneous head phantom as compared to the inhomogeneous head phantom, as less power reflections occur inside the homogeneous medium. A shift in the main beam direction has occurred due to the transition of the wave through the inhomogeneous phantom with different material characteristics.



*Fig. 3.22 Near field radiation pattern of the antenna at 50 mm inside the phantoms with the inhomogeneous and homogeneous head phantom (a) E-plane (b) H-plane.*



*Fig. 3.23 Normalized power radiation pattern at 50 mm radius centered around the designed antenna.*

Moreover, the maximum power penetration direction for both cases differs from each other. A 5-dB maximum power penetration difference can be observed while a 13-dB power



penetration difference exists at boresight of the antenna. The patterns show similar power distribution at the rear of the antenna ( $180^\circ$ ) because for both cases the back of the antenna radiates into air. From the overall characterization of the two phantoms, the homogeneous and inhomogeneous head phantom displays different radiation characteristics. When designing microwave radiating devices for highly sensitive applications in biomedical diagnosis, simulation using a homogeneous head phantom may result in an elevated representation of power penetrations. Hence an inhomogeneous head model is required when realistic scenarios call for accurate characterization of the internal fields/power for the medical diagnosis application.

### **3.5.4. Conclusions**

A comparison between a homogeneous and frequency-dependent inhomogeneous human head model is investigated in terms of biomedical antenna characterization parameters. A meander line antenna operating at 0.9 GHz is designed to operate while touching a homogeneous or inhomogeneous head phantom located in the boresight direction of the antenna. The homogeneous and inhomogeneous head phantoms are compared in terms of the electric field, magnetic field, radiation pattern at the near field, and the power penetration at 50 mm inside the phantoms. Visible differences in behavior are observed in terms of the field/power propagating into the two types of phantoms. The antenna radiation characteristics are highly dependent on the homogeneity/inhomogeneity characteristics of the human head, with variations in permittivity and reflections at boundaries influencing performance. Hence when designing microwave radiating devices for sensitive applications such as the medical diagnosis of a human head, the inhomogeneity of the human tissue layers should be considered.

## **3.6. Effect of a Superstrate**

### **3.6.1. Rationale**

A microwave antenna can act as the radiating element for stroke diagnosis, chemotherapy, and head imaging [16, 30-32]. Numerous antennas have been proposed to achieve signal propagation inside human tissue without touching the surface of the human body. A CPW-fed antenna designed for medical diagnosis is reported in [130], where the antenna is designed to be operating at the far field from the human body. Another antenna

for brain stroke detection is reported in [50], providing both the far field and near field characteristics of the antenna. However, the antenna also operates without touching the human body. A similar approach is taken when designing antennas for medical diagnosis in [16, 32, 94, 132].

Antennas that contact with the surface of human tissue are more likely to provide increased penetration compared to those operating in air due to reflections at the air-skin interface. Relatively few antenna designs are reported in the literature which are directly attached to the human body for operation. In [18], a bowtie shaped antenna matched to a human head model is reported. The top antenna conductor directly touches the human head surface to achieve impedance matching. The radiation pattern of the antenna is characterized at the boresight direction only. Antenna designs with a similar operation principle are reported in [79, 82] for breast cancer detection application where the antenna conductor plane is in direct connection with the skin layer of the breast. It is reported in [95, 133, 134] that a direct connection between the antenna and human tissue results in a poor antenna performance. However, there is no evidence of a direct comparison between antennas with and without direct contact of the conductor of the antenna with human tissue.

In some cases, direct contact between the antenna conductor layer and the human tissue is prevented by using a superstrate. A wideband antenna design is reported to detect early congestive heart failure employing a foam material as a superstrate and around the antenna to achieve durability during operation [102]. However, the foam material that is used outside of the antenna shielding the conductors from directly touching human tissue is not considered in the simulation. For thrombolytic treatment with microwave operated medical diagnosis systems, a patch antenna covered by a plastic container holding a matching liquid is utilized [30]. However, the impact of the container filled with water on the performance of the antenna was not investigated. An antenna utilizing a superstrate layer in the boresight direction of the antenna is shown in Section 4.2 of this thesis, but the performance of the antenna without a superstrate is not shown. An implantable antenna to monitor intracranial pressure of human head is presented in [107], equipped with a battery and data and power management circuitry encapsulated in a container. The container made of Alumina ( $\text{Al}_2\text{O}_3$ ) isolates the whole antenna system from the human tissue. In [103], an implantable antenna operating at 2.4 GHz is reported for biomedical applications which uses a superstrate layer of Rogers 6010 material to achieve separation of the human tissue from the antenna conducting

layer. Similar mechanisms to achieve antenna isolation from the human tissue are reported in [104, 105, 135]. In all these proposed implantable antennas, a comparative characterization of the presence of a superstrate layer is omitted so the usefulness and impact of the superstrate cannot be determined.

In this study we investigate the effectiveness of a superstrate layer on the performance of an on-head matched antenna, particularly with regards to power penetration pattern and SAR. Two on-head matched antennas, one with a superstrate and one without, are designed to compare the antenna performance. Both are impedance matched at a similar frequency range to achieve a more rational comparison. The overall lateral dimensions of the antennas are fixed at  $30 \times 30 \text{ mm}^2$  while achieving -10 dB impedance matching at around 0.9 GHz. The reflection coefficient, E- and H-fields, power penetration pattern, and SAR inside a human head phantom are evaluated, considering both homogeneous and inhomogeneous lossy tissue models to establish the effect of a superstrate in antenna designs for biomedical applications.

### 3.6.2. Design of the Antennas

The antennas depicted in Fig. 3.24 utilize FR4 dielectric material with a thickness of 1.6 mm. Antenna 1 in Fig. 3.24 (a) is designed to operate in contact with a human head without a superstrate layer. The thickness of the superstrate for Antenna 2 shown in Fig. 3.24 (b) is 0.5 mm and is also made of FR4. With the aid of the high permittivity of human head, the radiating conductor of Antenna 2 achieves a short-meandered length of  $a + b + c$  ( $0.12 \lambda_0$ ) while achieving a good impedance matching at around 0.9 GHz. This frequency was targeted as the lower microwave frequency region is reported to be more suitable compared to higher microwave frequencies to achieve increased signal propagation inside human tissue [24]. The aim for Antenna 2 was to keep identical overall footprint of  $30 \times 30 \text{ mm}^2$  of Antenna 1 for effective comparison. As the Antenna 2 lacks the advantage of being in direct contact with high permittivity human head phantom, the length of the conductive meander line is extended to  $d + e + f + g + h$  to achieve impedance matching at 0.9 GHz. The feed position also remains constant for both antennas in the middle of the ground plane on the reverse side.

The simulation setups depicted in Fig. 3.25 consider the antennas affixed to the surface of human head phantom, and were executed in CST 2017 [131]. For Antenna 1, the antenna conductor plane is in direct contact with the head phantom as shown in Fig. 3.25 (a), whereas Antenna 2 is buffered by the superstrate (Fig. 3.25 (b)). The antennas were evaluated against

both homogeneous and inhomogeneous human head phantoms. The homogeneous phantom is constructed with permittivity  $\epsilon_{phantom} = 35$  and conductivity  $\sigma_{phantom} = 0.5 \text{ S/m}$  [18] with dimensions  $80 \times 80 \times 60 \text{ mm}^3$ . The inhomogeneous head phantom is constructed using layered skin, bone and brain tissue materials from the CST 2017 library. The thickness used for the skin, bone and brain layers are 3 mm, 10 mm and 50 mm respectively. Fig. 3.25 (c) and (d) depicts the permittivity and loss tangent respectively of the utilized tissue materials to construct the phantom in terms of frequency.

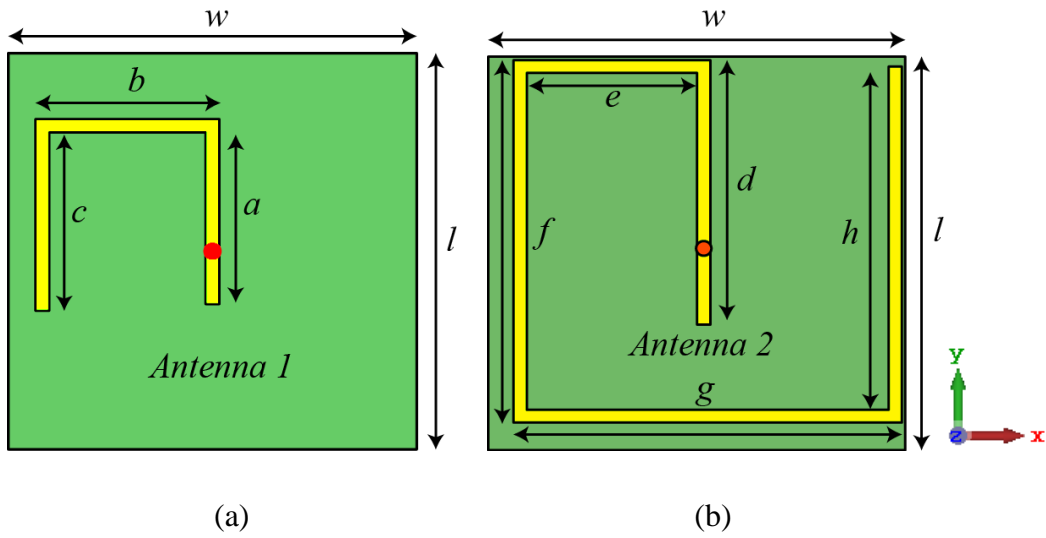


Fig. 3.24 Design of the human head phantom matched antennas. Antenna (a) without superstrate, (b) with superstrate. Dimensions (in mm):  $a = 13$ ,  $b = 13.5$ ,  $c = 13.5$ ,  $d = 20.8$ ,  $e = 12.9$ ,  $f = 28.5$ ,  $g = 29.4$ ,  $h = 27$ ,  $l = 30$ ,  $w = 30$ .

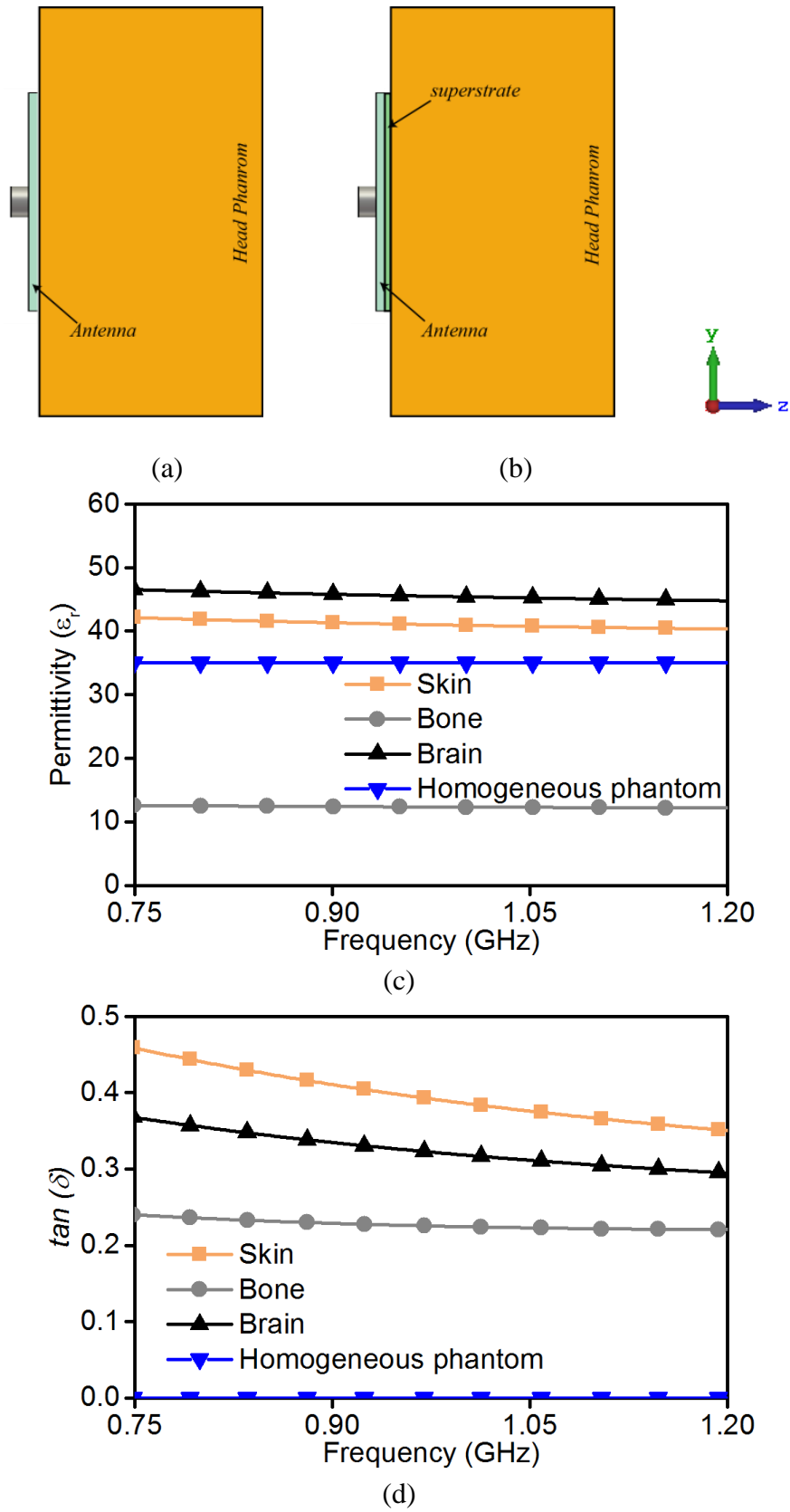
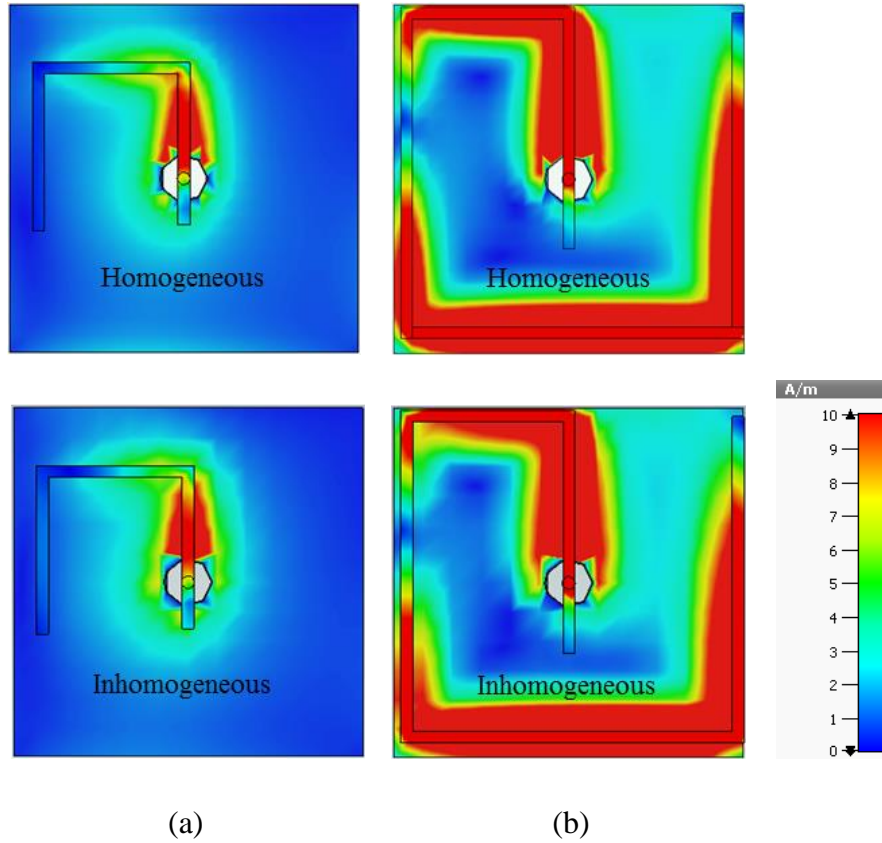


Fig. 3.25 Simulation setup of (a) Antenna 1 and (b) Antenna 2 with the head phantom. Head phantom tissue (c) permittivity, (d) loss tangent.

The current distribution patterns of the two antennas at 0.9 GHz are shown in Fig. 3.26. In Fig. 3.26 (a) the current flow intensity for Antenna 1 peaks near the feed point and decays towards the first 90° bend in the conducting line and is almost completely extinguished half way down the length of the line. Such a distribution occurs due to the direct connection between the antenna conducting plane and the conductive human head models. In Fig. 3.26 (b), the current distribution for Antenna 2 shows distributed current flow across almost the entire length of the conductive meander line of the antenna, indicating its length is mostly responsible for impedance matching at 0.9 GHz. The superstrate inhibits the current from directly flowing towards the conductive human head phantom. The surface current distributions of Antennas 1 and 2 remain largely similar for both homogeneous and inhomogeneous head models.



*Fig. 3.26 The surface current distribution of (a) Antenna 1, and (b) Antenna 2 at 0.9 GHz while operating on head.*

The  $|S_{11}|$  responses of the antennas are shown in Fig. 3.27. Antenna 1 with homogeneous head phantom possesses an impedance bandwidth of 0.25 GHz with the  $|S_{11}|$  response below -

25 dB at 0.9 GHz. The impedance dip of Antenna 2 occurs at 0.95 GHz, a 0.05 GHz offset from Antenna 1, with an impedance bandwidth of 0.14 GHz for the homogeneous head phantom. Nonetheless, the  $|S_{11}|$  response for Antenna 2 at 0.9 GHz is below -10 dB providing minimal reflection at the desired frequency. The discrepancy between the two antennas is due to the set requirement of maintaining a  $30 \times 30 \text{ mm}^2$  footprint for Antenna 2. To maintain a simple meandered loop shape, the length of the line is limited and can only reduce the centre of the impedance bandwidth down to 0.93 GHz. Similar  $|S_{11}|$  responses can be found with the inhomogeneous head phantom, with corresponding overall meander length issues for Antenna 2.

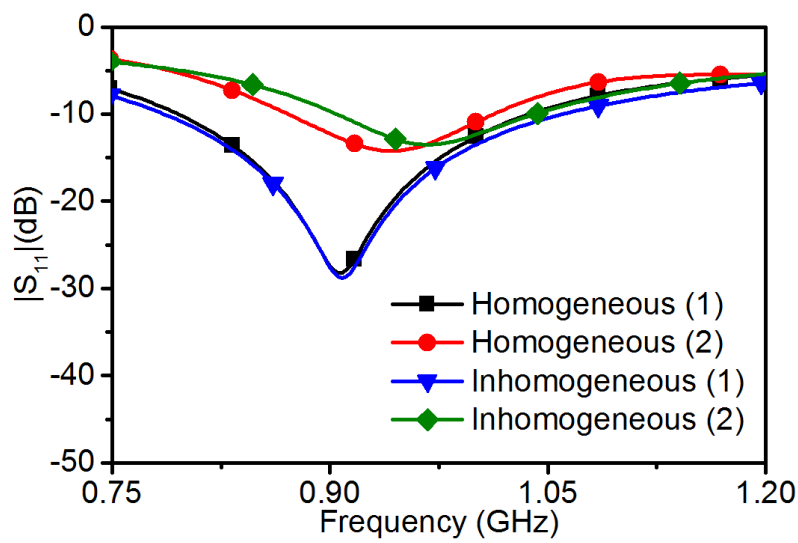
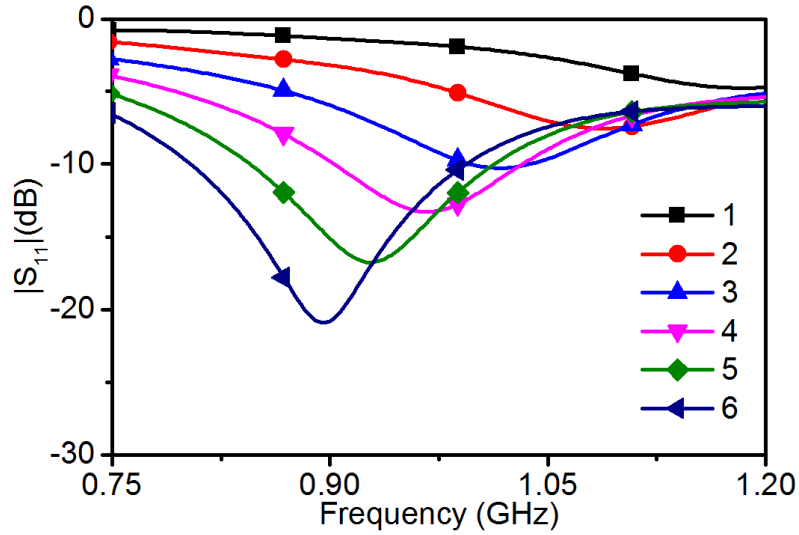


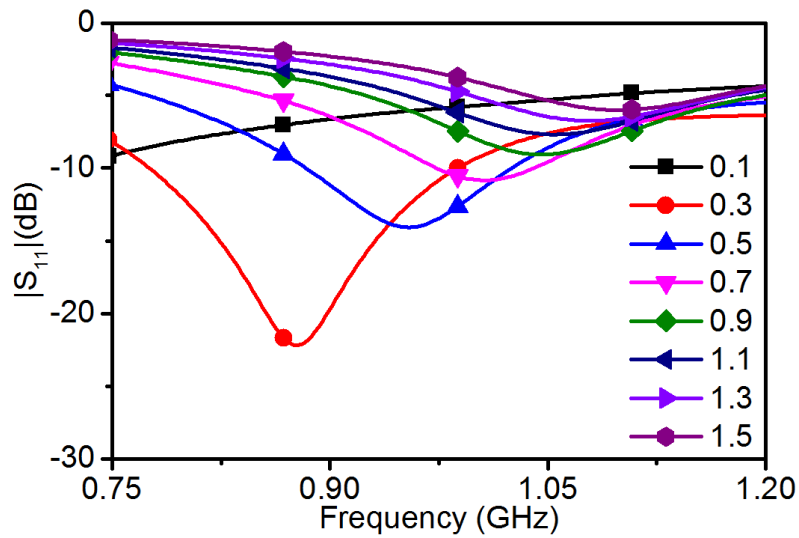
*Fig. 3.27 Reflection coefficient  $|S_{11}|$  of the Antenna 1 and Antenna 2 for homogeneous and inhomogeneous head phantom.*

The effect of the superstrate in terms of its thickness and permittivity is shown in [136, 137] for implantable antennas. Nonetheless, it is crucial to examine the effect of the superstrate thickness and permittivity for the proposed antenna when in contact with the surface of the human tissue. The parametric studies for the thickness and permittivity superstrate are shown in Fig. 3.28, where in Fig. 3.28(a) an increase in the permittivity of the superstrate results in the resonance shifting towards a lower frequency. This is due to the effective wavelength becoming shorter hence resulting in a lower resonant frequency. Fig. 3.28(b) shows that increasing the thickness of the superstrate moves the resonance towards a higher frequency. Increasing the thickness decreases the effective permittivity by insulating the antenna

conducting layer from the high dielectric human tissue material, hence the resonance movement towards a higher frequency.



(a)



(b)

Fig. 3.28 Parametric study on superstrate (a) permittivity and (b) thickness.

The free space (without the phantom)  $|S_{11}|$  response of the antennas is shown in Fig. 3.29. A resonance at 6 GHz and 6.25 GHz for Antenna 1 and Antenna 2 respectively is observed. When the phantom is in with the surface of the antennas, their resonances reduce to around 0.9 GHz due to the dielectric loading of the tissue materials.



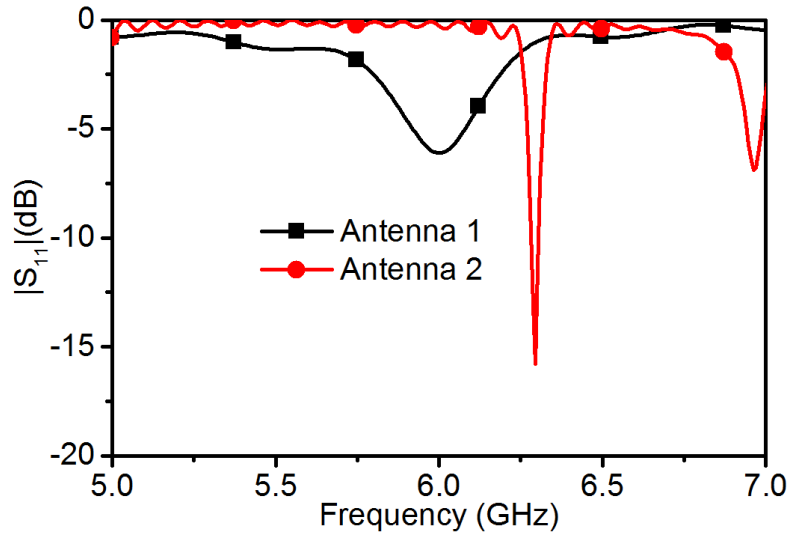


Fig. 3.29 Free space resonance of Antenna 1 and Antenna 2 (without the phantom at the boresight direction of the antennas).

The free space antenna efficiency is found to be 98% for the Antenna 1 and 92% for Antenna 2 at 0.9 GHz, which omits the losses caused by the tissue phantom materials.

### 3.6.3. Results and Discussions

#### 3.6.3.1. Simulation

The E-field and H-field distributions inside the human head phantom with the two antennas attached are depicted in Fig. 3.30 and Fig. 3.31 respectively. Stronger, more evenly distributed fields are seen inside the homogeneous human head phantom for Antenna 2 (in Fig. 3.30 (b) and Fig. 3.31 (b)) than Antenna 1 (in Fig. 3.30 (a) and Fig. 3.31 (a)). The superstrate layer in Antenna 2 shields the conductor from leaking energy directly into the lossy material, allowing significantly more to penetrate into the head.

Once the more realistic inhomogeneous head phantom is considered, Antenna 2 generates significantly more E- and H-field intensity than Antenna 1. Only a very small portion of the field penetrates the skin and bone layers into the brain for Antenna 1 mounted on the inhomogeneous phantom. This is because the propagation modelling must consider the successive reflections at the boundaries between the tissues, which can be significant due to the large variation in layer permittivity properties. This highlights the importance of utilizing an inhomogeneous model in the design of biomedical antennas.

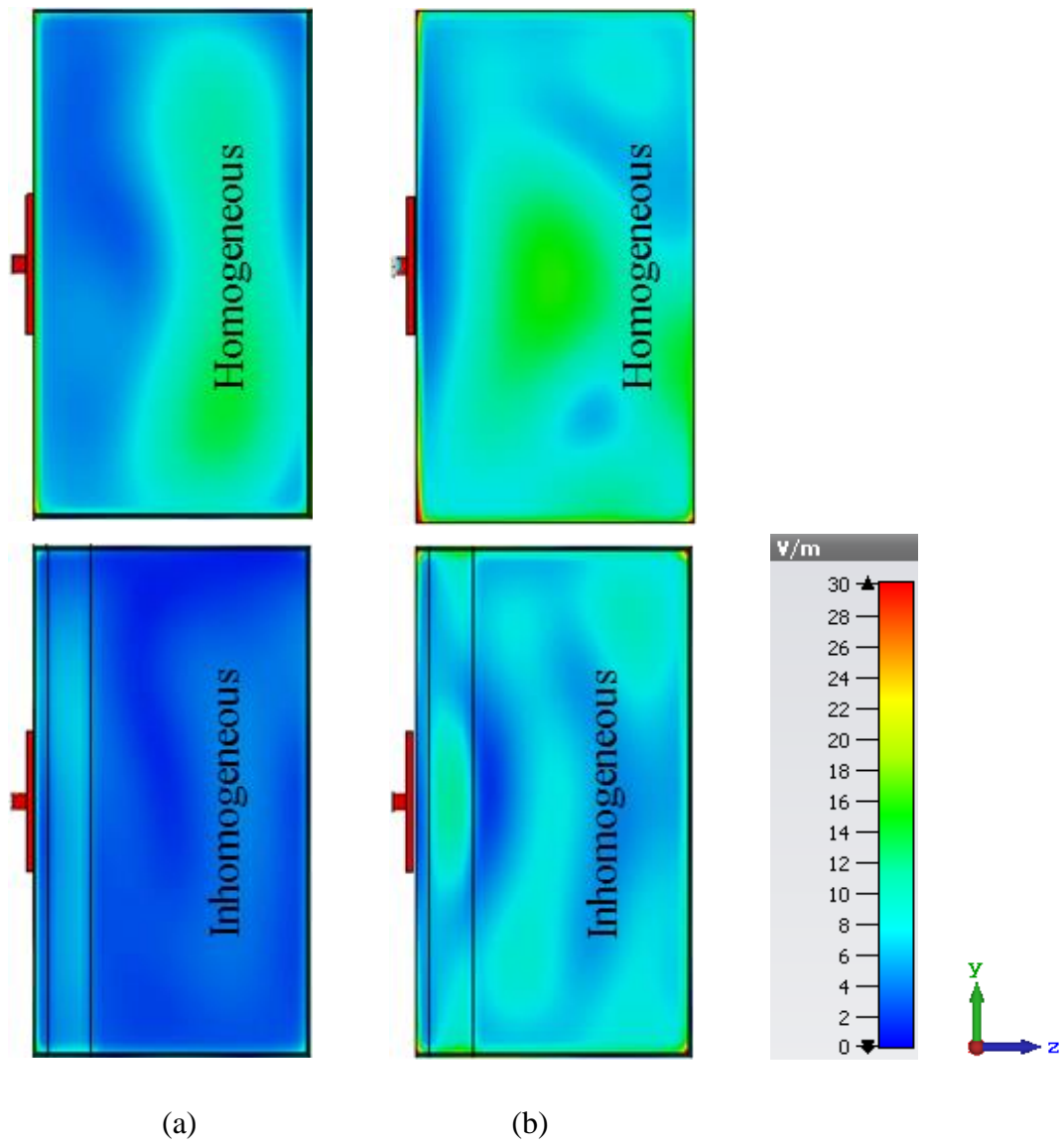


*Fig. 3.30 Distribution of the E-field inside human head phantom for (a) Antenna 1 and (b) Antenna 2 at 0.9 GHz.*

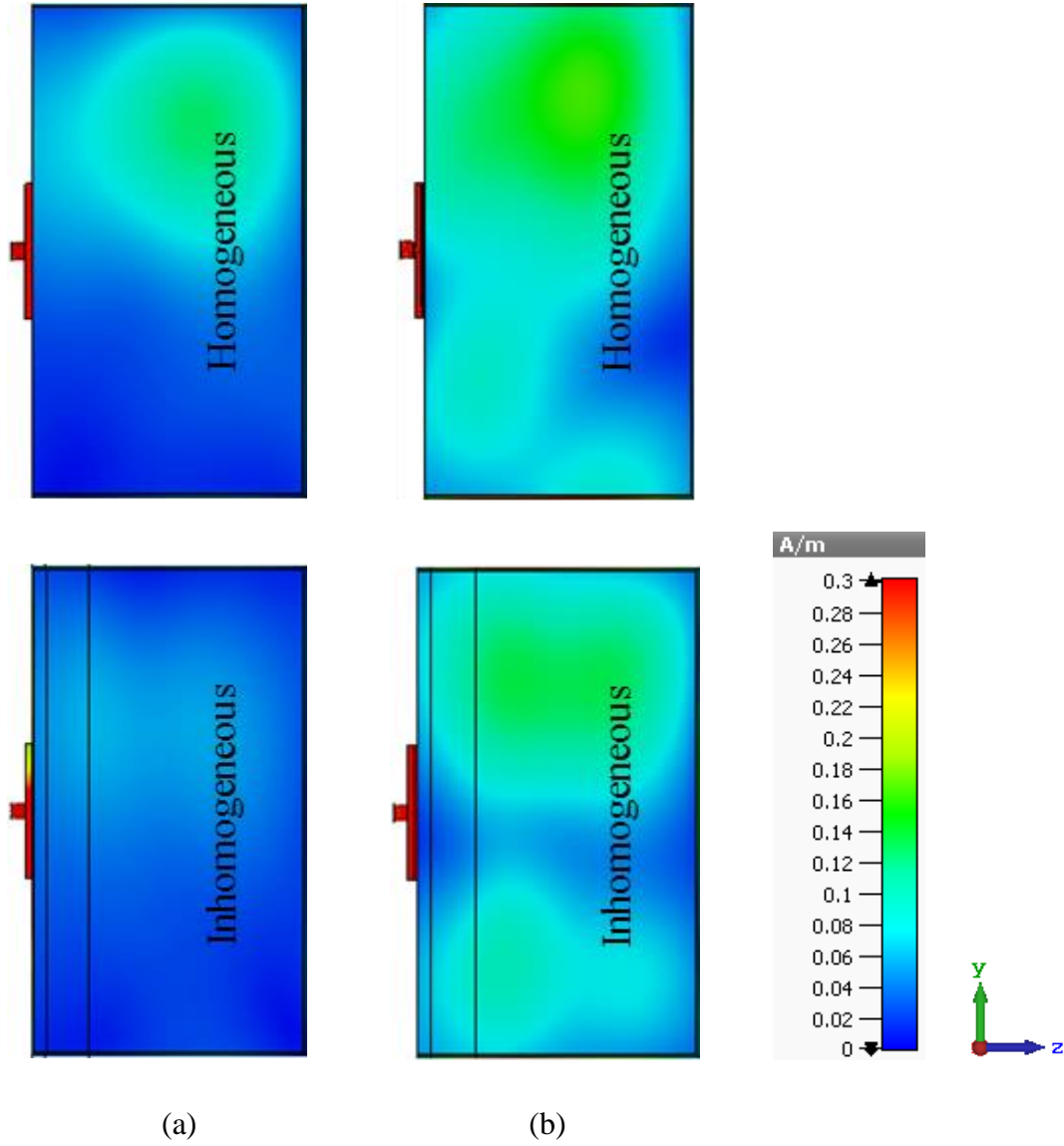


*Fig. 3.31 Distribution of the H-field inside human head phantom for (a) Antenna 1 and (b) Antenna 2 at 0.9 GHz.*

Fig. 3.32 illustrates the xz- and yz-plane normalized near field power radiation pattern of the antennas along a 50 mm radius from the antenna feed centre for the homogeneous phantom, where  $0^\circ$  represents the  $+z$  direction. Although the patterns are of similar shape, the power radiation level is approximately 6 dB lower for Antenna 1 compared to Antenna 2 towards the boresight direction ( $0^\circ$ ) into the homogeneous head phantom. This corroborates with the field results of Fig. 3.30 and Fig. 3.31. The FBR of the power radiation patterns for Antenna 1 and Antenna 2 are 11.18 dB and 11.4 dB respectively indicating a well-matched antenna system to the homogeneous head phantom.

The normalized near field power radiation patterns when the inhomogeneous head phantom is utilized are depicted in Fig. 3.33 for Antenna 1 and Antenna 2 at 0.9 GHz. The power penetration inside the inhomogeneous head phantom is 7 dB more for Antenna 2 as compared to Antenna 1 at the boresight direction of the antennas, and the FBR for Antenna 1 and Antenna 2 are 9.32 dB and 9.78 dB respectively. Variations in the main lobes of the antenna patterns are evident when the inhomogeneous head phantom is used, which are not there in the homogeneous case. These variations can be attributed to interference patterns generated by field reflections occurring at the interfaces between tissue layers.

As the human head comprises of inhomogeneous tissue characteristics, a simple homogeneous model is not adequate. The results of Fig. 3.30, Fig. 3.31, Fig. 3.32, and Fig. 3.33 indicate that to achieve more representative antenna design for biomedical applications such as on-head matched case, the inhomogeneity of human head needs to be considered.

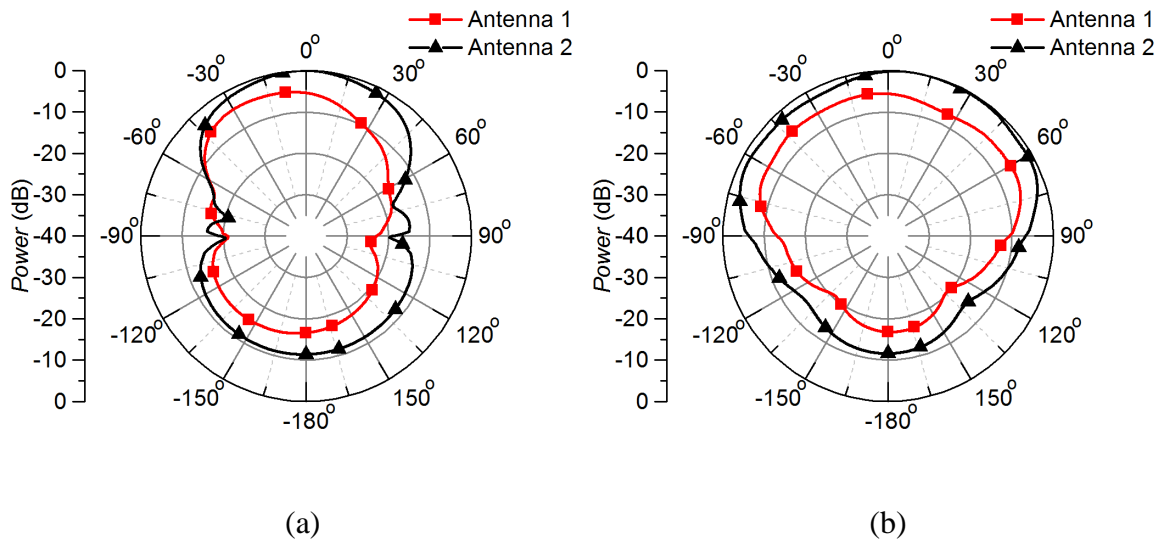


*Fig. 3.32 Normalized power radiation pattern at 50 mm distance from the antenna feed centre for homogeneous head phantom (a) xz-plane, (b) yz-plane at 0.9 GHz.*

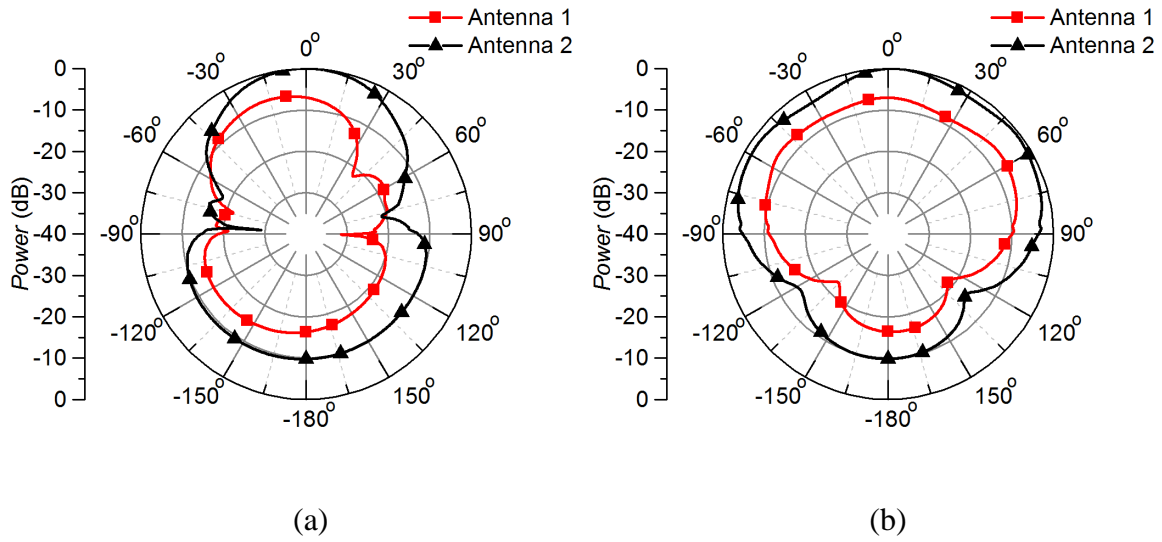


*Fig. 3.33 Normalized power radiation pattern at 50 mm distance from the antenna feed centre for inhomogeneous head phantom (a) xz-plane, (b) yz-plane at 0.9 GHz.*

The free space power radiation patterns of the two antennas are depicted in Fig. 3.34 where the antennas were simulated without the phantom. It can be observed that both antennas provide a power radiation pattern that has no obvious main beam direction in either plane. Antenna 2 provides with peak directionality at 60° angle from the boresight direction for both xz and yz plane whereas Antenna 1 has higher directivity at  $\pm 90^\circ$ . When compared to the antennas operating in contact with the phantom in Fig. 3.32 and Fig. 3.33, the free space power radiation pattern directivity decreased since resonance of the antenna shifts towards a higher frequency rather than staying at 0.9 GHz due to the removal of the dielectric loading. From these free space radiation patterns for the two antennas it can be observed that Antenna 1 radiates significantly less power compared to Antenna 2 for both the xz and yz planes. The key differences between Antenna 1 and Antenna 2 are the superstrate and the longer meander line length. If the superstrate removed from Antenna 2, Fig. 3.35 indicates that it maintains a similar radiation pattern. Hence, it is implied that the increased directivity in Antenna 2 is due to the longer meander line length.

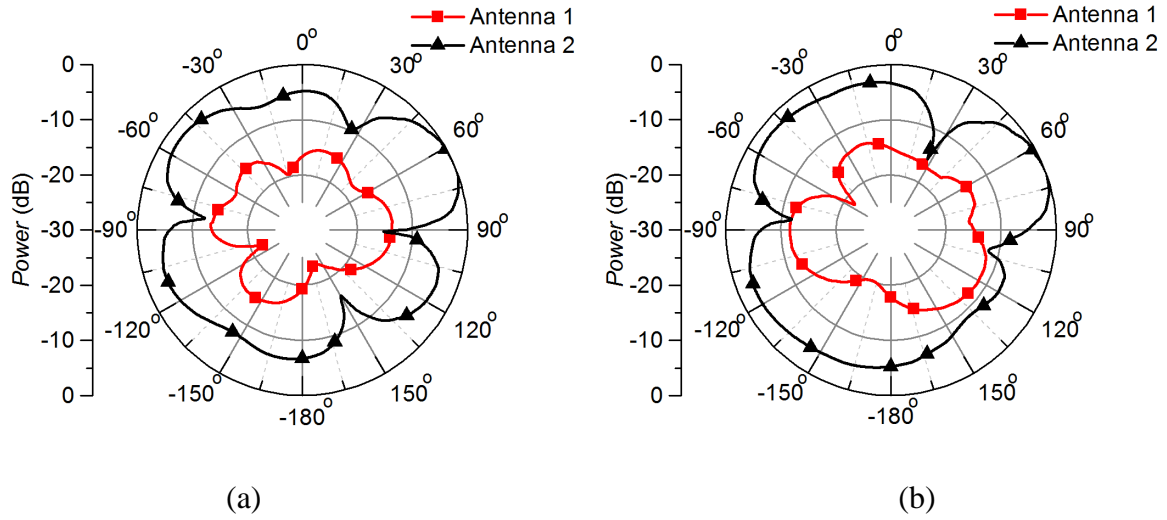


Fig. 3.34 Free space normalized power radiation pattern at 50 mm radius (a)  $xz$ -plane, (b)  $yz$ -plane at 0.9 GHz.

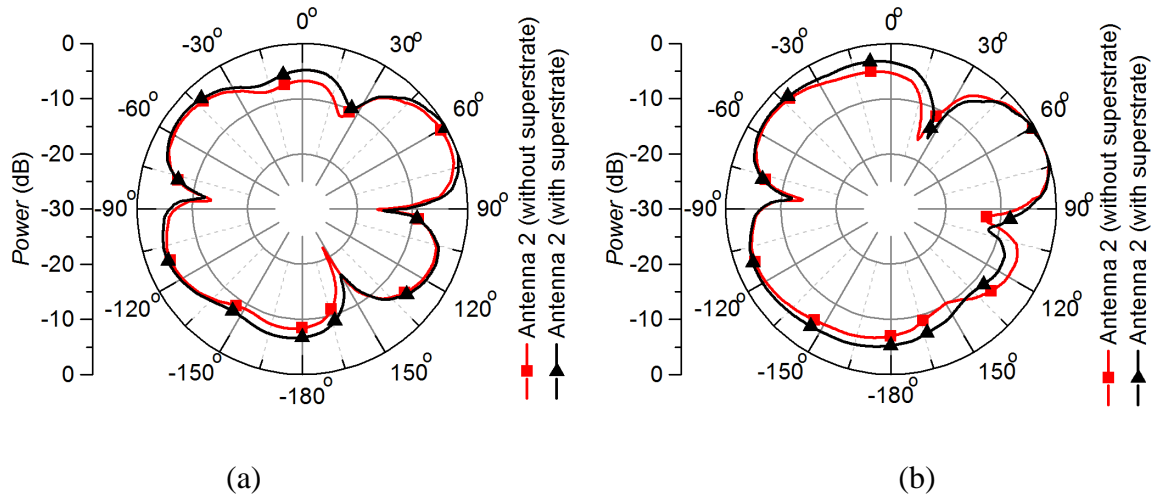
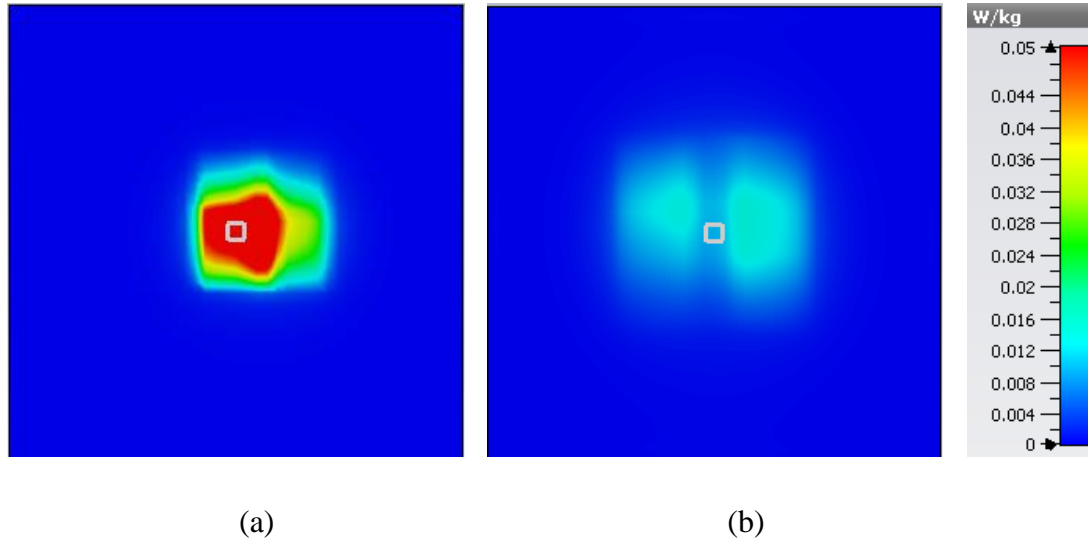


Fig. 3.35 Free space normalized power radiation pattern at 50 mm radius from Antenna 2 (a)  $xz$ -plane, (b)  $yz$ -plane at 0.9 GHz.

SAR is an important parameter for biomedical applications, especially when an antenna is operating near or on a human body. Using the built-in calculation system for human tissues in CST 2017 the SAR can be evaluated, indicating the absorption of energy by the tissue. As CST 2017 can only evaluate SAR for human tissue materials, the SAR response for the homogeneous head phantom (a bulk dielectric) cannot be calculated. Fig. 3.36 displays the computed SAR for Antenna 1 and Antenna 2 at 0.9 GHz at the surface of the skin layer of the inhomogeneous phantom. The maximum 10g average SAR for Antenna 1 and Antenna 2 are 0.0884 W/kg and 0.0153 W/kg when an input power of 1 mW is applied to each antenna.

Although the SAR for Antenna 1 is over 5 time more than Antenna 2, both of the SAR levels are well below the general human exposure limit of SAR [138].



*Fig. 3.36 Simulated SAR distribution of inhomogeneous head phantom for (a) Antenna 1 and (b) Antenna 2 for an input power of 1 mW.*

### 3.6.3.2. Measurement

The antennas are fabricated on FR4 substrates using the UV Precision Processing System (DL561U) from Design Comes True (DCT). Antenna 1 is without a superstrate, and the superstrate of Antenna 2 is attached on top using epoxy glue which has similar permittivity ( $\sim 3.5$ ) to the FR4 material. The antennas are fed through the ground plane using an SMA connector. Fig. 3.37 depicts the measured  $|S_{11}|$  response of the two antennas when they are attached to the fabricated inhomogeneous human head phantom shown in Fig. 3.2. Both the antennas exhibit similar characteristics to those predicted in the simulation for the inhomogeneous human head phantom in Fig. 3.27. The normalized near field power radiation pattern is shown in Fig. 3.38, with measurement points taken every  $10^\circ$  at a 50 mm radius for both xz- and yz-plane of the antennas. As the power radiation pattern are normalized to the peak value from both patterns, it can be observed that Antenna 2 directs  $\sim 8$  dB more power towards boresight than Antenna 1. The FBR for Antenna 1 is 6.5 dB whereas for Antenna 2 it is 17.7 dB, again indicating more substantial levels of power directed into the head phantom.

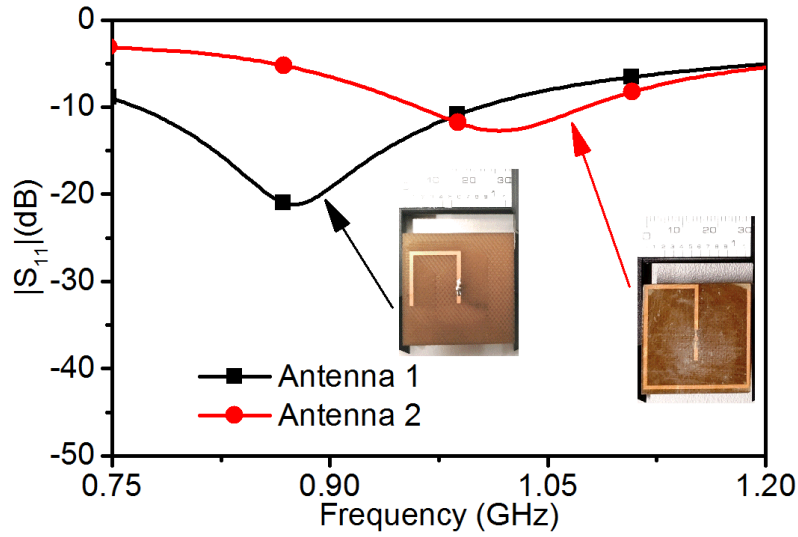


Fig. 3.37 Measured  $|S_{11}|$  response of the antennas attached with inhomogeneous phantom.

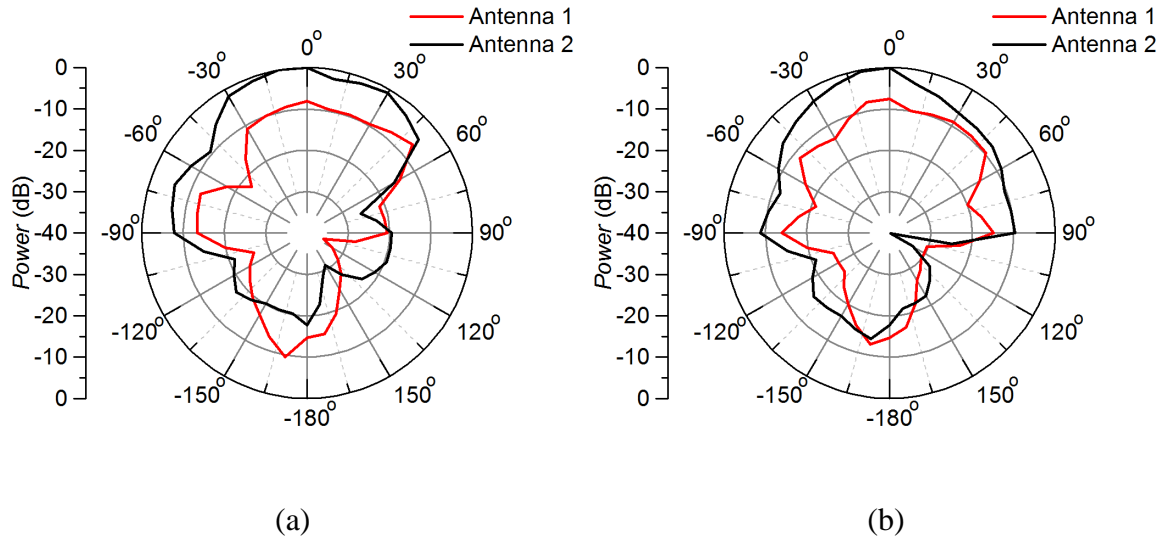


Fig. 3.38 Measured normalized power radiation pattern at 50 mm distance from the antenna feed centre for inhomogeneous head phantom (a)  $xz$ -plane, (b)  $yz$ -plane at 0.9 GHz.

### 3.6.4. Conclusion

Two antennas for on-head biomedical applications are designed with identical lateral dimension of  $30 \times 30 \text{ mm}^2$  and both operating at 0.9 GHz frequency. The antennas differ in relation to the presence (or not) of a superstrate layer between the antenna and a human head phantom. An analysis as to the effect of the superstrate layer is undertaken in terms of current distribution, E- and H-field penetration, near field power radiation pattern and SAR when utilizing both a homogeneous and inhomogeneous layered human head phantom. The antenna without the superstrate is less effective at achieving field/power penetration deep



inside the phantom, primarily due to the direct contact of the antenna conductors with the lossy high permittivity tissues. The antenna with the superstrate achieves more significant field/power penetration with a lower SAR on the skin surface due to the separation between the conductive phantom and the antenna elements. Hence, including a superstrate in the structure of an on-head matched antenna for biomedical applications can provide increased power penetration inside human head with lower SAR. When the power is increased to achieve higher penetration inside the tissue, the SAR at the surface of the tissue will also increase. However, such phenomena can be alleviated by introducing a superstrate which will lower the SAR for the same power radiation by reducing power loss (which is the cause of the increment in SAR) at the boundary of the superstrate and the tissue [136]. Moreover, the superstrate also acts as a shield to prevent shorting of the antenna by the conductive human tissue.

### **3.7. Chapter Summary**

The motivation behind modelling and fabricating a representative human body phantom is described in this chapter. A semi-solid phantom is developed to mimic the skin, bone and brain layers of a human head. A semi-solid phantom was selected so that materials can be formed into different shapes and can be stacked on each other along to allow multi-layer construction. Advantages of stable electromagnetic properties and a comparatively less complex measurement process are also garnered.

To improve the microwave power penetration inside an inhomogeneous human head, a dielectric-loaded waveguide is theorised to match to the wave impedance of layered head phantom. The measured results validate the approach with an increment in power penetration inside the human head of 1.33 dB at 2.45 GHz. An antenna feeding method is conceived to feed the designed dielectric loaded waveguide without the need for drilling a feed probe.

Antenna characterization in-front of a homogeneous and a frequency-dependent inhomogeneous human head is also investigated in this chapter. Noticeable differences in behaviour are observed in terms of the field/power propagation into the two types of phantoms. The antenna radiation characteristics are highly dependent on the homogeneity/inhomogeneity characteristics of the human head, with variations in permittivity and reflections at boundaries influencing performance.

Lastly, the effect of superstrate at the boresight of an on-head matched antenna for biomedical applications is analysed. Two antennas, one with the superstrate and one without the superstrate, are characterised. It is found that superstrate layer at the boresight direction of the antenna provides with ~8 dB increased power penetration with 0.0731 W/kg reduction of SAR compared to the antenna without the superstrate.

# Chapter 4 – Compact Antennas for Human Head Medical Diagnosis

## 4. Compact Antennas for Human Head Medical Diagnosis

Antennas are the front-end element for all wireless applications. Depending on the application, the required properties of the antenna vary. The radiation pattern of microwave antennas in biomedical applications is a crucial factor for the processing of scattered signals in microwave imaging systems. Increased front to back ratio of the antenna radiation pattern is highly desired [76]. Although this scattering problem has been identified, not much has been done to solve it in the literature. The penetration inside the human body depends on the transition loss between antenna-air-tissue for off-body antenna implementations. Penetration is better at lower frequencies, but the antenna size needs to be increased to achieve higher gain at these frequencies which is a significant drawback for microwave imaging. Furthermore, antenna elements for microwave imaging systems in the literature rarely consider the near field effects of the human body, resulting in diffracted radiation patterns and altered impedance bandwidth of the antenna in practical environments. This chapter

describes the challenges in antenna design and proposes solutions with novel antennas for human head medical diagnosis.

## **4.1. Challenges of Compact Antenna Design for Human Head Medical Diagnosis**

Due to the unavoidable signal loss occurring from the dielectric properties of human tissue at GHz frequencies, reflection-based microwave diagnostic systems provide poor reflection strength from the detection body. A higher signal to noise ratio (SNR) is demanded to mitigate this problem. Moreover, the reflection properties are also affected by the inhomogeneous layers faced by the propagating signal [139]. To improve the SNR, increased microwave field penetration inside the human head is essential. Hence, the radiation characteristics of the antenna in the microwave diagnosis system are one of the key factors in its performance.

Before entering the human brain, the microwave signal has to penetrate through the interfaces of air, skin and skull (bone), as shown in [15, 51]. A sensitivity analysis of such a system is described in [44], where the contrast of physical sensitivity is examined considering the overall system setup (e.g. coupling between array elements, structural components: cables, connectors, container walls, head under test in near-field measurement). To help mitigate these interfacial problems, an antenna element has to be directional and relatively impervious to the surrounding environment. Moreover, the air-skin boundary adds an unavoidable reflection loss [18], which can be decreased by designing an antenna which physically touches the human head. As such, the antenna can reduce the large reflection off the air-skin interface caused by an impedance mismatch.

Medical diagnosis utilizing the off-head antennas is still possible, requiring assumption based image reconstruction algorithms to mitigate the power penetration problem deep inside human tissue, and an exponential increment in computation time [12, 140, 141]. A non-negligible degradation of overall imaging performance results in microwave imaging algorithms [141].

There are few on-body matched antennas proposed in the literature to reduce the antenna-air-

skin transition loss for medical imaging systems, where most are designed for breast cancer detection [79, 80]. These antennas suffer from low FBR radiation over the whole operating frequency region due to the adoption of a coplanar structure. With strong back radiation, such an antenna system will suffer from multipath effects [142], which is a significant drawback for medical diagnostic applications. Moreover, such an imaging application requires multiple antennas, and neighboring antennas will suffer from substantial mutual coupling from elements. The power penetration inside the human tissue is not investigated in these works, overlooking a crucial parameter for such an application. A UWB on-body slot antenna for stroke detection with an operating range from 1 to 9 GHz has been proposed [88]. Apart from the bulky size, the antenna again suffers from a less than 8 dB FBR at the lower operating frequencies, a primary frequency region for microwave penetration inside human tissue. The SAR in human tissue is not characterized for this work. Another UWB antenna, this time for implantable applications, is designed to be matched with human head tissues [143]. The antenna performance is demonstrated in both near and far field. Although the antenna is claimed to be directional, the antenna exhibits a -10 dB FBR with the maxima occurring at the side lobes. Utilizing 2.5 mW of input power, the antenna created a maximum allowable SAR of 1.6 W/kg.

Recently, an on-body matched antenna is presented operating at the low-frequency region where the tissue penetration is high [18]. The antenna is designed using high permittivity Rogers RT/duroid 6010 substrate material ( $\epsilon_r = 10.2$ ), which reduces the antenna size. The antenna suffers from a far-field FBR of less than 15 dB over the operating frequency range. Only a far-field characterization of the antenna FBR is performed in simulation. The design uses a lossless homogeneous phantom, which has been shown to differ substantially from a realistic inhomogeneous and lossy near-field scenario and also has conductive surfaces in contact with the human head which will reduce power transfer efficiency and sensing capability [144]. The antenna achieves SAR characteristics of 0.06 W/kg at 0.5 mm inside the skin layer, which indicates a higher SAR where the antenna touches the skin.

## **4.2. Compact 3-D Antenna for Medical Diagnosis of the Human Head**

A novel compact 3-D antenna is presented in this section for medical diagnosis of the human head providing high directionality with increased front to back ratio and the lowest SAR compared to the literature. The near field radiation pattern of the proposed antenna provides with unidirectionality towards the considered human head phantom. The performance of the antenna is validated by utilizing simulation and measurement data.

### **4.2.1. Design Considerations**

The frequency band from 1 GHz to 2 GHz has been stated as being suitable for medical diagnosis as it achieves increased penetration with low power radiation to reduce SAR [32]. Higher frequencies struggle to penetrate through the human head due to smaller wavelength, and at lower frequencies, biological tissue tends to be highly lossy [24, 25].

It is also vital to achieving a unidirectional response for an antenna to be employed in microwave imaging applications [32, 61, 142]. A unidirectional response over a wideband is achievable utilizing the well-known probe-feeding method [145-148]. An L-shaped probe [148] or meandered probe [145, 147] can be used to achieve wide bandwidth. The L-shaped probe achieves increased bandwidth via coupling with a parasitic patch situated over the ground layer. A meandered probe approach meanders an extension of the probe, and in doing so connects with the patch element. These two approaches are combined to achieve wide bandwidth at a lower frequency, hence miniaturizing the probe fed patch antenna system. Moreover, the antenna structure can utilize high dielectric materials to achieve further miniaturization.

### **4.2.2. Configuration of the Proposed Antenna**

The proposed 3D antenna is shown in Fig. 4.1. The antenna is composed of five FR4 substrate layers extending from the ground at the bottom to the superstrate at the top where the antenna touches the skin of a human head. The structure of the antenna is a modified version of an inverted F antenna (IFA) [149, 150]. The dimensions of the antenna referring to Fig. 4.1 is tabulated in Table 4.1.

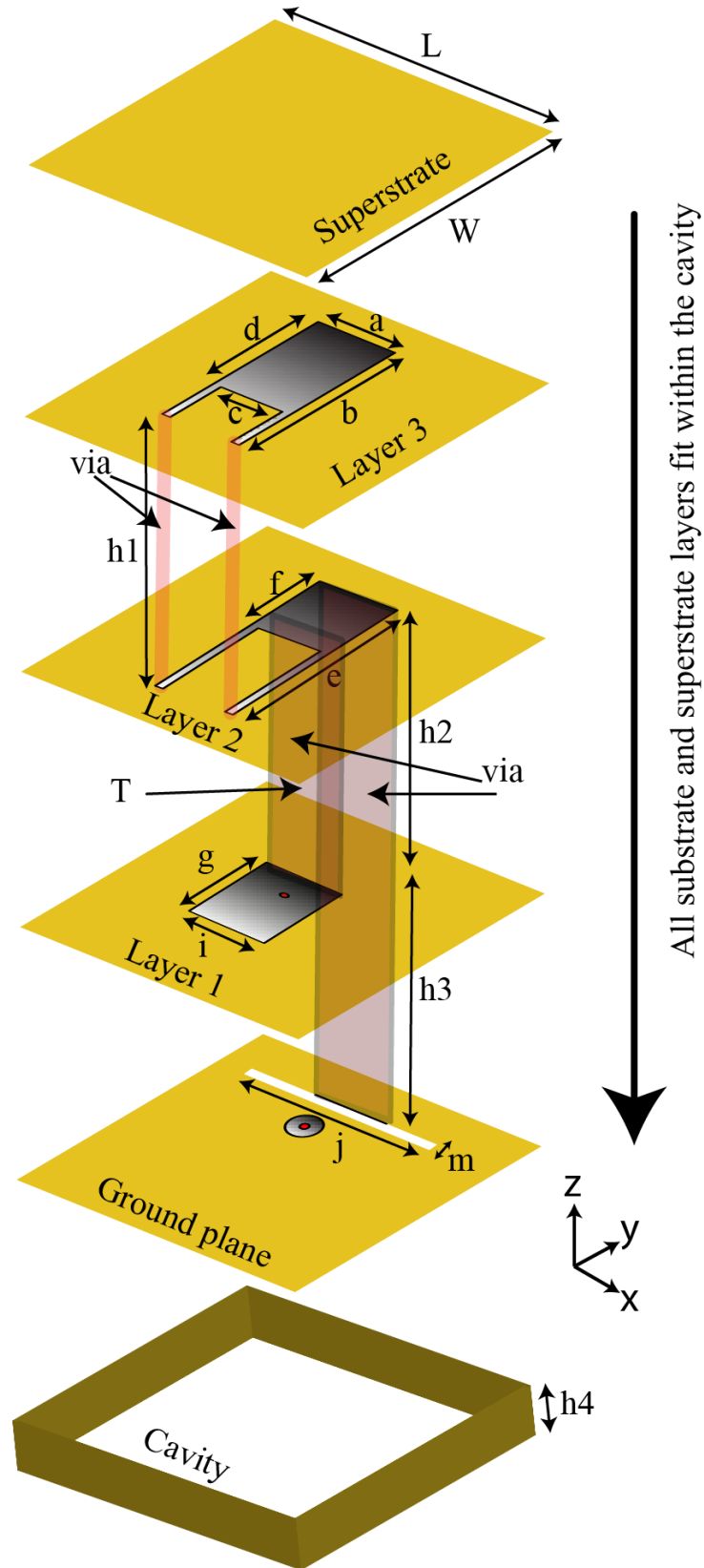


Fig. 4.1 Proposed stacked 3D-folded cavity-backed antenna layout where the ground plane is the back of the cavity, and the patch layers are physically separated using FR4 substrate.

Table 4.1: Dimensions of the proposed antenna

<i>Parameters</i>	<i>Values (mm)</i>
$L$	68
$W$	68
$a$	9.63
$b$	28.64
$c$	7.7
$d$	19.25
$e$	31.39
$f$	13.2
$g$	16.5
$h_1$	4.5
$h_2$	3
$h_3$	3
$h_4$	12
$i$	9.63
$j$	25

### 4.2.3. Design Evolution

The evolution of the proposed antenna from an IFA is divided into four key steps, depicted in Fig. 4.2. In the beginning, an IFA (Antenna 1) is fed to Layer 2 and shorted back to the ground using an  $h_2+h_3$  length shorting plate of width  $a$ . The open end of the IFA on layer two is then folded back on itself to Layer 3 to form Antenna 2. This architecture also increases the capacitance of the overall antenna structure which counter-effects the inductance introduced by the shorting plate of the IFA, resulting in a preliminary improvement in terms of impedance matching at the desired frequency as depicted in Fig. 4.3 for Antenna 2.



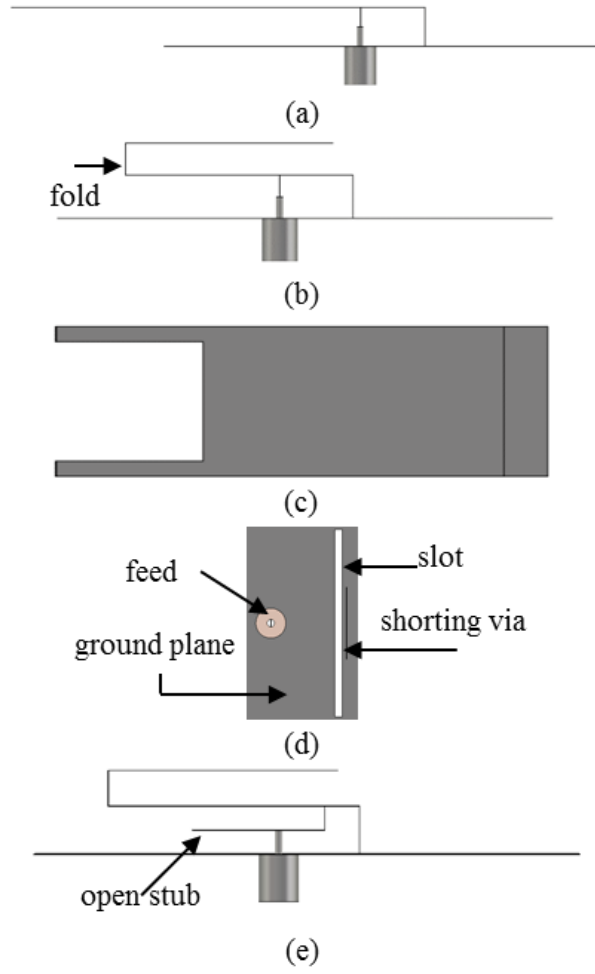


Fig. 4.2 Evolution of the 3D antenna (a) Antenna 1 (b) Antenna 2 (c) Antenna 3 – top view (d) Antenna 4 – bottom view (e) Antenna 5.

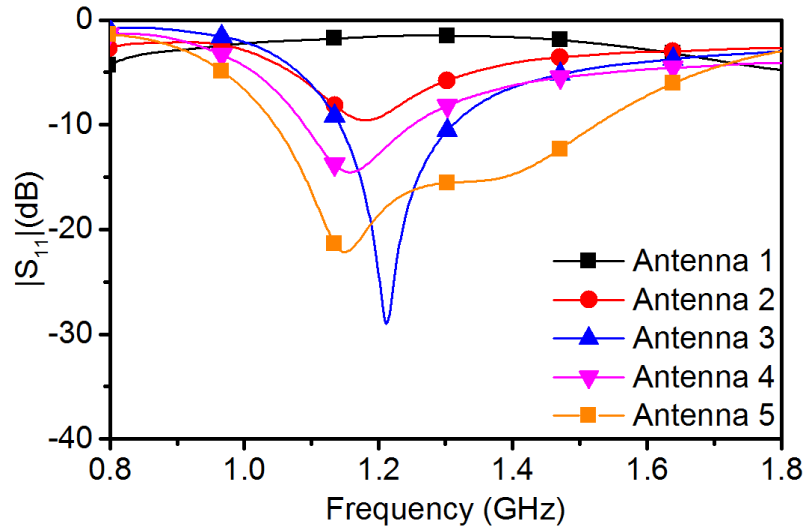


Fig. 4.3  $|S_{11}|$  response for the antennas shown in Fig. 4.2.

Next, an aperture of width ‘c’ is removed from layer 2, layer 3 and the via between them of height  $h_1$  to decrease and optimize the capacitance created by the folding and further tune the impedance, resulting in Antenna 3. This aperture also helps to balance the radiation pattern in the broadside direction. A non-radiating subwavelength slot is introduced in the ground plane near the shorting plate of the IFA (Antenna 4), improving the bandwidth at the lower frequency end. Finally, the IFA feed is interrupted by an offset copper plate terminated in an open circuit stub on Layer 1 (Antenna 5), which resembles an L-probe. The length  $g$  of the open stub can be used to optimize the impedance bandwidth of the antenna, as shown in Fig. 4.3 for Antenna 5.

Further to this, a cavity is introduced, which encloses the five substrate layers of the antenna to increase the directivity of the antenna towards the human head. The evolution of the antenna is performed while the superstrate of the antenna was in direct contact with the skin on the human head model. Since human tissue is generally characterized by high permittivity and conductivity, direct contact of antenna conductors with the skin will result in low power penetration efficiency [18], meaning that the superstrate layer is essential.

#### **4.2.4. Current Distribution**

The current distribution on the proposed antenna shows that the slot in the ground plane plays an important role in achieving the resonance at the desired frequency. The surface currents of the proposed antenna are shown in Fig. 4.4 at 1.15 GHz, 1.3 GHz and 1.45 GHz while the inhomogeneous phantom is attached to the antenna superstrate. It can be observed that the ground plane slot plays an important role in achieving the resonance at 1.15 GHz. The capacitance variance introduced by the coupling between the slot and the near most patches creates the resonance at the lower frequency.

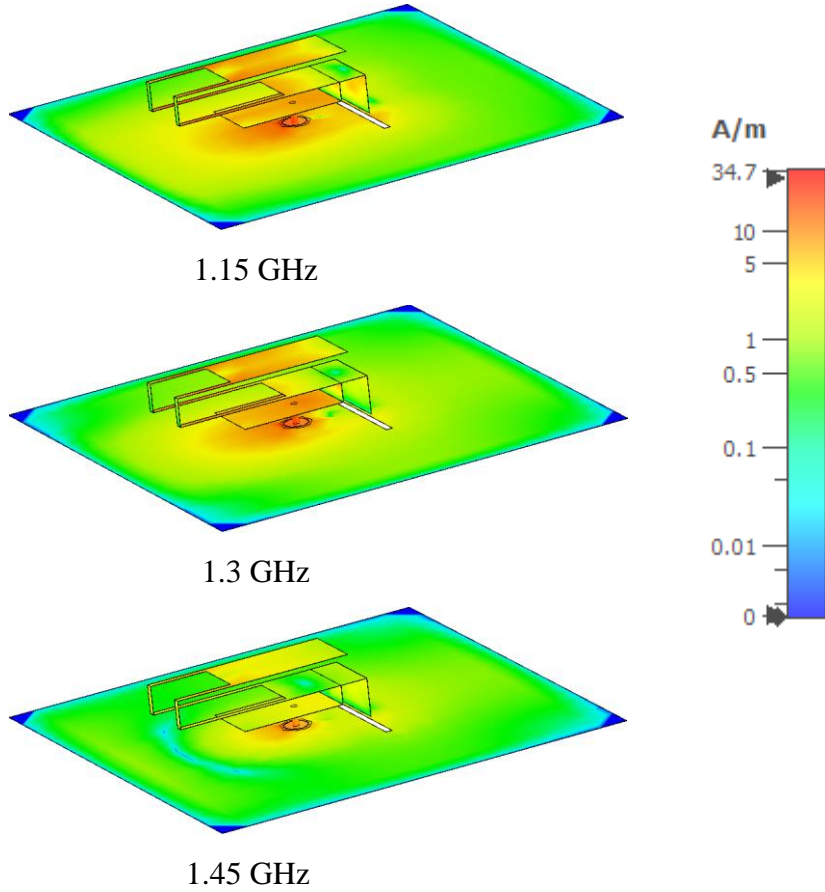


*Fig. 4.4 Surface current distribution with the inhomogeneous phantom attached at the boresight of the antenna.*

#### 4.2.5. Parametric Studies

The parameters ‘g’ and ‘j’ in Fig. 4.1 was found to be highly sensitive to dimensional changes and hence, their effects investigated in a parametric study. The results of this study are illustrated in Fig. 4.5 and Fig. 4.6. By changing the length ‘j’ of the slot while all other parameters remain constant, two crucial resonances can be found centred at 1.15 GHz and 1.35 GHz as depicted in Fig. 4.5. The slot induces a high impedance change with small variations in its length as it is in proximity to the coaxial feeding. The capacitance variance introduced by the coupling between the slot and the near most patch creates the resonance at different frequencies. Energy is unable to escape through the slot as the maximum dimension of the slot is  $0.13 \lambda$  (referring to the maximum operating frequency where the wavelength is smallest). By optimizing the two resonances, a wide bandwidth can be achieved. At  $j=25$  mm, the bandwidth is at its maximum.

Fig. 4.6 shows the effect of the length ‘g’ of patch element 1, which also plays a crucial role in achieving the optimum frequency response. It is the only patch-like element which comes in direct contact with the coaxial feed line. Hence small changes in the length alter the impedance of the overall structure. Keeping the other parameters constant, a decrease in the length ‘g’ can cause the extinction of the resonance at 1.35 GHz while the  $|S_{11}|$  response remains below -10 dB at 1.15 GHz. At  $g=16.5$  mm, maximum bandwidth is achieved with a low average  $|S_{11}|$  over the operating band.

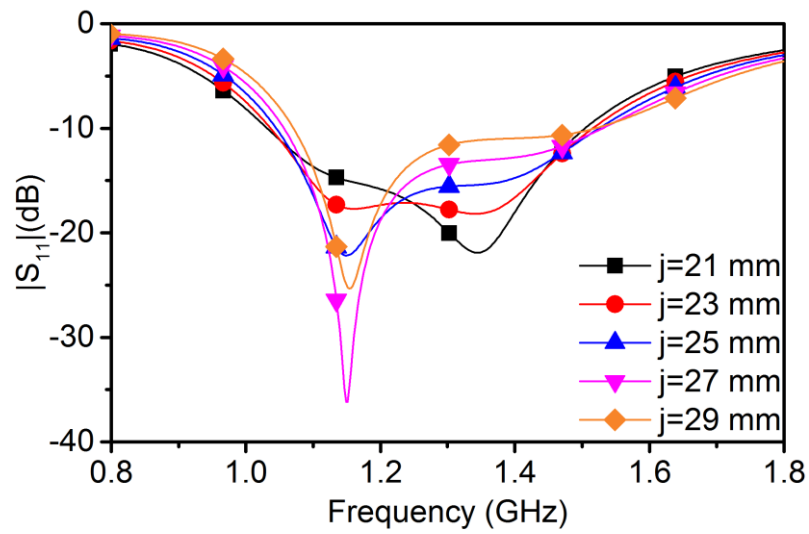


Fig. 4.5 Simulated  $|S_{11}|$  with different values of the slot length,  $j$ .

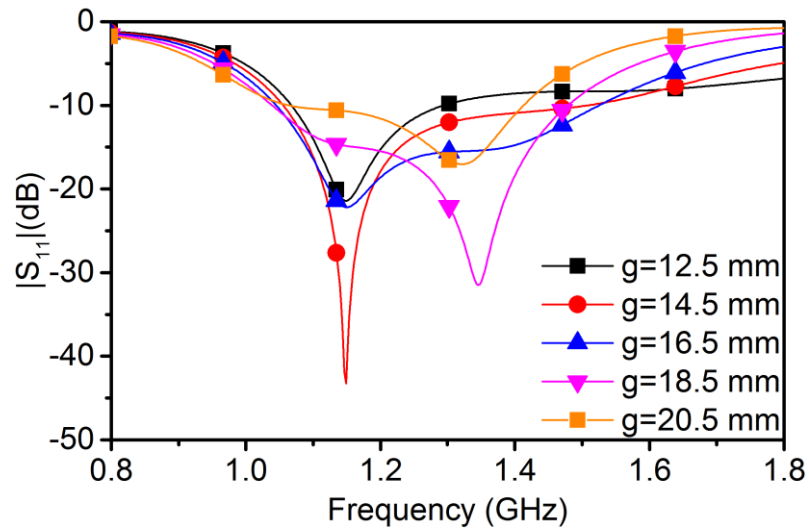


Fig. 4.6 Simulated  $|S_{11}|$  with different values of patch element 1 length,  $g$ .

#### 4.2.6. Human Tissue Effect on Antenna Performance

The thickness and dielectric properties of the tissue layers are studied to account for variances from person to person and for different ages to ensure the proposed antenna can provide an effective match with a human head. For a person greater than 5 years old, skin and bone thickness can vary from 0.5 to 1.5 mm and 3-10 mm, respectively [23]. The antenna  $|S_{11}|$  response is shown in Fig. 4.7 varying the skin thickness ‘m’. The simulation is performed for three different thickness of the skin layer over the variable range. Because of the dielectric inhomogeneity, the skin-bone layer introduces a strong reflection. With the increment of the thickness of the skin layer, the  $|S_{11}|$  decreases slightly since the distance between the antenna and the skin-bone interface increases with the increment in skin layer thickness. At  $m=0.5$  mm, the distance between the antenna and the bone layer is minimum which results in higher reflection loss, although  $|S_{11}|$  remains below -10 dB. At  $m=1$  and 1.5 mm, the  $|S_{11}|$  reduces to approximately -12 and -13 dB respectively over the operating band. Fig. 4.8 portrays the  $|S_{11}|$  response of the antenna while bone thickness is varied, with skin thickness constant at  $m=1.5$  mm. It can be perceived from the figure that bone thickness has a similar minor influence on the  $|S_{11}|$  response of the antenna as the skin thickness. As the bone thickness is increased from 3 to 11 mm the  $|S_{11}|$  response reduces from about -13 dB to below -15 dB. Overall, the slight deviations in the antenna  $|S_{11}|$  with the common ranges skin and bone thickness indicate that the proposed antenna is suitable for microwave biomedical applications with inhomogeneous tissues over a wide variety of human subjects.

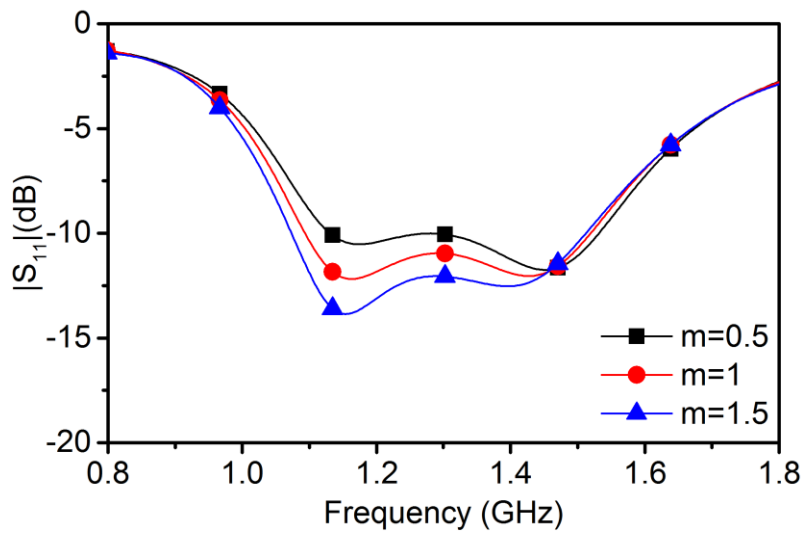


Fig. 4.7 Simulated  $|S_{11}|$  with different values of skin thickness,  $m$ .

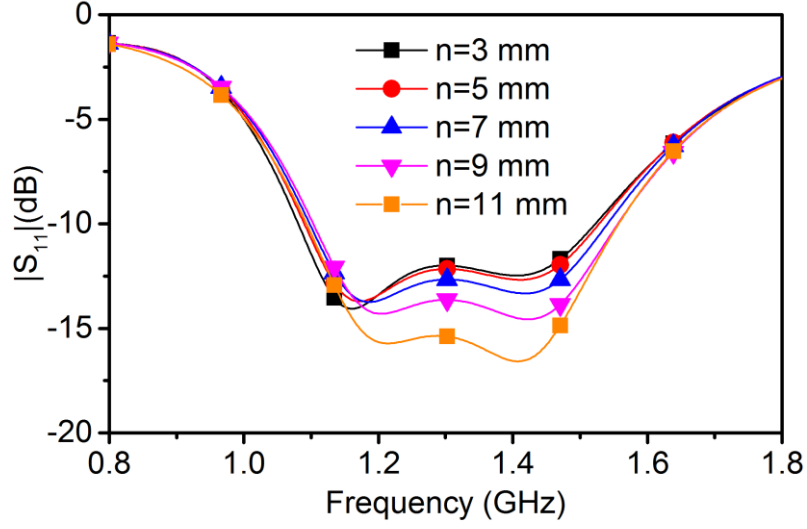


Fig. 4.8 Simulated  $|S_{11}|$  with different values of bone thickness,  $n$ .

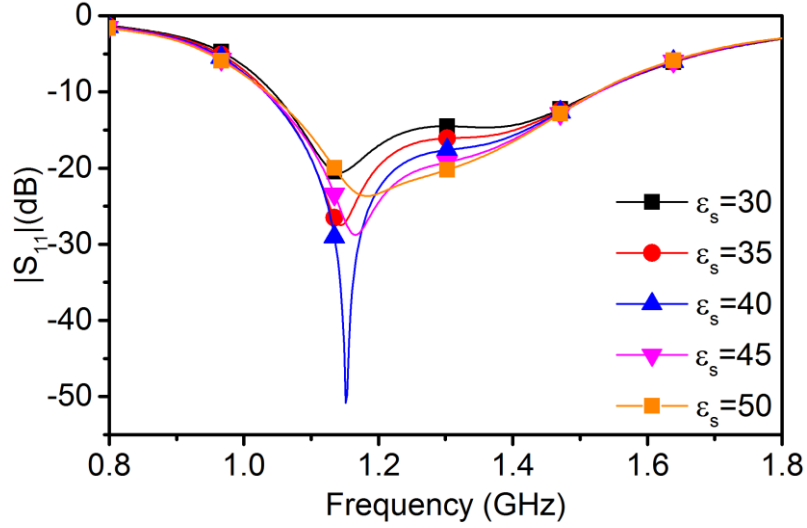


Fig. 4.9 Simulated  $|S_{11}|$  with different values of skin permittivity,  $\epsilon_s$ .

The simulated  $|S_{11}|$  performance variation owing to changes in the common spectrum of skin permittivities is depicted in Fig. 4.9. As the skin layer is in contact with the superstrate of the antenna, it is intuitive the change in permittivity of skin will have an effect on  $|S_{11}|$  response. Incrementing  $\epsilon_s$  results in an overall reduction in the  $|S_{11}|$ , although there is a very slight reduction in impedance bandwidth at the lower frequency end. The  $|S_{11}|$  typically stays below -15 dB over the drastic changes in skin permittivity of the phantom. Fig. 4.10 shows the change in  $|S_{11}|$  response for the alteration of bone permittivity while other tissue permittivities stay constant. Although the bone permittivity is not changed dramatically, the variation is analyzed to account for the realistic scenario of different human heads [23]. Only a minor

change is observed in the  $|S_{11}|$  response due to the change in bone permittivity ( $\epsilon_b$ ) from 10 to 14, represented by an incremental reduction of about 0.5 dB per unit.

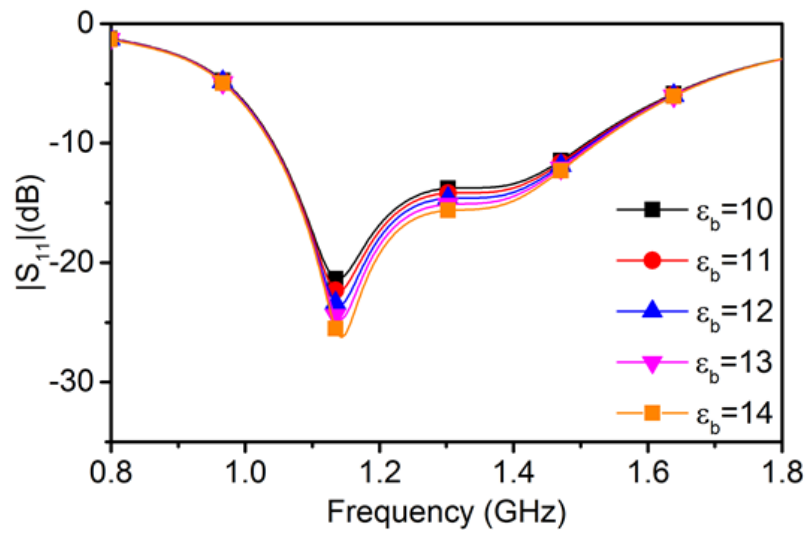
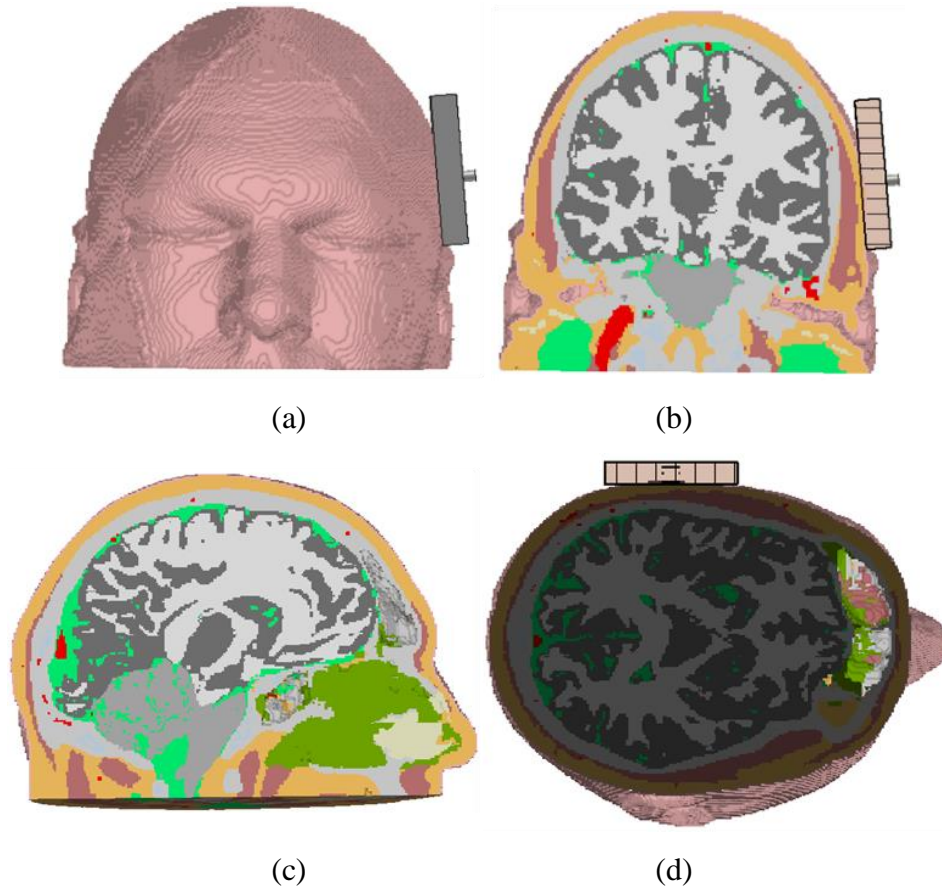


Fig. 4.10 Simulated  $|S_{11}|$  with different values of bone permittivity,  $\epsilon_b$ .

#### 4.2.7. Experiment Setup

Fig. 4.11 depicts the proposed antenna attached to the human head phantom known as the “Hugo” model. The model is extracted from “bio model 2.0” accessed via CST Microwave Studio 2017. The “Hugo” model was created by dissecting a 38 years old male’s head in the US National Library of Medicine's Visible Human Project. A model resolution of  $1 \text{ mm} \times 1 \text{ mm} \times 1 \text{ mm}$  is considered to achieve high accuracy and similarity with a real-life scenario when reconstructing the head phantom from the voxel model. This resolution increases the number of mesh cells considered during the simulation, consequently increasing the time of the simulation.



*Fig. 4.11 (a) Front view, (b) coronal plane, (c) sagittal plane, and (d) transverse plane of the antenna attached to the Hugo head model.*

#### **4.2.8. Field Distribution Inside Human Head**

The E- and H-field penetration inside the Hugo phantom at xz-plane is depicted in Fig. 4.12 (a) and (b). It can be observed that the majority of the field is directed inside the phantom, while minimal field intensity can be seen at the rear of the antenna. A similar response can be observed in Fig. 4.13, where the E-field and H-field distribution inside the Hugo phantom in the yz-plane are shown. Due to the non-planar characteristics of the human head model, a portion of the E-field exists in the gap created by the curvature at the lower operating frequency region. Nonetheless, the maximum field penetration occurs towards the considered phantom, and the gap exhibits minimal impact on the antenna performance.



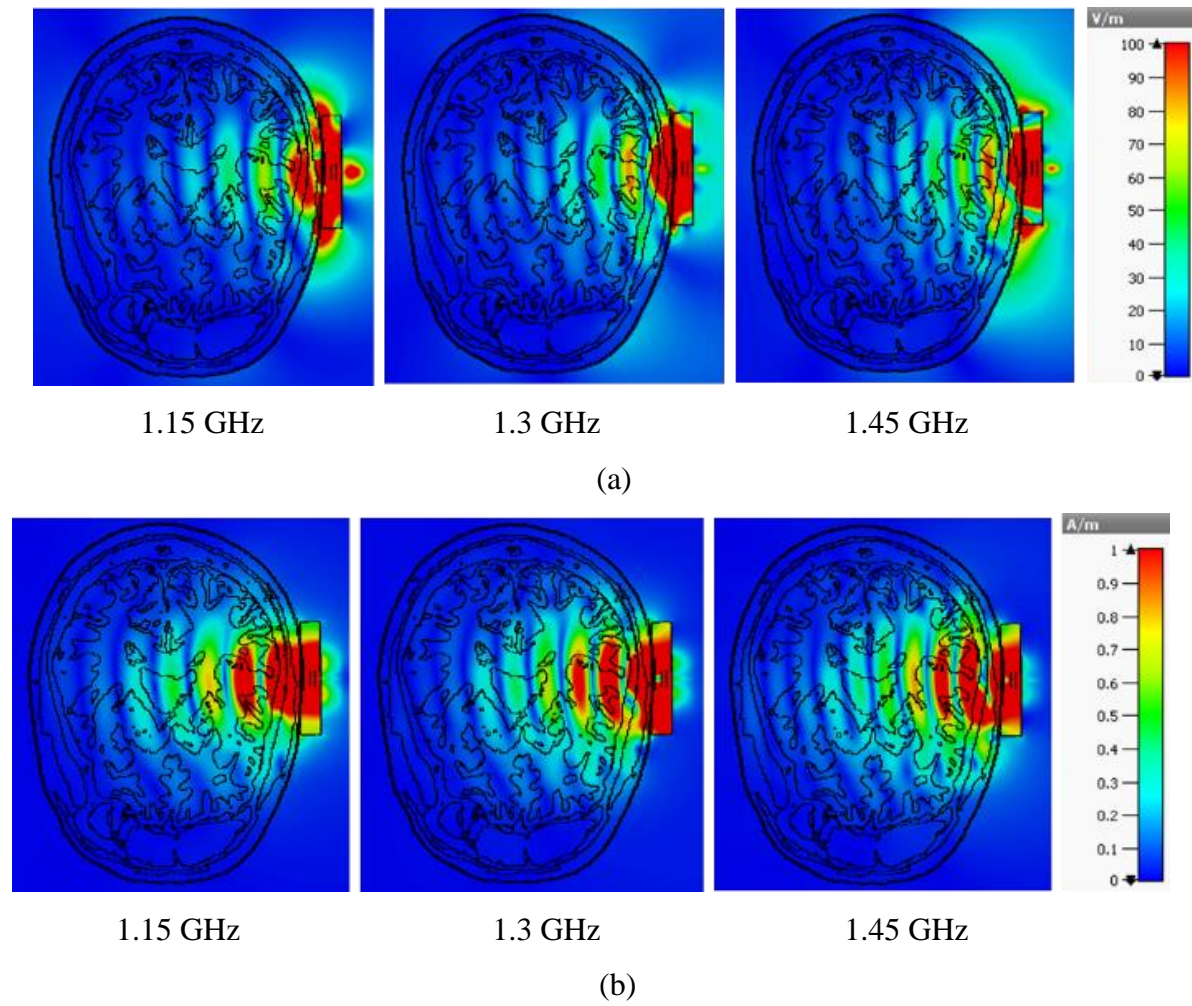


*Fig. 4.12 (a) E-field (b) H-field distribution of the antenna with realistic head model at  $xz$ -plane.*

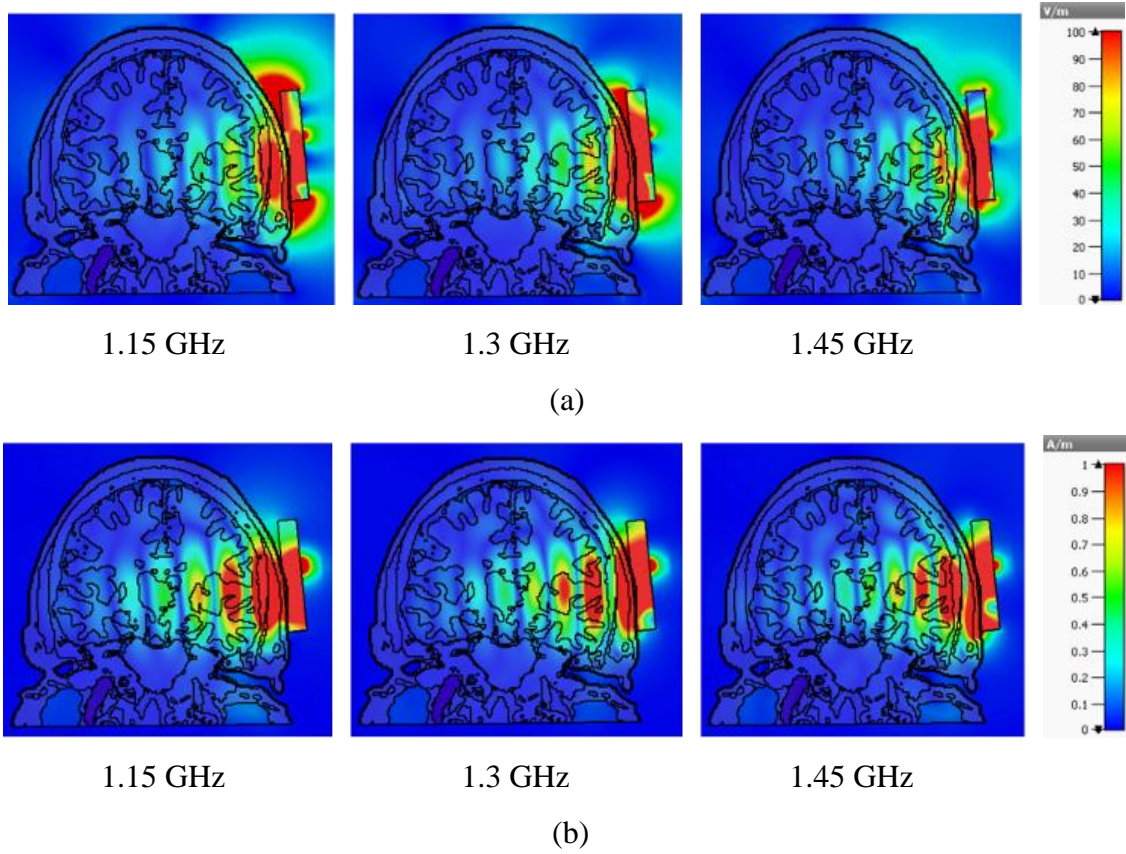


*Fig. 4.13 (a) E-field (b) H-field distribution of the antenna with the realistic head model at yz-plane.*

#### 4.2.9. Sensitivity Analysis

Owing to the compact size and enhanced microwave penetration inside the human head, the proposed antenna can be used for brain imaging for early detection of cancerous tissue, brain stroke, etc. A raster scanning setup is shown in Fig. 4.14 (a) and (b) where 8 antenna elements are placed adjacent to each other surrounding the Hugo head model [58]. Fig. 4.14 (c) depicts a potential placement of a haemorrhage inside the Hugo brain of  $25 \times 25 \times 10 \text{ mm}^3$  dimension [58] as an example of a brain inclusion to be diagnosed.

The S-parameter response of the healthy brain setup (i.e. no haemorrhage) when one antenna is excited is provided as Fig. 4.15 (a). The  $|S_{11}|$  response of the excited antenna is relatively unchanged for the raster scanning setup compared to that predicted from the single antenna simulation. The mutual coupling between the adjacent antennas is well below -20 dB even though they are arranged in proximity. The use of the cavity at the rear of the antenna increases the directivity and thus decreases the mutual coupling between the antennas in the

raster scanning setup.

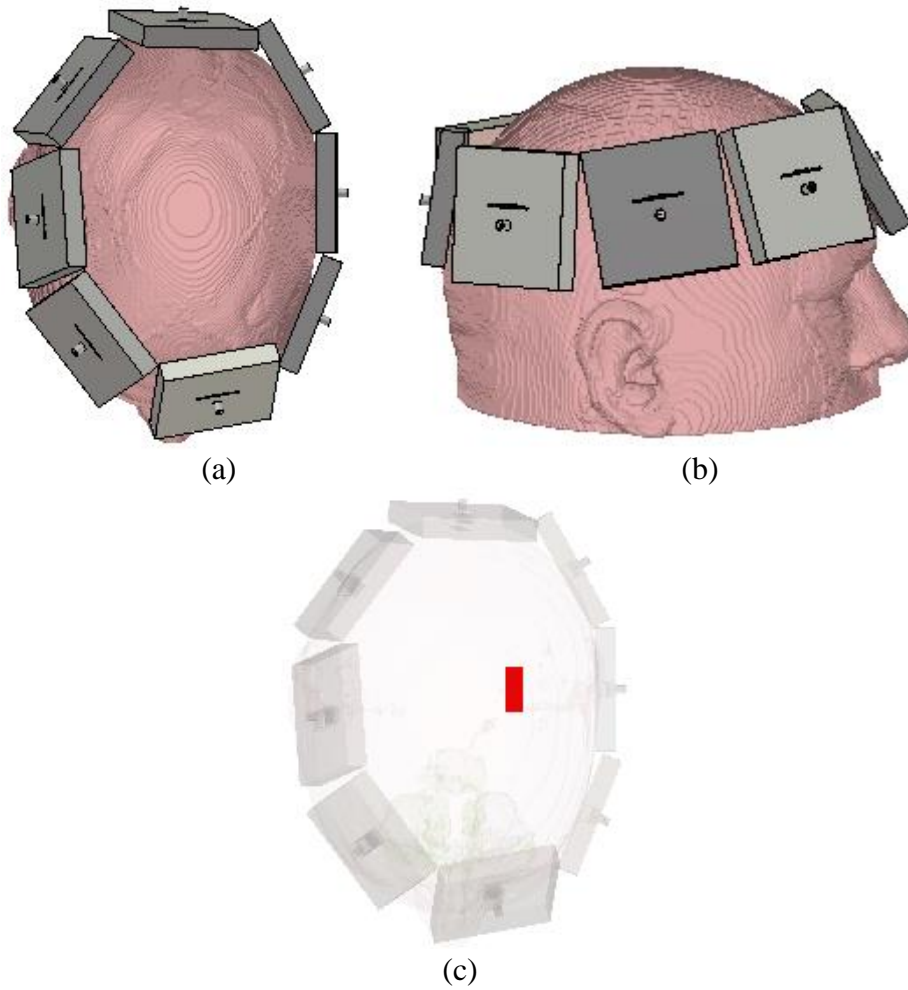


*Fig. 4.14 (a) Top view of the 8-antenna element setup, (b) side view, (c) unhealthy brain with artificial hemorrhage inserted.*

Fig. 4.15 (b) depicts the  $|S_{11}|$  for the case of a healthy and unhealthy brain with the artificial haemorrhage placed inside the Hugo head model at a distance of 26.5 mm from the antenna. The clear difference in the responses indicate the useful reflected signals from the haemorrhage, which can be utilized for identification [58]. The distance between the antenna and the artificial haemorrhage is varied in the range from 10.5 mm to 42.5 mm to analyse the depth sensitivity of the proposed antenna in terms of detecting a change inside the brain tissue. The resulting  $|S_{11}|$  responses are shown in Fig. 4.15 (c) where for a distance from 10.5 mm to 42.5 mm, the useful change of reflection coefficient can be noticed throughout the operating frequency band of the antenna. To investigate the sensitivity of the antenna to

smaller haemorrhages, the cross-section of the artificial haemorrhage is varied from  $25 \times 25 \text{ mm}^2$  to as small as  $5 \times 5 \text{ mm}^2$ . A distinct change in  $|S_{11}|$  can be observed for all cases, as shown in Fig. 4.15 (d), where significant reflection sensitivity to the haemorrhage model is exhibited at the higher end of the operating frequency range of the antenna.

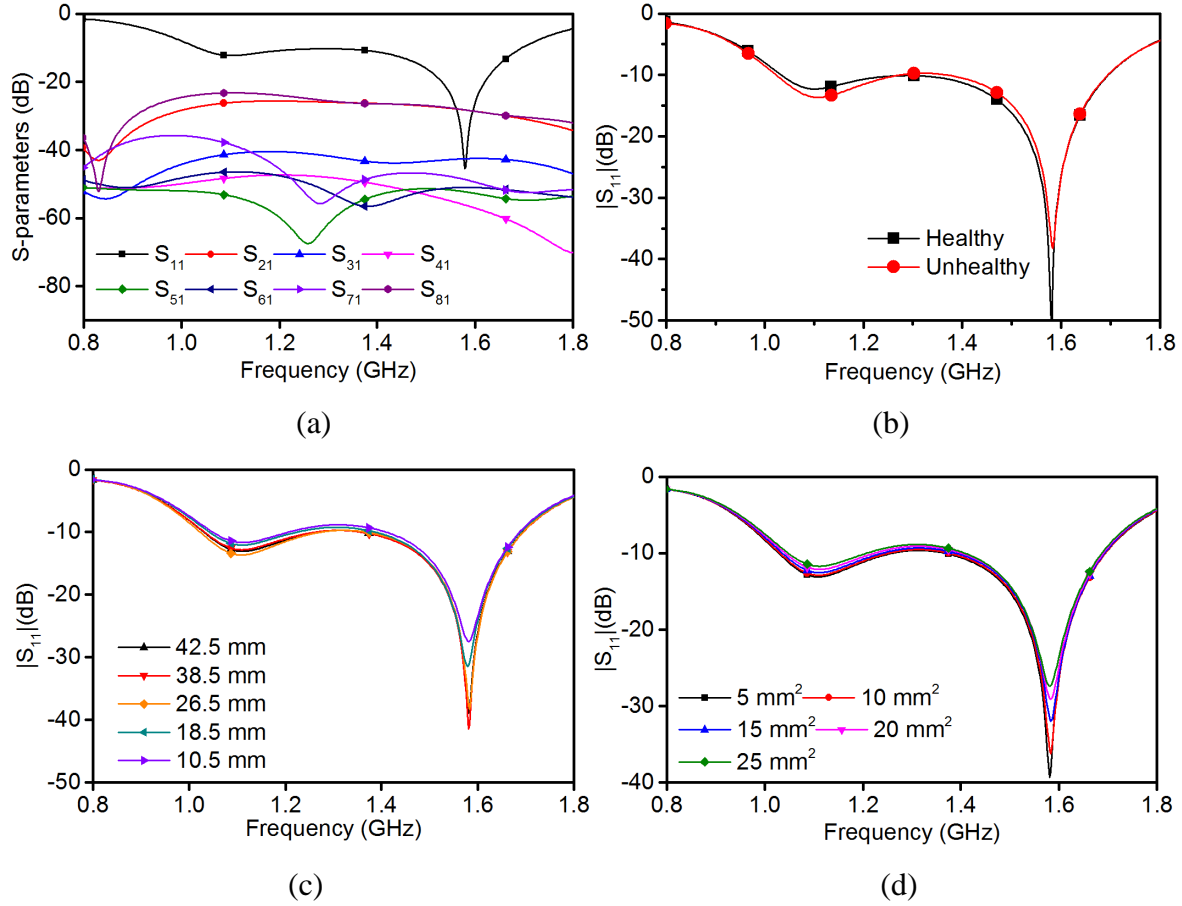


Fig. 4.15 (a)  $|S_{11}|$  of the excited antenna and mutual coupling with other antennas, (b)  $|S_{11}|$  response of the antenna with healthy and unhealthy (hemorrhage) head model, (c)  $|S_{11}|$  with change in hemorrhage distance from the antenna, and (d)  $|S_{11}|$  with change in  $h$ .

The range resolution inside the human brain can be found using the equation below [151]:

$$\delta_r = \frac{c}{2.N.B.\sqrt{\epsilon_{brain}}} \quad (4.1)$$

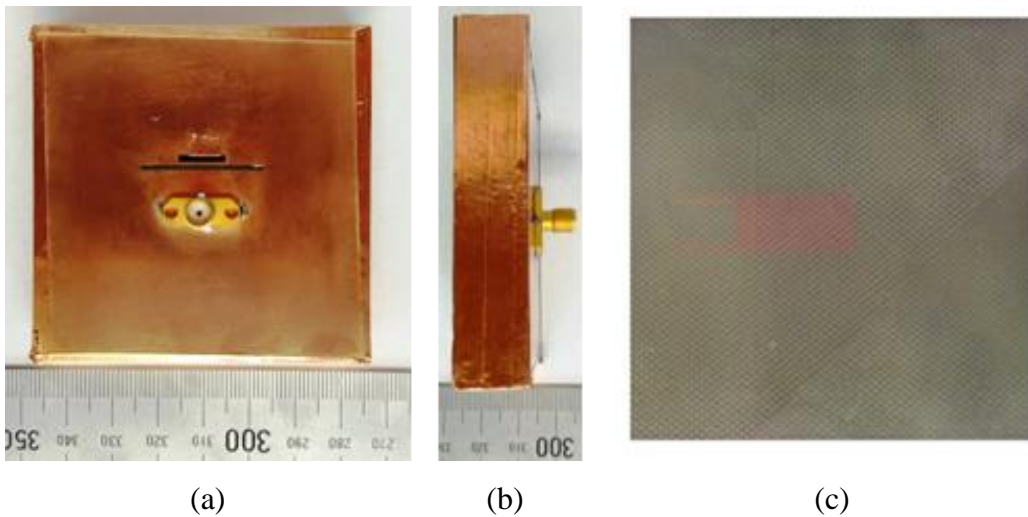
Where  $\delta_r$  is the range resolution,  $B$  is the bandwidth of the antenna,  $c$  is the speed of light,  $N$  is the number of pulses in stepped sampling modulation, and  $\epsilon_{brain}$  is the permittivity of the brain. Using this equation, for  $N = 10$ , the range resolution is found to be 3.7 mm.



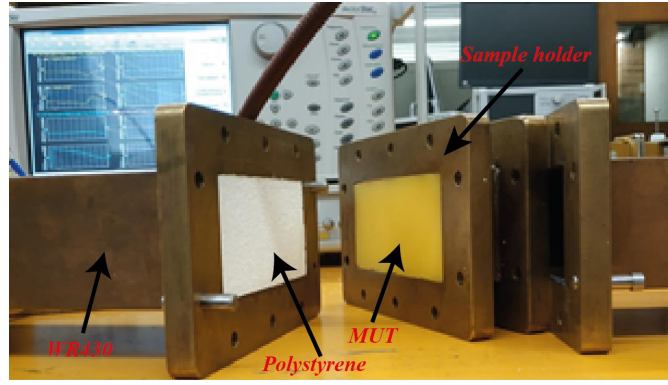
#### 4.2.10. Fabrication of the Antenna

Fig. 4.16 illustrates the fabricated antenna. The connections between each of the patches were established using bendable epoxy plated copper sheet. An SMA connector is connected to the metallized surface on Layer 1 and grounded at the ground plane of the antenna cavity depicted in Fig. 4.16 (a). The cavity boundary at the sides of the antenna body is realized using an epoxy copper sheet as seen in Fig. 4.16 (b). The superstrate FR4 at the boresight of the antenna can be seen in Fig. 4.16 (c).

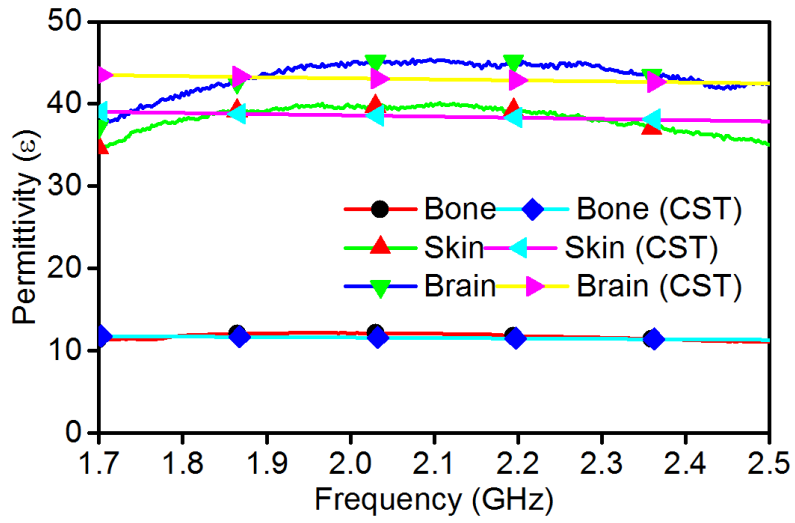
For the antenna measurement, we have fabricated a three-layer phantom using the procedure described in Section 3.3.4 of this thesis. The dielectric characteristics of each fabricated tissue layer were experimentally verified utilizing the procedure described in [126]. The measurement setup is depicted in Fig. 4.17 (a) where polystyrene foam is used before and after the material under test (MUT) to hold the sample straight while measuring inside a WR430 waveguide. A flanged sample holder is used to hold the sample between two WR 430 waveguide tubes. It can be observed from the measured results in Fig. 4.17 (a) and (b) that the fabricated phantom layer characteristics show a similar response to the tissue characteristics in the CST tissue library (taken from [115]) within the operating range of WR 430 waveguide.



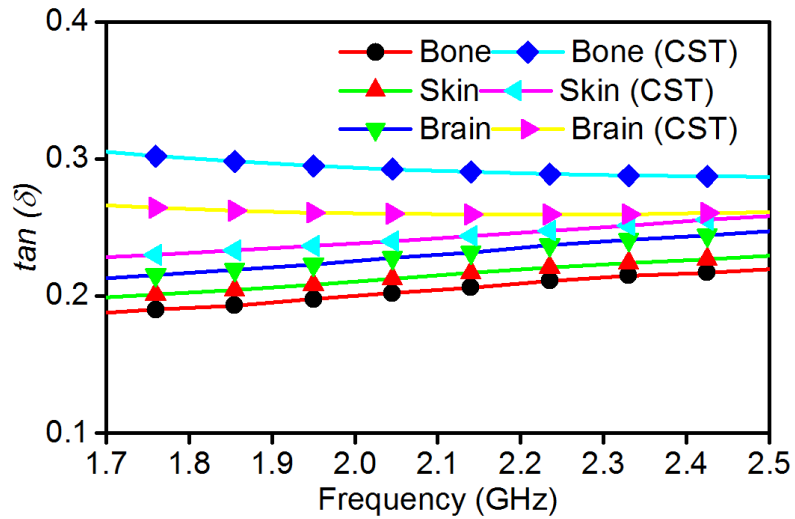
*Fig. 4.16 Fabricated antenna prototype (a) back (b) side (c) front of the antenna.*



(a)



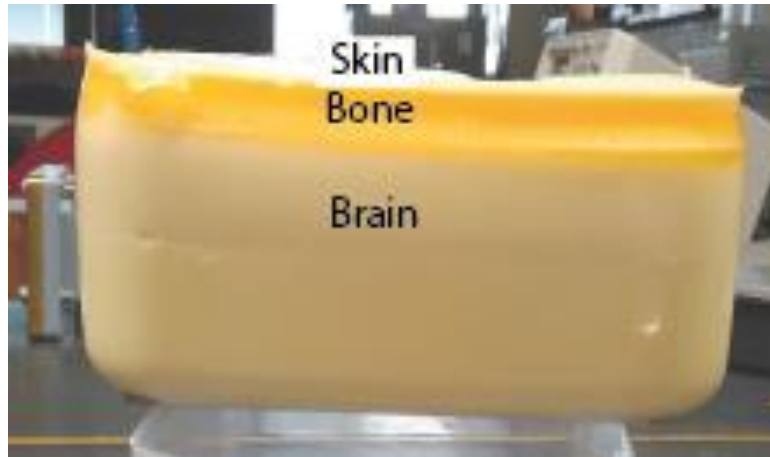
(b)



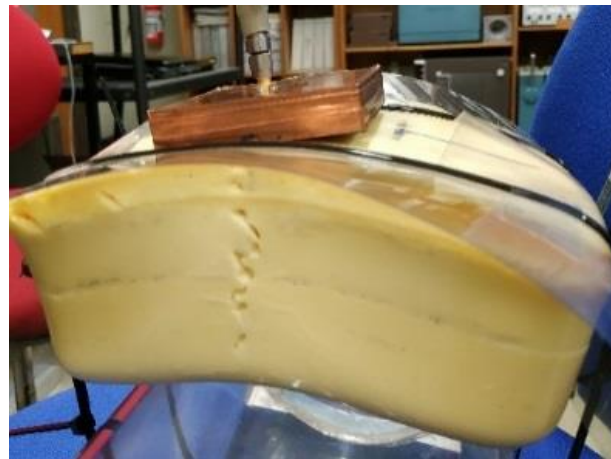
(c)

Fig. 4.17 (a) Evaluation of the inhomogeneous layer material properties (b) measured permittivity versus reference [115] (c) measured loss tangent versus reference [115].

A casting method was used with the equivalent mimicking materials outlined in [23] to achieve the desired inhomogeneity. The brain mimicking material was firstly cast in a container to the desired thickness, where it was left to cool and solidify for approximately 5 days. The bone layer was then mixed and poured on top of the solidified brain mimicking material and in a similar fashion to the cooling process for the brain material the bone material was left to solidify for a further 5 days. The skin layer was finally cast and left to solidify [125].



(a)



(b)

*Fig. 4.18 (a) Fabricated inhomogeneous human head phantom (b) antenna measurement against a curved phantom.*

The dimensions of the final inhomogeneous phantom are approximately  $170 \times 110 \times 70 \text{ mm}^3$ . The constructed three-layer phantom is shown in Fig. 4.18 (a). The phantom is curved around a holder wheel of 150 mm radius to approximate the curvature of the human head to

obtain a more realistic representation of a human head. This setup, with the attached antenna, is shown in Fig. 4.18 (b).

#### 4.2.11. Measurement Setup and Results

The antenna is measured while in contact with the inhomogeneous phantom shown in Fig. 4.18 (b) to achieve experimental verification. Fig. 4.19 shows the  $|S_{11}|$  response of the antenna both in simulation and measurement. The result curves show reasonable similarity in terms of shape, although the depth of the dips is reversed and a wider bandwidth is evident in measurement. The bandwidth achieved from the simulation ranges from 1.03 GHz to 1.7 GHz, while the measured result extends from 0.9 GHz to 1.8 GHz. The discrepancies are due to the fabricated phantom being a simplified layered model compared to the intricate detail of the Hugo simulation. Also, the uncertainty of FR4 material characteristics plays a significant role in the  $|S_{11}|$  response discrepancy. Nonetheless, the measurement result covers the whole bandwidth achieved from the simulation and hence achieves the desired result with an operational frequency band from approximately 1 – 1.7 GHz. The cracks initiated from the holes created by the electrically small monopole used to measure the field intensity inside the inhomogeneous human head phantom as the structure was bent. The antenna was measured in two scenarios: 1. with a flat surface phantom, 2. with a curved phantom. The  $|S_{11}|$  response shown in Fig. 4.19 for the two setups indicates the effect of curve and the cracks found in the curved phantom. For the flat surface phantom, a dip in the  $|S_{11}|$  response at 1.45 GHz can be observed. However, when the phantom is curved with the holes/cracks now prominent, the dip shifts to 1.65 GHz. However, the overall bandwidth of the antenna increases, so the overall effect of the cracks doesn't negatively impact the performance.

The radiation pattern measurement setup is depicted in Fig. 4.20. No power amplifier was used to evaluate the radiation pattern of the antenna as the proposed antenna was sufficient for detection without additional signal amplification. An electrically small monopole antenna fabricated out of semi-rigid coaxial cable was utilized as an E-field probe for antenna radiation pattern measurement in both the E- and H-plane. The angle of measurement was changed manually, and readings were taken with an Anritsu MS4644B VNA, and data is transferred to a computer via USB. The normalized simulated and measured E- (xz-plane) and H-plane (yz-plane) radiation patterns of the proposed antenna are shown in Fig. 4.21 for 1.15, 1.3 and 1.45 GHz. For the simulated result, field probes were positioned on a constant



radius to record the radiation pattern, with the boresight value 50 mm inside the brain layer. The probe was set 50 mm inside the brain (measured from the end of the bone layer) and circled around the phantom to achieve the same distance while measuring the radiation pattern. When the phantom and air transition is reached by the probe, the probe is set on top of the skin layer of the phantom while still maintaining a distance of 50 mm from the antenna origin. The probe was inserted into the phantom at 20° increments from the origin, which aids the inhomogeneous phantom to preserve its dimensions without major damage. The radiation pattern is reasonably symmetrical for both simulated and measured results, and the E-plane 3 dB beamwidth (45.5°) is narrower compared to the H-plane 3 dB beamwidth (52.4°) with a peak ~10 degrees off-boresight. The radiation patterns have a stable main beam direction for the three different frequencies evaluated. The simulated and measured results show minor discrepancies, which can be primarily attributed to the coarse number of measurement points taken in the measured pattern and reflections from the measurement setup. A front to back ratio of more than 17 dB was observed indicating the majority of radiation is directed into the phantom to achieve high power penetration.

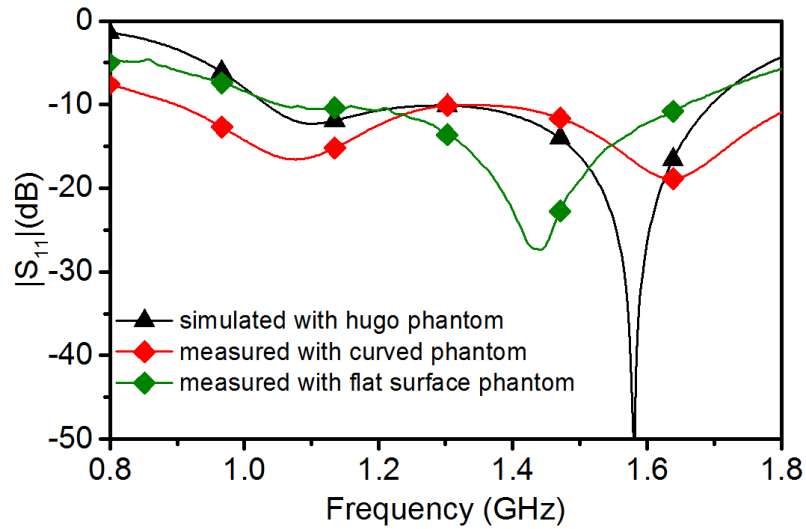


*Fig. 4.19 Simulated and measured  $|S_{11}|$  response of the antenna for the flat surface phantom and the curved phantom.*

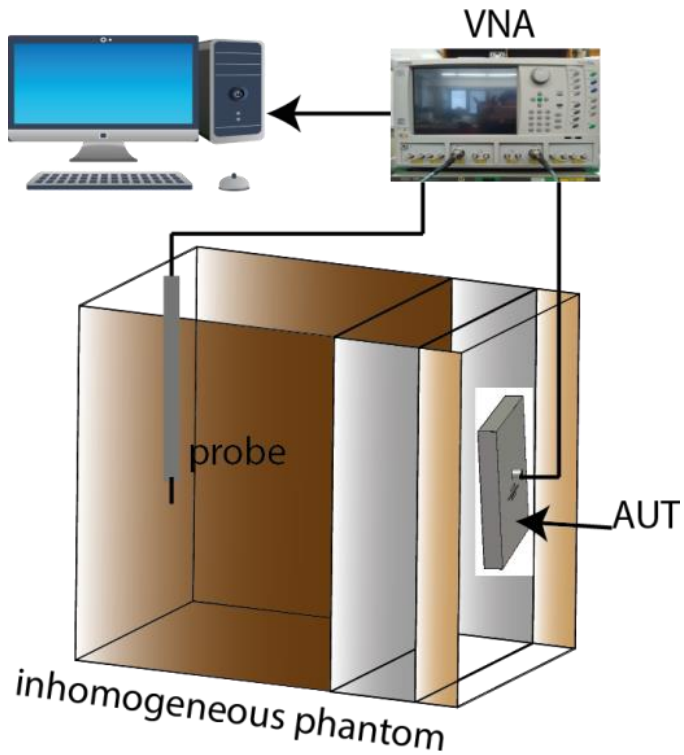


*Fig. 4.20 Schematic of the radiation measurement setup in the inhomogeneous phantom.*

Fig. 4.22 shows the normalized power penetration for the proposed antenna at different distances into the human head phantom, starting from the antenna-skin interface and extending inside the brain material to a depth of 70 mm from the skin surface. The power penetration falls off gradually with the distance from the skin surface, which can be attributed to the unavoidable loss of tissue (high water content material).

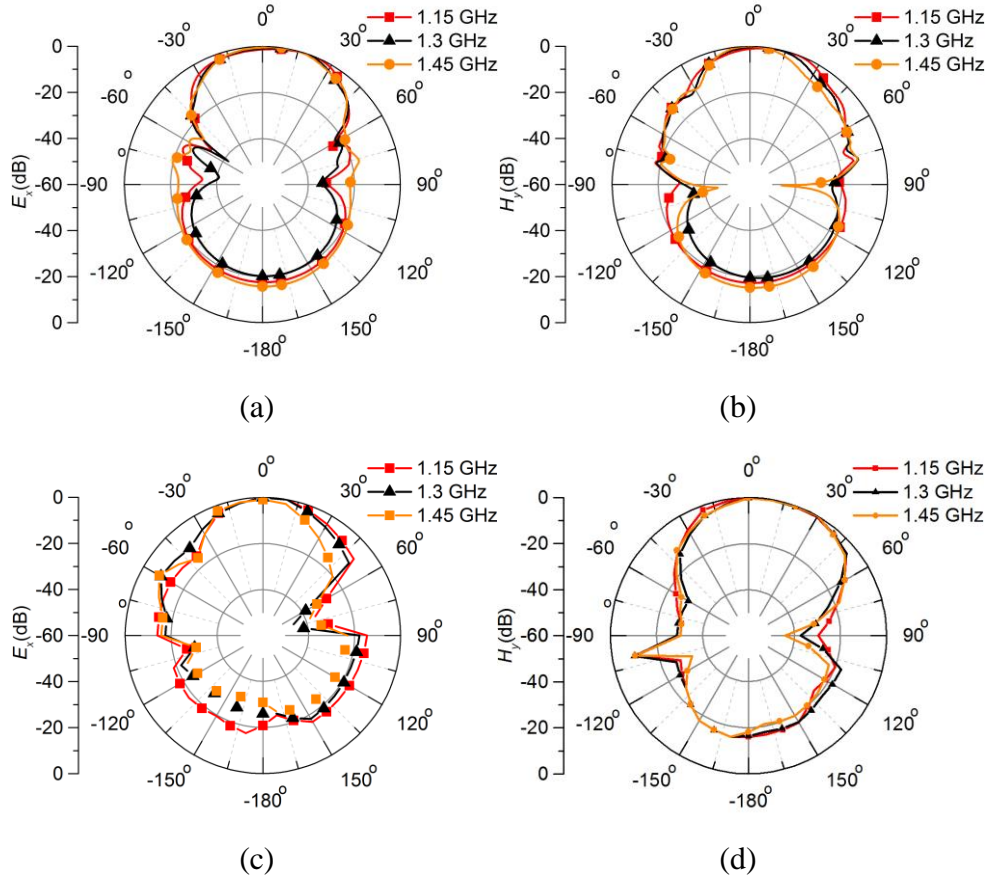


Fig. 4.21 Simulated (a) E-plane (xz-plane) and (b) H-plane (yz-plane) and measured (c) E-plane (xz-plane) and (d) H-plane (yz-plane) near-field pattern at 50 mm distance inside human brain.

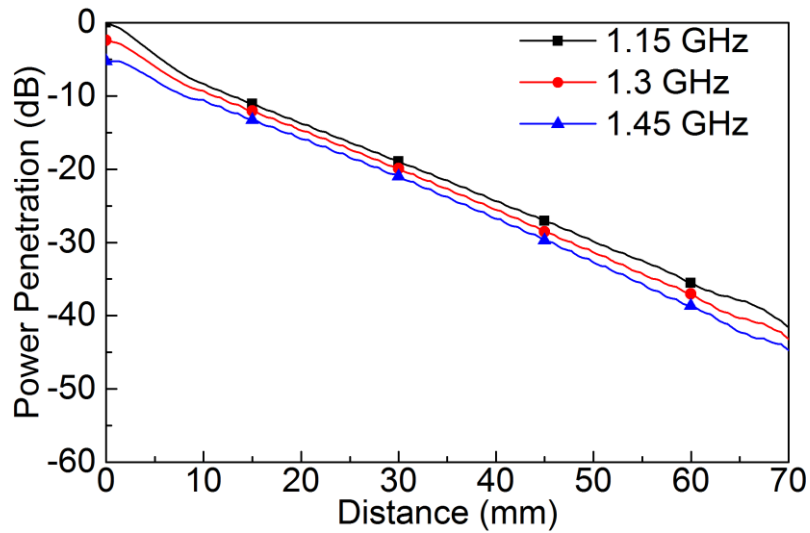


Fig. 4.22 Simulated power penetration at different distances inside inhomogeneous human head phantom at different frequencies.

#### 4.2.12. SAR for the Antenna

Fig. 4.23 shows the SAR distribution simulated in CST for the proposed antenna attached to the surface of the skin layer of the Hugo human head model with an input power of 1 mW for the frequencies 1.15 GHz, 1.3 GHz, and 1.45 GHz respectively. The maximum SAR value on the surface of the skin is 0.0147 W/kg (10g) occurring at 1.45 GHz, which is two orders of magnitude below the IEEE public radiation exposure limit of 1.6 W/kg [138]. It is also lower than those reported in the literature for on-body antenna systems for medical diagnosis, being 0.06 W/kg at 0.5 mm inside the skin layer and 0.03 W/kg at 5 mm inside the skin layer for the antenna shown in [18] and 0.48 W/kg for the antenna shown in [58]. The SAR decreases with depth into the tissue material (as seen in Fig. 4.22(a)), hence the proposed antenna achieves an even lower SAR of 0.0105 W/kg at the depth quoted in [18]. This low value enables the input power to the antenna to be increased to achieve an increased field penetration inside the human head if desired while remaining under the SAR exposure limit. Fig. 4.23 (b) depicts the maximum SAR penetration deep inside the human head tissue in the direction normal to the center of the proposed antenna. For each tissue layer, the maximum SAR reduces, and at 40 mm distance from the top of the skin layer (inside the brain), the maximum SAR approaches 0.002 W/kg.

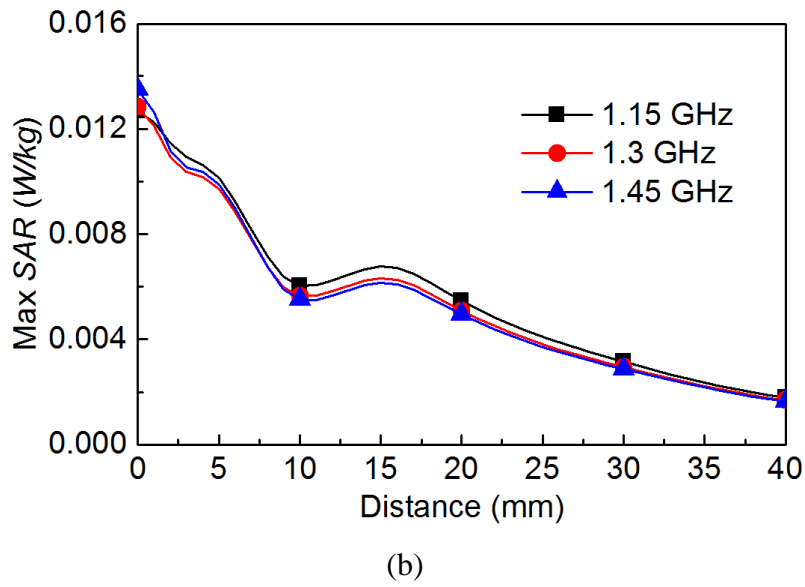
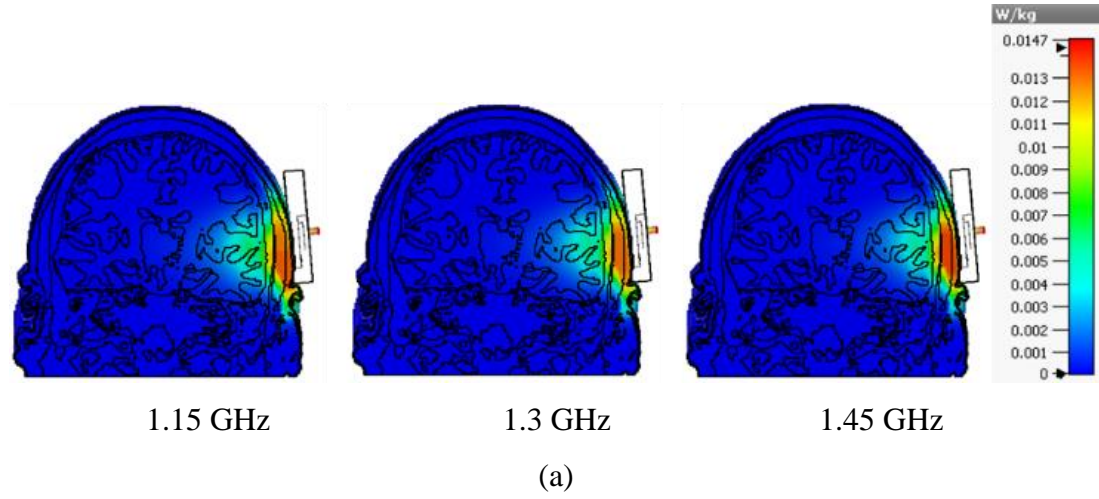


Fig. 4.23 (a) Simulated maximum SAR distribution with an input power of 1 mW inside in Hugo phantom (b) Simulated maximum SAR in terms of penetration distance.

#### 4.2.13. Comparison with the Literature

A comparison of antennas made for similar medical applications is provided in Table 4.2 taking note of the electrical size, maximum SAR, FBR and considered phantom type with the proposed antenna achieving approximately equivalent or better performance across all metrics.

*Table 4.2 Performance comparison between similar antennas*

Antenna	Electrical size	Max SAR (W/kg)	Phantom	FBR
[18]	$0.05 \lambda \times 0.05 \lambda$	0.06 (10g)	Homogeneous human head	3.5 dB at low frequency and 16.5 dB at high frequency
[16]	$0.22 \lambda \times 0.22 \lambda$	Not shown	Inhomogeneous human head	19 dB
[152]	$0.35 \lambda \times 0.26 \lambda$	Not shown	Not considered	0 dB
[64]	$0.35 \lambda \times 0.15 \lambda$	Not shown	Inhomogeneous human head	Not shown
[153]	$0.1 \lambda \times 0.09 \lambda$	4	Inhomogeneous muscle	Not shown
This work	$0.23 \lambda \times 0.23 \lambda$	0.0147 (10g)	Inhomogeneous human head	Minimum 17 dB throughout the operating band

#### **4.2.14. Conclusion**

A 3-D compact folded antenna for on-head microwave imaging applications is proposed. The antenna utilizes a slot loaded ground plane to achieve wideband operation and is then enclosed in a cavity to achieve a highly directional radiation pattern inside the human head without increasing the lateral dimensions of the antenna. Parametric studies are provided to characterize the behavior of the key radiating elements, and to show that the antenna remains operational over typical thicknesses and permittivities human head tissues. Significant power penetration inside the brain is achieved while the antenna is affixed to an inhomogeneous human head phantom, with an operational frequency range from 1 - 1.7 GHz. The antenna is compact, achieving dimensions of  $0.23\lambda \times 0.23\lambda$  and  $0.04\lambda$  in terms of the lowest operating frequency. The maximum SAR value on the skin surface of 0.0147 W/kg (10g) is the lowest found amongst the literature for antennas operating on-head. The proposed 3-D compact antenna has applications in the medical imaging and diagnosis of the human head. The

negligible dependency on the tissue permittivity and thickness means the proposed antenna can account for natural variations from human to human and potentially for biomedical diagnosis of other parts of the body, whilst exhibiting a detectable change in reflection properties for an inclusion inside the brain of a particular human being diagnosed.

### **4.3. Compact CPW Fed Wideband Directional Antenna for Medical Diagnosis**

For some biomedical applications, antennas with a broad bandwidth can be advantageous. A novel compact CPW fed antenna is presented in this section for the medical diagnosis of the human head providing high directionality with increased front to back ratio and lowest SAR compared to the literature. The near field radiation pattern of the proposed antenna provides with unidirectionality towards the considered human head phantom. Moreover, the operating bandwidth is increased to achieve suitability for a wideband medical imaging application. The performance of the antenna is validated by utilizing simulation and measurement data.

#### **4.3.1. Rationale of the Design**

The suitability of an antenna for medical diagnosis applications depends on multiple factors such as antenna directionality [61], operating frequency and bandwidth [24, 25], the level of reflection at the air to skin interface [18, 144], impedance matching with heterogeneous tissue layers [144], biocompatibility [154] and compactness [25]. To increase the suitability, some of these factors are enhanced in the literature. A directional antenna can achieve a highly resolved visualization for biomedical imaging compared to omnidirectional antenna [61]. Signals at the low microwave frequency region (e.g. 0.5-3 GHz) can penetrate through human tissue more readily than those at higher frequencies (e.g. 3-20 GHz) because human tissue becomes highly conductive at higher frequencies [28]. There is a range of different optimal frequencies proposed to penetrate effectively inside different individual human tissues, with the optimal frequency for wireless power transmission in the GHz-range when the dimensions of the transmit antenna are much smaller than a wavelength [24]. Moreover, the required bandwidth from an antenna can be narrowband [66, 155] or wideband [32] depending on the diagnosis application and the data retrieval methods. For biomedical applications, the smallest size of a detectable body in a radar scanning system is proportional

to the width of scanning bandwidth [32]. Hence, a wide bandwidth is highly desired to detect a minuscule anomaly inside the human head.

The reflection intensity at the air to skin interface due to the differences in dielectric properties of human skin and air [27] is such that it can result in an almost undetectable level of signal penetration into the human body. The small amount of signal that does penetrate this boundary gets further attenuated by the lossy tissue layers. The human body is a composite of different layers of biological tissues containing different quantities of water [27]. Each layer of human tissue, e.g. skin, bone, brain, etc., exhibits diverse permittivity characteristics at different frequencies, which leads to inhomogeneous and dispersive behaviour [23]. These inhomogeneous human tissues must be considered when designing antennas for microwave diagnostic systems [144] to achieve efficient microwave penetration inside the body. Excessive exposure to microwave signals may cause harm to the human body, and can be quantified by the SAR of the tissue when radiation is applied [156]. As a requirement of international regulatory standards [138], SAR needs to be minimized in a microwave imaging system to achieve safety and compatibility with the human body.

Numerous antennas have been proposed for microwave imaging in the literature, among which only a few are dedicated to human head imaging. These head imaging antennas can be divided into two types: off-body and on-body antennas. A three-dimensional antenna that operates in the air near the human head (off-body) achieves a fractional bandwidth (FBW) of 67% and a FBR of less than 10 dB over this band [32]. The antenna has poor directionality and high reflection intensity from the air to skin transition, with a maximum SAR of 0.02 W/kg for 10-g averaging. Another off-body antenna with a complex three-dimensional structure [16] achieves high directionality throughout the operating frequency range, but the antenna performance degrades due to low FBW of only 9.4%. An off-body antenna operating within the near field of a human head [42] achieves an FBW of 73%. The antenna radiation is characterized for both near and far-field, where both radiation characteristics suffer from an FBR of less than 10 dB. The antenna exhibits a maximum SAR of 0.016 W/kg for 10-g averaging. In [51], a slot-loaded three-dimensional antenna operating in the near field of the human head is reported. The antenna exhibits wideband performance with an FBW of 97%, with the lowest operating frequency of 1.1 GHz for the dimensions of  $70 \times 15 \times 15 \text{ mm}^3$ . However, the antenna exhibits a near field radiation pattern FBR of less than 10 dB. An off-body three-dimensional antenna for brain tumour detection is proposed in



[20] which achieves an electrically small dimension at the lowest operating frequency of 1.41 GHz. Whilst the antenna displays an FBW of 87% while operating in air, it lacks directionality with an FBR of 9 dB. A similar unidirectional antenna for traumatic brain injuries detection attains an FBW of 102% with FBR of less than 9 dB for an overall dimension of  $70 \times 30 \times 15 \text{ mm}^3$  [13]. All the antennas discussed above operate in air (off-body) with a human head at the boresight direction of the antenna. Most of them suffer from an FBR of less than 10 dB likely due in part to reflections at the air/skin interface, and they have a complicated three-dimensional structure. An advantage of these antennas operating off-body is the low permittivity of the surrounding air environment assists in attaining large FBWs of more than 80%. Nonetheless, these antennae suffer from reflection at the air to skin interface.

There are very few on-body antennas that exhibit direct contact between the antenna and the human tissue reported in the literature for microwave imaging. In [102], a foam embedded antenna system is proposed to detect congestive heart failure. While the antenna technically operates in contact with the human body, the foam effectively creates an equivalent air spacer from the human tissue. Furthermore, the antenna is not independently characterized for on-body applications, achieving an FBW of 29% from 0.71 GHz to 0.95 GHz with an FBR of 8 dB when tested in air. A bow-tie shaped antenna for a hyperthermia applicator is proposed in [157]. A demineralized water bolus is used in the antenna design to achieve miniaturized dimensions while impedance matching with the human body. Nonetheless, as water is a lossy medium, to begin with, the antenna suffers from reduced efficiency and a complicated and uncomfortable setup involving direct contact of the water with the human body. An antenna operating on-head operates in the low microwave frequency region to achieve increase penetration, achieves an FBW of 120% from 0.5 GHz to 2 GHz [18]. To achieve a compact dimension, Rogers RT/duroid 6010 substrate with a permittivity of  $\epsilon_r = 10.2$  is used. The antenna is multi-layered, and the resonant response of the antenna is highly dependent on the conductivity of the measuring body. The antenna simulation uses homogeneous phantom, which has been shown to differ substantially from a realistic inhomogeneous and lossy near-field scenario. It also has conductive surfaces in contact with the human head, which will reduce power transfer efficiency and sensing capabilities [144]. Most of the antennas discussed above also consider homogeneous phantom, and sometimes lossless human tissue, which differs significantly from the real-world characteristics of human tissues. Recently, in

[158], a 3d antenna for human head diagnosis is presented. The antenna is compact and highly directional towards human head within its operating frequency range. Nonetheless, the antenna is designed for narrow band application.

This section presents a novel wideband cavity-backed CPW fed monopole antenna matched to an inhomogeneous and lossy human head phantom to address the problems associated with antennas for microwave diagnosis discussed above. The presented antenna exhibits a wide bandwidth at the lower microwave frequency region where the penetration into the lossy dielectric medium is high. The antenna is directional with high FBR throughout the operating frequency region while operating in contact with the inhomogeneous human head phantom. A miniaturization technique utilizing a meandered line is shown to achieve operation at lower microwave frequencies, and a rectangular cavity is introduced to minimize radiation to the environment surrounding the antenna, improve FBR, and increase power penetration inside the head. The key parameters of the antenna design are studied for their influence on the overall performance and characterized for the thickness and permittivity disparity of human tissues, which can vary with age and from person to person. The SAR distribution of the proposed antenna is analysed to validate its suitability for operation near the human body.

#### **4.3.2. Configuration of the Proposed Antenna**

CPW structures have the advantage of being uniplanar, increasing their integration ability and ease of fabrication. In this work, a T-shaped CPW monopole signalling strip is positioned at the middle of a circular ground plane. A detailed schematic of the conductive layer is provided in Fig. 4.24 with the dimensions of the antenna parameters. A cavity with the dimension  $a \times a \times h \text{ mm}^3$  is mounted at the rear of the proposed antenna to achieve a unidirectional radiation response throughout the operating frequency region. The cavity is hollow and made of copper, and the proposed antenna is placed in the centre of the cavity, as shown in Fig. 4.24 (c), such that the top surface of the superstrate is aligned with cavity aperture. The cavity is isolated from all sides of the printed metallic elements of the antenna. A coaxial feed is sandwiched between the substrate and the superstrate connecting the coaxial pin to the monopole and the outer shield to the CPW ground, separated by distance 'g'. The dimension of the antenna, referring to Fig. 4.24, is shown in Table 4.3.

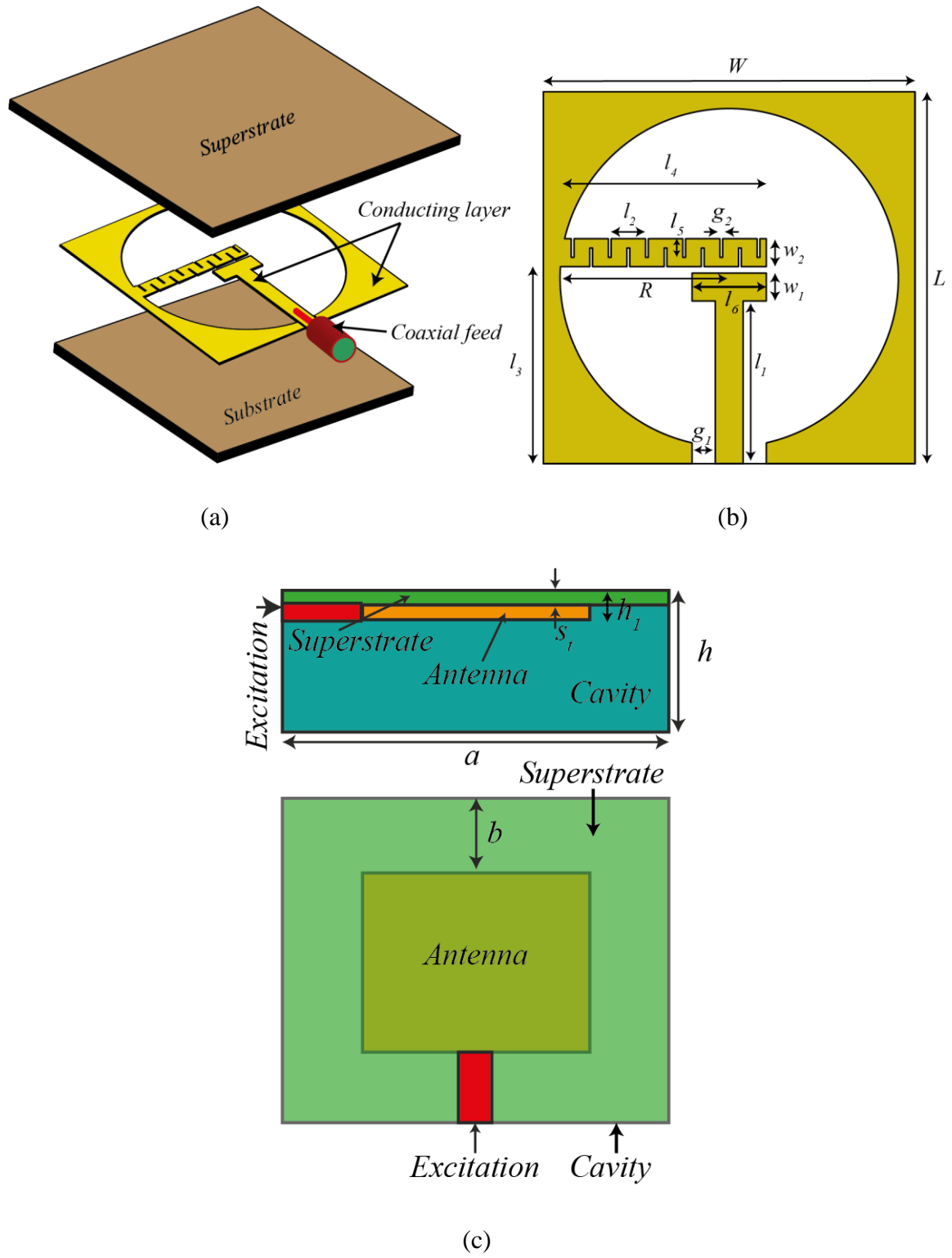


Fig. 4.24 (a) Proposed CPW antenna layout using FR4 substrate and superstrate (b) Antenna schematic diagram, (c) Addition of the cavity backing.

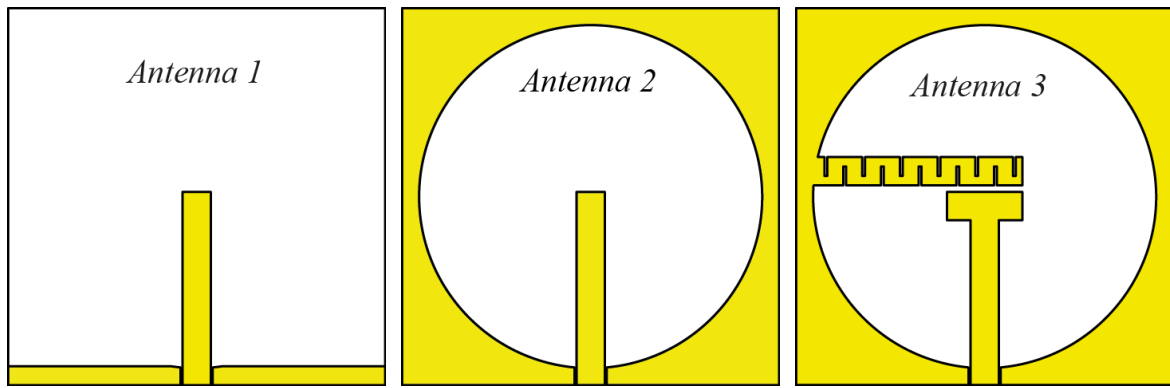
Table 4.3: Dimensions of the proposed antenna

<i>Parameters</i>	<i>Values (mm)</i>
$L$	40
$W$	40
$l_1$	17.5
$l_2$	3.7
$l_3$	21.2
$l_4$	22
$l_5$	2
$l_6$	8
$w_1$	3
$w_2$	3
$g_1$	0.2
$g_2$	0.3
$a$	60
$b$	10
$h$	23.2
$h_1$	3.235
$S_t$	1.6

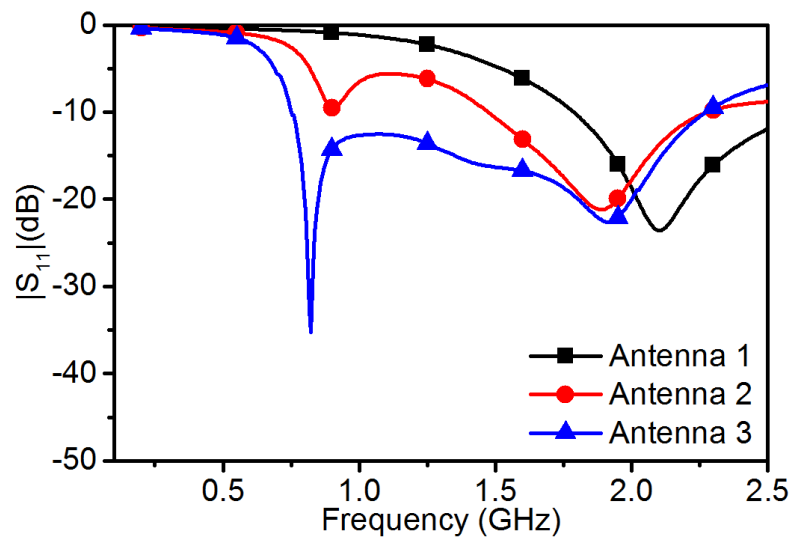
### 4.3.3. Design Evolution

The proposed antenna is designed while operating on an inhomogeneous human head phantom and aims to achieve wideband operation occupying as much of the low microwave frequency region (i.e. 0.5-3 GHz) as possible as this has been shown to increase the penetration inside the human head [18]. The conceptual antenna design evolution is depicted in Fig. 4.25 (a) from a basic CPW monopole (Antenna 1) to the final prototype (Antenna 3). Fig. 4.25 (b) shows that the  $|S_{11}|$  response of Antenna 1 achieves impedance matching centred at 2.1 GHz with a -10 dB bandwidth of around 0.86 GHz. The Smith chart response of the Antenna 1 is shown in Fig. 4.25 (c) where the lower end of the desired operating band below 0.9 GHz is mostly out of the  $VSWR = 2$  circle. The overall electrical length of the antenna

needs to be increased to achieve impedance matching at a lower frequency. A circular slot is introduced to ground the monopole (Antenna 2) increasing the overall length and achieve uniform beam towards the broadside direction. The Smith chart response of Antenna 2 depicts an additional loop at lower frequencies, resulting in two  $|S_{11}|$  dips in Fig. 4.25 (b). However, the lower frequencies do not meet the  $|S_{11}| < -10$  dB requirement. A new concept consisting of a meandered line extending from the left side of the circular slot towards the upper edge of the monopole is depicted as Antenna 3 to achieve impedance matching at lower frequencies. It provides a long current path along the meandered line, introducing inductance to decrease the capacitance of the loop response shown in the Smith chart of Antenna 2 at low frequencies. The amount of inductance added by the meandered line can be optimized by adjusting the gap between the meandered lines. It achieves impedance matching at frequencies as low as 0.75 GHz and increases the overall bandwidth to 1.5 GHz. The monopole is top-loaded with a rectangular strip, giving the overall monopole structure a T-shape to achieve further impedance matching and miniaturization. It is used as a design tool to couple to the meandered line and further optimize the antenna impedance. The final version of the proposed antenna is shown as Antenna 3 achieving an overall current path length of 367.5 mm, which is approximately one wavelength at the lowest operating frequency. The Smith chart response of Antenna 3 shows the impedance of the antenna where frequencies from 0.75 GHz to 2.25 GHz fall comfortably within the boundary of  $VSWR = 2$  circle. An advantage of using the proposed meandered line matching technique is it can be accommodated within the existing dimensions of the antenna resulting in an overall antenna footprint of 40 mm x 40 mm, or approximately  $0.1\lambda_0^2$  at the longest wavelength.



(a)



(b)

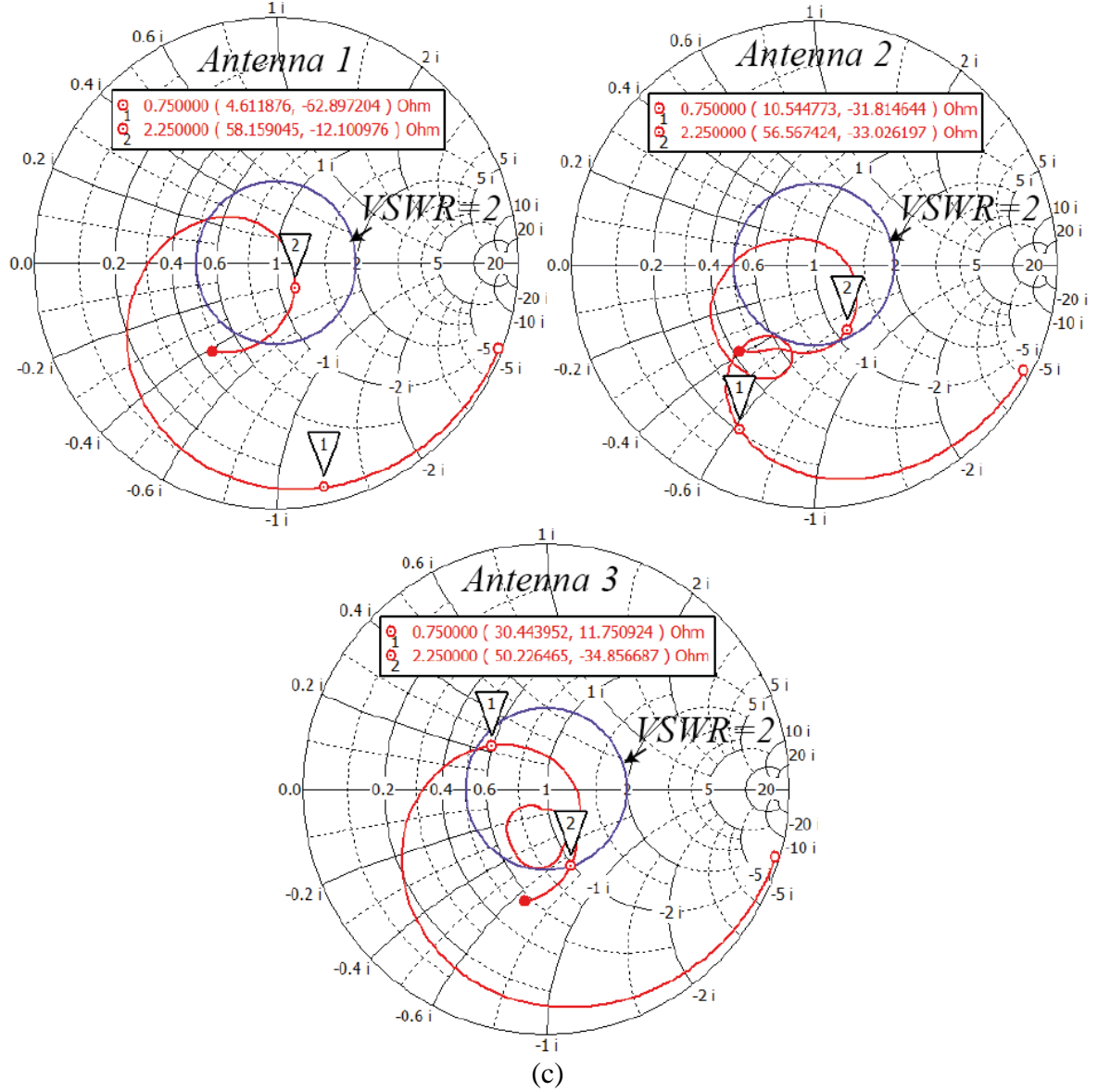
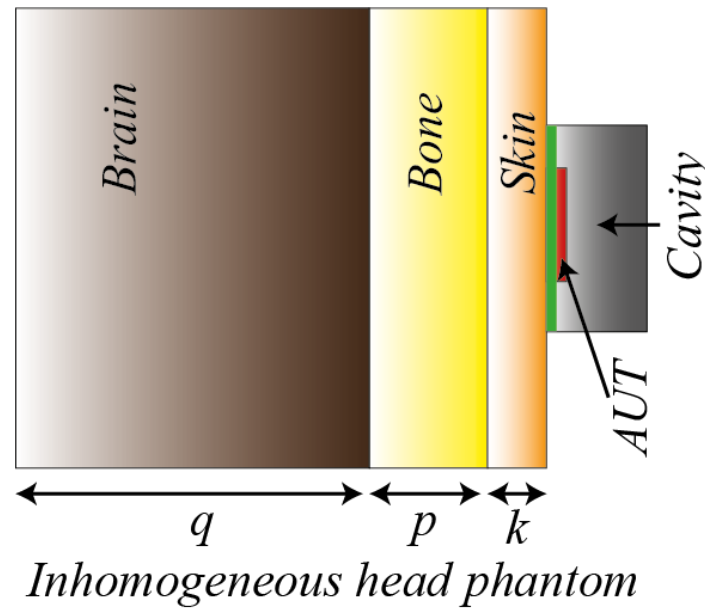


Fig. 4.25 (a) Antenna evolution from CPW monopole to the proposed antenna, (b) simulated  $|S_{11}|$  response of Antennas 1, 2, and 3, (c) Smith chart response of Antennas 1, 2, and 3.

#### 4.3.4. Simulation Setup

Fig. 4.26 portrays the simulation setup in the CST 2017 software [131] for the proposed antenna where the skin, bone and brain characteristics mimic the sampled human tissue characteristics in [27-29], and are taken from the CST material library. The primary thicknesses of the skin, bone and brain for the simulation is taken to be  $k=3 \text{ mm}$ ,  $p=10 \text{ mm}$ , and  $q=70 \text{ mm}$  respectively. The brain layer thickness is chosen so that it is a multiple of lowest operating frequency wavelength (accounting for brain permittivity) to achieve wave

propagation characteristics inside the brain. The superstrate of the antenna is attached to the skin layer with the cavity situated at the back.



*Fig. 4.26 Antenna simulation setup with the inhomogeneous human head phantom. Dimensions (in mm):  $k=3$ ,  $p=10$ ,  $q=70$ .*

#### 4.3.5. Current Distribution

The behaviour of the proposed antenna can be visually described with the aid of the current distribution on the antenna conductors. The role of the T-shaped monopole feed, circular slot, and the meandered line for the operating frequencies 0.7 GHz, 1.3 GHz and 2 GHz are seen in Fig. 4.27 using the surface current distribution while the inhomogeneous phantom is affixed to the superstrate layer of the antenna. At 0.7 GHz the current extends around the circumference of the circular slot and is highly concentrated along the meandered line and monopole edges, tracing the longest electrical path. As the frequency increases to 1.3 the 2 GHz, the circular slot boundary shows lower current density with reduced coupling between the meandered line and the top of the T-shaped monopole. The current path is primarily restricted between the monopole and the meandered line.



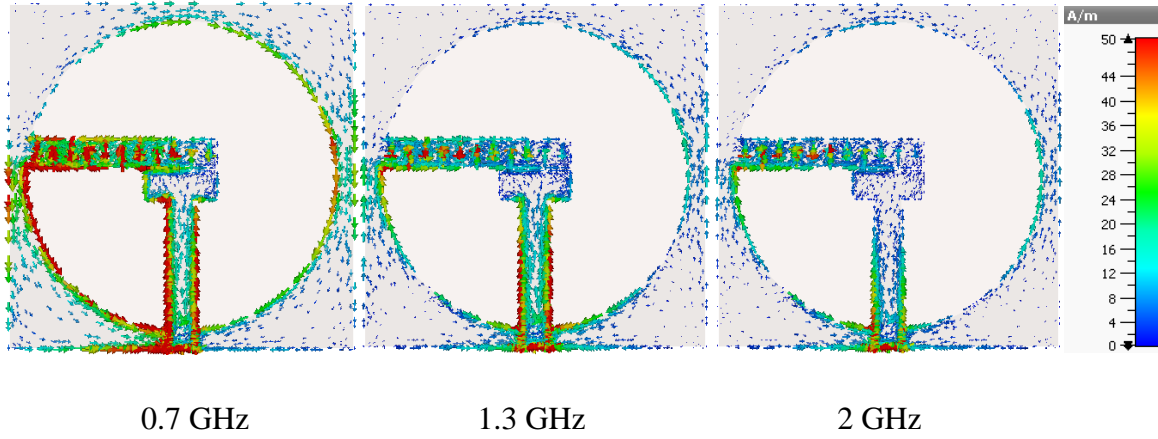


Fig. 4.27 Surface current distribution of the CPW antenna with the inhomogeneous head phantom attached to the superstrate.

#### 4.3.6. Role of the Superstrate

As the superstrate plays an important role in the design of an antenna for human head diagnosis applications, a parametric study of the thickness of the superstrate is undertaken, and the results are shown in Fig. 4.28. When the thickness of the superstrate  $S_t = 0$  mm (i.e. no superstrate) the  $|S_{11}|$  response of the antenna is relatively flat with frequency, as direct contact between lossy human tissue and the antenna conductor dramatically reduce the radiation efficiency of the antenna by absorbing the energy. The heat generated by the antenna will be transferred directly to the human tissue [18]. When  $S_t = 0.6$  mm, improved impedance matching at lower frequencies is observed compared to the proposed antenna (with  $S_t = 1.6$  mm). However, the impedance at the upper-frequency region is sensitive to this dimension, due to the proximity of the high permittivity human tissue material, restricting the bandwidth of the antenna. As  $S_t$  increases further to 1 and 1.6 mm the impedance bandwidth increases to its maximum of about 1.7 GHz ( $\sim 104\%$  or over 3:1) from 0.788 GHz to 2.5 GHz for the proposed antenna. Exceeding this results in a loss of the low-frequency matching, as seen for  $S_t = 2$  mm.

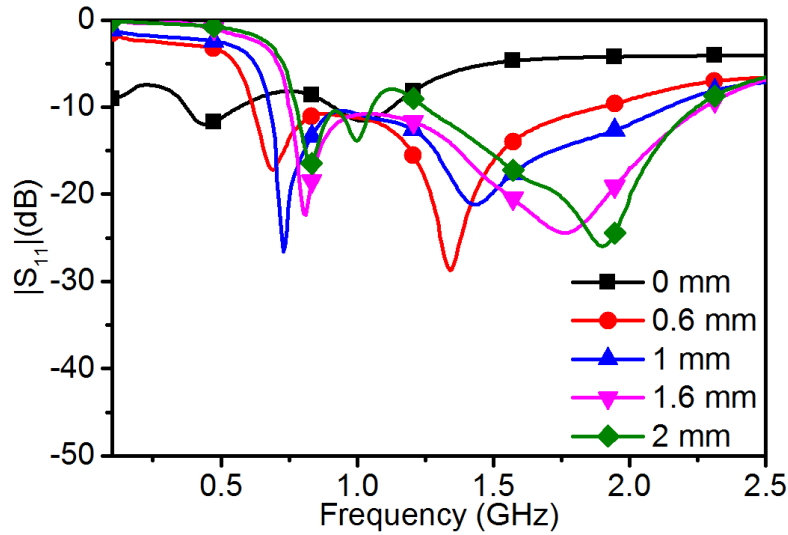
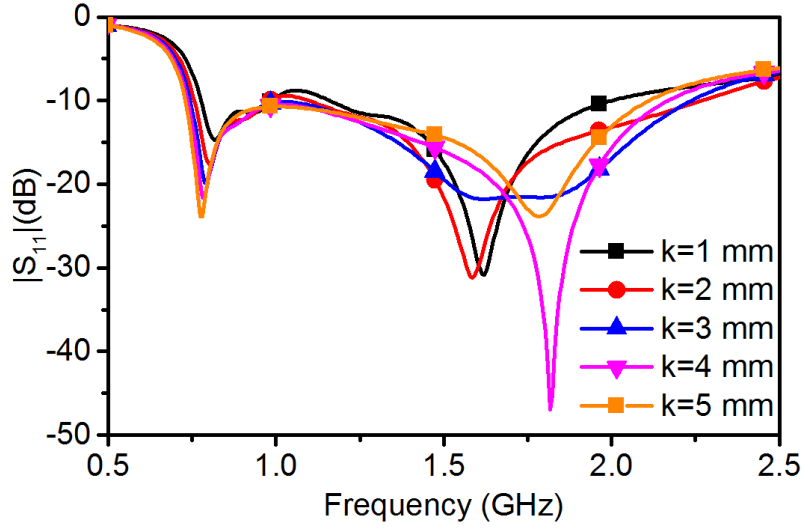


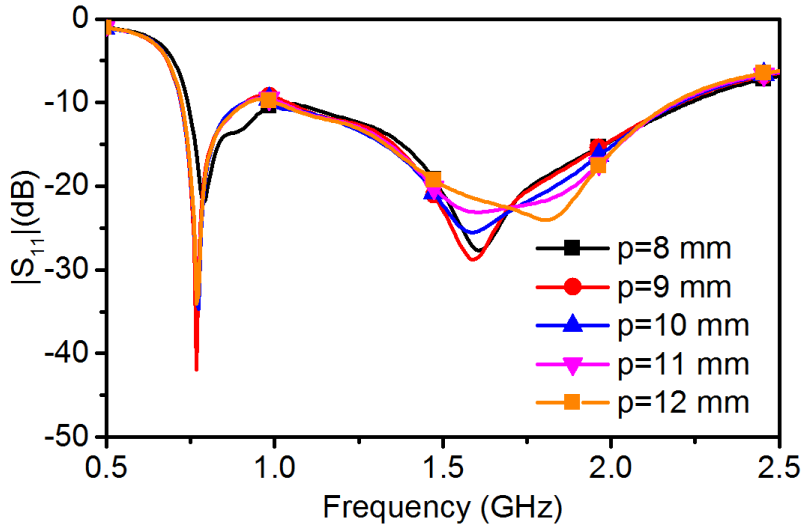
Fig. 4.28 Simulated  $|S_{11}|$  with different thicknesses of the superstrate,  $S_i$ .

#### 4.3.7. Parametric Studies

For a medical diagnosis, it is crucial to achieving relative independence of antenna performance to the standard variations in human tissue characteristics from person to person due to body composition and age. The bone and skin thickness can vary between 3 to 10 mm and 0.5 to 1.5 mm, respectively, for a person aged older than five years [23]. Parametric studies are conducted for the proposed antenna concerning these variables and are depicted in Fig. 4.29 (a) and (b) to achieve robustness against such changes. Fig. 4.29 (a) shows the  $|S_{11}|$  response for different thicknesses of skin and bone. By varying the skin thickness,  $k$ , from 1 mm to 5 mm, the wide bandwidth performance of the proposed antenna remains relatively intact, with impedance matching at the upper end of the frequency range degrading slightly and approaching the -10 dB limit for  $k = 1$  mm. The proposed antenna  $|S_{11}|$  performance is less sensitive to the thickness changes of the bone layer. Varying bone thickness from 8 mm to 12 mm results in a negligible change in the  $|S_{11}|$  response occurs over the entire bandwidth as depicted in Fig. 4.29 (b).



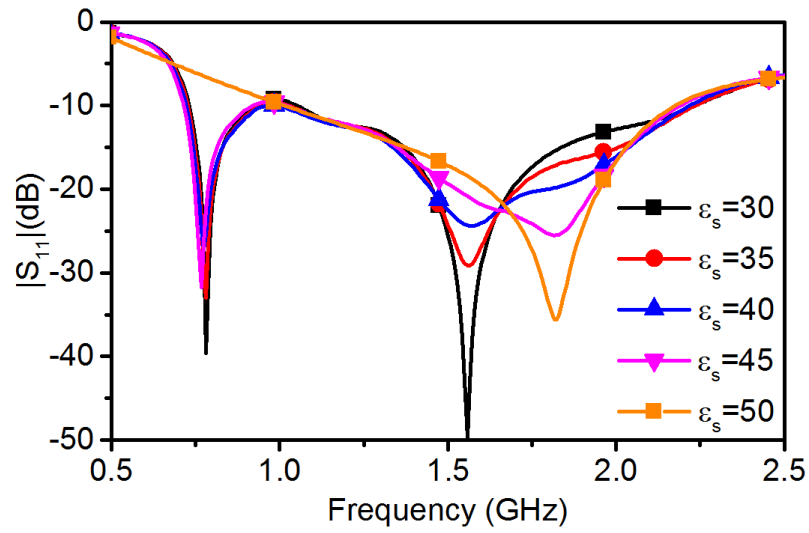
(a)



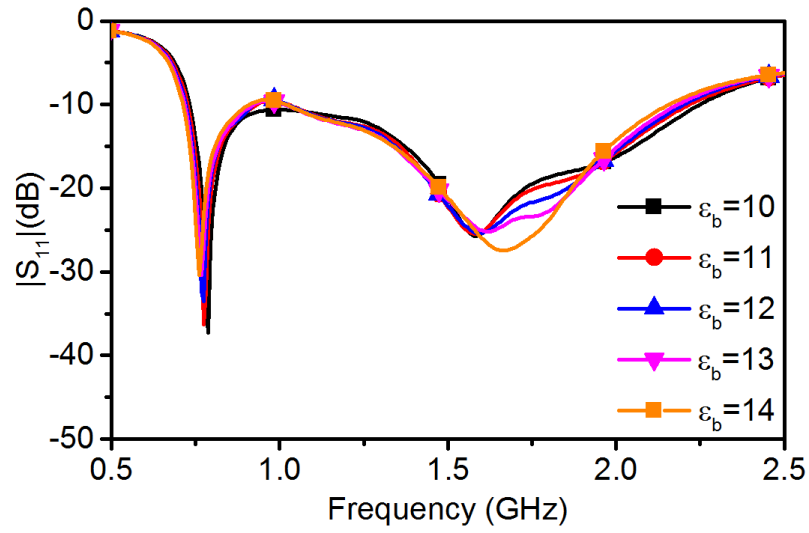
(b)

Fig. 4.29 Simulated  $|S_{11}|$  with different thicknesses of the (a) skin and (b) bone.

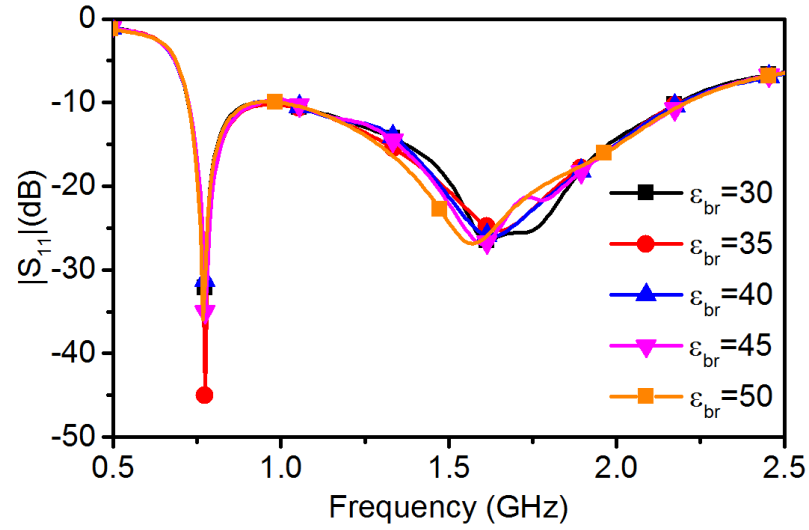
The permittivity of skin ( $\epsilon_s$ ) bone ( $\epsilon_b$ ) and brain ( $\epsilon_{br}$ ) is varied from 30 to 50, 10 to 14 and 30 to 50 respectively to determine the sensitivity of the proposed antenna for different permittivity characteristics of human skin and bone. In Fig. 4.30 (a), changes in permittivity of the skin induce variations in  $|S_{11}|$  depth in the higher frequency region; however, the overall impedance bandwidth remains relatively unchanged.



(a)



(b)



(c)

Fig. 4.30 Simulated  $|S_{11}|$  with different dielectric permittivity of the (a) skin,  $\epsilon_s$ , (b) bone,  $\epsilon_b$ , (c) brain,  $\epsilon_{br}$ .

When the skin permittivity reaches 50, the impedance matching at the lower end of the desired frequency band starts to decrease. For changes in the bone permittivity the impedance performance of the antenna changes at both resonant frequencies as presented in Fig. 4.30 (b).

For variations in the brain permittivity, the antenna  $|S_{11}|$  shows minor sensitivity at higher resonant frequency region as depicted in Fig. 4.30 (c). In essentially all cases studied, the wide impedance bandwidth of the proposed antenna stays as predicted, providing a stable operating band when used on humans with naturally varying head characteristics.

#### 4.3.8. Experiment Setup

To compare the field radiation performance of the antenna with an actual human head phantom, a realistic head phantom “Hugo” is extracted from “bio model” of CST microwave studio software attaining a resolution of  $1 \text{ mm}^3$  for the model. Fig. 4.31 shows the placement of the proposed antenna attached on the “Hugo” head phantom.

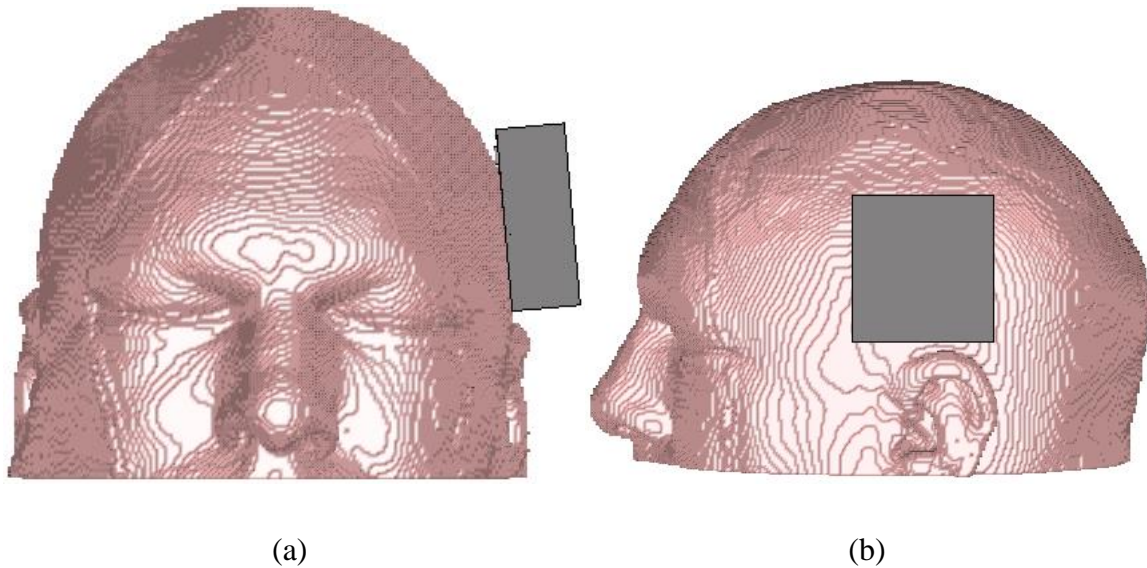


*Fig. 4.31 (a) Front and (b) side view of the “Hugo” head when the antenna attached to the “Hugo” head model.*

#### 4.3.9. Field Distribution Inside Human Head

Fig. 4.32 and Fig. 4.33 displays the simulated E and H field penetration inside and outside of the “Hugo” human head phantom in xz-plane and yz plane for the proposed antenna when

operating on-head. With the increment in frequency, the near field beam pattern becomes narrower, relative to the operating frequency wavelength. The field penetration is directed normal to the antenna surface towards the brain layer of the phantom. The directive penetration inside human head phantom is coupled with negligible field intensity at the rear of the antenna, resulting in minimal interference from objects surrounding the head. Such an antenna characteristic with performance tolerance to variations of permittivity and thicknesses of the human tissue layers makes the proposed antenna suitable for diagnosis of a wide range of different human heads.

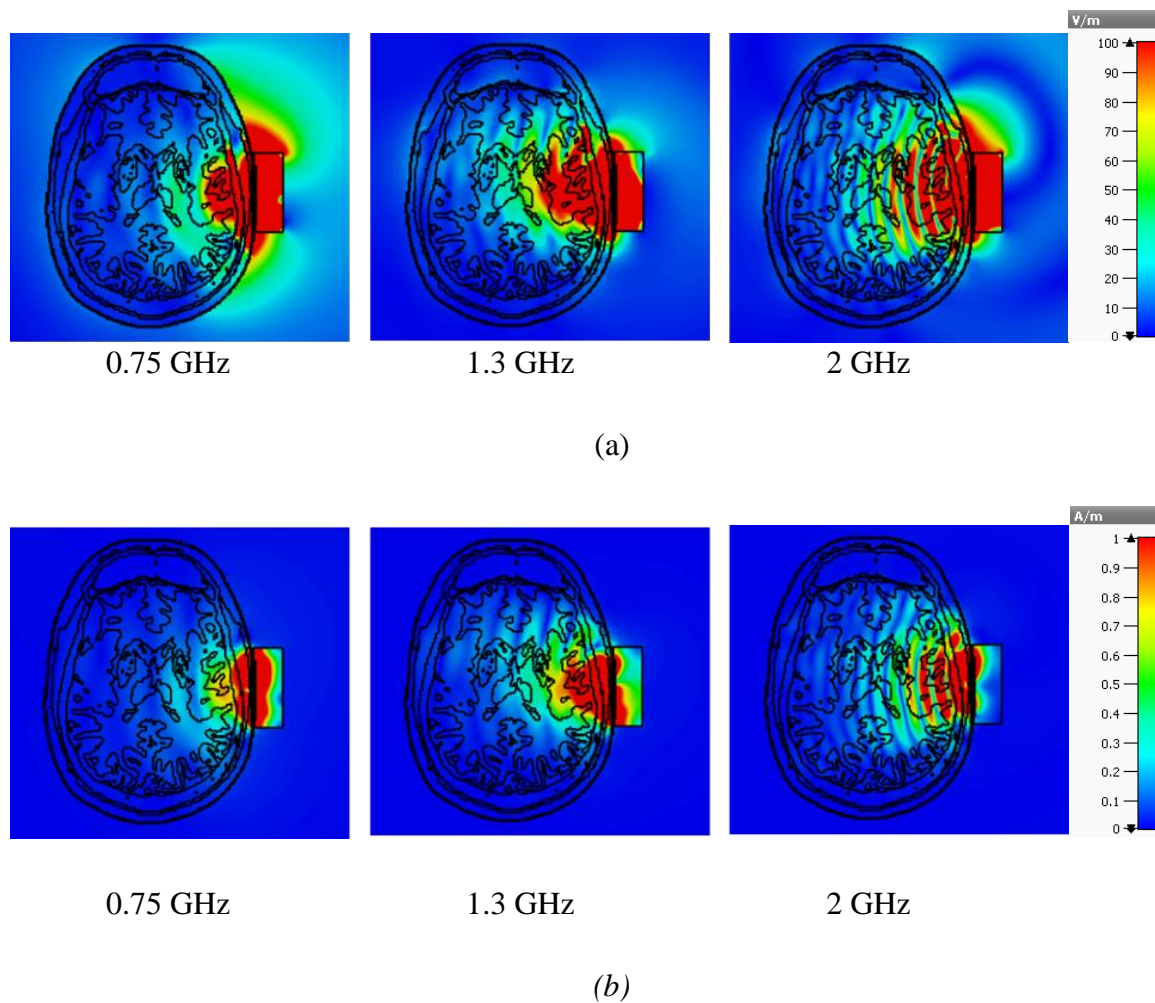
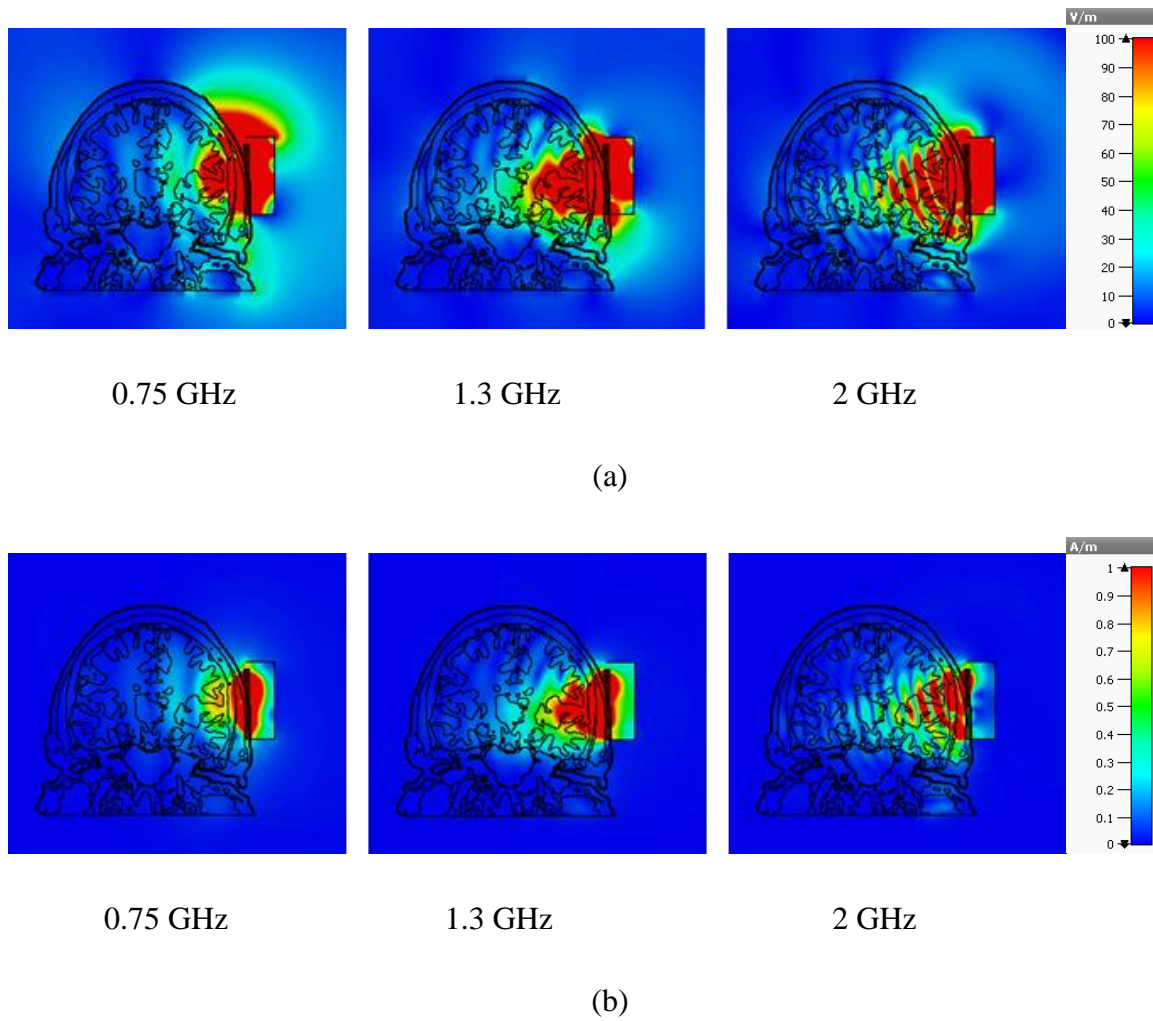


Fig. 4.32 (a) Front and side view of the “Hugo” head, distribution of the (b) E-field and (c) H-field of the proposed antenna inside the inhomogeneous head phantom at  $xz$ -plane.





*Fig. 4.33 Distribution of the (a) E-field and (b) H-field of the proposed antenna inside the inhomogeneous head phantom at yz-plane.*

#### 4.3.10. Fabrication of the Antenna and Inhomogeneous Human Head Phantom

The wideband CPW antenna is fabricated, and a photograph is shown in Fig. 4.34. The proposed antenna element is situated in the middle of the rectangular cavity. Hence the external dimensions of the antenna sub/superstrate are made equal to those of the cavity to remove the need for any supporting material below the antenna. A coaxial extension line is used to connect the antenna without disturbing the dimensions of the cavity. The superstrate and substrate are affixed using epoxy glue and kept under pressure for ~6 hours to achieve a

bond with minimal gap between the layers. The antenna is then attached to the aperture of the cavity. For the antenna measurement, we have fabricated a three-layer phantom using the procedure described in Section 3.3.4 of this thesis.

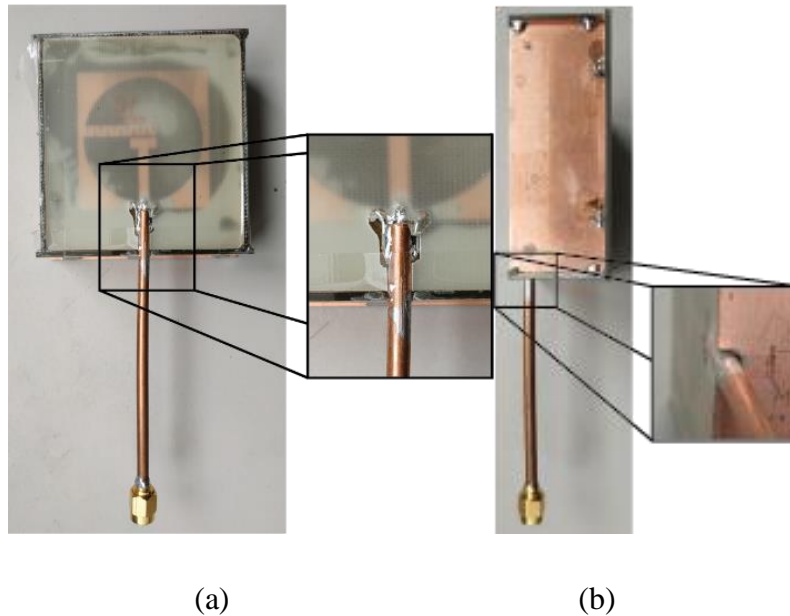


*Fig. 4.34 Proposed antenna made from FR4 material and a copper cavity (a) front view, (b) side view.*

#### **4.3.11. Measurement Setup and Results**

The simulated and measured  $|S_{11}|$  of the fabricated antenna with and without the cavity is shown in Fig. 4.35 when the antenna is attached to the human head phantom. The  $|S_{11}|$  response without the cavity shows good agreement between simulated and measured results, with slight changes likely due to the permittivity variance of the FR4 dielectric material due to its inhomogeneous fibreglass structure. The measured results with cavity attached display slightly more variation across the impedance bandwidth when compared to the simulated results. The feeding structure of the antenna within the cavity impacts the measured results. However, all results indicate that the wide useable bandwidth endures.



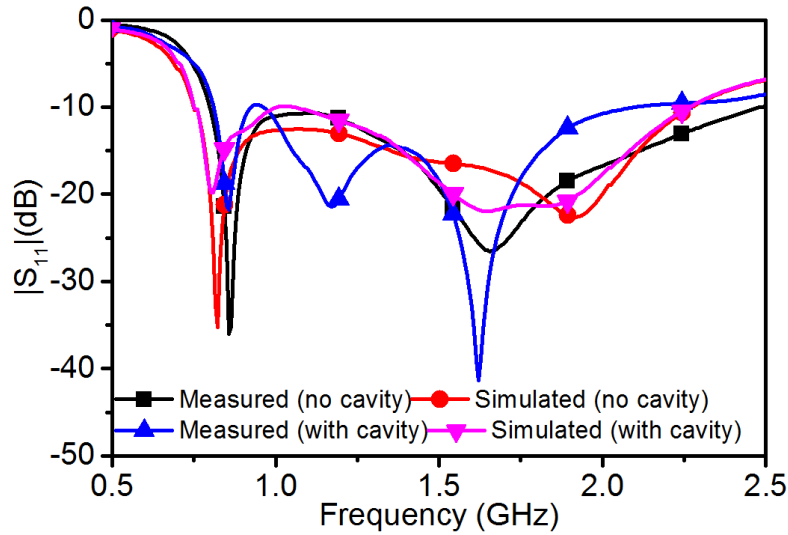


*Fig. 4.35 Simulated and measured  $|S_{11}|$  of the proposed antenna with and without the cavity.*

The simulation of the proposed antenna indicated radiation was directed inside the human head, enabling maximum power penetration in imaging and analysis applications. To validate this, the radiation pattern measurement setup shown in Fig. 4.36 (a) was used to attain the power response inside the human head phantom. A 2-port vector network analyzer (Anritsu MS4644B) is connected to the antenna and an E-field probe, which is an electrically small monopole antenna made using semi-rigid coaxial cable. The power pattern measurement is carried out in both the E and H plane. The measurement angle of the probe position around the antenna is varied manually to attain discrete values of the radiation pattern at a radius of 50 mm from the geometric centre of the top surface of the antenna as depicted in Fig. 4.36 (b).

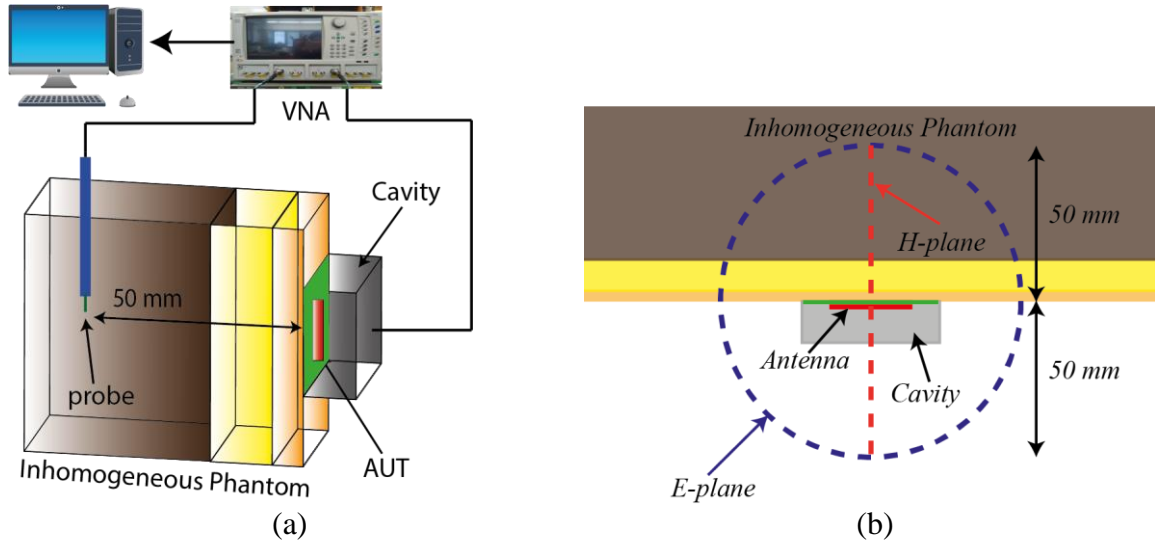
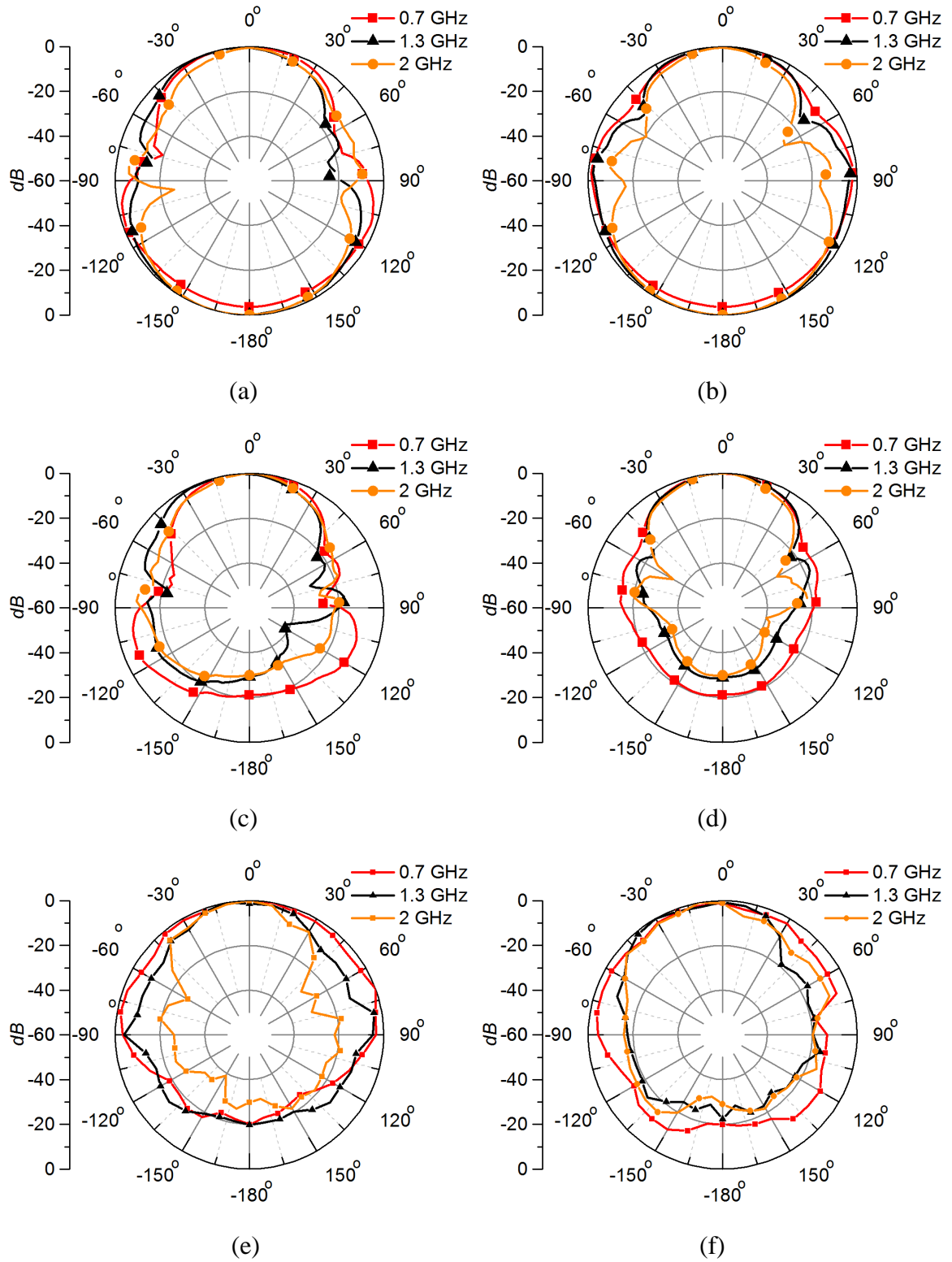


Fig. 4.36 (a) Radiation measurement schematic (b) cross-section view.

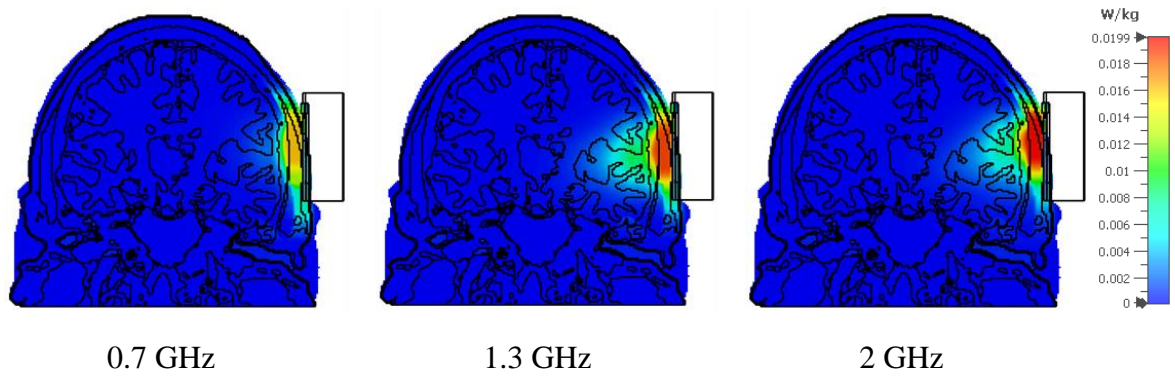
A comparison between the simulated and measured near field power pattern of the on-head mounted antenna with and without the cavity is shown in Fig. 4.37. It can be observed from Fig. 4.37 (a) and (b), the simulated E and H plane patterns low directivity with an FBR of roughly 0 dB at higher operating frequencies and about 3.63 dB at 0.7 GHz, indicating that without the cavity the antenna directs a large portion of radiation away from the head. After introducing the cavity, the simulated pattern becomes highly directive with an FBR of more than 20 dB in both E and H plane (as seen in Fig. 4.37 (c) and (d)) in front of the inhomogeneous head phantom. The measured radiation pattern obtained using the setup shown in Fig. 4.37 with the cavity at the back of the antenna is depicted in Fig. 4.37 (e) and (f). A high degree of similarity between the simulation and measurement result is observed for the cavity-backed CPW antenna, substantiating the FBR over 20 dB.



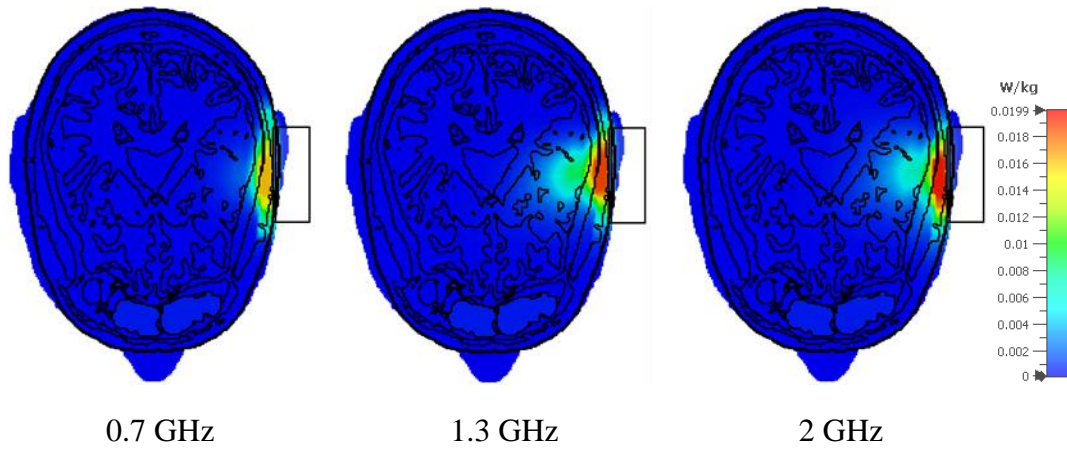
*Fig. 4.37 Simulated power pattern in the: (a) E-plane (xz-plane) and (b) H-plane (yz-plane) without the cavity; (c) E-plane and (d) H-plane with the cavity; and the measured pattern in (e) E-plane and (f) H-plane with the cavity.*

#### **4.3.12. SAR for the Antenna**

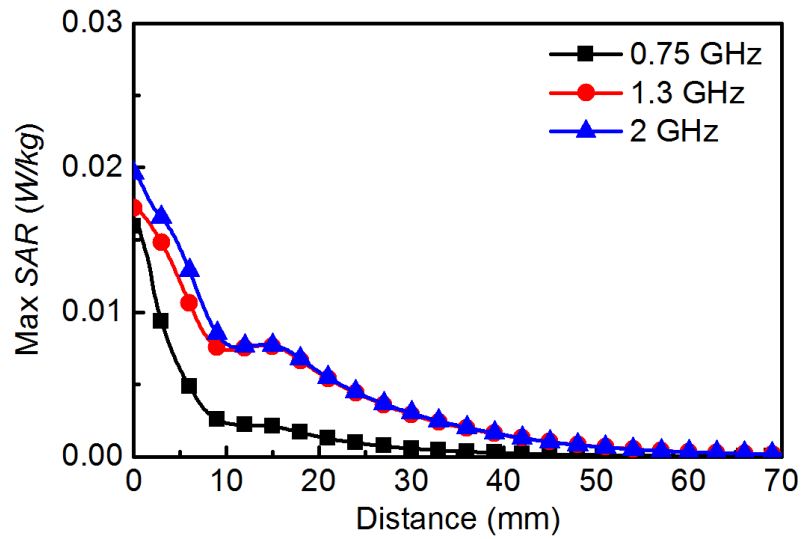
The SAR exposure for the proposed antenna in Hugo head phantom is depicted in Fig. 4.38. It is evident that only a very small aperture on the tissue phantom has a SAR reading, with an upper limit of 0.019 W/kg (10 g) on the surface of the skin at 2 GHz. The SAR penetration inside the inhomogeneous head can be seen in Fig. 4.38 (a) and (b), which is greater at higher frequencies. The SAR starts to fall gradually with the increment in distance from the antenna inside the head (Fig. 4.38 (c)), and at a distance of 70 mm the SAR approaches 0 W/kg. The limit of public radiation exposure governed by IEEE standards is 1.6 W/kg (10 g) [138]. Hence the proposed antenna is well below the exposure limit. Moreover, the antenna has the lowest SAR over a wideband compared to the relevant literature discussed here, considering the maximum SAR level on the surface of the skin. Although lower SAR levels for similar applications can be observed in the literature, those antennas operate a distance away from the considered phantom resulting in loss through the air and reduced signal penetration. Such SAR characteristic makes the proposed antenna suitable for operating near a human head providing an appropriate solution for medical diagnosis systems.



(a)



(b)



(c)

Fig. 4.38 Simulated SAR distribution of the inhomogeneous head phantom for the proposed antenna attached to the skin surface with an input power of 1 mW (a) front view, (b) side view (c) Simulated maximum SAR with distance from the skin surface.

### 4.3.13. Comparison with the Literature

A comparison of antennas made for similar medical applications is provided in Table 4.4 taking note of the electrical size, FBW, maximum SAR, FBR and considered phantom type with the proposed antenna achieving approximately equivalent or better performance across all metrics.

Table 4.4: Performance comparison between similar antennas.

Antenna	Electrical size	FBW	Max SAR (W/kg)	Phantom	FBR
[18]	$0.05 \lambda \times 0.05 \lambda$	120 %	0.06 (10g)	Homogeneous human head	3.5 dB at low frequency and 16.5 dB at high frequency
[16]	$0.22 \lambda \times 0.22 \lambda$	9.4 %	Not shown	Inhomogeneous human head	19 dB
[152]	$0.35 \lambda \times 0.26 \lambda$	171 %	Not shown	Not considered	0 dB
[64]	$0.35 \lambda \times 0.15 \lambda$	90.9 %	Not shown	Inhomogeneous human head	Not shown
[153]	$0.1 \lambda \times 0.09 \lambda$	22.22 %	4	Inhomogeneous muscle	Not shown
This work	$0.1 \lambda \times 0.1 \lambda$	104%	0.019 (10g)	Inhomogeneous human head	Minimum 20 dB throughout the operating band

#### 4.3.14. Conclusions

A wideband CPW fed compact antenna is proposed for medical diagnosis applications. The antenna utilizes an inhomogeneous human head tissue medium in contact with the antenna superstrate. Compact antenna dimensions of  $0.1 \times 0.1 \times 0.008 \lambda$  are achieved utilizing a combination of a T-shaped feed line and a meandered line extended from the edge of a circular slot, whilst the single conductor layer approach decreases the antenna construction complexity. A cavity is also then added to reduce radiation directed away from the head which can interfere with diagnosis systems. A fractional bandwidth of 104% is achieved with the centre frequency at 1.64 GHz. The maximum SAR on skin surface is below 0.037 W/kg (10g). The antenna is highly directive towards the inhomogeneous tissue when mounted on-head, exhibiting a FBR of more than 20 dB throughout its operating band. Parametric studies are carried out to determine suitability of the proposed antenna with varying human head characteristics in terms of tissue thickness and permittivity. Minimal dependency on both the thickness and permittivity characteristics of the different tissues was observed making the antenna suitable for the medical diagnosis of a wide variety of patients. Such characteristics also make the antenna potential candidate for the medical diagnosis of other parts of the human body.

#### 4.4. Chapter Summary

Two antennas for biomedical applications are shown in this chapter, a 3-D configuration and a uniplanar wideband CPW design. Specific focus has been given to make the antennas compact, generate a high FBR and minimise leakage of the radiation away from the head, and to keep the SAR as low as possible.

The 3-D antenna provides a FBR of 17 dB with SAR less than 0.0147 W/kg throughout the operating frequency range from 1 - 1.7 GHz with a compact dimension of  $0.23 \times 0.23 \times 0.04 \lambda$  with respect to the lowest operating frequency. A raster scanning setup is also evaluated where 8 antenna elements are placed adjacent to each other surrounding the Hugo head model, demonstrating that the 3-D antenna is suitable for biomedical imaging applications.

The CPW antenna achieves a FBR of 20 dB with SAR less than 0.037 W/kg from 0.788 - 2.5 GHz. Again, the antenna size is compact at  $0.1 \times 0.1 \times 0.008 \lambda$  with respect to the lowest operating frequency pre-addition of the cavity. A comparison of antennas made for similar

medical applications shows that the electrical size, FBW, maximum SAR, and FBR of the CPW antenna is equivalent or better across all metrics. Both of the antennas are deemed highly suitable for on-body biomedical applications by evaluating performance utilizing a representative human head phantom.



## Chapter 5 – Summary of the Research

### **5. Implantable Antennas for Biomedical Applications**

Whilst the previous sections of this thesis have focussed on increasing microwave power penetration into a human body, this chapter discusses a preliminary investigation into an implantable antenna for efficient reception of penetrated power for biomedical wireless power transfer applications in the HF (High Frequency) band. The challenges associated with implantable antenna design and the characterization of the proposed human body implantable antenna are described.

#### **5.1. Challenges for Implantable Antennas**

The challenges associated with designing an implantable antenna comprise of all the challenges of biomedical antennas that are discussed in the previous chapters, with the addition of the issues highlighted in the sections below.

##### **5.1.1. Biocompatibility**

The biocompatibility of the material must be determined before utilising it in the design of an implantable antenna for the human body [159-162]. If the material does not meet the criteria of biocompatibility, it can result in an antenna system that is hazardous for the human body.

Hence, biocompatible materials must be chosen when designing an antenna for implantable systems [162-165].

### **5.1.2. Polarization**

The polarization of the antenna is an important factor that contributes to the performance of an implantable antenna [17]. As an implantable antenna is unlikely to shift from its primary position inside the human body, the antenna needs to be polarization matched with the external antenna to achieve high efficiency [17, 161]. If the antenna is linearly polarized, it will be hard to achieve increased efficiency for implantable application such as wireless power transmission inside the human body [104, 161, 166-168]. However, if the implantable antenna is circularly polarized, then the transmission between the external antenna (or the transmitter antenna) and the implanted antenna (or the receiver antenna) will not be affected by the orientation of the two antennas.

### **5.1.3. Dielectric Loss**

The human body comprises of lossy dielectric materials, mostly comprising of water [27]. The lossy characteristics of water can make microwave propagation inefficient. Moreover, the inhomogeneous characteristics of the human body impede transmitted wave propagation inside the human body towards an implantable antenna [139]. Hence, dielectric loss is an important parameter that needs to be considered in the design of an implantable antenna for the microwave medical applications.

### **5.1.4. Flexible Materials**

Implantable antennas found in the literature are commonly made out of solid materials that are not flexible [104, 107, 160, 161, 166-168], which may limit their installation in a strict and predefined location inside the body. If a flexible biocompatible material is used to realise the implantable antenna, it can be highly beneficial for biomedical systems and allow greater diversity in application.

## **5.2. Rationale**

The ongoing improvement of medical techniques have enabled physicians to accelerate the healing of injuries to internal parts of the human body. Various techniques have been

employed, such as immunosuppressants [169], growth factors [170], etc. Recently, electrical stimulation methods are being suggested to accelerate the healing process of internal injuries [171-175]. Specifically, nerve injuries that occur in the human body are reported to have their healing aided by electrical stimulation [176, 177]. Physical electrodes are used to provide electrical stimulation to the nerve. These approaches require a wired connection to the internal electrodes from the outside of the human body. A wired connection can increase chances of infection and become toxic to the human body. A wireless connection is a solution to these problems which can be achieved by implementing a wireless device to perform the stimulation, incorporating an implantable antenna.

In this section, an inductively coupled antenna is presented for wireless power reception on implantable devices inside the human body, providing low SAR compared to the maximum exposure limit assigned by IEEE standards [138]. The resonant inductive coupling of the proposed antenna provides increased power transmission inside human body. The performance of the antenna is validated by utilizing both simulation and measurement data.

Wireless power transfer systems are one of the most interesting and challenging research areas that has been going on for more than a century [178]. Current research in the field of biomedicine aims to supply wireless power to implantable devices [179-188]. A multi-band antenna with the lowest operating frequency of 402 MHz is reported in [180] to achieve wireless power transmission for implants inside the human body. However, the measured reflection coefficient result shows discrepancy from the simulation result. Another implantable antenna is reported in [189] which shows very low coupling strength of -26 dB at only 2 cm distance. Moreover, the voltage/power received by the antenna is omitted from the results. For far-field operation at 915 MHz an implantable antenna is designed where the coupling between the external and internal antenna is below -30 dB for a distance of 5 mm [104]. A loop antenna is reported in [188] where the reflection coefficient of the antenna is shown to be below -15 dB at 5 MHz, however no transmission or coupling results were presented. Also, the antenna response is not evaluated considering a proper phantom simulation which can result in variance in antenna characteristics while operating inside a real human body.

### 5.3. Implantable Antenna Design

The proposed implantable antenna is shown in Fig. 5.1 (a). The antenna is designed on a Polydimethylsiloxane (PDMS) substrate, which is a biocompatible material. Thin PDMS substrates are also bendable, flexible, and reversely deformable. The antenna is patterned on the top surface of a 0.9 mm thick layer of PDMS utilizing gold as the conducting metal. Gold is among the best biocompatible metals that can be found in nature [190]. Table 5.1 provides the dimensions of the proposed antenna, which has an overall footprint of  $21 \times 18 \text{ mm}^2$ . The power transmission mechanism of the antenna system is based on resonant inductive coupling, where the power is transferred by the magnetic field of the inductive coil at the resonant frequency. As it is not possible to achieve self-resonance of the inductive coils at 5 MHz with such a small dimension, a capacitor is used to achieve resonance.

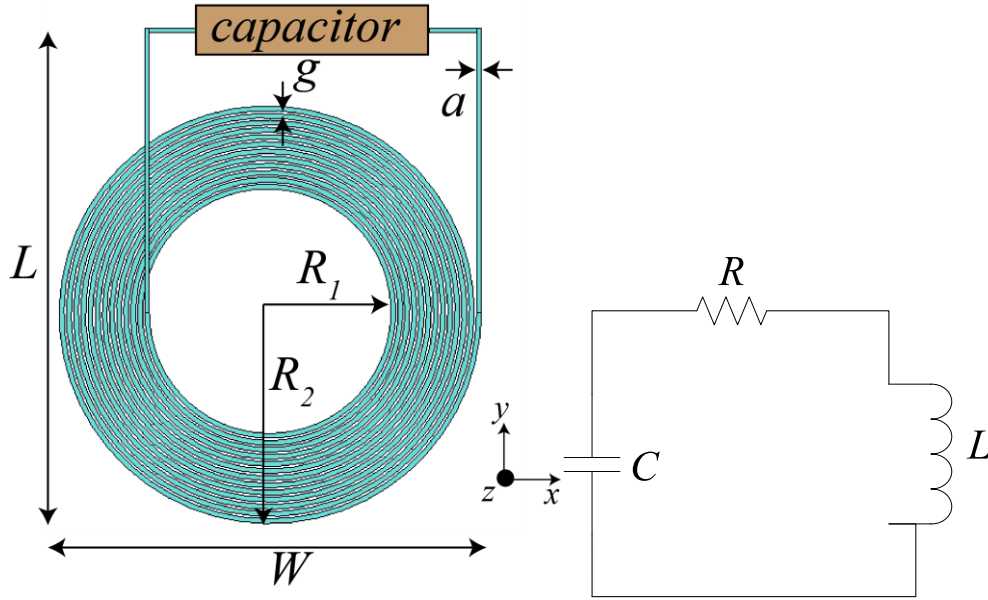


Fig. 5.1 (a) Proposed design of the implantable antenna on PDMS substrate (b) Circuit representation of the antenna.

Table 5.1: Dimensions of the proposed antenna

<i>Parameters</i>	<i>Values (cm)</i>
$L$	2.1
$W$	1.8
$a$	0.02
$g$	0.01
$R_1$	0.5
$R_2$	0.875
Number of turns, $N$	12.5 turns

The setup shown in Fig. 5.2 is adopted to simulate the transmission between external and internal antennas, where the internal antenna is implanted into the fat layer at “ $e$ ” distance from the surface of the skin. The external antenna is set at a distance of “ $d$ ” from the skin surface outside the body.

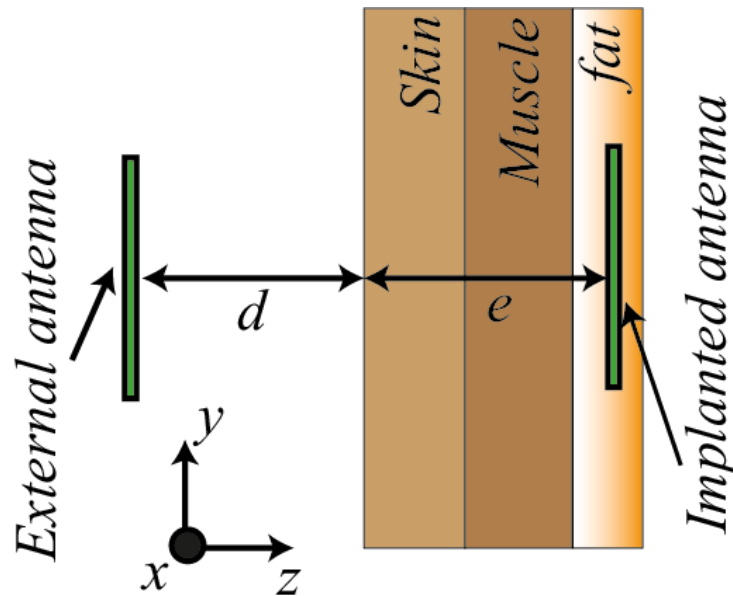
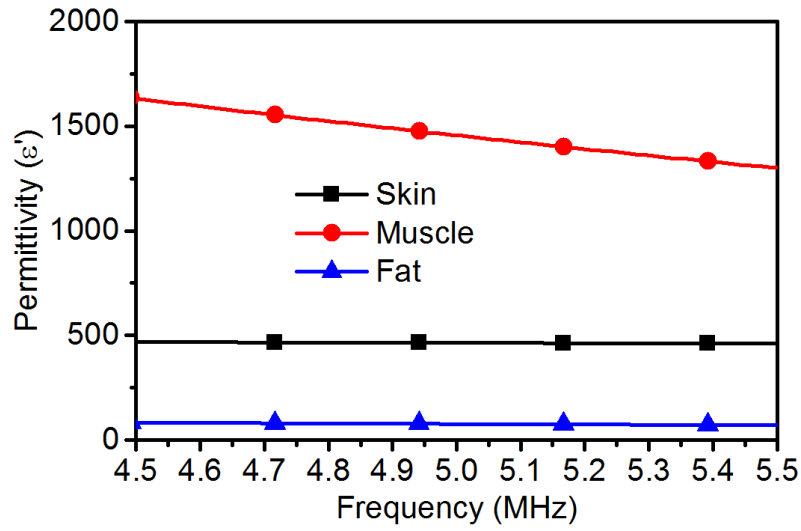


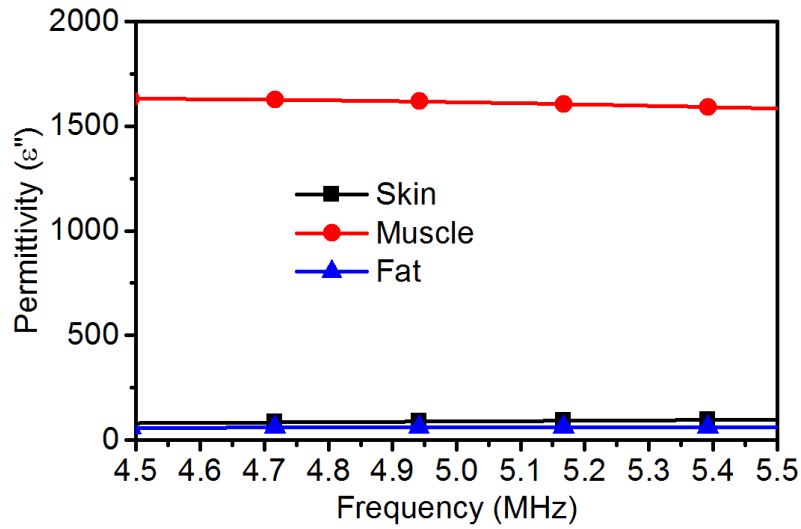
Fig. 5.2 Simulation setup of the implanted antenna and the external antenna.

The tissue material parameters used in this experiment are shown in Fig. 5.3 which are taken from CST simulation software [27-29]. In the simulation both the external and the implanted

antenna are of identical design as shown in Fig. 5.1 (a). Both antennas are operating at a resonant frequency of 5 MHz.



(a)



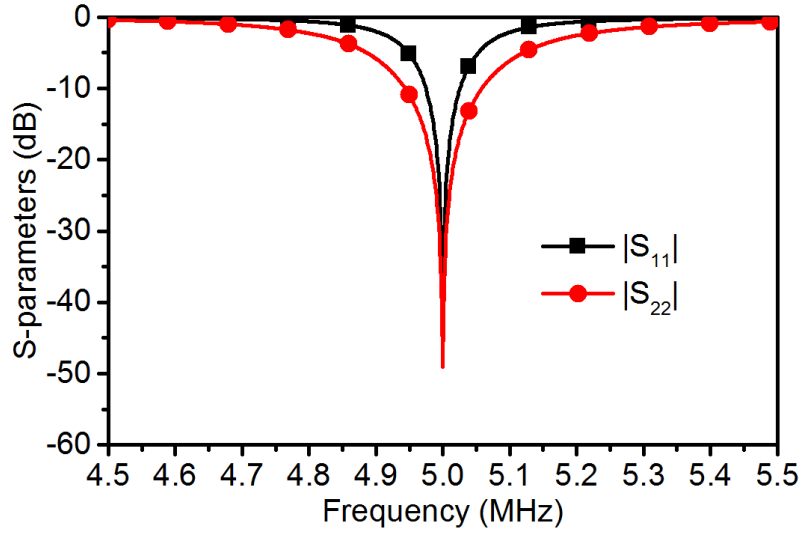
(b)

Fig. 5.3 Characteristics of the considered phantom material (a) real, (b) imaginary permittivity.

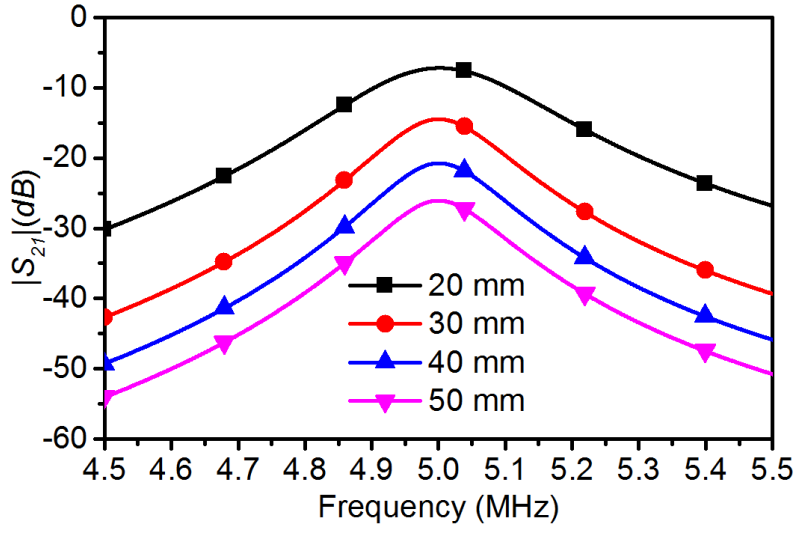
The circuit representation of the antenna is depicted in Fig. 5.1 (b) where ' $L$ ' represents the multi-turn coil, ' $C$ ' represents the capacitor to terminate the resonant coils inductance and ' $R$ ' represents the resistive losses. As the coil antennas are operating well below their self-

resonant frequency, a compensation capacitor ‘ $C$ ’ is required to achieve the resonance at the desired frequency [191]. For the inductance of  $3.1\ \mu H$  of the coil for the implantable antenna, a capacitor value of  $327\ pF$  is required to resonate at a frequency of 5 MHz. For the external antenna, and inductance of  $7.8\ \mu H$  means a capacitor value of  $130\ pF$  is needed to achieve resonant coupling.

The reflection coefficients of the antenna are depicted in Fig. 5.4 (a), indicating both the external and internal antennas are resonant at 5 MHz. The transmission response between the two antennas is recorded with variation in the distance “ $d$ ”, and the results are presented in Fig. 5.4 (b). The distance from the surface of the skin to the implanted antenna is kept constant at  $e = 1.5\ mm$ . Intuitively, the transmission between the antennas decreases with increased distance, from a value of -7 dB at 20 mm to -27 dB at 50 mm whereas a coupling strength of -26 dB in [189] and -39 dB in [104] is reported from previous research at 20 mm distance. The  $|S_{21}|$  response of the antenna can be improved by utilizing an enhanced external antenna operating at the desired frequency [192]. Fig. 5.5 shows a maximum SAR of 0.217 W/kg caused by the implantable antenna for an output power of 1 mW which is lower compared to the maximum SAR exposure limit of 1.6 W/kg assigned by IEEE standards [138].



(a)



(b)

Fig. 5.4 (a) Reflection coefficients ( $|S_{11}|$  and  $|S_{22}|$ ) of the two antennas, (b) Transmission coefficients ( $|S_{21}|$ ) for different distances, “d”.



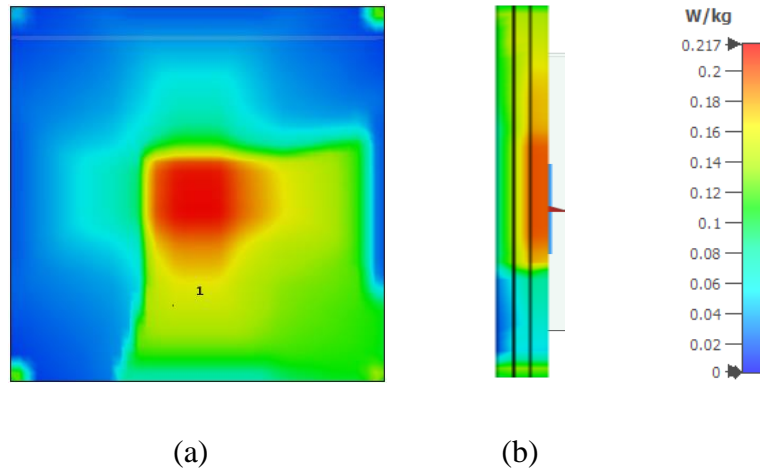


*Fig. 5.5 Simulated maximum SAR distribution with an input power of 1 mW inside the inhomogeneous phantom for 10g averaging (b) Simulated maximum SAR from the implant antenna surface till the surface of the skin.*

Even though both of the coil antennas are identical, due to the environmental change caused by the considered tissue layers the antennas require different capacitance values to be resonantly coupled. However, some of the implantable designs found in the literature omit this environmental change for internal and external antennas (e.g. [188]). To examine the influence of this, the same simulation setup shown in Fig. 5.2 is used without altering the capacitance of the implanted antenna to account the human tissue materials, and the response is depicted in Fig. 5.6. The resonance of the implanted antenna is no longer at 5 MHz and the transmission between the antennas is below -30 dB for a distance of 30 mm, compared to the -15 dB achieved previously.

To investigate the effect of polarization mismatch the external antenna is rotated 90° at xy-plane, and from the response depicted in Fig. 5.7 there is minimal difference in transmission performance  $|S_{21}|$  at a distance of 30 mm compared to the response shown in Fig. 5.4 (b). Although the antennas are linearly polarized at 5 MHz (as indicated in the axial ratio performance extracted from the far-field response of the antennas in Fig. 5.8), the orientation of the external antenna has minimal effect on the transmission performance as they are resonantly coupled in the near field of each other.

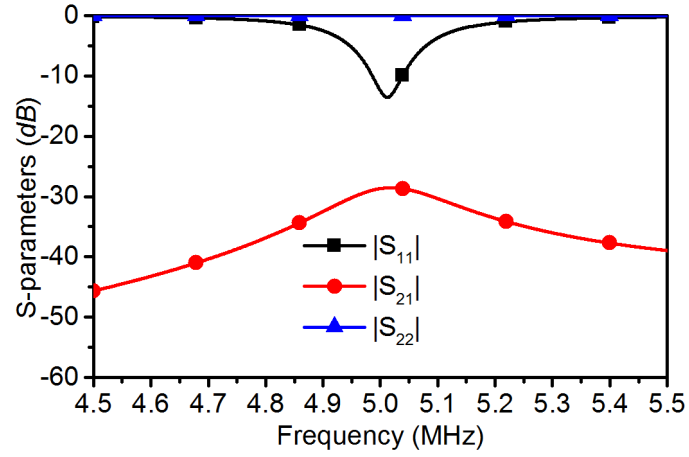


Fig. 5.6 S-parameters of the power transfer system without adjusting capacitance to account for the phantom materials, with the external antenna at port 1 and the implanted antenna at port 2.

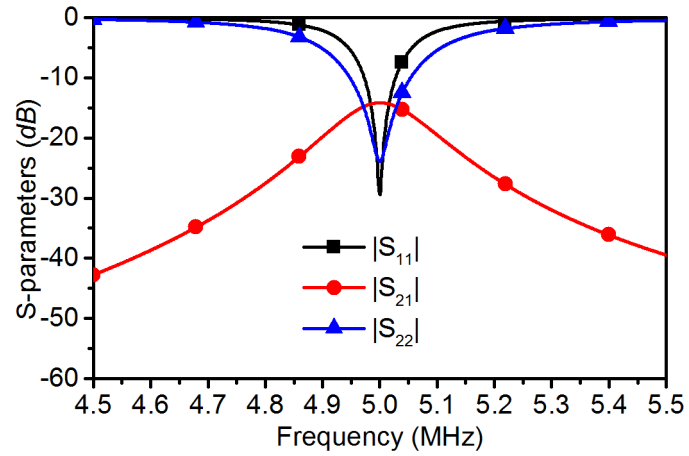
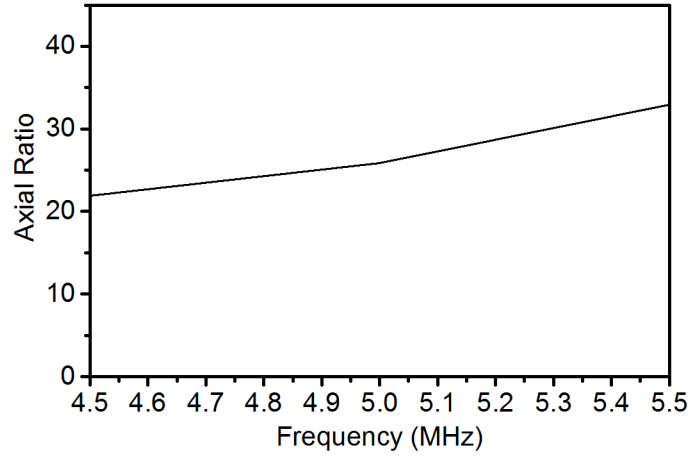


Fig. 5.7 S-parameter response of the internal and external antennas when the external antenna is rotated 90° in the xy-plane ( $d = 30$  mm).



*Fig. 5.8 Axial ratio of the antenna*

### **5.3.1. Fabrication and Measurement of the Implantable**

#### **Antenna**

As mentioned above, PDMS is used as the substrate for the antenna with gold as the conductor material. A stencil is used to mask the PDMS and gold is deposited using an E-Beam evaporator (LEB) at RMIT University creating the bottom layer as shown in Fig. 5.9. The top layer conductor is deposited on a new PDMS layer of 0.9 mm thickness using another stencil. A connection is made through the PDMS as indicated by the red line in Fig. 5.9. The resulting antenna is shown in the picture in Fig. 5.10.

The capacitor for the implantable antenna is realized using PDMS as the dielectric material between two conductor plates, as seen in Fig. 5.9. The following equation is used to determine the capacitance required:

$$A = \frac{C \cdot d}{\epsilon_r \epsilon_0} \quad (1)$$

where, ' $A$ ' is the area of the capacitor, ' $\epsilon_r$ ' is the relative permittivity of PDMS, ' $\epsilon_0$ ' is the vacuum permittivity, ' $C$ ' is the desired capacitance, and ' $d$ ' is the distance between the two parallel plates. With  $\epsilon_r = 2.8$  [58] and  $d = 0.87$  mm, the area for the capacitor is found to be  $A = 11.47$  mm to achieve a capacitance of  $327$  pF.

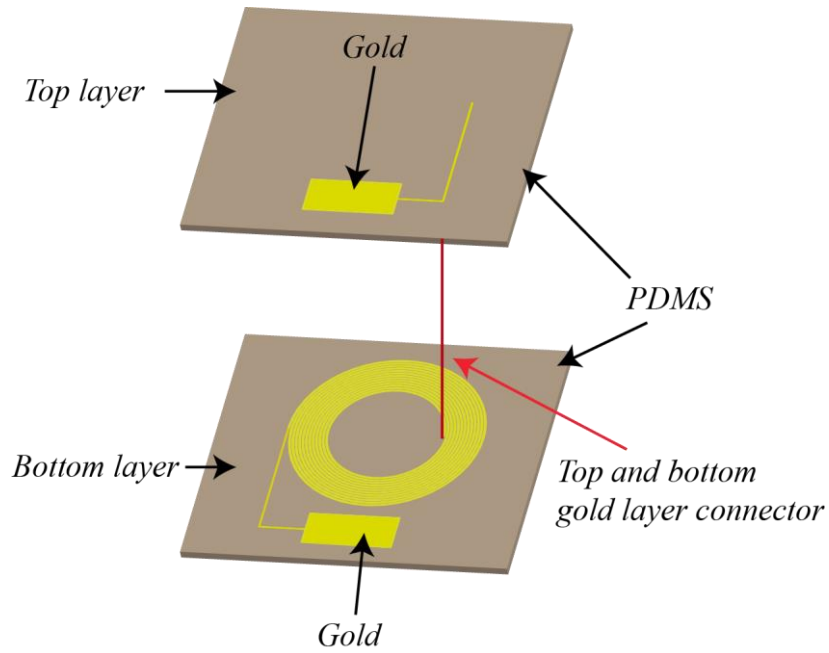


*Fig. 5.9 Fabrication steps of the antenna.*

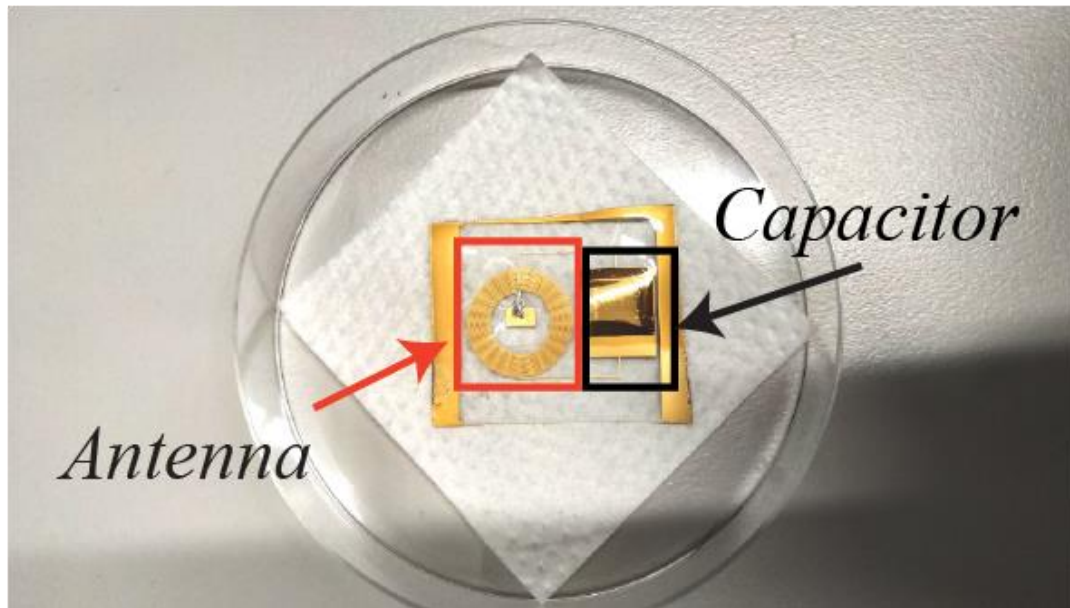
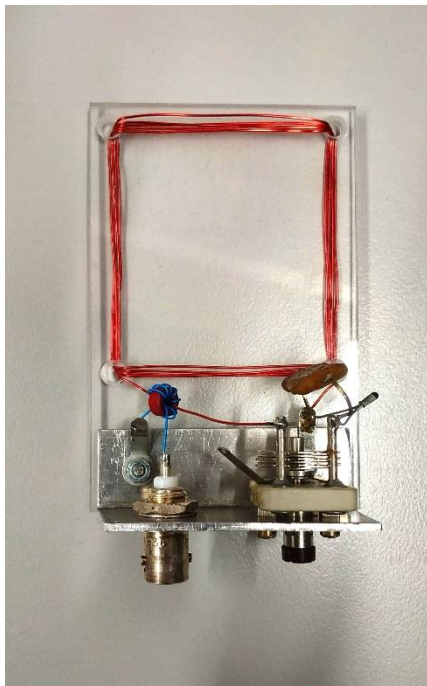


*Fig. 5.10 Fabricated antenna using gold on PDMS substrates*

Fig. 5.11 (a) depicts the external antenna used to measure the characteristics of the implantable antenna. Copper wire is employed to form the antenna coil and a variable capacitor is used to tune the resonant response in terms of frequency. The implantable antenna is immersed in a “complete media” solution composed of 10% Fetal Bovine Serum (FBS), 1% Penicillin-Streptomycin and Dulbecco's Modified Eagle's Medium (DMEM),

which is used as a cell culture media [193, 194] (Fig. 5.11 (b)). The reflection and transmission coefficient for the measurement setup (shown in Fig. 5.11 (b)) with the new external antenna design is simulated considering the “complete medium” having a permittivity of  $\epsilon_{cm} = 100$  at 5 MHz [195, 196]. The coupling strength between the external antenna and the implantable antenna is -5.43 dB for  $d = 30$  mm with the reflection coefficient below -33 dB for both antennas at 5 MHz, as shown in Fig. 5.12 (a). The measured reflection coefficient of the external antenna is depicted in Fig. 5.12 (b) when the implantable antenna is placed on top of the external antenna coil with a plastic petri dish of thickness of 1 mm separating the two. The resonant frequency is centered at 5 MHz. As the connection of the implantable antenna to a VNA is not possible in this case, a terminal connection was created by using a multimeter at both sides of the capacitor of the implantable antenna. The received voltage from the implantable antenna is shown in Fig. 5.12 (c), with its peak at 35 mV when the implantable antenna at 1 mm distance from the transmitter antenna with a 5 dBm input power. The received voltage slowly decays to 5 mV at 3 cm distance.



(a)



(b)

*Fig. 5.11 (a) External coil antenna, (b) implantable antenna inside a “complete media” solution,*

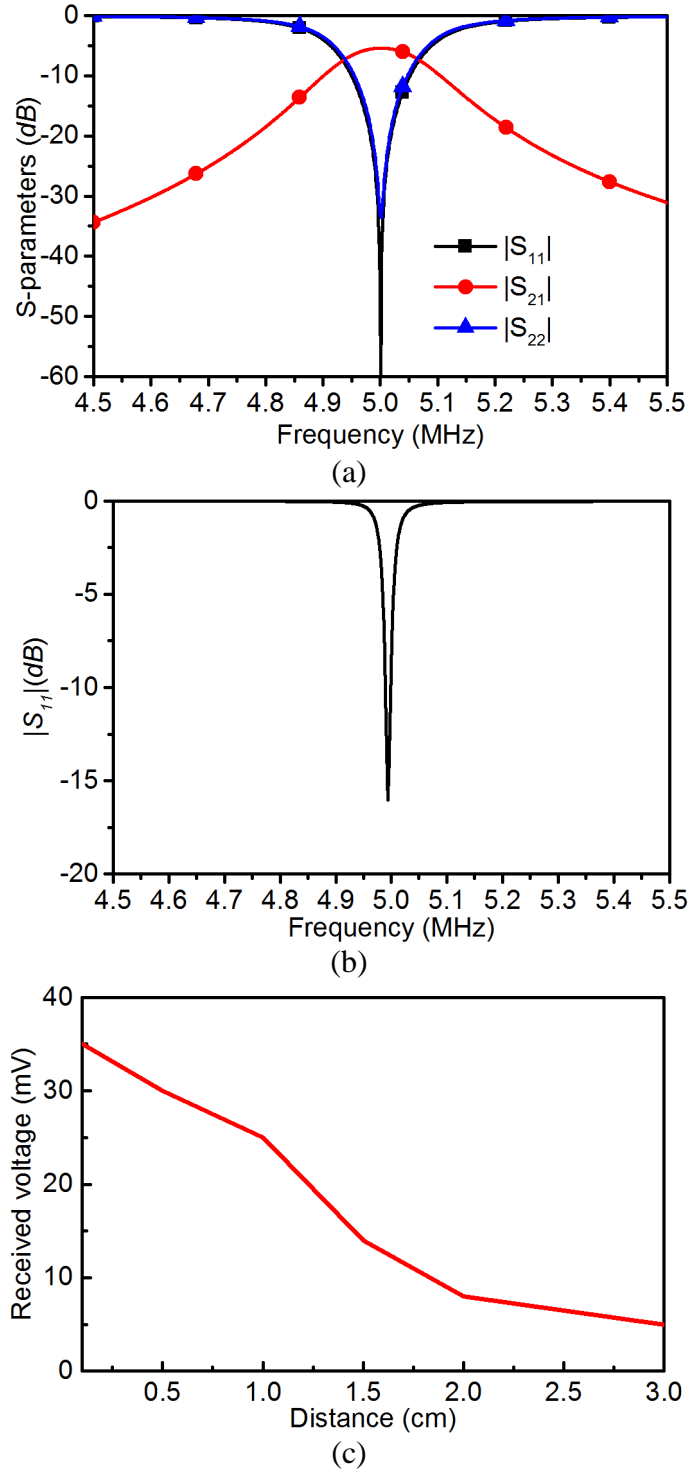


Fig. 5.12 (a) Simulated reflection and transmission coefficient mimicking the setup shown in Fig. 5.11 (b), (b) Measured reflection coefficient of the antenna for setup shown in Fig. 5.11 (b), (c) Voltage received by the implantable antenna at different distances.

The implantable antenna provides a coupling strength of -7 dB at 20 mm, whereas a coupling strength of -26 dB in [189] and -39 dB in [104] is achieved for the same distance. Although

a direct comparison of coupling strength is not possible as measurement environment differs from the referred works, the large coupling strength difference at the same distance is a tenable indicator of impressive performance.

To simulate operation inside the skin, muscle and fat layer, the antenna will be immersed in the “complete media” to determine its performance as a stimulator for tissue regeneration. The phantom fabricated in the previous section is made of skin, bone and brain equivalent material whereas, this antenna was designed for a tissue combination of skin, muscle and fat. As the fabricated phantom is not suitable for this scenario, the designed antenna is measured inside the “complete media” to mimic the real-life antenna operating environment. In this research, the implantable antenna’s application was to stimulate nerves for regeneration. The “complete media” used in the measurement setup of the antenna is commonly used as a cell culture media [193, 194] which is placed at the potential regeneration location. As this would be the environment in which the antenna will operate, the “complete media” was a logical choice for the application-oriented antenna performance measurement. As utilization of pork mince (or any other mince) as shown in the references will not serve the purpose of this research, an indirect comparison was provided to indicate the performance of the implantable antenna. A maximum SAR of 0.217 W/kg is achieved by the antenna, well under the IEEE Standards [138] for maximum SAR exposure of 1.6 W/kg. Moreover, the antenna is realised on a flexible biocompatible substrate (PDMS) providing medical application advantages over other non-flexible [104, 189] materials.

## **5.4. Conclusions**

An implantable antenna is designed using a flexible and biocompatible PDMS substrate. A capacitor is realized to achieve resonant coupling to an external antenna at 5 MHz by utilizing PDMS as the dielectric sandwiched between gold plates to achieve biocompatibility, rather than inserting conventional lumped components. As the antenna is dependent on resonant coupling, the antenna orientation has minimal effect to the transmission response.

With only 5 dBm of input power a maximum voltage of 35 mV is achieved, which can be improved further by enhancing the external antenna system. The implantable antenna was characterized inside a heterogeneous human phantom solution known as “complete media”.

The proof of concept antenna is biocompatible, bendable, and its HF operation range makes it a promising candidate for implantable biomedical applications.



# Chapter 6 – Summary of the Research

## 6. Summary of the Research

The previous chapters of this thesis present the research performed to acquire the theory, design, and realisation of antennas for biomedical applications which increase the microwave power penetration inside the human body. Overcoming the existing limitations of microwave antennas for biomedical applications was the primary objective of this research, making a microwave antenna-based system more suitable and efficient for medical diagnosis or treatment. In this chapter, a summary of this research work is drawn. Some future work to extend this research further is also proposed, which forecasts the potential for further enhancement of microwave biomedical diagnostics systems.

### 6.1. Conclusions of the Thesis

This research work aims at improving microwave power penetration inside human body along with designing antennas for biomedical applications. The specific requirements for antenna for these purposes includes high directivity towards the human body with large front to back ratio (FBR), low specific absorption rate (SAR), compactness, low-cost, and the ability to operate on-body. The accomplishment of all these requirements in this work makes multiple contributions to the field of microwave medicine.

It is shown in the introductory chapters that it is necessary to increase power penetration inside the human body for medical diagnosis applications. Designing antennas for biomedical applications is challenging with respect to simulations and measurements due to the complex and lossy material characteristics, and structure of the human body. To achieve increased power penetration into the human body for microwave medical diagnosis, the optimum frequency range is reported to be from 1 GHz to 2 GHz.

The existing state of the art microwave antenna designs for medical diagnostic systems shown in the literature generally consider an impractical simplified version of a human body model. Only a few of the reported antennas utilise a more realistic human body phantom. Most of these antennas also operate in air away from the body, which causes additional loss due to reflection at the air-skin transition. Moreover, proposed designs which utilize homogenous, lossless, or irregular shaped body phantoms cannot be relied upon to behave in a similar way when used in a practical application. A judiciously designing on-body antenna that considers the complex human body structure should achieve higher power penetration for biomedical diagnosis.

An investigation into homogeneous and frequency dependent inhomogeneous human body phantoms is carried out in Chapter 3. It is shown that the electromagnetic field/power penetration characteristics of an antenna exhibit a noticeable difference between using a homogeneous or frequency-dependent inhomogeneous phantom. The radiation characteristics are highly dependent on the homogeneity/inhomogeneity characteristics of the human head, with variations in permittivity and reflections at boundaries influencing performance.

The power penetration of a biomedical antenna is improved in this thesis by means of a multi-layer wave impedance formulation for an inhomogeneous human head phantom. A 1.33 dB power penetration increment at 2.45 GHz is achieved by utilizing a dielectric-loaded waveguide, theorised to match to the wave impedance of the layered head phantom. The dielectric waveguide is fed by a patch antenna removing the complexity of rectangular waveguide pin feeding into a brittle dielectric loading.

The effect of adding a superstrate layer to an antenna designed for on-body biomedical applications is explored. It is shown that adding a superstrate layer, increases the power

penetration inside an inhomogeneous human body phantom by  $\sim 8$  dB with a reduction of SAR of 0.0731 W/kg compared to an antenna without the superstrate. This is due to the superstrate isolating the antenna conductors from direct contact with the lossy human tissue.

A 3-D antenna and a CPW wideband antenna for microwave head imaging applications are proposed in Chapter 4, which are both shown to be compact with dimensions of  $0.23 \times 0.23 \times 0.04 \lambda$  and  $0.1 \times 0.1 \times 0.008 \lambda$  with respect to the lowest operating frequency. Both the antennas are designed considering the penetration of the microwave signals inside the human body, directivity, FBR, and SAR. The evolution of the developed antennas is described with the assistance of parametric studies. The effect of changes in human tissue characteristics on the antennas is also explored, which is pertinent as the thickness and dielectric composition of each tissue type varies from person to person. It is shown that the antennas are relatively resilient to changes in tissue characteristics and can operate efficiently in different environments. The near field power radiation patterns of the antennas inside a realistic human head model are evaluated, and a FBR of 17 dB and 20 dB is achieved for the 3-D antenna and CPW wideband antenna respectively. The maximum SAR for the 3-D and CPW antenna are recorded to be 0.0147 W/kg and 0.037 W/kg respectively, making them relatively harmless to the human body. A comparison with the current state of the art literature for similar antenna designs reveals that the antennas provide effective power penetration, lowest SAR, increased FBR and compact dimensions.

Chapter 5 conducts a foundation study into an implantable antenna design for biomedical applications. The antenna is developed in the biocompatible materials of PDMS for the substrate, and gold for the conductors. The coil based implantable antenna is inductively coupled to a transmitted antenna operating outside the body. In order to make the coupling resonant at 5 MHz, a capacitor is formed out of the gold conductors and PDMS substrate (rather than embedding lumped elements) and is connected to the terminals of the coil antenna. The fabricated antenna performance is validated in “complete medium” which is used as the cell culture media to resemble the operational environment of the antenna. A maximum received voltage 35 mV is measured from the implantable antenna by applying 5 dBm at the transmitter antenna.

## 6.2. Future Work

Although many of the challenges associated with creating antennas for biomedical applications have been addressed in this research, there is still future work that can be investigated for further development and improvement. A sample of potential future research is proposed in the following points.

- The novel antenna concepts discovered in this research can be utilized to realise an antenna design on a flexible material. Flexibility of substrate will enable the antennas to conform to the surface of the measuring body, improving the power penetration inside the human body further by minimising field leakage. However, not just any flexible material can be used, as biocompatibility would be a key requirement.
- Beamforming approaches could be implemented utilizing the proposed antennas in an array architecture. This would enable the antenna beam to cover different angles of measurement without moving the position of the antennas. This way, relocation of the antennas during treatment may not be required to get a clear and insightful diagnosis inside the measuring body, and could also decrease the post processing steps.
- The proposed antennas could be integrated a complete head imaging system, complete with signal processing stages to extract the image of the head from the generated signal reflections. This will further validate the applicability of the antennas for biomedical applications, and in the future potentially be ready for human trials.
- The implantable antenna conceived in this thesis can be explored further to make it more robust and miniaturise its operation for easier implantation.
- The implantable antenna could be interfaced with a scaffold structure to trigger direct nerve stimulation and/or bone healing.
- Implantable antenna structures could be designed to act as the power delivery method for surface acoustic wave triggered drug delivery.

# REFERENCES

- [1] E. N. Marieb and K. Hoehn, *Human anatomy & physiology*: Pearson Education, 2007.
- [2] A. M. Naidech, "Intracranial hemorrhage," *American journal of respiratory and critical care medicine*, vol. 184, pp. 998-1006, 2011.
- [3] F. Khan, I. J. Baguley, and I. D. Cameron, "4: Rehabilitation after traumatic brain injury," *Medical Journal of Australia*, vol. 178, pp. 290-295, 2003.
- [4] N. D. Zasler, D. I. Katz, and R. D. Zafonte, *Brain injury medicine: principles and practice*: Demos Medical Publishing, 2012.
- [5] K. Goniewicz, M. Goniewicz, W. Pawłowski, and P. Fiedor, "Road accident rates: strategies and programmes for improving road traffic safety," *European journal of trauma and emergency surgery*, vol. 42, pp. 433-438, 2016.
- [6] F. Bray, J. Ferlay, I. Soerjomataram, R. L. Siegel, L. A. Torre, and A. Jemal, "Global cancer statistics 2018: GLOBOCAN estimates of incidence and mortality worldwide for 36 cancers in 185 countries," *CA: a cancer journal for clinicians*, vol. 68, pp. 394-424, 2018.
- [7] D. A. Economics, "The economic impact of stroke in Australia," *Melbourne: National Stroke Foundation*, 2013.
- [8] J. Ferlay, I. Soerjomataram, M. Ervik, R. Dikshit, S. Eser, C. Mathers, et al., "Cancer incidence and mortality worldwide: IARC CancerBase," *GLOBOCAN 2012 v10*, vol. 11, 2012.
- [9] W. Zhang, S. Guo, W. S. P. Carvalho, Y. Jiang, and M. J. Serpe, "Portable point-of-care diagnostic devices," *Analytical Methods*, vol. 8, pp. 7847-7867, 2016.
- [10] L. Fass, "Imaging and cancer: a review," *Molecular oncology*, vol. 2, pp. 115-152, 2008.
- [11] A. Mobashsher and A. Abbosh, "Compact 3-D slot-loaded folded dipole antenna with unidirectional radiation and low impulse distortion for head imaging applications," *IEEE Transactions on Antennas and Propagation*, vol. 64, pp. 3245-3250, 2016.
- [12] A. Zamani, A. M. Abbosh, and A. T. Mobashsher, "Fast frequency-based multistatic microwave imaging algorithm with application to brain injury detection," *IEEE Transactions on Microwave Theory and Techniques*, vol. 64, pp. 653-662, 2016.
- [13] A. T. Mobashsher, A. M. Abbosh, and Y. Wang, "Microwave system to detect traumatic brain injuries using compact unidirectional antenna and wideband transceiver with verification on realistic head phantom," *IEEE Transactions on Microwave Theory and Techniques*, vol. 62, pp. 1826-1836, 2014.
- [14] P. Palmer and G. Hanson, "Diagnostic imaging in the community: a manual for clinics and small hospitals, 2011," *Pan-American Health Organization, World Health Organization*, 2011.
- [15] A. T. Mobashsher and A. Abbosh, "On-site Rapid Diagnosis of Intracranial Hematoma using Portable Multi-slice Microwave Imaging System," *Scientific reports*, vol. 6, 2016.
- [16] M. Rokunuzzaman, M. Samsuzzaman, and M. T. Islam, "Unidirectional Wideband 3-D Antenna for Human Head-Imaging Application," *IEEE Antennas and Wireless Propagation Letters*, vol. 16, pp. 169-172, 2017.
- [17] H. Bahrami, S. A. Mirbozorgi, R. Ameli, L. A. Rusch, and B. Gosselin, "Flexible, polarization-diverse UWB antennas for implantable neural recording systems," *IEEE transactions on biomedical circuits and systems*, vol. 10, pp. 38-48, 2016.
- [18] X. Li, M. Jalilvand, Y. L. Sit, and T. Zwick, "A compact double-layer on-body matched bowtie antenna for medical diagnosis," *IEEE Transactions on Antennas and Propagation*, vol. 62, pp. 1808-1816, 2014.
- [19] M. R. Casu, M. Vacca, J. A. Tobon, A. Pulimeno, I. Sarwar, R. Solimene, et al., "A COTS-Based Microwave Imaging System for Breast-Cancer Detection," *IEEE Transactions on Biomedical Circuits and Systems*, vol. 11, pp. 804-814, 2017.

- [20] S. A. Rezaeieh, A. Zamani, and A. Abbosh, "3-D wideband antenna for head-imaging system with performance verification in brain tumor detection," *IEEE Antennas and Wireless Propagation Letters*, vol. 14, pp. 910-914, 2015.
- [21] D. B. Rodrigues, P. F. Maccarini, S. Salah, T. R. Oliveira, P. J. Pereira, P. Limão-Vieira, *et al.*, "Design and optimization of an ultra wideband and compact microwave antenna for radiometric monitoring of brain temperature," *IEEE transactions on biomedical engineering*, vol. 61, pp. 2154-2160, 2014.
- [22] J. M. Beada'a, A. M. Abbosh, S. Mustafa, and D. Ireland, "Microwave system for head imaging," *IEEE Transactions on Instrumentation and Measurement*, vol. 63, pp. 117-123, 2014.
- [23] A. Drossos, V. Santomaa, and N. Kuster, "The dependence of electromagnetic energy absorption upon human head tissue composition in the frequency range of 300-3000 MHz," *IEEE transactions on microwave theory and techniques*, vol. 48, pp. 1988-1995, 2000.
- [24] A. S. Poon, S. O'Driscoll, and T. H. Meng, "Optimal frequency for wireless power transmission into dispersive tissue," *IEEE Transactions on Antennas and Propagation*, vol. 58, pp. 1739-1750, 2010.
- [25] R. Chandra, H. Zhou, I. Balasingham, and R. M. Narayanan, "On the opportunities and challenges in microwave medical sensing and imaging," *IEEE Transactions on Biomedical Engineering*, vol. 62, pp. 1667-1682, 2015.
- [26] A. T. Mobashsher, A. Mahmoud, and A. Abbosh, "Portable wideband microwave imaging system for intracranial hemorrhage detection using improved back-projection algorithm with model of effective head permittivity," *Scientific reports*, vol. 6, 2016.
- [27] C. Gabriel, S. Gabriel, and y. E. Corthout, "The dielectric properties of biological tissues: I. Literature survey," *Physics in medicine & biology*, vol. 41, p. 2231, 1996.
- [28] S. Gabriel, R. Lau, and C. Gabriel, "The dielectric properties of biological tissues: II. Measurements in the frequency range 10 Hz to 20 GHz," *Physics in medicine & biology*, vol. 41, p. 2251, 1996.
- [29] S. Gabriel, R. Lau, and C. Gabriel, "The dielectric properties of biological tissues: III. Parametric models for the dielectric spectrum of tissues," *Physics in Medicine & Biology*, vol. 41, p. 2271, 1996.
- [30] M. Persson, A. Fhager, H. D. Trefná, Y. Yu, T. McKelvey, G. Pegenius, *et al.*, "Microwave-Based Stroke Diagnosis Making Global Prehospital Thrombolytic Treatment Possible," *IEEE Transactions on Biomedical Engineering*, vol. 61, pp. 2806-2817, 2014.
- [31] M. Asili, P. Chen, A. Z. Hood, A. Purser, R. Hulsey, L. Johnson, *et al.*, "Flexible microwave antenna applicator for chemo-thermotherapy of the breast," *IEEE Antennas and Wireless Propagation Letters*, vol. 14, pp. 1778-1781, 2015.
- [32] A. T. Mobashsher and A. M. Abbosh, "Compact 3-D Slot-Loaded Folded Dipole Antenna With Unidirectional Radiation and Low Impulse Distortion for Head Imaging Applications," *IEEE Transactions on Antennas and Propagation*, vol. 64, pp. 3245-3250, 2016.
- [33] P. Wang, Z. Li, P. Liu, and Y. Pei, "Super resolution in depth for microwave imaging," *Applied Physics Letters*, vol. 115, p. 044101, 2019.
- [34] S. Mukherjee, L. Udpa, S. Udpa, E. J. Rothwell, and Y. Deng, "A Time Reversal-Based Microwave Imaging System for Detection of Breast Tumors," *IEEE Transactions on Microwave Theory and Techniques*, vol. 67, pp. 2062-2075, 2019.
- [35] N. Abdollahi, D. Kurrant, P. Mojabi, M. Omer, E. Fear, and J. LoVetri, "Incorporation of ultrasonic prior information for improving quantitative microwave imaging of breast," *IEEE Journal on Multiscale and Multiphysics Computational Techniques*, vol. 4, pp. 98-110, 2019.
- [36] V. L. Coli, P. Tournier, V. Dolean, I. E. Kanfoud, C. Pichot, C. Migliaccio, *et al.*, "Detection of Simulated Brain Strokes Using Microwave Tomography," *IEEE Journal of Electromagnetics, RF and Microwaves in Medicine and Biology*, vol. 3, pp. 254-260, 2019.

- [37] M. Asefi, A. Baran, and J. LoVetri, "An Experimental Phantom Study for Air-Based Quasi-Resonant Microwave Breast Imaging," *IEEE Transactions on Microwave Theory and Techniques*, vol. 67, pp. 3946-3954, 2019.
- [38] S. Y. Semenov and D. R. Corfield, "Microwave tomography for brain imaging: Feasibility assessment for stroke detection," *International Journal of Antennas and Propagation*, vol. 2008, 2008.
- [39] N. K. Nikolova, "Microwave imaging for breast cancer," *IEEE microwave magazine*, vol. 12, pp. 78-94, 2011.
- [40] M. Shokry and A. Allam, "UWB antenna for brain stroke and brain tumour detection," in *Microwave, Radar and Wireless Communications (MIKON), 2016 21st International Conference on*, 2016, pp. 1-3.
- [41] S. Symeonidis, W. G. Whittow, M. Zecca, and C. Panagamuwa, "Bone fracture monitoring using implanted antennas in the radius, tibia and phalange heterogeneous bone phantoms," *Biomedical Physics & Engineering Express*, vol. 4, p. 045006, 2018.
- [42] A. T. Mobashsher, K. Bialkowski, A. Abbosh, and S. Crozier, "Design and experimental evaluation of a non-invasive microwave head imaging system for intracranial haemorrhage detection," *PloS one*, vol. 11, p. e0152351, 2016.
- [43] R. K. Amineh, M. Ravan, A. Trehan, and N. K. Nikolova, "Near-field microwave imaging based on aperture raster scanning with TEM horn antennas," *IEEE Transactions on Antennas and Propagation*, vol. 59, pp. 928-940, 2011.
- [44] K. Moussakhani, J. J. McCombe, and N. K. Nikolova, "Sensitivity of microwave imaging systems employing scattering-parameter measurements," *IEEE Transactions on Microwave Theory and Techniques*, vol. 62, pp. 2447-2455, 2014.
- [45] R. K. Amineh, A. Trehan, and N. K. Nikolova, "TEM horn antenna for ultra-wide band microwave breast imaging," *Progress In Electromagnetics Research B*, vol. 13, pp. 59-74, 2009.
- [46] K. Y. Yazdandoost and R. Miura, "Miniaturized UWB implantable antenna for brain-machine-interface," in *Antennas and Propagation (EuCAP), 2015 9th European Conference on*, 2015, pp. 1-5.
- [47] M. Jamlos, M. Jamlos, and A. Ismail, "High performance novel UWB array antenna for brain tumor detection via scattering parameters in microwave imaging simulation system," in *Antennas and Propagation (EuCAP), 2015 9th European Conference on*, 2015, pp. 1-5.
- [48] M. A. I. Aziz, M. M. Rana, M. A. Islam, and R. Inum, "Effective Modeling of GBC Based Ultra-Wideband Patch Antenna for Brain Tumor Detection," in *2018 International Conference on Computer, Communication, Chemical, Material and Electronic Engineering (IC4ME2)*, 2018, pp. 1-4.
- [49] M. A. Jamlos, A. H. Ismail, M. F. Jamlos, and A. Narbudowicz, "Hybrid graphene-copper UWB array sensor for brain tumor detection via scattering parameters in microwave detection system," *Applied Physics A*, vol. 123, p. 112, 2017.
- [50] A. T. Mobashsher and A. Abbosh, "Development of compact directional antenna utilising plane of symmetry for wideband brain stroke detection systems," *Electronics Letters*, vol. 50, pp. 850-851, 2014.
- [51] A. T. Mobashsher, K. S. Bialkowski, and A. M. Abbosh, "Design of Compact Cross-Fed Three-Dimensional Slot-Loaded Antenna and Its Application in Wideband Head Imaging System," *IEEE Antennas and Wireless Propagation Letters*, vol. 15, pp. 1856-1860, 2016.
- [52] A. T. Mobashsher and A. Abbosh, "Three-dimensional human head phantom with realistic electrical properties and anatomy," *IEEE Antennas and Wireless Propagation Letters*, vol. 13, pp. 1401-1404, 2014.
- [53] A. T. Mobashsher, A. M. Abbosh, and Y. Wang, "Microwave system to detect traumatic brain injuries using compact unidirectional antenna and wideband transceiver with verification on

- realistic head phantom," *Microwave Theory and Techniques, IEEE Transactions on*, vol. 62, pp. 1826-1836, 2014.
- [54] A. T. Mobashsher and A. Abbosh, "Slot-loaded folded dipole antenna with wideband and unidirectional performance for L-band applications," *Antennas and Wireless Propagation Letters, IEEE*, vol. 13, pp. 798-801, 2014.
  - [55] M. T. Islam, A. T. Mobashsher, and N. Misran, "A novel feeding technique for a dual band microstrip patch antenna," *IEICE transactions on communications*, vol. 93, pp. 2455-2457, 2010.
  - [56] M. T. Islam, A. T. Mobashsher, and N. Misran, "Coplanar waveguide fed printed antenna with compact size for broadband wireless applications," *Journal of Infrared, Millimeter, and Terahertz Waves*, vol. 31, pp. 1427-1437, 2010.
  - [57] A. T. Mobashsher, M. T. Islam, and N. Misran, "Wideband compact antenna with partially radiating coplanar ground plane," *Applied Computational Electromagnetics Society Journal*, vol. 26, pp. 73-81, 2011.
  - [58] A. S. Alqadami, K. S. Bialkowski, A. T. Mobashsher, and A. M. Abbosh, "Wearable Electromagnetic Head Imaging System Using Flexible Wideband Antenna Array Based on Polymer Technology for Brain Stroke Diagnosis," *IEEE transactions on biomedical circuits and systems*, vol. 13, pp. 124-134, 2018.
  - [59] J.-N. Hwang and F.-C. Chen, "Reduction of the peak SAR in the human head with metamaterials," *IEEE Transactions on Antennas and Propagation*, vol. 54, pp. 3763-3770, 2006.
  - [60] (2019). *Near Field and Far Field Regions of an Antenna*. Available: <https://www.everythingrf.com/community/what-are-near-field-and-far-field-regions-of-an-antenna>
  - [61] A. T. Mobashsher and A. M. Abbosh, "Performance of Directional and Omnidirectional Antennas in Wideband Head Imaging," *IEEE Antennas and Wireless Propagation Letters*, vol. 15, pp. 1618-1621, 2016.
  - [62] G. Mansutti, A. T. Mobashsher, and A. M. Abbosh, "Millimeter-wave substrate integrated waveguide probe for near-field skin cancer detection," in *2018 Australian Microwave Symposium (AMS)*, 2018, pp. 81-82.
  - [63] A. S. Alqadami, K. S. Bialkowski, A. T. Mobashsher, and A. M. Abbosh, "Wearable Electromagnetic Head Imaging System Using Flexible Wideband Antenna Array Based on Polymer Technology for Brain Stroke Diagnosis," *IEEE transactions on biomedical circuits and systems*, vol. 13, p. 10, 2018.
  - [64] M. S. R. Bashri, T. Arslan, W. Zhou, and N. Haridas, "Wearable device for microwave head imaging," in *Microwave Conference (EuMC), 2016 46th European*, 2016, pp. 671-674.
  - [65] M. S. R. Bashri, T. Arslan, and W. Zhou, "Flexible antenna array for wearable head imaging system," in *Antennas and Propagation (EUCAP), 2017 11th European Conference on*, 2017, pp. 172-176.
  - [66] L. Guo and A. Abbosh, "Microwave head imaging using multi-frequency tomography," in *Electromagnetics in Advanced Applications (ICEAA), 2016 International Conference on*, 2016, pp. 666-669.
  - [67] A. Pirhadi, H. Bahrami, and J. Nasri, "Wideband high directive aperture coupled microstrip antenna design by using a FSS superstrate layer," *IEEE transactions on antennas and propagation*, vol. 60, pp. 2101-2106, 2012.
  - [68] H. Bahrami, S. A. Mirbozorgi, L. A. Rusch, and B. Gosselin, "Biological channel modeling and implantable UWB antenna design for neural recording systems," *IEEE Transactions on Biomedical Engineering*, vol. 62, pp. 88-98, 2015.



- [69] A. T. Mobashsher and A. Abbosh, "Utilizing symmetry of planar ultra-wideband antennas for size reduction and enhanced performance," *IEEE Antennas and Propagation Magazine*, vol. 57, pp. 153-166, 2015.
- [70] A. Santorelli, E. Porter, E. Kang, T. Piske, M. Popović, and J. D. Schwartz, "A time-domain microwave system for breast cancer detection using a flexible circuit board," *IEEE Transactions on Instrumentation and Measurement*, vol. 64, pp. 2986-2994, 2015.
- [71] F. S. Di Clemente, M. Helbig, J. Sachs, U. Schwarz, R. Stephan, and M. Hein, "Permittivity-matched compact ceramic ultra-wideband horn antennas for biomedical diagnostics," in *Proceedings of the 5th European Conference on Antennas and Propagation (EUCAP)*, 2011, pp. 2386-2390.
- [72] F. S. Di Clemente, R. Stephan, U. Schwarz, and M. Hein, "Miniature body-matched double-ridged horn antennas for biomedical UWB imaging," in *2012 IEEE-APS Topical Conference on Antennas and Propagation in Wireless Communications (APWC)*, 2012, pp. 574-577.
- [73] J. Yang, F. Kong, and K. Li, "Broad tunable nanoantenna based on graphene log-periodic toothed structure," *Plasmonics*, vol. 11, pp. 981-986, 2016.
- [74] M. Abbak, M. Cayoren, and I. Akduman, "Microwave breast phantom measurements with a cavity-backed Vivaldi antenna," *IET Microwaves, Antennas & Propagation*, vol. 8, pp. 1127-1133, 2014.
- [75] A. Abbosh, "Ultra-wideband quasi-Yagi antenna using dual-resonant driver and integrated balun of stepped impedance coupled structure," *IEEE Transactions on Antennas and Propagation*, vol. 61, pp. 3885-3888, 2013.
- [76] A. T. Mobashsher and A. Abbosh, "Performance of directional and omnidirectional antennas in wideband head imaging," *IEEE Antennas and Wireless Propagation Letters*, vol. 15, pp. 1618-1621, 2016.
- [77] X. Li, E. J. Bond, B. D. Van Veen, and S. C. Hagness, "An overview of ultra-wideband microwave imaging via space-time beamforming for early-stage breast-cancer detection," *IEEE Antennas and Propagation Magazine*, vol. 47, pp. 19-34, 2005.
- [78] M. Klemm, I. J. Craddock, J. A. Leendertz, A. Preece, and R. Benjamin, "Radar-based breast cancer detection using a hemispherical antenna array—experimental results," *IEEE transactions on antennas and propagation*, vol. 57, pp. 1692-1704, 2009.
- [79] E. Porter, H. Bahrami, A. Santorelli, B. Gosselin, L. A. Rusch, and M. Popović, "A Wearable Microwave Antenna Array for Time-Domain Breast Tumor Screening," *IEEE transactions on medical imaging*, vol. 35, pp. 1501-1509, 2016.
- [80] E. Porter, E. Kirshin, A. Santorelli, M. Coates, and M. Popović, "Time-domain multistatic radar system for microwave breast screening," *IEEE Antennas and Wireless Propagation Letters*, vol. 12, pp. 229-232, 2013.
- [81] M. A. Al-Joumayly, S. M. Aguilar, N. Behdad, and S. C. Hagness, "Dual-band miniaturized patch antennas for microwave breast imaging," *IEEE antennas and wireless propagation letters*, vol. 9, pp. 268-271, 2010.
- [82] H. Bahramiabarghouei, E. Porter, A. Santorelli, B. Gosselin, M. Popovic, and L. A. Rusch, "Flexible 16 Antenna Array for Microwave Breast Cancer Detection," *Biomedical Engineering, IEEE Transactions on*, vol. 62, pp. 2516-2525, 2015.
- [83] M. Jalilvand, X. Li, L. Zwirello, and T. Zwick, "Ultra wideband compact near-field imaging system for breast cancer detection," *IET Microwaves, Antennas & Propagation*, vol. 9, pp. 1009-1014, 2015.
- [84] C. Zheng, X. Jiang, B. Kang, X. Li, and Z. Geng, "Design of an on-body matched wide-slot UWB antenna for brain activities detection," in *2017 Sixth Asia-Pacific Conference on Antennas and Propagation (APCAP)*, 2017, pp. 1-3.

- [85] P. M. Meaney, D. Goodwin, A. H. Golnabi, T. Zhou, M. Pallone, S. D. Geimer, *et al.*, "Clinical microwave tomographic imaging of the calcaneus: A first-in-human case study of two subjects," *IEEE transactions on biomedical engineering*, vol. 59, pp. 3304-3313, 2012.
- [86] S. Symeonidis, W. G. Whittow, and C. Panagamuwa, "Characterisation of an antenna system implanted into a limb phantom for monitoring of bone fracture healing," in *2016 Loughborough Antennas & Propagation Conference (LAPC)*, 2016, pp. 1-4.
- [87] M. D. Perez, S. R. M. Shah, J. Velandar, M. Raaben, N. B. Asan, T. Blokhuis, *et al.*, "Microwave sensors for new approach in monitoring hip fracture healing," in *2017 11th European Conference on Antennas and Propagation (EuCAP)*, 2017, pp. 1838-1842.
- [88] X. Li, L. Zwirello, M. Jalilvand, and T. Zwick, "Design and near-field characterization of a planar on-body UWB slot-antenna for stroke detection," in *Antenna Technology (iWAT), 2012 IEEE International Workshop on*, 2012, pp. 201-204.
- [89] A. Kiourti, J. R. Costa, C. A. Fernandes, and K. S. Nikita, "A broadband implantable and a dual-band on-body repeater antenna: Design and transmission performance," *IEEE transactions on antennas and propagation*, vol. 62, pp. 2899-2908, 2014.
- [90] S. Dumanli, "On-body antenna with reconfigurable radiation pattern," in *RF and Wireless Technologies for Biomedical and Healthcare Applications (IMWS-Bio), 2014 IEEE MTT-S International Microwave Workshop Series on*, 2014, pp. 1-3.
- [91] A. Ruaro, J. Thaysen, and K. B. Jakobsen, "Cavity-backed on-body antenna for customised hearing instrument applications," *Electronics Letters*, vol. 51, pp. 1235-1236, 2015.
- [92] T. Tuovinen, M. Berg, and E. Salonen, "Low-profile on-body communication antenna configuration with embedded electronics inside," in *Antennas & Propagation Conference (LAPC), 2015 Loughborough*, 2015, pp. 1-4.
- [93] K. Kwon, J. Tak, and J. Choi, "Design of a Dual-Band On-Body Antenna for a Wireless Medical Repeater System," *The Journal of Korean Institute of Electromagnetic Engineering and Science*, vol. 24, pp. 239-246, 2013.
- [94] L.-J. Xu, Z. Duan, Y.-M. Tang, and M. Zhang, "A Dual-Band On-Body Repeater Antenna for Body Sensor Network," *IEEE Antennas and Wireless Propagation Letters*, vol. 15, pp. 1649-1652, 2016.
- [95] K. N. Bocan, M. H. Mickle, and E. Sejdić, "Simulating, modeling, and sensing variable tissues for wireless implantable medical devices," *IEEE Transactions on Microwave Theory and Techniques*, vol. 66, pp. 3547-3556, 2018.
- [96] A. Cai, T. See, and Z. N. Chen, "Study of human head effects on UWB antenna," in *Antenna Technology: Small Antennas and Novel Metamaterials, 2005. IWAT 2005. IEEE International Workshop on*, 2005, pp. 310-313.
- [97] Z. N. Chen, A. Cai, T. S. See, X. Qing, and M. Y. W. Chia, "Small planar UWB antennas in proximity of the human head," *IEEE Transactions on Microwave Theory and Techniques*, vol. 54, pp. 1846-1857, 2006.
- [98] K. Y. Yazdandoost, "UWB antenna for body implanted applications," in *Microwave Conference (EuMC), 2012 42nd European*, 2012, pp. 932-935.
- [99] K. Y. Yazdandoost and R. Miura, "SAR studies for UWB implanted antenna for Brain-Machine-Interface application," in *Antennas and Propagation (EuCAP), 2016 10th European Conference on*, 2016, pp. 1-4.
- [100] K. M. Thotahewa, J.-M. Redouté, and M. R. Yuce, "SAR, SA, and temperature variation in the human head caused by IR-UWB implants operating at 4 GHz," *IEEE transactions on microwave theory and techniques*, vol. 61, pp. 2161-2169, 2013.
- [101] H. Bahrami, B. Gosselin, and L. A. Rusch, "Design of a miniaturized UWB antenna optimized for implantable neural recording systems," in *New Circuits and Systems Conference (NEWCAS), 2012 IEEE 10th International*, 2012, pp. 309-312.

- [102] S. A. Rezaeieh, A. Zamani, K. Bialkowski, and A. Abbosh, "Foam embedded wideband antenna array for early congestive heart failure detection with tests using artificial phantom with animal organs," *IEEE Transactions on Antennas and Propagation*, vol. 63, pp. 5138-5143, 2015.
- [103] Z.-J. Yang, S.-Q. Xiao, L. Zhu, B.-Z. Wang, and H.-L. Tu, "A Circularly Polarized Implantable Antenna for 2.4-GHz ISM Band Biomedical Applications," *IEEE Antennas Wirel. Propag. Lett.*, vol. 16, pp. 2554-2557, 2017.
- [104] C. Liu, Y. Zhang, and X. Liu, "Circularly polarized implantable antenna for 915 MHz ISM-band far-field wireless power transmission," *IEEE Antennas and Wireless Propagation Letters*, vol. 17, pp. 373-376, 2018.
- [105] S. Ma, L. Sydänheimo, L. Ukkonen, and T. Björninen, "Split-Ring Resonator Antenna System With Cortical Implant and Head-Worn Parts for Effective Far-Field Implant Communications," *IEEE Antennas and Wireless Propagation Letters*, vol. 17, pp. 710-713, 2018.
- [106] Y. Zhang, C. Liu, X. Liu, K. Zhang, and X. M. Yang, "A Wideband Circularly Polarized Implantable Antenna for 915-MHz ISM-band Biotelemetry Devices," *IEEE Antennas and Wireless Propagation Letters*, vol. 17, pp. 1473-1477, 2018.
- [107] S. A. A. Shah and H. Yoo, "Scalp-implantable antenna systems for intracranial pressure monitoring," *IEEE Transactions on Antennas and Propagation*, vol. 66, pp. 2170-2173, 2018.
- [108] E. Sieni, P. Sgarbossa, F. Dughiero, M. Forzan, P. Di, M. E. M. Barba, *et al.*, "Effect of tissue inhomogeneity on electric field intensity for electrochemotherapy treatment," *Proc. 2018 Electrostatics Joint Conference*, p. 10, 2018.
- [109] H. Gray, *Anatomy of the human body* vol. 8: Lea & Febiger, 1878.
- [110] (2019). *Computer Simulation Technology (CST)*. Available: <https://www.cst.com/>
- [111] (2019). *High Frequency Structural Simulator (HFSS)*. Available: <https://www.ansys.com/products/electronics/ansys-hfss>
- [112] (2019). *FEKKO*. Available: <https://altairhyperworks.com/product/FEKO>
- [113] (2019). *IE3D*. Available: <https://www.rfglobalnet.com/doc/full-wave-3-d-em-simulator-for-both-planar-an-0001>
- [114] (2019). *2 - Aqua Bodies*. Available: [https://www.usgs.gov/special-topic/water-science-school/science/water-you-water-and-human-body?qt-science\\_center\\_objects=0#qt-science\\_center\\_objects](https://www.usgs.gov/special-topic/water-science-school/science/water-you-water-and-human-body?qt-science_center_objects=0#qt-science_center_objects)
- [115] F. C. Commission. (2019, 8/1/2019). *Body Tissue Dielectric Parameters*. Available: <https://www.fcc.gov/general/body-tissue-dielectric-parameters>
- [116] I. S. Karanasiou, N. K. Uzunoglu, and A. Garetsos, "Electromagnetic analysis of a non-invasive 3D passive microwave imaging system-Abstract," *Journal of electromagnetic waves and applications*, vol. 18, pp. 379-380, 2004.
- [117] M. Akter, T. Hirai, Y. Hiai, M. Kitajima, M. Komi, R. Murakami, *et al.*, "Detection of hemorrhagic hypointense foci in the brain on susceptibility-weighted imaging: clinical and phantom studies," *Academic radiology*, vol. 14, pp. 1011-1019, 2007.
- [118] M. Sperandio, M. Guermandi, and R. Guerrieri, "A four-shell diffusion phantom of the head for electrical impedance tomography," *IEEE Transactions on Biomedical Engineering*, vol. 59, pp. 383-389, 2011.
- [119] G. Hartsgrrove, A. Kraszewski, and A. Surowiec, "Simulated biological materials for electromagnetic radiation absorption studies," *Bioelectromagnetics: Journal of the Bioelectromagnetics Society, The Society for Physical Regulation in Biology and Medicine, The European Bioelectromagnetics Association*, vol. 8, pp. 29-36, 1987.
- [120] A. Mashal, F. Gao, and S. C. Hagness, "Heterogeneous anthropomorphic phantoms with realistic dielectric properties for microwave breast imaging experiments," *Microwave and optical technology letters*, vol. 53, pp. 1896-1902, 2011.

- [121] N. Joachimowicz, C. Conessa, T. Henriksson, and B. Duchêne, "Breast phantoms for microwave imaging," *IEEE Antennas and Wireless Propagation Letters*, vol. 13, pp. 1333-1336, 2014.
- [122] T. Kobayashi, T. Nojima, K. Yamada, and S. Uebayashi, "Dry phantom composed of ceramics and its application to SAR estimation," *IEEE transactions on Microwave Theory and Techniques*, vol. 41, pp. 136-140, 1993.
- [123] H. Tamura, Y. Ishikawa, T. Kobayashi, and T. Nojima, "A dry phantom material composed of ceramic and graphite powder," *IEEE Transactions on Electromagnetic Compatibility*, vol. 39, pp. 132-137, 1997.
- [124] Y. Nikawa, M. Chino, and K. Kikuchi, "Soft and dry phantom modeling material using silicone rubber with carbon fiber," *IEEE transactions on microwave theory and techniques*, vol. 44, pp. 1949-1953, 1996.
- [125] M. Lazebnik, E. L. Madsen, G. R. Frank, and S. C. Hagness, "Tissue-mimicking phantom materials for narrowband and ultrawideband microwave applications," *Physics in medicine and biology*, vol. 50, p. 4245, 2005.
- [126] T. Baum, L. Thompson, and K. Ghorbani, "Complex dielectric measurements of forest fire ash at X-band frequencies," *IEEE Geoscience and Remote Sensing Letters*, vol. 8, pp. 859-863, 2011.
- [127] R. Salama, S. Kharkovsky, R. Liyanapathirana, and U. Gunawardana, "Wireless power transmission in human tissue for nerve stimulation," *IET Microwaves, Antennas & Propagation*, vol. 10, pp. 670-675, 2016.
- [128] K. P. Whittall, A. L. Mackay, D. A. Graeb, R. A. Nugent, D. K. Li, and D. W. Paty, "In vivo measurement of T2 distributions and water contents in normal human brain," *Magnetic resonance in medicine*, vol. 37, pp. 34-43, 1997.
- [129] P. Hasgall, E. Neufeld, M. Gosselin, A. Klingenböck, and N. Kuster, "IT'IS Database for thermal and electromagnetic parameters of biological tissues," *Version 2.6*, 2015.
- [130] A. Mobashsher and A. Abbosh, "CPW-fed low-profile directional antenna operating in low microwave band for wideband medical diagnostic systems," *Electronics Letters*, vol. 50, pp. 246-248, 2014.
- [131] C. M. Studio, "3D EM Simulation software," *Computer Simulation Technology*, 2017.
- [132] U. Schwarz, F. Thiel, F. Seifert, R. Stephan, and M. Hein, "Ultrawideband antennas for magnetic resonance imaging navigator techniques," *IEEE Transactions on Antennas and Propagation*, vol. 58, pp. 2107-2112, 2010.
- [133] Y. Liu, Y. Chen, H. Lin, and F. H. Juwono, "A novel differentially fed compact dual-band implantable antenna for biotelemetry applications," *IEEE Antennas and Wireless Propagation Letters*, vol. 15, pp. 1791-1794, 2016.
- [134] S. Bakogianni and S. Koulouridis, "An Implantable Planar Dipole Antenna for Wireless MedRadio-Band Biotelemetry Devices," *IEEE Antennas and Wireless Propagation Letters*, vol. 15, pp. 234-237, 2016.
- [135] L.-J. Xu, Y.-X. Guo, and W. Wu, "Miniaturized circularly polarized loop antenna for biomedical applications," *IEEE Transactions on Antennas and Propagation*, vol. 63, pp. 922-930, 2015.
- [136] P. Soontornpipit, C. M. Furse, and Y. C. Chung, "Design of implantable microstrip antenna for communication with medical implants," *IEEE Transactions on Microwave theory and techniques*, vol. 52, pp. 1944-1951, 2004.
- [137] A. E. Mohamed, M. S. Sharawi, and A. Muqaibel, "Implanted dual-band circular antenna for biomedical applications," *Microwave and Optical Technology Letters*, vol. 60, pp. 1125-1132, 2018.
- [138] "IEEE Standard for Safety Levels with Respect to Human Exposure to Radio Frequency Electromagnetic Fields, 3 kHz to 300 GHz Amendment 1: Specifies Ceiling Limits for Induced

- and Contact Current, Clarifies Distinctions between Localized Exposure and Spatial Peak Power Density," *IEEE Std C95.1a-2010 (Amendment to IEEE Std C95.1-2005)*, pp. 1-9, 2010.
- [139] I. Dove, "Analysis of radio propagation inside the human body for in-body Localization purposes," *Master's thesis, University of Twente*, 2014.
  - [140] S. Mustafa, B. Mohammed, and A. Abbosh, "Novel preprocessing techniques for accurate microwave imaging of human brain," *IEEE Antennas and Wireless Propagation Letters*, vol. 12, pp. 460-463, 2013.
  - [141] E. Ricci, E. Cianca, T. Rossi, M. Diomedi, and P. Deshpande, "Performance evaluation of novel microwave imaging algorithms for stroke detection using an accurate 3D head model," *Wireless Personal Communications*, vol. 96, pp. 3317-3331, 2017.
  - [142] L. M. Van Nieuwstadt, "Microwave measurement system for breast cancer imaging: An experimental prototype towards time-domain inverse scattering," *University of Michigan*, 2011.
  - [143] R. Elyassi and G. Moradi, "Flexible and moon-shaped slot UWB implantable antenna design for head implants," *International Journal of Microwave and Wireless Technologies*, pp. 1-9, 2017.
  - [144] K. N. Bocan, M. H. Mickle, and E. Sejdić, "Simulating, Modeling, and Sensing Variable Tissues for Wireless Implantable Medical Devices," *IEEE Transactions on Microwave Theory and Techniques*, 2018.
  - [145] H. Wong, Q. W. Lin, H. W. Lai, and X. Y. Zhang, "Substrate integrated meandering probe-fed patch antennas for wideband wireless devices," *IEEE Transactions on Components, Packaging and Manufacturing Technology*, vol. 5, pp. 381-388, 2015.
  - [146] H. Malekpoor and S. Jam, "Analysis on bandwidth enhancement of compact probe-fed patch antenna with equivalent transmission line model," *IET Microwaves, Antennas & Propagation*, vol. 9, pp. 1136-1143, 2015.
  - [147] H.-W. Lai and K.-M. Luk, "Design and study of wide-band patch antenna fed by meandering probe," *IEEE transactions on antennas and propagation*, vol. 54, pp. 564-571, 2006.
  - [148] K. Q. Da Costa, V. Dmitriev, D. Nascimento, and J. d. S. Lacava, "Broadband L-probe fed patch antenna combined with passive loop elements," *IEEE Antennas and Wireless Propagation Letters*, vol. 6, pp. 100-102, 2007.
  - [149] H. Wong, K.-M. Luk, C. H. Chan, Q. Xue, K. K. So, and H. W. Lai, "Small antennas in wireless communications," *Proceedings of the IEEE*, vol. 100, pp. 2109-2121, 2012.
  - [150] H. Nakano and J. Yamauchi, "Printed slot and wire antennas: A review," *Proceedings of the IEEE*, vol. 100, pp. 2158-2168, 2012.
  - [151] S. L. Coetzee, "Narrow band high resolution radar imaging," *University of London*, 2007.
  - [152] R. Leyva-Hernandez, J. A. Tirado-Mendez, H. Jardon-Aguilar, R. Flores-Leal, and L. Y. Miranda, "Reduced size elliptic UWB antenna with inscribed third iteration sierpinski triangle for on-body applications," *Microwave and Optical Technology Letters*, vol. 59, pp. 635-641, 2017.
  - [153] H. Dobšíček Trefná, J. Vrba, and M. Persson, "Evaluation of a patch antenna applicator for time reversal hyperthermia," *International Journal of Hyperthermia*, vol. 26, pp. 185-197, 2010.
  - [154] V. Karthik and T. Rama Rao, "Estimation of Specific Absorption Rate Using Infrared Thermography for the Biocompatibility of Wearable Wireless Devices," *Progress In Electromagnetics Research*, vol. 56, pp. 101-109, 2017.
  - [155] Y. B. Li, L. L. Li, B. B. Xu, W. Wu, R. Y. Wu, X. Wan, *et al.*, "Transmission-type 2-bit programmable metasurface for single-sensor and single-frequency microwave imaging," *Scientific reports*, vol. 6, p. 23731, 2016.
  - [156] P. Bernardi, M. Cavagnaro, S. Pisa, and E. Piuze, "Specific absorption rate and temperature increases in the head of a cellular-phone user," *IEEE transactions on microwave theory and techniques*, vol. 48, pp. 1118-1126, 2000.

- [157] P. Takook, M. Persson, J. Gellermann, and H. D. Trefná, "Compact self-grounded Bow-Tie antenna design for an UWB phased-array hyperthermia applicator," *International Journal of Hyperthermia*, vol. 33, pp. 387-400, 2017.
- [158] M. Rokunuzzaman, A. Ahmed, T. C. Baum, and W. S. T. Rowe, "Compact 3-D Antenna for Medical Diagnosis of the Human Head," *IEEE Transactions on Antennas and Propagation*, vol. 67, pp. 5093-5103, 2019.
- [159] S. Das and D. Mitra, "A compact wideband flexible implantable slot antenna design with enhanced gain," *IEEE Transactions on Antennas and Propagation*, vol. 66, pp. 4309-4314, 2018.
- [160] M. Manoufali, K. Bialkowski, B. Mohammed, P. C. Mills, and A. Abbosh, "Compact Implantable Antennas for the Cerebrospinal Fluid Monitoring," *IEEE Transactions on Antennas and Propagation*, vol. 67, pp. 4955-4967, 2019.
- [161] G. Samanta and D. Mitra, "Dual-Band Circular Polarized Flexible Implantable Antenna Using Reactive Impedance Substrate," *IEEE Transactions on Antennas and Propagation*, vol. 67, pp. 4218-4223, 2019.
- [162] R. B. Green and E. Topsakal, "Biocompatible Antennas for Implantable Biosensor Systems," in *2019 International Workshop on Antenna Technology (iWAT)*, 2019, pp. 70-72.
- [163] S. Pandey and V. R. Gupta, "Implantable Antenna for Blood Glucose Monitoring," in *Optical And Microwave Technologies*, ed: Springer, 2018, pp. 65-70.
- [164] M. M. Farhad, A. J. Islam, M. S. R. Bhuiyan, S. Chakraborty, B. Barua, and A. Biswas, "Design of a compact low loss multi-slotted antenna for WBAN applications and performance analysis at ISM band," in *2018 4th International Conference on Electrical Engineering and Information & Communication Technology (iCEEICT)*, 2018, pp. 354-359.
- [165] A. Biswas, M. S. B. Nesar, A. Muktedir, A. J. Islam, and N. Chakma, "A compact microstripline-fed on-body matched antenna for wireless medical applications," in *2018 4th International Conference on Electrical Engineering and Information & Communication Technology (iCEEICT)*, 2018, pp. 426-431.
- [166] Y. Zhang, C. Liu, X. Liu, K. Zhang, and X. Yang, "A wideband circularly polarized implantable antenna for 915 MHz ISM-band biotelemetry devices," *IEEE Antennas and Wireless Propagation Letters*, vol. 17, pp. 1473-1477, 2018.
- [167] R. Li, Y.-X. Guo, and G. Du, "A conformal circularly polarized antenna for wireless capsule endoscope systems," *IEEE Transactions on Antennas and Propagation*, vol. 66, pp. 2119-2124, 2018.
- [168] Z.-J. Yang, L. Zhu, and S. Xiao, "An implantable circularly polarized patch antenna design for pacemaker monitoring based on quality factor analysis," *IEEE Transactions on Antennas and Propagation*, vol. 66, pp. 5180-5192, 2018.
- [169] M. Medeiros, J. Lumini, N. Stern, G. Castañeda-Hernández, and G. Filler, "Generic immunosuppressants," *Pediatric Nephrology*, vol. 33, pp. 1123-1131, 2018.
- [170] J. Ishihara, A. Ishihara, K. Fukunaga, K. Sasaki, M. J. White, P. S. Briquez, *et al.*, "Laminin heparin-binding peptides bind to several growth factors and enhance diabetic wound healing," *Nature communications*, vol. 9, p. 2163, 2018.
- [171] S. Ud-Din and A. Bayat, "Effects of electrical stimulation on cutaneous wound healing: Evidence from in vitro studies and clinical trials," in *Conductive Polymers*, ed: CRC Press, 2018, pp. 373-386.
- [172] C. Lallyett, C.-Y. C. Yeung, R. H. Nielson, L. A. Zeef, D. Chapman-Jones, M. Kjaer, *et al.*, "Changes in S100 Proteins Identified in Healthy Skin following Electrical Stimulation: Relevance for Wound Healing," *Advances in skin & wound care*, vol. 31, pp. 322-327, 2018.
- [173] G. Tai, M. Tai, and M. Zhao, "Electrically stimulated cell migration and its contribution to wound healing," *Burns & trauma*, vol. 6, p. 20, 2018.

- [174] Y. Long, H. Wei, J. Li, G. Yao, B. Yu, D. Ni, *et al.*, "Effective Wound Healing Enabled by Discrete Alternative Electric Fields from Wearable Nanogenerators," *ACS nano*, vol. 12, pp. 12533-12540, 2018.
- [175] K. Schonenberger and V. Vriz, "Wound healing electrode set," ed: Google Patents, 2019.
- [176] Y. Shapira, V. Sammons, J. Forden, G. F. Guo, A. Kipp, J. Girgulis, *et al.*, "Brief electrical stimulation promotes nerve regeneration following experimental in-continuity nerve injury," *Neurosurgery*, vol. 85, pp. 156-163, 2018.
- [177] J. Senger, V. Verge, H. Macandili, J. Olson, K. Chan, and C. Webber, "Electrical stimulation as a conditioning strategy for promoting and accelerating peripheral nerve regeneration," *Experimental neurology*, vol. 302, pp. 75-84, 2018.
- [178] W. Zhang and C. C. Mi, "Compensation topologies of high-power wireless power transfer systems," *IEEE Transactions on Vehicular Technology*, vol. 65, pp. 4768-4778, 2015.
- [179] X. Li, C.-Y. Tsui, and W.-H. Ki, "A 13.56 MHz wireless power transfer system with reconfigurable resonant regulating rectifier and wireless power control for implantable medical devices," *IEEE Journal of Solid-State Circuits*, vol. 50, pp. 978-989, 2015.
- [180] R. Das and H. Yoo, "A multiband antenna associating wireless monitoring and nonleaky wireless power transfer system for biomedical implants," *IEEE Transactions on Microwave Theory and Techniques*, vol. 65, pp. 2485-2495, 2017.
- [181] S. Rao and J.-C. Chiao, "Body electric: Wireless power transfer for implant applications," *IEEE Microwave Magazine*, vol. 16, pp. 54-64, 2015.
- [182] A. N. Abdulfattah, C. C. Tsimenidis, B. Z. Al-Jewad, and A. Yakovlev, "Performance Analysis of MICS-based RF Wireless Power Transfer System for Implantable Medical Devices," *IEEE Access*, vol. 7, pp. 11775-11784, 2019.
- [183] K. Agarwal, R. Jegadeesan, Y.-X. Guo, and N. V. Thakor, "Wireless power transfer strategies for implantable bioelectronics," *IEEE reviews in biomedical engineering*, vol. 10, pp. 136-161, 2017.
- [184] A. M. Jawad, R. Nordin, S. K. Gharghan, H. M. Jawad, and M. Ismail, "Opportunities and challenges for near-field wireless power transfer: A review," *energies*, vol. 10, p. 1022, 2017.
- [185] A. Amar, A. Kouki, and H. Cao, "Power approaches for implantable medical devices," *sensors*, vol. 15, pp. 28889-28914, 2015.
- [186] R. Jegadeesan, K. Agarwal, Y.-X. Guo, S.-C. Yen, and N. V. Thakor, "Wireless power delivery to flexible subcutaneous implants using capacitive coupling," *IEEE Transactions on Microwave Theory and Techniques*, vol. 65, pp. 280-292, 2016.
- [187] M. K. U. Sikder, J. Fallon, M. N. Shivdasani, K. Ganesan, P. Seligman, and D. J. Garrett, "Wireless induction coils embedded in diamond for power transfer in medical implants," *Biomedical microdevices*, vol. 19, p. 79, 2017.
- [188] J. Koo, M. R. MacEwan, S.-K. Kang, S. M. Won, M. Stephen, P. Gamble, *et al.*, "Wireless bioresorbable electronic system enables sustained nonpharmacological neuroregenerative therapy," *Nature medicine*, vol. 24, p. 1830, 2018.
- [189] H. Zhang, L. Li, C. Liu, Y. X. Guo, and S. Wu, "Miniaturized implantable antenna integrated with split resonate rings for wireless power transfer and data telemetry," *Microwave and Optical Technology Letters*, vol. 59, pp. 710-714, 2017.
- [190] J. Xu, M. Yu, C. Peng, P. Carter, J. Tian, X. Ning, *et al.*, "Dose Dependencies and Biocompatibility of Renal Clearable Gold Nanoparticles: From Mice to Non-human Primates," *Angewandte Chemie International Edition*, vol. 57, pp. 266-271, 2018.
- [191] J. Garnica, R. A. Chinga, and J. Lin, "Wireless power transmission: From far field to near field," *Proceedings of the IEEE*, vol. 101, pp. 1321-1331, 2013.
- [192] L.-J. Xu, Y. Bo, W.-J. Lu, L. Zhu, and C.-F. Guo, "Circularly Polarized Annular Ring Antenna With Wide Axial-Ratio Bandwidth for Biomedical Applications," *IEEE Access*, vol. 7, pp. 59999-60009, 2019.

- [193] K. Pawelec, C. Yoon, R. Giger, and J. Sakamoto, "Engineering a platform for nerve regeneration with direct application to nerve repair technology," *Biomaterials*, p. 119263, 2019.
- [194] E. Soriano, J. del Valle, C. Roselló Busquets, N. de la Oliva, R. Martínez Mármol, M. Hernaiz Llorens, *et al.*, "Cholesterol depletion regulates axonal growth and enhances central and peripheral nerve regeneration," *Frontiers in cellular neuroscience*, vol. 13, p. 40, 2019.
- [195] W. Arnold and U. Zimmermann, "Dielectric properties of zwitterion solutions," ed: Portland Press Limited, 1993.
- [196] A. Docoslis, N. Kalogerakis, L. A. Behie, and K. V. Kaler, "A novel dielectrophoresis-based device for the selective retention of viable cells in cell culture media," *Biotechnology and bioengineering*, vol. 54, pp. 239-250, 1997.